
Dynamics of the bar and the bulge of the Andromeda galaxy (M31)

Matías Andrés Blaña Díaz



München 2018

Dynamics of the bar and the bulge of the Andromeda galaxy (M31)

Matías Andrés Blaña Díaz

Dissertation
an der Fakultät für Physik
der Ludwig–Maximilians–Universität
München

vorgelegt von
Matías Andrés Blaña Díaz
aus Santiago, Chile

München, den 14. Februar 2018

Erstgutachter: Prof. Dr. Ortwin Gerhard

Zweitgutachter: PD. Dr. Roberto Saglia

Tag der mündlichen Prüfung: 19. März 2018

To my beautiful and beloved Carolina

When lost, go back to basics.

Rolf Neumann

Contents

Zusammenfassung	xv
Abstract	xvii
1 Introduction	1
1.1 Classical bulges and pseudobulges	3
1.1.1 Distinguishing bulge classes by their main properties	3
1.1.2 Classical bulges	6
1.1.3 Pseudobulges	9
1.2 Barred galaxies	13
1.2.1 Bars and Box/Peanut Bulges	16
1.2.2 Dynamical evolution of bars	17
1.2.3 Downfall of bars	17
1.2.4 Gas dynamics in barred galaxies	18
1.3 The Andromeda galaxy	19
1.3.1 The galactic centre: Nuclei & Supermassive Black Hole	21
1.3.2 The composite bulge: classical bulge, B/P bulge and thin bar	22
1.3.3 The stellar disc	24
1.3.4 The stellar halo	25
1.3.5 The gas and dust distribution	26
1.3.6 The dark matter and dynamical mass distribution	27
1.3.7 The satellites of Andromeda	28
1.4 Main goals and outline of the thesis	28
2 Dynamical Models for M31 - Bulge & Bar	31
2.1 Introduction	32
2.2 Observational data: M31 IRAC 3.6 μm image	34
2.3 Method	35
2.3.1 Simulations	35
2.3.2 Technique to obtain the best-matching model	38
2.4 Results	41
2.4.1 Morphology: bulge isophotal twist & bar angle θ_{bar}	41
2.4.2 Morphology: position angle, boxiness, ellipticity & asymmetry	45

2.4.3	Photometry: M31's surface-brightness – two bulge components?	48
2.4.4	Parameter space for the ICB	51
2.4.5	Best model properties	54
2.4.6	The thin bar of M31	63
2.5	Triaxial models for the bulge of M31 in the literature.	68
2.6	Conclusions	69
2.A	Initial Conditions and Bar Formation	70
3	M2M models for M31's bar and composite bulge	71
3.1	Introduction	72
3.2	Modelling the bulge of M31	73
3.2.1	Made-to-measure method	74
3.2.2	Inputs to the M2M modelling from B17: initial N-body model and projection angles	75
3.2.3	Fitting the photometry and IFU kinematics	76
3.2.4	Adjusting the dark matter mass within the bulge (M_{DM}^{B}), and fitting the HI rotation curve	80
3.2.5	Bar pattern speed adjustment (Ω_{p})	82
3.2.6	Potential solver and orbital integration	82
3.2.7	M2M fitting procedure and parameters	83
3.2.8	Method to find the best model in the parameter space	85
3.3	Results	92
3.3.1	Parameter space: the best M2M models	93
3.3.2	Properties of the best M2M model	108
3.4	Conclusions	127
3.A	Cube of parameters	128
4	Final summary	133
4.1	M31 context and implications	135
5	Outlook and Future Work	139
5.1	Chemodynamical modelling of M31	139
5.2	Improved M2M models for M31: substructures	140
5.3	Future spectroscopic observations of M31 and the dust modelling	141
5.4	Gas dynamics in M31: outer ring and inner streams	141
5.5	Microlensing modelling of M31	142
Appendix		159
5.6	Constants and units	159
5.7	Basic relations	159
5.8	Stellar dynamics	160
5.9	Tables	161

List of Figures

1.1	The Andromeda galaxy (M31, NGC224)	2
1.2	Bulge properties	3
1.3	Bulge properties II: Sérsic index	4
1.4	Galaxy evolution mechanisms	7
1.5	Sombrero galaxy	8
1.6	The Illustris simulation	10
1.7	ΛCDM high resolution simulations	11
1.8	Pseudobulges	12
1.9	Galaxy NGC1300	13
1.10	Galaxy NGC 4921	14
1.11	Morphological classification of spiral galaxies	15
1.12	Lindblad resonances.	16
1.13	Gas simulation	19
1.14	M31 environment and the streams	20
2.1	Orientation diagram of M31	41
2.2	M31 IRAC 3.6 μm and Model 1 images	42
2.3	Bar PA and maximum PA	43
2.4	ellipse profiles for M31 and models	46
2.5	Surface-brightness profiles for M31 and model1	49
2.6	Classical bulge initial parameter space	52
2.7	Model 1 maps	55
2.8	Line-of-sight kinematic profiles of M31 and Model 1 and Model 0	56
2.9	Line-of-sight kinematic maps of Model 1	58
2.10	Circular velocity and angular frequency of Model 1 and HI rotation curve of M31	61
2.11	Cumulative mass profile of Model 1	62
2.12	Thin bar of Model 1 at two snapshots	64
2.13	Model 5 map	67
3.1	FOC parameters	84
3.2	Chi-square versus time	85
3.3	Photometric and kinematic relative errors	86
3.4	Photometric relative error map	87

3.5	Chi-square subsets diagram	90
3.6	Parameter $\Delta\hat{\chi}_{\text{sum}}^2$: best models	93
3.7	Subsets part 1	95
3.8	Photometry and dispersion maps with residuals	96
3.9	Mass-to-light versus metallicity and age	100
3.10	Mass profiles	101
3.11	Circular velocity profiles	102
3.12	Dark matter density profiles	103
3.13	Subsets part 2	105
3.14	Velocity maps and residuals	107
3.15	Bar angle	108
3.16	Surface-brightness maps and residuals	110
3.17	Bulge surface-brightness maps and residuals	111
3.18	Bulge components surface-brightness maps	112
3.19	Surface-brightness profiles	113
3.20	M31 orientation diagram	115
3.21	M31 absorption map	116
3.22	Kinematic maps and isophotes of M31 and the best model	118
3.23	Kinematic maps and isophotes of the best model bulge components	119
3.24	Surface-brightness and kinematic disc cuts	120
3.25	Surface-brightness and kinematic bulge cuts	121
3.26	Intrinsic kinematic profiles	122
3.27	Best model circular velocity profiles, angular frequency profiles and resonances	126
3.28	Subset results for the NFW grid of model, part 1	129
3.29	Subset results for the NFW grid of model, part 2	130
3.30	Subset results for the Einasto grid of model	131
5.1	M31 metallicity map	139
5.2	M31 gas simulation	142
5.3	Optical depth $\langle\tau\rangle$	143

List of Tables

1.1	Main properties of M31	21
2.1	Parameters for M31 and Model 1 at different times.	53
3.1	Best Einasto models	89
3.2	Best NFW models	89
3.3	Bulge components with different $\Upsilon_{3.6}$ values	99
3.4	Photometric parameters	114
5.1	Solar absolute magnitudes	162
5.2	Spectral types	162
5.3	Redshift, age and time conversion	162

Zusammenfassung

Die Andromedagalaxie ist unsere nächste benachbarte Scheibengalaxie und ein bevorzugtes Objekt für die detaillierte Modellierung und Untersuchung der evolutionären Prozesse, die Galaxien bilden.

Im ersten Teil dieser Arbeit wird die Zusammensetzung des triaxialen Bulge von M31 mit einem umfangreichen Set von N-body Modellen untersucht, die einen Box/Peanut (B/P) - Bulge sowie einen klassischen Bulge (CB) enthalten. Wenn man mit den $3.6\mu\text{m}$ Daten der IRAC (Infrared-Array-Camera) vergleicht, stimmt nur ein Modell gleichzeitig mit allen morphologischen Eigenschaften des M31 Bulge überein, und erfordert einen klassischen Bulge und einen B/P-Bulge mit $1/3$ und $2/3$ der gesamten Masse des Bulge. Wir finden fest, dass reine B/P-bulge Modelle keine genügend hohe Konzentrationen zeigen, um dem Sersic Index (n) und dem effektives Radius des M31-Bulge zu entsprechen. Stattdessen benötigt das beste Modell auch eine klassische Bulgekomponente mit Masse $M^{\text{CB}}=1.1 \times 10^{10} M_{\odot}$ und dreidimensionalem Halbmassenradius $r_{\text{half}}^{\text{CB}}=0.53 \text{ kpc}$ (140 arcsec). Die B/P-Bulgekomponente hat eine Masse von $M^{\text{B/P}}=2.2 \times 10^{10} M_{\odot}$ und einen Halbmassenradius von $r_{\text{half}}^{\text{B/P}}=1.3 \text{ kpc}$ (340 arcsec). Der B/P-Bulge des Modells erstreckt sich in der Ebene der Scheibe bis $r^{\text{B/P}}=3.2 \text{ kpc}$ (840 arcsec), ebenso wie die Bulge von M31. In diesem Composite-Bulge-Modell erklärt die klassische Bulge-Komponente den beobachteten Geschwindigkeitsdispersionsabfall im Zentrum für $R < 190 \text{ pc}$ (50 arcsec), während die B / P-Bulgekomponente die beobachtete schnelle Rotation und die kinematische Verdrehung der beobachteten Nullgeschwindigkeitslinie reproduziert. Die Balkenrotationsgeschwindigkeit dieses Modells ist $\Omega_p=38 \text{ km s}^{-1} \text{ kpc}^{-1}$, wobei die Korotation bei $r_{\text{cor}}=5.8 \text{ kpc}$ (1500 arcsec) liegt. Die äußere Lindblad-Resonanz (OLR) liegt dann bei $r_{\text{OLR}}=10.4 \text{ kpc}$, nahe dem 10 kpc-Ring von M31, was darauf hindeutet, dass diese Struktur mit der OLR des Balkens in Beziehung gesetzt werden kann. Durch Vergleich mit einem früheren Entwicklungsschritt schätzen wir, dass sich der flache Balken von M31 in der Scheibenebene auf $r_{\text{bar}}^{\text{thin}} \sim 4.0 \text{ kpc}$ (1000 arcsec) und in der Projektion auf $R_{\text{bar}}^{\text{thin}} \sim 2.3 \text{ kpc}$ (600 arcsec) erstreckt.

Im zweiten Teil diskutieren wir verbesserte made-to-measure Modelle, die beginnend mit dem zuvor gefundenen besten N-Body Komposit-Bulge-Modell konstruiert wurden, unter Verwendung von neuen VIRUS-W IFU kinematischen Beobachtungen, der IRAC $3.6 \mu\text{m}$ Photometrie und der HI Scheiberotationskurve. Wir untersuchen den Parameterraum für das Masse-zu-Licht-Verhältnis ($\Upsilon_{3.6}$), die Balkenrotationsgeschwindigkeit des B/P-Bulge und Balkens (Ω_p) und die Masse der dunklen Materie innerhalb von 3.2 kpc des Bulge (M_{DM}^{B}). Mit einem Einasto-Profil für die dunkle Materie finden wir für den Bereich der besten Modelle $\Upsilon_{3.6}=0.72 \pm 0.02 M_{\odot} L_{\odot}^{-1}$,

$\Omega_p = 40 \pm 5 \text{ km s}^{-1} \text{ kpc}^{-1}$ und $M_{\text{DM}}^{\text{B}} = 1.2_{-0.4}^{+0.2} \times 10^{10} \text{ M}_{\odot}$. Diese Modelle haben eine totale dynamische Masse im zusammengesetzten Bulge von $M_{\text{dyn}}^{\text{B}} = 4.25_{-0.29}^{+0.10} \times 10^{10} \text{ M}_{\odot}$ mit einer dunkle Materie Masse von 27% und einer gesamten stellaren Masse von $M_{\star}^{\text{B}} = 3.09_{-0.12}^{+0.10} \times 10^{10} \text{ M}_{\odot}$ (73%), wovon der klassische Bulge $M_{\star}^{\text{CB}} = 1.18_{-0.07}^{+0.06} \times 10^{10} \text{ M}_{\odot}$ (28%) und der B/P-Bulge $M_{\star}^{\text{BP}} = 1.91 \pm 0.06 \times 10^{10} \text{ M}_{\odot}$ (45%) enthalten. Wir haben auch Modelle mit NFW-Profilen für die dunkle Materie untersucht, wobei festgestellt wurde, dass die Einasto-Modelle zwar besser als die NFW-Modelle zur Bulgestellarkinematik passen, die erhaltenen Hauptparameter jedoch innerhalb der Fehler übereinstimmen. Die M_{DM}^{B} Werte stimmen mit adiabatisch kontrahierten kosmologischen NFW Halos mit der Virialmasse von M31 überein. Das beste Modell hat zwei Bulgekomponenten mit völlig unterschiedlichen Kinematiken, die nur zusammen die photometrischen und kinematischen Beobachtungen von M31 erfolgreich reproduzieren ($v_{\text{los}}, \sigma_{\text{los}}, h3, h4$). Die Modellierung umfasst Staubabsorptionseffekte, die asymmetrische Merkmale reproduzieren, die in den kinematischen Beobachtungen gefunden wurden.

Unsere Ergebnisse liefern neue Einschränkungen für die frühe Bildungsgeschichte und die Entwicklung von M31 angesichts der niedrigeren Masse, die für die klassische Bulge-Komponente im Vergleich zu früheren Messungen gefunden wurde, des bevorzugten flachen Profils der dunklen Materie, sowie angesichts der säkularen Evolution von M31, die durch der massiven B/P-Bulge und Balken impliziert wird, und seine Wechselwirkungen mit dem klassischen Bulge und der Scheibe durch Resonanzen.

Abstract

The Andromeda galaxy is our nearest neighbour disk galaxy and a prime target for detailed modelling and study of the evolutionary processes that shape galaxies.

In the first part of this thesis the nature of M31's triaxial bulge is analysed with an extensive set of N-body models built with Box/Peanut (B/P) bulges as well as classical bulges (CBs). Comparing with the IRAC (Infrared-Array-Camera) $3.6\ \mu\text{m}$ data, only one model matches simultaneously all the morphological properties of M31's bulge, and requires a classical bulge and a B/P bulge with 1/3 and 2/3 of the total bulge mass respectively. We find that our pure B/P bulge models do not show concentrations high enough to match the Sérsic index (n) and the effective radius of M31's bulge. Instead, the best model requires a classical bulge component with mass $M^{\text{CB}}=1.1 \times 10^{10}\ \text{M}_\odot$ and three-dimensional half-mass radius $r_{\text{half}}^{\text{CB}}=0.53\ \text{kpc}$ (140 arcsec). The B/P bulge component has a mass of $M^{\text{B/P}}=2.2 \times 10^{10}\ \text{M}_\odot$ and a half-mass radius of $r_{\text{half}}^{\text{B/P}}=1.3\ \text{kpc}$ (340 arcsec). The model's B/P bulge extends to $r^{\text{B/P}}=3.2\ \text{kpc}$ (840 arcsec) in the plane of the disk, as does M31's bulge. In this composite bulge model, the classical bulge component explains the velocity dispersion drop observed in the centre within $R < 190\ \text{pc}$ (50 arcsec), while the B/P bulge component reproduces the observed rapid rotation and the kinematic twist of the observed zero velocity line. This model's pattern speed is $\Omega_p=38\ \text{km s}^{-1}\ \text{kpc}^{-1}$, placing corotation at $r_{\text{cor}}=5.8\ \text{kpc}$ (1500 arcsec). The outer Lindblad resonance (OLR) is then at $r_{\text{OLR}}=10.4\ \text{kpc}$, near the 10 kpc-ring of M31, suggesting that this structure may be related to the bar's OLR. By comparison with an earlier snapshot, we estimate that M31's thin bar extends to $r_{\text{bar}}^{\text{thin}}\sim 4.0\ \text{kpc}$ (1000 arcsec) in the disk plane, and in projection extends to $R_{\text{bar}}^{\text{thin}}\sim 2.3\ \text{kpc}$ (600 arcsec).

In the second part we construct a large set of made-to-measure models improving the previously found best N-body composite bulge model, using as fitting constraints new VIRUS-W IFU kinematic observations, the IRAC $3.6\ \mu\text{m}$ photometry, and the disc's HI rotation curve. We explore the parameter space for the $3.6\ \mu\text{m}$ mass-to-light ratio ($\Upsilon_{3.6}$), the pattern speed of the B/P bulge and the thin bar (Ω_p), and the dark matter mass content within 3.2 kpc) of the bulge (M_{DM}^{B}). Considering Einasto dark matter profiles, we find the best fitting models for $\Upsilon_{3.6}=0.72\pm 0.02\ \text{M}_\odot\ \text{L}_\odot^{-1}$, $\Omega_p=40\pm 5\ \text{km s}^{-1}\ \text{kpc}^{-1}$ and $M_{\text{DM}}^{\text{B}}=1.2_{-0.4}^{+0.2}\times 10^{10}\ \text{M}_\odot$. These models have a total dynamical mass within the composite bulge of $M_{\text{dyn}}^{\text{B}}=4.25_{-0.29}^{+0.10}\times 10^{10}\ \text{M}_\odot$ including 27% of dark matter and a stellar mass of $M_\star^{\text{B}}=3.09_{-0.12}^{+0.10}\times 10^{10}\ \text{M}_\odot$ (73%), where the classical bulge has $M_\star^{\text{CB}}=1.18_{-0.07}^{+0.06}\times 10^{10}\ \text{M}_\odot$ (28%) and the B/P bulge has $M_\star^{\text{BP}}=1.91\pm 0.06\times 10^{10}\ \text{M}_\odot$ (45%). We also explored models with NFW dark matter profiles, finding that while the Einasto models fit the

bulge stellar kinematics better than the NFW models, the obtained main parameters agree within the errors. The M_{DM}^{B} values agree with adiabatically contracted cosmological NFW haloes with M31's virial mass. The best model has two bulge components with completely different kinematics that only together successfully reproduce the M31 photometric and kinematic maps ($v_{\text{los}}, \sigma_{\text{los}}, h3, h4$). The modelling includes dust absorption effects that reproduce asymmetric features detected in the kinematic observations.

Our results provide new constraints for the early formation history of M31 given the lower mass found for the classical bulge component compared to previous estimates, the preferred cored dark matter profile, as well as the secular evolution of M31 implied by the massive B/P bulge and thin bar, and its interactions with the classical bulge and the disc through resonances.

Chapter 1

Introduction

Galaxies in the Universe are dynamical, forming and evolving at multiple temporal and spatial scales. Their early formation history, at redshifts of $z > 1$ ($\text{Age}_{\text{Universe}} < 5.9 \text{ Gyr}$), is mostly characterised by the hierarchical formation, where galaxies in clusters grow by mergers. These processes were violent, fast and shaped different species of galaxies that lead to some types of galaxies in the realm of galaxies, such as elliptical galaxies and dwarf galaxies. Other types of galaxies formed later, such as disc galaxies, which can contain classical bulges that were formed during the early formation phase. Galaxies in the local universe, at redshifts of $z < 0.1$ ($\text{Age}_{\text{Universe}} > 12.4 \text{ Gyr}$), are more mature galaxies which show a much lower merger rate compared to earlier times. Those that live in less crowded environments evolve mostly by secular evolution. Disk galaxies can have substructures like spiral arms and bars that form and evolve secularly by the slow rearrangements of mass, energy and angular momentum.

The Andromeda galaxy (M31, NGC224) is the largest and the most massive galaxy in the Local Group, and it is the nearest neighbouring spiral galaxy (Fig.1.1) located at 780 kpc (2.5 million light years) from the Milky Way (MW) (McConnachie et al. 2005). Its proximity presents us an excellent opportunity to better understand and to disentangle the different substructures, going from parsec scales up to several kiloparsecs, which allows us to better study the formation and the evolution of galaxies. M31 shows most of the typical substructures observed in other external galaxies: a classical bulge, a box/peanut bulge, a thin bar, a stellar disc that exhibit spiral arms at 5 kpc and two ring-like structures at 10 kpc and 15 kpc, a stellar halo, satellite galaxies and accretions streams. The centre is dominated by a massive and strongly triaxial bulge as shown in Fig.1.1, and historically it has been considered as a classical bulge. Although there have been some previous studies that estimate the properties of the bar of M31, it is only very recently that it has been considered the possibility of the coexistence of a classical bulge entangled to a box/peanut bulge and a thin bar. The most important goals of this thesis is to present the first quantitative mass estimation in the literature of the different bulge components that are present in Andromeda, and ultimately to present the first constraints for the dark matter mass within the bulge volume that considers a barred galaxy model for M31.

Before we submerge into the details of M31 and its classical bulge, its box/peanut bulge, and other substructures, I present a concise introduction to the different formation mechanisms and properties of the different types of bulges in the universe.

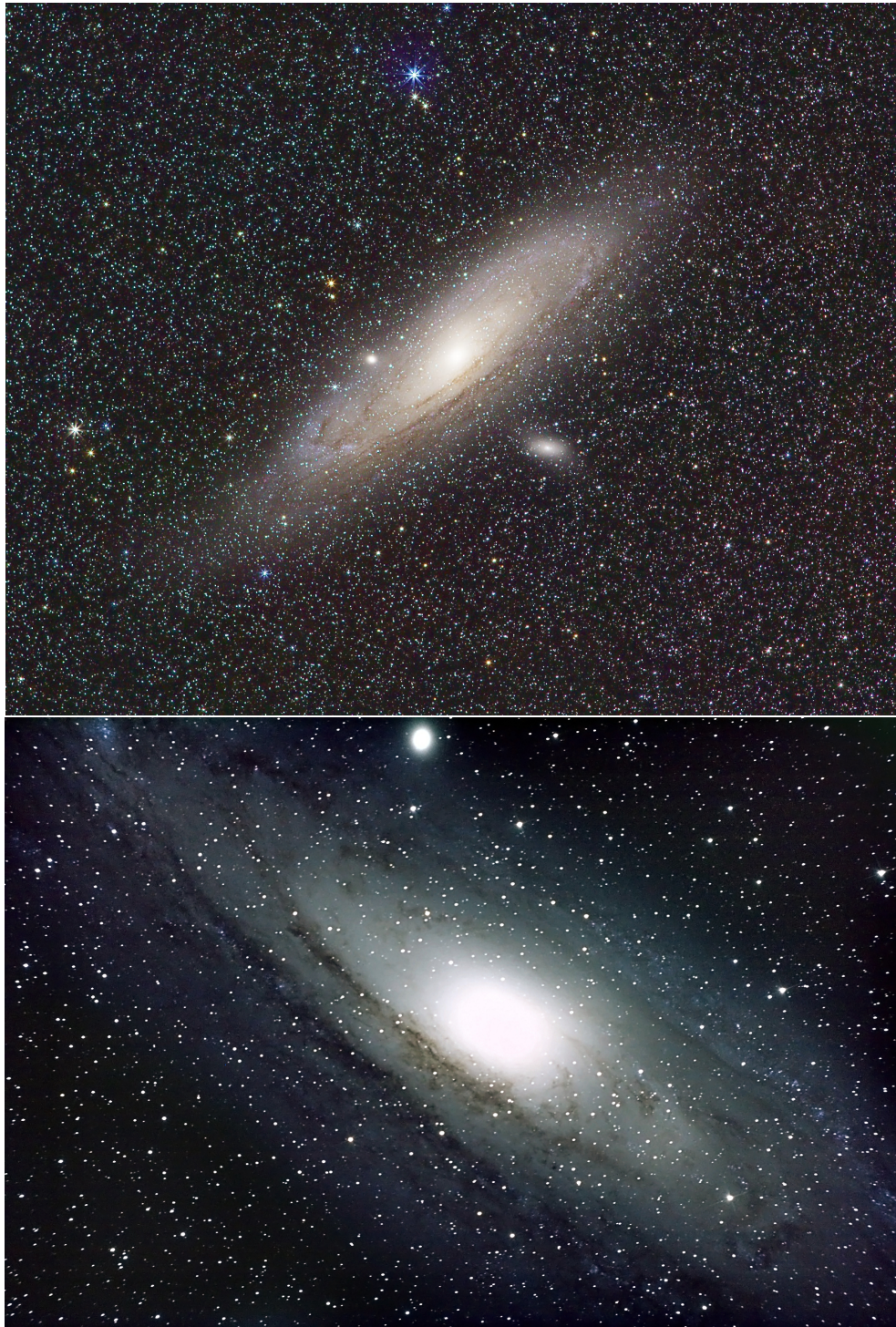


Figure 1.1: Top panel: the Andromeda galaxy (M31, NGC224) with the satellite galaxies M32 (NGC 221) and M110 (NGC 205), located respectively left and right from the image's centre, with the North pointing to the right, and the East pointing to the top. Bottom panel: a zoom into the M31 bulge, with M32 located over M31's centre, with the North pointing to the bottom and the East pointing to the right. Photographies, a courtesy from the astronomer and astrophotographer Torben Simm.

1.1 Classical bulges and pseudobulges

Disk galaxies may present an over-density of stars in their centres, a substructure defined as a bulge, which can be found in two main classes: classical bulges and pseudobulges (Kormendy & Kennicutt 2004; Kormendy 2013). Classical bulges are believed to be generated from mergers or gravitational collapse, while pseudobulges arise gradually from a process known as secular evolution. Pseudobulges can be further classified in two main different subtypes: boxy/peanut (B/P) bulges that are part of a bar built from stellar disc material; and discy bulges, which are formed from gas accreted in the centre forming stars. Furthermore, all three types of bulges could be simultaneously found in a particular galaxy, and it is therefore important to quantify the contribution of each bulge component in large samples of galaxies if we want to better understand the formation and evolution of galaxies. For example, by determining the contribution the classical bulge component in a galaxy, we can better constrain and infer how was the early stage of a galaxy.

1.1.1 Distinguishing bulge classes by their main properties

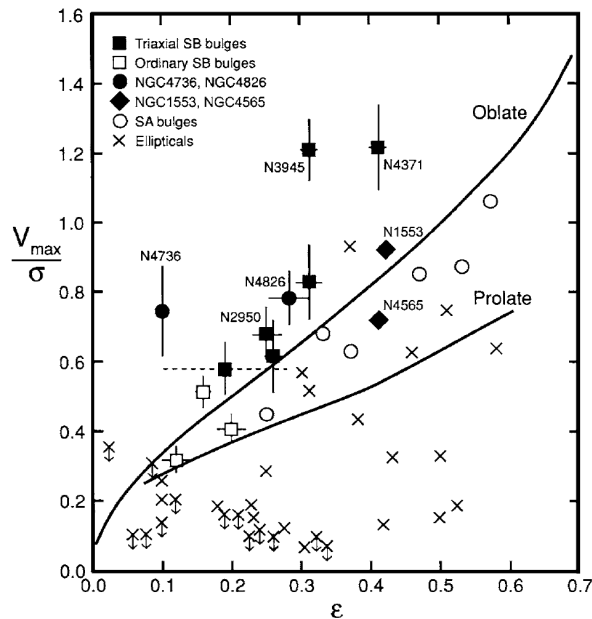


Figure 1.2: Taken from (Kormendy & Kennicutt 2004). Maximum velocity to dispersion ratio (V_{\max}/σ) within the half mass radius as function of the observed ellipticity ($\epsilon=1 - \text{axial ratio}$) for different types of galaxies. The “oblate” curve shows systems that have isotropic dispersion and are flattened only by rotation. The “prolate” curve shows systems that can rotate more slowly because they are partially flattened by dispersion anisotropy. (Symbols explained in the figure, with open symbols corresponding to classical bulges, and filled symbols to pseudobulges).

The number of pseudobulges in near disk galaxies is almost as abundant as classical bulges (Carollo et al. 1997, 1998). In a sample of 75 galaxies (Kormendy & Kennicutt 2004), the clas-

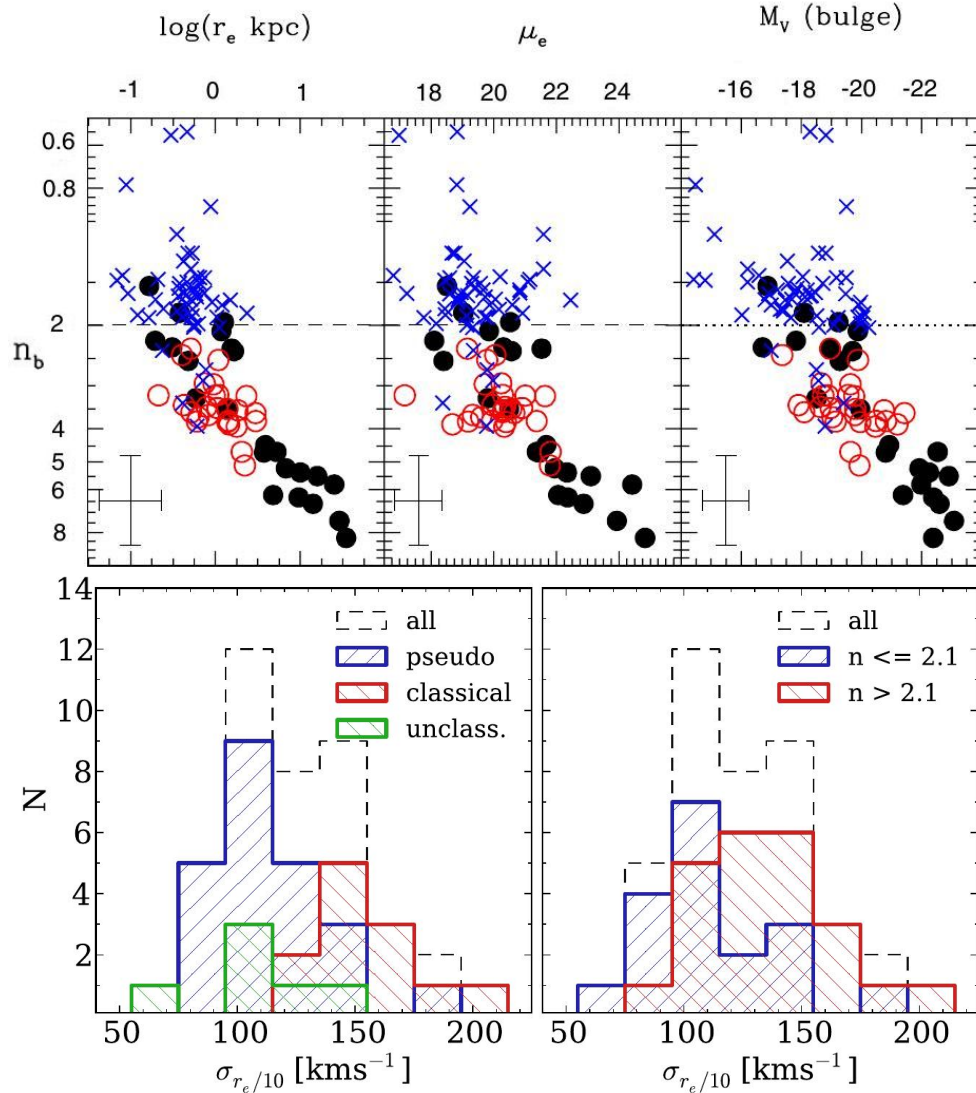


Figure 1.3: Sérsic index as bulge type indicator. Top panels: taken from (Fisher & Drory 2008). Correlations of the Sérsic index n_b as function of the absolute magnitude (M_V), half-light radius (r_e), and the surface-brightness at the half-light radius (μ_e). Bulge types: Pseudobulges (blue crosses), classical bulges (red circles) and elliptical galaxies (black filled circles, from Kormendy et al. 2008). The average uncertainty of the parameters of all bulges is represented by the error bars in the bottom left corner of each panel. Bottom panels: taken from (Fabricius et al. 2012) Histograms of the central velocity dispersions $\sigma_{r_e/10}$. The bottom left panel discriminates bulge types by morphology, and the bottom right panel discriminates them by their Sérsic index n .

sical bulges are present in 69% of 13 S0-Sa galaxy types, 50% of 10 Sab, 22% of 23 Sb, 11% of 19 Sbc and 0% of 10 Sc and later types. Most of the remaining galaxies are pseudobulges or classical bulges with characteristics of pseudobulges. These sample studies also show that the Hubble galaxy type correlates with the bulge type. Classical bulges are more frequently found in

early-type disk galaxies, while pseudobulges are more frequent in late-type disks. Furthermore, different types of bulges can coexist in a galaxy resulting in a composite bulge, which can present a classical bulge, a disky pseudobulge and a B/P bulge simultaneously (Erwin et al. 2015). These components can influence each other in their dynamical evolution, where for example the classical bulge can gain rotation from the bar (Saha et al. 2012).

How are classical bulges and pseudo-bulges observationally distinguished? Several relations have been discovered that show correlations between the main parameters of a galaxy, and furthermore, these relations group galaxies depending on their morphology. Some of these relations are: (I) the Fundamental Plane (FP) that relates the effective radius, central velocity dispersion, and central surface-brightness of a galaxy (R_e , σ_o , I_e) (Djorgovski & Davis 1987); (II) The Faber-Jackson relation Faber & Jackson (1976), which is a projection of the Fundamental Plane that relates the central luminosity and the velocity dispersion of a galaxy ($L \propto \sigma^\alpha$, with $\alpha \sim 4$). Typically elliptical galaxies and classical bulges follow this relation, while pseudobulges don't; (III) the M-sigma relation (Merritt 1999), connecting the dispersion of a galaxy with the mass of the central supermassive black hole. Again, this relation is followed by classical bulges, ellipticals but not pseudobulges; (IV) and the $V_{\max}/\sigma - \epsilon$ diagram shown in Figure 1.2 from Kormendy & Kennicutt (2004) with relations derived from the Virial Theorem for oblate and prolate systems. A system can be flattened by rotation (large V_{\max}/σ), or it can be flattened by an anisotropy in the dispersion (smaller V_{\max}/σ). Comparing with this relation Kormendy & Kennicutt (2004) finds that for the same flattening pseudobulges have typically higher rotation than classical bulges.

Also with the goal of separating pseudobulges and classical bulges, Fisher & Drory (2008) (see Figure 1.3) use a sample of spiral galaxies with bulges and to determine their photometric properties such as the Sérsic index n , the effective radius R_e , and the disk scale length R_d , to distinguish pseudobulges from classical bulges. They conclude that usually pseudobulges have Sérsic indices $n \lesssim 2$ and classical bulges indices $n \gtrsim 2$. Fabricius et al. (2012) (see Figure 1.3) additionally show a correlation between the Sérsic index, the velocity dispersion and the rotation. They compare the Sérsic index and the velocity dispersion averaged within one tenth of the effective radius $\sigma_{R_e/10}$. Their sample shows that classical bulges, defined morphologically or through a Sérsic index of $n \gtrsim 2.1$, tend to have higher $\sigma_{R_e/10}$, rarely getting lower than 100 km s^{-1} and with a mean of the sample of $\sim 150 \text{ km s}^{-1}$. Pseudobulges, defined with $n \lesssim 2.1$, show lower $\sigma_{R_e/10}$, some as low as $\sim 50 \text{ km s}^{-1}$, and a mean value of 100 km s^{-1} for the sample. However these classification criteria have only statistical meanings, as a particular galaxy, and its bulge, may actually present properties of both types of bulges.

A summary of the main properties that distinguish classical bulges and pseudobulges is:

- the surface-brightness profiles in pseudo-bulges are closer to an exponential law, flatter than the profile of classical bulges, which are better represented by a de-Vaucouleurs $r^{1/4}$ -law.
- when fitted by a Sérsic profile, the Sérsic index of $n \sim 2$ is a threshold, being higher for classical bulges, and lower for pseudobulges.
- pseudobulges have a higher rotation/dispersion (V/σ) ratio than classical bulges.

- pseudobulges have smaller velocity dispersions than the expected through the Faber-Jackson relation for classical bulges.
- pseudo bulges show high star formation in their centres.
- B/P bulges have the kinematic properties of barred galaxies, which includes cylindrical rotation, a bar pattern speed (Ω_p), and a correlation between the line-of-sight velocity (v_{los}) and the $h3$ Gauss Hermite coefficient (Bureau & Athanassoula 2005).

1.1.2 Classical bulges

The astronomical term bulge appeared when astronomers discovered over-densities in the centres of disk galaxies. They resemble elliptical galaxies and according to current theories, they were formed in a similar manner, by an early gravitational collapse or by mergers of galaxies. The diagram in Fig.1.4 from Kormendy (2013) synthesises the four main mechanisms that drive the formation and the evolution of galaxies, which are separated in fast-internal process (proto-galactic collapse), fast-external process (galaxy mergers), slow-internal process (internal secular evolution), and finally slow-external process (environmental secular process). Fast process, such as major galaxy mergers, strongly and quickly change the dynamical state of each galaxy, forming a new system within a few gigayears time scale. Secular process that drive the evolution in galaxies by bars, oval distortions, spiral arms and rings, slowly change the system in several gigayears time scale. In addition to these mechanisms, there are other process involved in the evolution of galaxies that extend beyond this thesis topic such as star formation, gas recycling, metal enrichment, stellar feedback and active galactic nuclei (AGN) feedback.

The class of bulges that are formed by collapse or mergers (fast mechanisms) are address as classical bulges (CB), which have been reproduced in many studies through the mentioned mechanisms (Toomre 1977; Naab & Burkert 2003; Bournaud et al. 2005). An example of a galaxy with a massive and extended classical bulge is the Sombrero galaxy in Fig.1.5 where in addition to the disc seen almost edge on, it is possible to see the spheroidal substructure with a light distribution extending from the centre out to high distances perpendicular to the plane of the disc.

Classical bulges in disk galaxies are naturally reproduced in cosmological Lambda cold dark matter (Λ CDM) simulations such as: the Millennium I (MI), II and XXL Springel et al. (2005); Angulo et al. (2012); Boylan-Kolchin et al. (2009), the Illustris simulation (Fig.1.6) Vogelsberger et al. (2014b,a), the Aquarius project Springel et al. (2008) and the Via Lactea I and II (Fig.1.7) Diemand et al. (2007, 2008) projects. In these simulations the particles that represent the dark matter distribution are initially placed within a box volume following a power spectrum and at a high redshift ($z=127$ for MI) where the box has periodic boundary conditions. The force of gravity is calculated and the system is evolved in time within a box according to a given cosmology, that expands accelerating in time due to the contribution of the dark energy given by the cosmological equations until the present time (redshift $z=0$). The peaks of the density at $z=127$ are the seeds where additional dark matter is accreted creating small size dark matter haloes (DMHs). In time these haloes merge with other haloes creating more massive dark matter

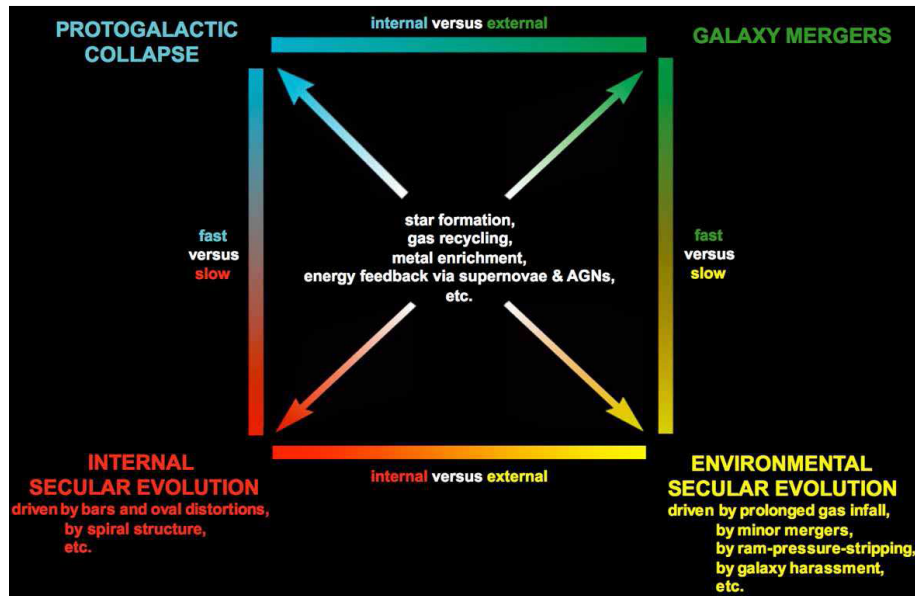


Figure 1.4: Galaxy evolution mechanisms schematic from [Kormendy \(2013\)](#). The galactic evolution process are divided into four mechanisms. From fast mechanisms (top) to slow ones (bottom). And from internal mechanisms of evolution (left) to externally triggered or “environmental” mechanism (right).

haloes (DMHs), ending at redshift $z=0$ with a cosmic web-shaped structure at large scales (see Fig.1.6) where the filaments are formed by galaxies with DMHs of various masses and the nodes are the most massive galaxies.

Approximately 71.4% of the total mass-energy density in the universe is dark energy, the other 24% consists of dark matter, and only 4.6% is baryonic matter (atoms) that accounts for all the gas, dust and stars in the universe (NASA/WMAP Science Team). However, these fractions correspond to averages over a large volume of the cosmic web, and at a local region the exact contribution may change. Within galaxy clusters and galaxies the main contributions are given by the baryonic matter (18%) and the dark matter (82%) making the last then the most important contributor to the gravitational force at galactic scales.

The dark matter haloes are extremely important for the formation of the stars in galaxies, due to the gravitational potential well that the haloes generate, keeping the hot gas of the galaxy within the halo, which then cools and forms stars, and later they also recapture the gas expelled from the feedback of the stars and the AGNs. While galaxies form stars from the gas, they also merge with each other, building more massive galaxies, a process defined as hierarchical formation. If the merging galaxies have depleted their gas the merger is a “dry” merger that leads to the formation of galaxies with a spheroidal structure, such as elliptical galaxies. Some galaxies also accrete gas with high angular momentum content, forming then a stellar disk surrounding the inner spheroid or the classical bulge.

The hierarchical process in simulations like Illustris generate galaxies in different environments like galaxy clusters or field galaxies, different masses, and of different morphologies like elliptical galaxies, dwarf galaxies and disk galaxies with bulges. However, observations



Figure 1.5: Sombrero galaxy M104 or NGC 4594. Image Credit: NASA/Hubble Heritage Team.

of the Sloan Digital Sky Survey (SDSS) indicate that the number of disc galaxies without a bulge is higher than in the simulations, being also a strong function of their stellar mass (Dutton 2009). Classical bulges usually have concentrated light profiles, recovering Sérsic indices typically higher than 2 and up to $n \sim 8$, showing a De Vaucouleurs profile when $n=4$ (Kormendy & Kennicutt 2004; Fisher & Drory 2008). Low-mass disc galaxies (up to $2.5 \times 10^{10} M_{\odot}$) have smaller Sérsic indices ($n \sim 1.3$), while higher-mass have typically $n \sim 4$. For MW type galaxies ($M_{\star} \sim 10^{11} M_{\odot}$) only 0.1% are bulgeless, while for M33 type galaxies ($M_{\star} \sim 10^{10} M_{\odot}$) bulgeless galaxies are more common, having 45% of them Sérsic indices lower than 1.5. This situation has been difficult to reproduce in simulations, where simulated disk galaxies tend to form generally massive classical bulges, although under favourable situations simulated dwarf disk galaxies suppress the formation of a bulge due to strong outflows from supernovae that remove low-angular-momentum gas, inhibiting the bulge formation (Governato et al. 2010).

While some observed classical bulges that are supported mostly by random motion are reproduced in simulations by dry mergers of collision-less systems, other observed bulges show substantial rotation, which can be reproduced in some cases by gas rich or “wet” simulated mergers (Keselman & Nusser 2012).

In addition to the hierarchical scenario to form classical bulges, we also have the monolithic collapse formation scenario where the bulge is formed already with a high mass from a massive gas cloud (Eggen et al. 1962). Another proposed mechanism to form early bulges consists of

instabilities in the early disk, forming clumps and star clusters that then spiral in due to dynamical friction, merging later and forming a bulge (Noguchi 1999; Immeli et al. 2004; Bournaud et al. 2007). While this formation mechanism involves the merging of progenitor systems, these progenitors originated in the early disk, and therefore the resulting bulge could be more closely related with other types of bulges discussed in the following section.

1.1.3 Pseudobulges

Not all stellar over-densities in the centres of disc galaxies are formed as classical bulges. Current detailed observations suggest that some bulges can form from process occurred in the disc and are named pseudobulges (Kormendy 2013). Pseudobulge are subdivided in two subclasses:

- **Disky bulges:** formed when gas falls in the centre of the disc galaxy, forming stars with a disky density distribution. Additionally, they can form nuclear rings and nuclear bars as seen in the galaxies NGC 6782 and NGC 4314 in Fig.1.8 (top panels).
- **Box/peanut (B/P) bulges:** named due their unusual morphology, where the bulge can have isophotes with a boxy shape, and in some cases peanut shape or even X-shaped structure where the ends of the X extend perpendicular to the plane of the disk. A fascinating example of this class of bulge is the galaxy in ESO 597G036 shown in Fig.1.8 (bottom panel). The formation mechanism for this bulges was first shown with N-body galaxy models which naturally developed a B/P bulge depending on the initial conditions (Raha et al. 1991), when the disk of a galaxy goes through an instability forming a bar, which goes itself through a vertical instability named buckling instability (or pipe/fire-hose instability) that thickens the bar in the vertical direction forming a boxy or X-shape/peanut shape structure called a B/P bulge (see also section 1.2.1).

The formation mechanisms of the pseudobulges make difficult to distinguish them from the disk, because they are born from the disk and they are not entirely dynamically decoupled from the disk. On the contrary, classical bulges can in principle be more easily decoupled, because the forming process through collapse or mergers result in dynamical properties that differ from the disk components. This is important for the photometric decomposition of the bulge and the disc using one function for each component, where the decomposition is physically justified, while in the pseudobulges the components are not so clear. The decomposition of a B/P bulge can be even more complicated than in disky bulges, due to the complex dynamics of the related bar.

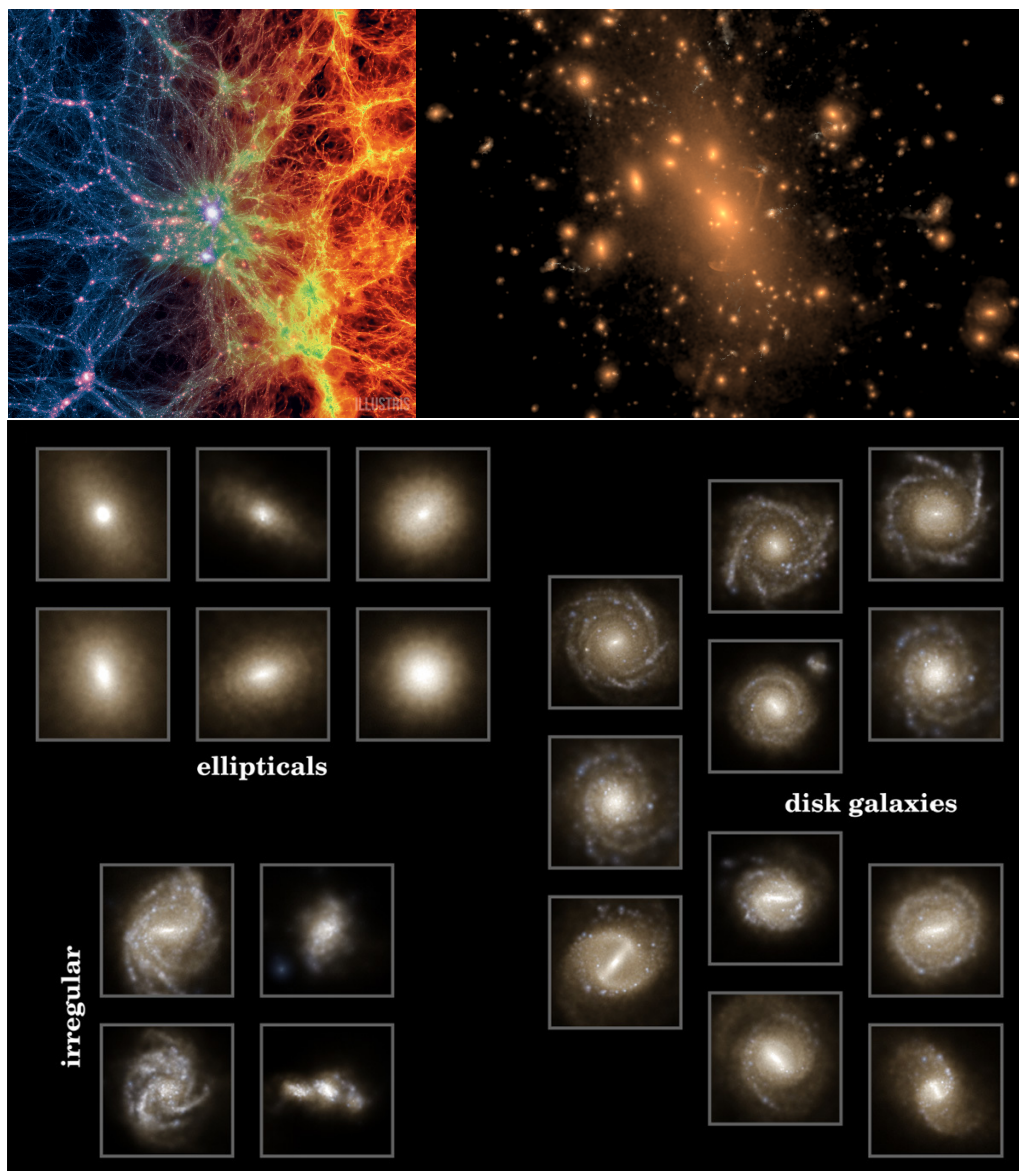


Figure 1.6: From the Illustris Collaboration. Top left: snapshot of the Illustris simulation at $z=0$ centred on the most massive cluster, 15 Mpc/h deep. Shows dark matter density (left side) transitioning to gas density (right side). Top right: stellar light at $z=0$ of the most massive cluster. Bottom: Hubble diagram of the resulting galaxies in Illustris at $z=0$. Disc galaxies show bars and/or bulges. Note: image from <http://www.illustris-project.org/>.

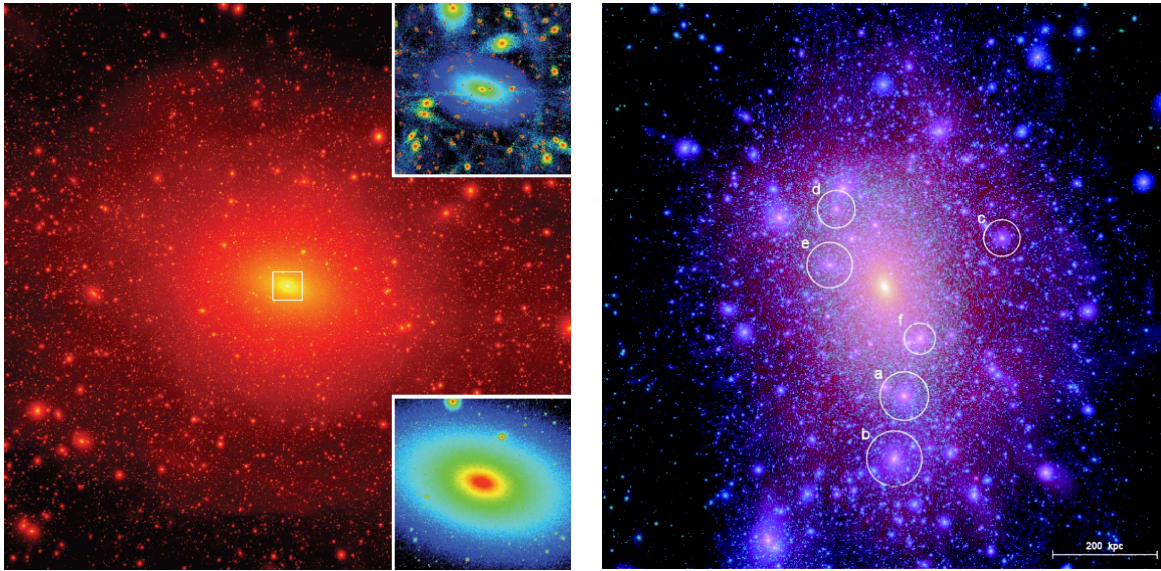


Figure 1.7: Left panel: The Via Lactea II (VLII) simulation showing a projected dark matter squared-density map from a cube of 800 kpc per side [Diemand et al. \(2008\)](#). The insets focus on an inner cube of 40 kpc per side (outlined in white), and shows the local mass density (bottom inset) and the local phase-space density (top inset). The VLII simulation has a mass resolution of $4100 M_{\odot}$ [and a force resolution of 40 pc. The mass within $r_{200}=402$ kpc of the centre (the radius enclosing 200 times the mean matter density) is $1.9 \times 10^{12} M_{\odot}$. Right panel: The Aquarius simulation taken from [Springel et al. \(2008\)](#). We see a dark matter distribution in a cubic region of side $2.5 \times r_{50}$ centred on the main halo in the Aq-A-1 simulation. The figure also shows the substructures within the more massive DM halo, showing with marking circles six DM subhaloes (a – f), which also have substructures.

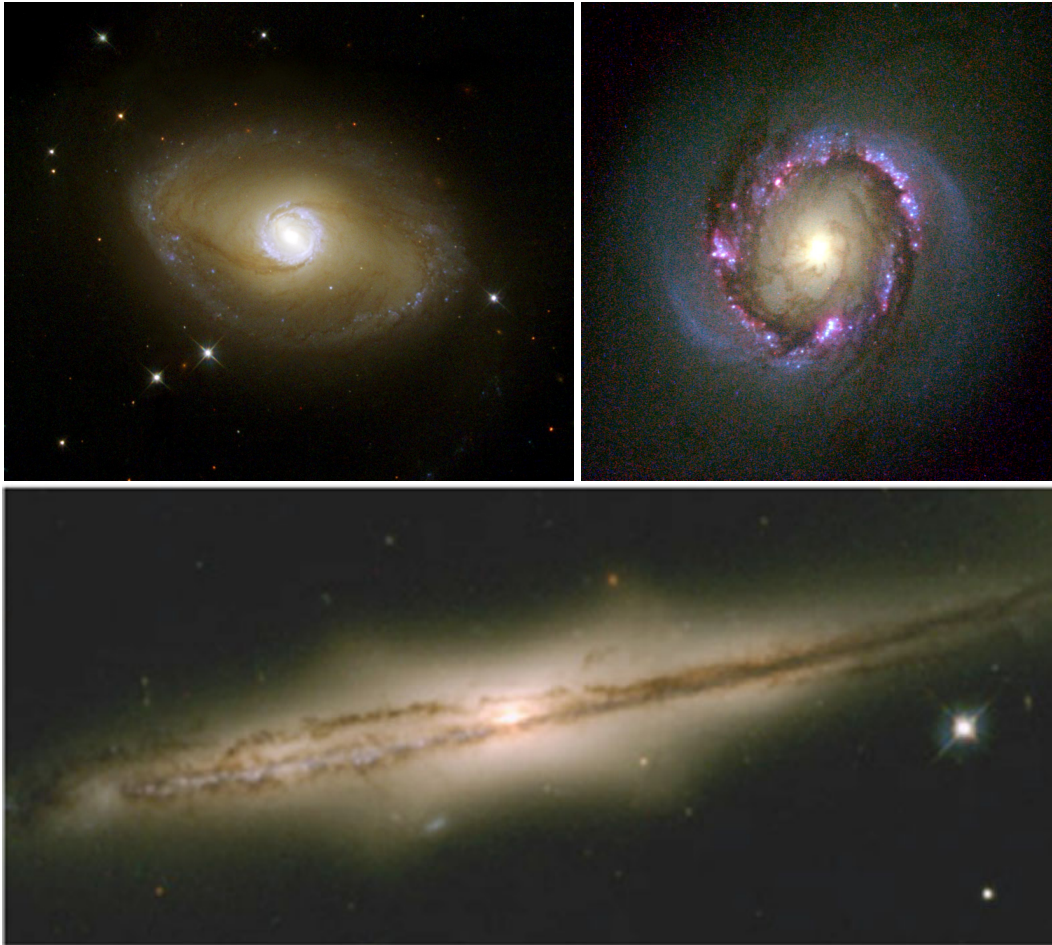


Figure 1.8: Top panels: Disky bulges in galaxies NGC 6782 (left) and NGC 4314 (right). Both galaxies present also a bar. Bottom panel: Galaxy with a box/peanut bulge in ESO 597-G036. This galaxy is seen edge on making very prominent the X-shaped vertical structure of the bar. Dust lanes are present in the plane of the disk. Credit: NASA, ESA and the Hubble Heritage Team (STScI/AURA).

1.2 Barred galaxies



Figure 1.9: Galaxy NGC 1300. Hubble Space Telescope image. NASA, ESA, and The Hubble Heritage Team STScI/AURA).

Nearly 70% of the nearby disk galaxies exhibit a bar in their centres when observed in the infrared (Block & Wainscoat 1991; Menendez-Delmestre et al. 2007), while in the V band can be 50%. Observations also suggest that the bar fraction in disc galaxies evolves with time, being only 20% at $z=0.8$, increasing up to 60% at $z=0.2$ (using COSMOS HST data) (Elmegreen et al. 2004; Gavazzi et al. 2015; Sheth et al. 2008). The bar is a structure that dominates the dynamics in the centre of disc galaxies, and apart from mergers or AGNs, bars are the most important machine that drive their evolution at low redshift. Disc barred galaxies can be found in a range of sizes and masses, from dwarf barred disc galaxies with stellar masses of $\sim 10^{10} M_{\odot}$ (such as the Large Magellanic Cloud) to massive disc galaxies with a stellar mass of $\sim 10^{11} M_{\odot}$. They also present a wide diversity of shapes having for example a massive bar like NGC 1300 in the Eridanus Cluster shown in Fig.1.9, with an elongated bar with two prominent spiral arms extending from the ends. It is also visible in the centre a disky bulge component and a nuclear ring. Other barred galaxies have much less prominent and elongated bars such as NGC 4921 in the Coma cluster shown in figure 1.10, show a shorter and rounder bar with spiral arms trailing the bar and several additional spiral arms tightly wound.

Disc galaxies can share morphological patterns of their bars and their spiral arms, which allows to group them as in Fig.1.12 where the diagram from Kormendy (2013) summarises the most typical cases: SB(r) are spiral galaxies with a ring of stars and gas big enough to intersect both extremes of the bar. In the SB(s) the arms of the spiral start from the ends of the bar. Sanders & Tubbs (1980) simulations of gas that responds to a barred potential indicate that weak, fast bars



Figure 1.10: Galaxy NGC 4921 in the Coma cluster. Hubble Space Telescope image. NASA, ESA and K. Cook (Lawrence Livermore National Laboratory, USA).

favour SB(s) structure and strong slow bars favour SB(r) structure.

The simplest stellar dynamical theory of the orbital structure of bars in disc galaxies proposes a scenario where the structure of the bar can be built with different families of stable orbits that are in resonance with the rotation period of the bar. A bar can rotate with an angular frequency Ω_p , typically referred as bar pattern speed (or configuration rotation in other contexts). Ω is the mean angular frequency radial profile and κ is the associated epicyclic frequency profile derived from the circular velocity profile ($V_c(R)$):

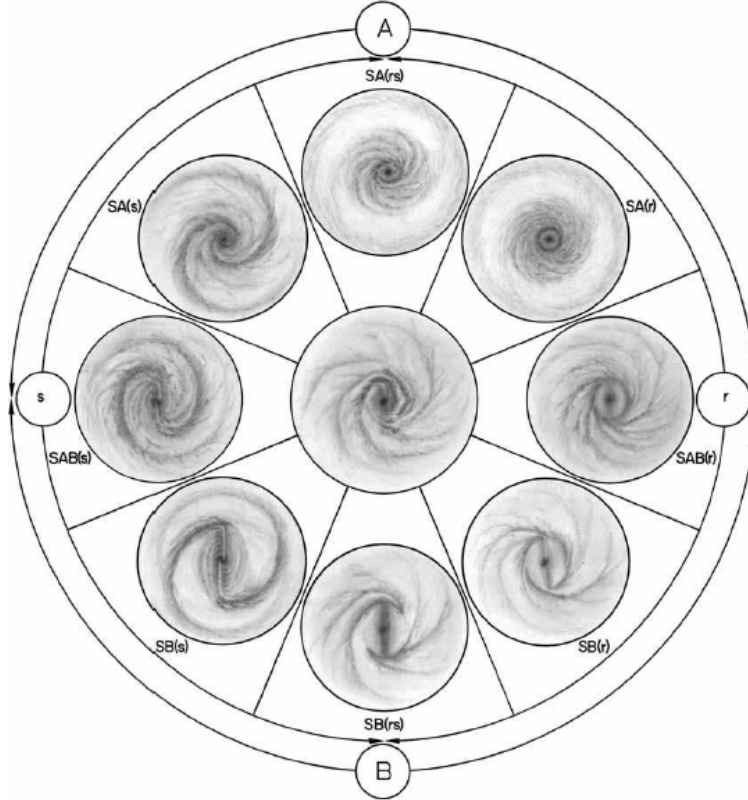


Figure 1.11: From [Kormendy \(2013\)](#). Morphological classification of spiral disc galaxies (S) composed by different substructures such as exclusive presence of spiral arms (SA(s)) with an additional ring (SA(r)), or with the addition of a bar (SB(s)) and with also rings (SB(r)). And the case with spiral arms as massive as the bar (SAB(s)).

$$\Omega(R) = \frac{V_c(R)}{R} \quad (1.1)$$

$$\kappa^2(R) = \frac{2\Omega(R)}{R} \frac{d}{dR} (R^2 \Omega(R)) \quad (1.2)$$

The most important orbital resonances produced by the bar are: the inner Lindblad resonance that lay within the bar (Ω_{ILR}) where $\Omega_p = \Omega - \kappa/2$, which depending on the shape of the circular velocity profile, may have an inner inner Lindblad resonance (Ω_{IILR}) and an outer inner Lindblad resonance (Ω_{OILR}); then the co-rotation resonance Ω_{cor} at the co-rotation radius r_{cor} that may lay at the end of the bar or beyond ([Contopoulos 1980](#)), where in the corotating frame of reference of the bar with $\Omega_p = \Omega$, the stars remain fixed at this radius; and finally the outer Lindblad resonance (Ω_{OLR}) with $\Omega_p = \Omega + \kappa/2$ that can generate ring-shaped structures in the gas distribution in the disc ([Schwarz 1981](#); [Buta & Combes 1996](#); [Rautiainen & Salo 2000](#)). The families of orbits that inhabit and support the bar by the resonances it produces, are the $x1$ type of orbits, which inhabit between ILR and corotation. The $x2$ type orbit also inhabit the interior of the bar within ILR, but they do not support the bar structure as they are not aligned with the bar, extending perpendicular

to the bar.

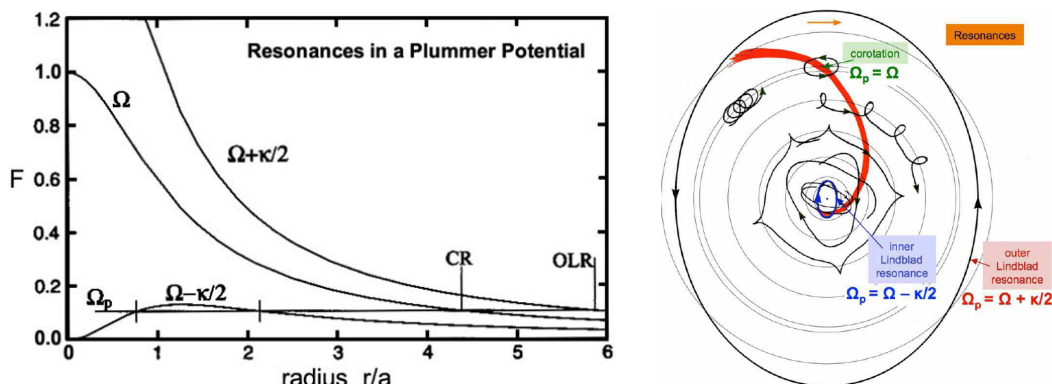


Figure 1.12: From [Kormendy \(2013\)](#). Left panel: Examples of Lindblad resonances in a Plummer potential. Right panel: example of the location of the orbits with Lindblad resonances within a galaxy.

How are bars formed? There are several scenarios for bar formation, and the formation can be triggered by an internal or an external perturbation. In the linear regime theory, bars are formed from a global linear instability by perturbations that can grow until the disk is reshaped into a barred distribution ([Kalnajs 1970](#)). The review of [Sellwood \(1996\)](#) reports that even in N-body simulations of disc galaxies stable to global bar mode linear instabilities, the discs can form a bar by a non-linear mechanism, where two spiral arms can grow until their masses are sufficiently large to impose a triaxial gravitational potential that traps the stars within the inner Lindblad resonance produced by pattern speed of the spiral arms, building the bar.

In the previous scenario bars are formed from internal perturbations that grow. However, such perturbation can also be generated externally by the tidal perturbation of satellite galaxies passing nearby. [Martinez-Valpuesta et al. \(2016\)](#) showed that fly-by encounters of galaxies with similar masses and sizes, disc galaxies that in isolation would not form a bar, do form it after the encounter. Furthermore, they also find that models that form a bar in isolation, can obtain bars with similar properties when these models form a bar by an encounter. However, bars that can be formed exclusively by interactions do have significant differences with bars that can also form in isolation.

1.2.1 Bars and Box/Peanut Bulges

In section 1.1.3 are described box/peanut (B/P) bulges, showing an observed example in Fig.1.8. As we mentioned there, [Raha et al. \(1991\)](#) find that a B/P bulge can be formed in N-body simulations when the disc forms a bar that later goes through a vertical instability called the buckling/fire-hose/pipe-hose instability, generating the B/P bulge in the centre, which transitions to the thin bar further out that is aligned with the B/P bulge. Stars with orbits in vertical resonances with the bar would strongly contribute to create a boxy shape. Some of these orbits are perturbations of the $x1$ family of orbits in the vertical direction (z) called $x1v1$ or also “banana” orbits due to their shape ([Skokos et al. 2002a,b](#); [Patsis & Katsanikas 2014b](#)). The B/P bulge can

also be composed by “pretzel” orbits, usually more centrally located than the banana orbits (Portail et al. 2015b), (see also Patsis & Katsanikas 2014a). The connection between B/P bulges and bars shown in simulations leads to the speculation that almost all the observed boxy bulges are in fact bars looked near edge-on. Combes & Sanders (1981) also point out that buckled N-body bars look like observed boxy bulges when seen end-on, and like the observed peanut bulges when seen side-on (as the galaxy in Fig. 1.8), supporting the idea that both types of observed bulges are the same structure just seen from different perspectives.

The review of Athanassoula (2012) summarises the morphological differences between buckled N-body barred galaxies that have different initial conditions. Disc galaxies where the dark matter halo has an equal or higher contribution to the circular velocity profile in the inner parts of the disc, result in strong and elongated bars with a strong X-shape of the isophotes and a long thin bar component. Disc galaxies with a lower contribution of the dark matter to the circular velocity (or disc dominated), result in weak shorter bars with a more boxy-shape isophotes.

1.2.2 Dynamical evolution of bars

The most important dynamical properties of a bar are its stellar mass distribution, the mass distribution of the dark matter halo (and the classical bulge or the stellar halo if they are present/significant), and the pattern speed of the bar Ω_p . Bars are classified as fast if they satisfy the criteria $\mathcal{R} = r_{\text{cor}}/r_{\text{bar}}^{\text{thin}} \leq 1.4$ (and slow if $\mathcal{R} > 1.4$) (Debattista & Sellwood 2000), where r_{cor} is corotation radius and $r_{\text{bar}}^{\text{thin}}$ is the half length of the thin bar.

What are the stellar dynamical mechanisms operating during the bar’s formation and evolution? The Athanassoula (2012) review summarises the most important ones: bars can lose angular momentum emitted mainly from (near-)resonant material at the inner Lindblad resonance of the bar, and absorbed mainly by (near-)resonant material in the outer disk and in the spheroid substructures such as the classical bulge, the stellar halo or the dark matter halo. This reduces the pattern speed of the bar, moving the corotation radius further out. This allows the bar to grow by trapping more material from the disc.

The spheroidal components can also delay the formation of the bar and slow down its growth, however later after the bar forms, they strengthen the bar by absorbing its angular momentum allowing it to grow (Binney & Tremaine 2008).

In N-body models, the change of the bar pattern speed also depends on the initial conditions: disc dominated barred models decrease their pattern speed at a slower rate than discs that are dominated by the dark halo, which leads to a correlation that fast bars tend to be weak bars, and slow bars tend to be strong bars (Athanassoula 2012).

1.2.3 Downfall of bars

It has been proposed that bars could destroy themselves by a mass growth in the central region of the bar (Hasan & Norman 1990), which could be produced by the gas inflow through a secular evolution process. An increment of the mass in the centre results in an increment of the rotation velocity or frequency, shifting the location of the Lindblad resonances $\Omega_p = \Omega - \kappa/2$, and also making the profile less flat or constant. This makes more difficult for the $x1$ orbits at

different radii to precess together at the same Ω_p . At the same time the bar is transferring angular momentum to the disk and the spheroids, slowing down its pattern speed.

[Shen & Sellwood \(2004\)](#) shows that bars can also be destroyed or diminish by central concentrated (hard) mass distributions such as super massive black holes (SMBH), or extended distributions spread across $r \sim 10^2 \text{pc}$ (soft) such as molecular clouds, discy pseudobulges or massive compact nuclear star clusters. “Hard” masses destroy bars more easily than “soft” masses. Furthermore, in chapter 2 (and [Blana et al. 2017](#)) are presented extremely concentrated classical bulges that lead to the dissolution of the bar.

What happen to a destroyed bar? [Kormendy & Illingworth \(1982\)](#) suggests that some bars may evolve into lens components. The large velocity dispersion observed in the lens may be consistent with this. [Elmegreen & Elmegreen \(1985\)](#) find that bars in early-type galaxies have bars with flat surface-brightness profiles, while late-type galaxies have bars with exponential profiles. The azimuthal phase-mixing process in an early-type bar would produce a lens or late-type, while the phase-mixing of a late-type would produce just another late-type galaxy without a bar.

This may lead to two important points regarding the destruction of bars: (1) secular evolution tends to destroy the bar that drives it; (2) even if a disk galaxy does not show a bar, a bar-driven secular evolution may have taken place in the past.

1.2.4 Gas dynamics in barred galaxies

The presence of a bar in a disc galaxy can be extremely important for the dynamics of the gas it contains. Bar-less disc galaxies that contain a gaseous disc with a rotational velocity profile similar to the circular velocity profile produced by an axi-symmetric potential, will remain near gravitational equilibrium. However, within the potential of a bar, the gas cannot follow a circular orbit, which is possible for the stellar disc that behaves as a collision-less “fluid”, but the gas, being collisional, cannot. This results in regions of converging streams with large velocity gradients producing shocks. Similar effects can be found in disc galaxies with other non-axisymmetric structures, such as massive spiral arm substructures. [Prendergast \(1983\)](#) proposed that radial dust lanes in bars could be the observational signatures of shocks that drive the gas fall, given that the dust can trace star forming regions that can be produced in these shocked regions. [Athanasoulas \(1992\)](#) explored this further through simulations, finding that the gas shocks occur where the dust is found in observed barred galaxies. The nearly radial shocks also imply a loss of the energy of the gas, falling and feeding the core of the galaxy and triggering star formation. The average sinking velocity rate of the gas obtained is 1 km s^{-1} (or $\sim 1 \text{ kpc Gyr}^{-1}$) implying that in a few milliard years the gas of the inner part of the disk may fall into the central region, a process that is much slower in a pure disc galaxy. The dynamics of the gas within the bar can form very complex substructures as shown by the simulations of [Kim et al. \(2012\)](#) shown in Fig. 1.13, with gas streams coming from the disc that reach the end of the bar where the gas is shocked. Depending on the resulting gas velocity, two streams are formed. They are elongated along the bar major axis with gas falling to the centre. This dissipative process constantly transports the gas from the outer parts to the inner region, where a ring is formed that is elongated perpendicularly to the bar in a x_2 orbit. From there the gas can fall into the very centre, forming a nuclear ring

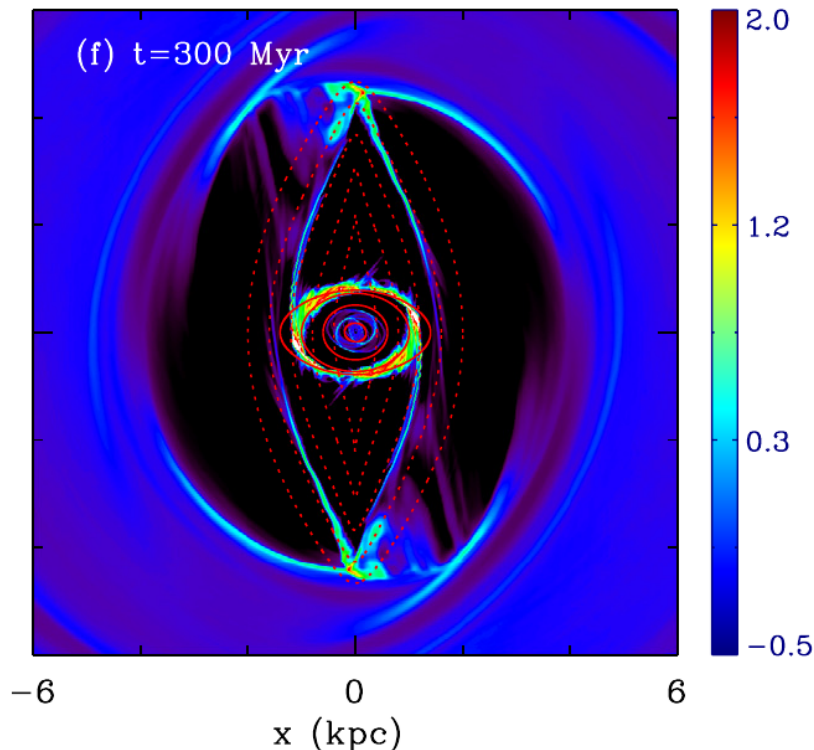


Figure 1.13: From [Kim et al. \(2012\)](#). Density of the gas in a barred potential after 300 Myr of evolution, with the bar rotating anti-clockwise.

or a spiral structure. The general cause of the gas inflow is the gravitational torques produced by the bar, being the shocks the more direct cause. Furthermore, the gas distribution in the centre within 100 pc can change depending on the sound speed value and the mass of the central super massive black hole if present (see their Fig. 9).

Other substructure in disc galaxies can also be important in the dynamics of a galaxy such as super massive black holes, nuclear star cluster, spiral arms, rings and stellar haloes. M31 presents various of these substructures that we describe in the following section.

In addition to barred galaxies we also observe oval galaxies: these disk galaxies lack of a bar, but they have secular evolution generated by non-axisymmetry where the effects are similar to those produced by bars, and consequently evolving in a similar way. The oval shape is supposed to be supported by triaxial dark matter haloes ([Kormendy 2013](#)).

1.3 The Andromeda galaxy

Andromeda (M31, NCG224) is a barred disc galaxy and it is the largest and most massive member of the Local Group (LG). M31 is located at 785 ± 25 kpc from the Sun ([McConnachie et al. 2005](#)), which implies an angular to physical distance relation on the sky of $1 \text{ arcsec} = 3.8 \text{ pc}$ or $1^\circ = 13.7 \text{ kpc}$. It hosts many satellite dwarf spheroidal galaxies, irregular galaxies and the spiral galaxy M33, as well as gaseous and stellar streams of disrupted galaxies extending out to

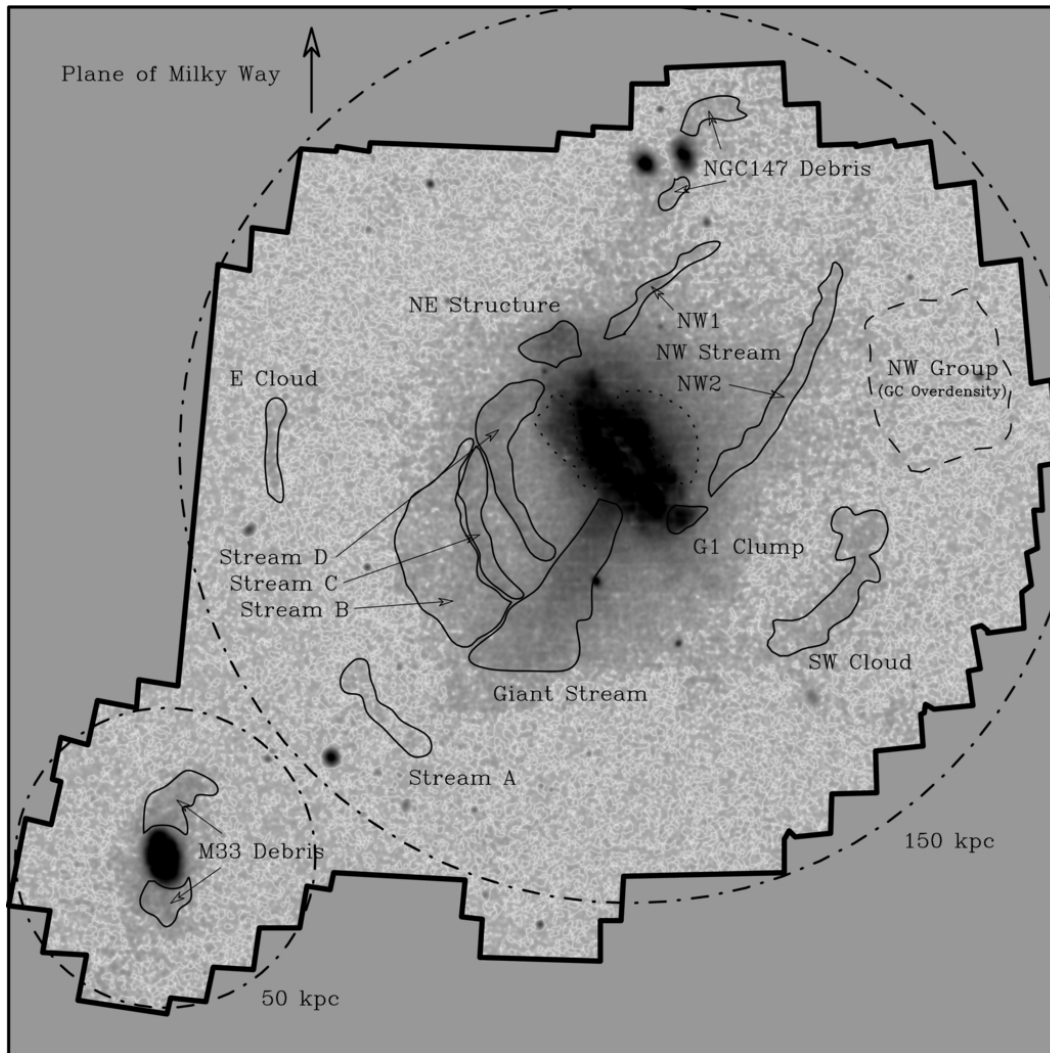


Figure 1.14: Environment of M31 from [Lewis et al. \(2013\)](#), showing several stellar substructures in the halo of M31, such as the Giant Stream, tidal debris associated with M33 and NGC 147, like the Eastern Cloud and the broad strip of stars associated with Stream D. The M32 satellite is located in the very centre of M31. The dashed curve marks an overdensity of globular clusters identified in [Mackey et al. \(2010\)](#). In the disc of M31, the dotted curves represent the inner shells and loops thought to be wraps of the giant stellar stream. The large dot-dashed circle marks a radius of 150 kpc from the center of M31, and the smaller marks 50 kpc from the centre of M33.

$R \sim 150$ kpc from M31's centre, as shown by [Lewis et al. \(2013\)](#) in Fig.1.14. In Table 1.1 we summarise some of the main properties of M31. The Andromeda galaxy presents most of the typical substructures and components observed in other disc galaxies as well, listing them from the centre: (1) central super massive black hole (SMBH), (2) nuclear star cluster system, (3) nuclear disc, (4) classical bulge, (5) B/P bulge, (6) thin bar, (7) stellar disc, (8) gaseous disc, (9) spiral arms and a ring-like structure, (10) stellar halo, (11) dark matter halo, and (12) dwarf satellite galaxies. The photometric decomposition of [Courteau et al. \(2011\)](#) using the IRAC1

Table 1.1: Main properties of M31.

Sky position	RA:00h 42' 44.3503s ⁽¹⁾
(J2000.0)	DEC +41° 16' 08.634" ⁽¹⁾
Distance from the MW	0.78 ± 0.04 Mpc ⁽²⁾
Heliocentric radial velocity	-300 ± 4 km s ⁻¹ ⁽³⁾
Galactocentric radial velocity	-122 ± 8 km s ⁻¹ ⁽³⁾
Disc inclination i	77° ⁽⁴⁾
PA of the disc photometric major axis PA_{disk}	38° ⁽⁵⁾
PA of the bulge photometric major axis PA_{bulge}	$51.3 \pm 1.2^\circ$ ⁽⁶⁾
PA of the projected bulge and bar major axis $PA_{\text{bulge,bar}}$	$55.7 \pm 1.2^\circ$ ⁽⁶⁾
Sérsic index ($3.6 \mu\text{m}$) n	2.4 ± 0.2 ⁽⁷⁾
Sérsic effective radius ($3.6 \mu\text{m}$) R_e	1.1 ± 0.1 kpc ⁽⁷⁾
Sérsic surface-brightness ($3.6 \mu\text{m}$) μ_e	16.1 ± 0.1 mag arcsec ⁻² ⁽⁷⁾
Exponential disk scale length ($3.6 \mu\text{m}$) R_d	5.8 ± 0.1 kpc ⁽⁷⁾
Exponential surface-brightness ($3.6 \mu\text{m}$) μ_o	16.79 ± 0.02 mag arcsec ⁻² ⁽⁷⁾

Notes: (1) NASA/IPAC Extragalactic Database. NASA/IPAC. Retrieved 2017-11-03, (2) [McConnachie et al. \(2005\)](#), (3) [de Vaucouleurs et al. \(1991\)](#), (4) [Corbelli et al. \(2010\)](#), (5) [de Vaucouleurs \(1958\)](#), (6) [Blana et al. \(2017\)](#), (7) [Courteau et al. \(2011\)](#) (their model F).

data finds that the stellar nucleus, bulge, disk, and stellar halo components contribute respectively with roughly 0.05%, 23%, 73%, and 4% of the total light of M31 out to 200 kpc along the minor axis, with errors of 20%. However, the authors do not consider the bar in M31 which can have a strong impact on the decomposition. In the following sections I briefly describe some of the main substructures focussing on the ones most related to the bulge of M31, ordering them from the centre of the galaxy to the outer halo.

1.3.1 The galactic centre: Nuclei & Supermassive Black Hole

The centre of M31 is dominated by the “triple nucleus” consisting of three stellar substructures: P1, P2 and P3. While P2 is located in the centre, P1 locates 1.5 pc from the centre and it has been proposed it is part of P2 and it is made by orbiting material located at the apocentre of their orbits, where it spends a longer time, producing the overdensity of an otherwise elongated discy stellar distribution (named here P1-P2) ([Tremaine 1995](#)). Both P1 and P2 dominate in red colour light due to their old stars however, P3 dominates in blue colour due to its younger A stars and it is thought to be a nuclear stellar disc orbiting in the Kepler potential the central supermassive black hole (SMBH) reaching high rotation velocities $v=674 \pm 81$ km s⁻¹ at 0.19 pc, and a maximum of $v=1183 \pm 201$ km s⁻¹ ([Bender et al. 2005](#)). The P1+P2 disc its made of old metal rich stars and it has a radius of ~ 8 pc (2 arcsec) with a combined luminosity of $L_{\text{P1+P2}} \sim 3 \times 10^6 L_\odot$ and a stellar mass of $M_{\text{P1+P2}} \sim 2 \times 10^7 M_\odot$ ([Merritt 2013](#)). The P3 disc of young stars (200 Myr) with A stars has a radius of ~ 0.8 pc (0.2 arcsec) with a stellar mass of $M_{\text{P3}} \sim 4 \times 10^3 M_\odot$ with $\sim 15 \times 10^3$ stars (Salpeter IMF) ([Bender et al. 2005](#); [Lauer et al. 2012](#)). Nuclear star clusters are compact

star clusters located at galactic centres, with masses between $\sim 10^6 M_\odot$ to $\sim 10^7 M_\odot$ and typical effective radius of $\sim 10^{1\pm 0.5}$ pc. According to Tremaine & Ostriker (1982) the nucleus and the bulge of M31 are dynamically independent. Nuclear clusters are common in late-type galaxies, being present in 70% to 30% depending on the specific type. They are also common in dwarf spheroidal galaxies (dSph), but are rare in irregulars. Beaton et al. (2007) limit photometrically the nucleus of M31 to be within $R < 3$ arcsec (11 pc).

The SMBH mass is $M_\bullet = 1.4_{-0.3}^{+0.9} \times 10^8 M_\odot$ (Bender et al. 2005), derived using Hubble Space Telescope STIS spectroscopy of the nucleus P1+P2 (and the embedded P3) and the Schwarzschild modelling of P3 (Thomas et al. 2004). The black hole sphere of influence of radius r_{sph} is where the stellar mass equals this, then $M_\bullet(r_{\text{sph}}) = M_\star(r_{\text{sph}})$, finding $r_{\text{sph}} = 3$ arcsec (10 pc). Another definition of the sphere of influence is $r_{\text{cusp}} \approx G M_\bullet \sigma^{-2}$, where we obtain $r_{\text{cusp}} \approx 5.5$ arcsec (20 pc) with $\sigma = 170 \text{ km s}^{-1}$ (Saglia et al. 2010). The black hole contribution to the rotation curve remains negligible through the bulge and the outer stellar disk due to the point mass nature of its gravitational potential. And it also corresponds to $\sim 1\%$ of the mass budget of the bulge.

The M-sigma relation ($M_\bullet - \sigma_{\text{bulge}}$) and similar relations trace a correlation between dynamical properties of classical bulges such as the stellar velocity dispersion, the stellar mass or its size with the SMBH mass (Saglia et al. 2016). In the final summary in Section 4.1 are discussed the implications of the stellar masses found for the classical bulge component of M31 and the predictions for the SMBH mass this gives.

1.3.2 The composite bulge: classical bulge, B/P bulge and thin bar

Historically, the bulge of M31 has been mostly considered as a pure classical bulge, in spite of the observations done by Lindblad (1956) which detected the presence of a bar in the centre revealed by the an isophotal twist between the bulge major axis and the disc major axis. Mould (2013) review on M31's bulge associate most of its properties with a classical bulge, with only some "pseudo-bulge trimmings". This is justified given the orientation of M31, close to edge-on, that makes it difficult to distinguish a bar and a boxy/peanut bulge, particularly in the visual band, and that the main properties such as the bulge Sérsic index ($n > 2$), the bulge to total light fraction roughly $B/T > 0.4$, suggesting that this substructure has the typical characteristics of a classical bulge.

The barred and B/P bulge nature of M31's bulge is revealed by the triaxial and boxy morphology of the bulge isophotes that is better evidenced and quantified in the infrared bands as done by Beaton et al. (2007) and Blana et al. (2017), and also by the bulge kinematic signatures that are typical of a B/P bulge (Opitsch et al. 2018), similar to the Milky Way's B/P bulge (Wegg & Gerhard 2013; Portail et al. 2015a), showing additionally a classical bulge component (Athanasoula & Beaton 2006). Furthermore, Blana et al. (2017) find that the masses of each bulge component are similar in magnitude, with 1/3 for the classical bulge, and 2/3 for the B/P bulge component, and with a concentrated classical bulge with a half mass radius of ~ 500 pc.

The best measurements of the M31 bulge stellar kinematics, gas kinematics and chemical abundances were done by Saglia et al. (2010) using slit spectroscopy, and then later extended by Opitsch et al. (2018); Saglia et al. (2018) with full maps with IFU observations, where both

studies are consistent with each other, finding the following:

The stellar kinematics measurements of [Opitsch et al. \(2018\)](#) indicate that the stellar velocity dispersions in the bulge are much higher than previous measurements, reaching 166 km s^{-1} (50 km s^{-1} higher than [McElroy 1983](#)), implying then a higher dynamical mass than previous estimation. However, the most important measurement are the kinematics signatures of the bar in M31. As we explained in section 1.2.1, B/P bulges in N-body simulations are bars that buckled in the vertical direction that conserve many of the properties of the thin bar. The authors measure high stellar velocities in the centre that increase monotonically, and within the barred region (600 arcsec) they detect a clear correlation between the line-of-sight velocity (v_{los}) and the $h3$ Gauss Hermite coefficient values, that change to an anti-correlation in the disc region ([Bureau & Athanassoula 2005](#)). They detect other signs for triaxiality in the bulge such as a misalignment between the photometric major axis, and the kinematic major axis, which would be aligned if the system was axis-symmetric with an oblate geometry as in [Kent \(1989\)](#). They also detected a signature of cylindrical rotation in the stellar velocity in the bar region, that is commonly observed in other barred galaxies ([Saha & Gerhard 2013](#); [Molaeinezhad et al. 2016](#)).

Their stellar population analysis determine that the central 100 arcsec of M31's bulge is dominated by old stars ($\text{Age}=13 \pm 0.7 \text{ Gyr}$) that are metal rich ($[Z/H] \approx 0.1 \pm 0.04 \text{ dex}$) with a strong negative radial gradient within 100 arcsec and enhanced in α -elements with $\alpha/\text{Fe} \approx 0.21 \text{ dex}$. Beyond 100 arcsec the most remarkable feature in the metallicity map is the bar that clearly stands out with an elongated region of high metallicity of solar values ($0.02 \pm 0.01 \text{ dex}$) with almost no gradient along the elongation, which is approximately aligned with the bar projected major axis at $\text{PA}=55^\circ 7$ predicted in [B17](#). The maps of the age and α -elements are approximately axisymmetric where no significant signatures of the bar are detected, with average values of $12 - -13 \text{ Gyr}$ and $\langle \alpha/\text{Fe} \rangle \sim 0.25 \pm 0.3 \text{ dex}$. The B/P bulge, that is the inner vertically extended region of the bar, shows slightly sub solar metallicity values of $-0.04 \pm 0.03 \text{ dex}$. The V-band mass-to-light ratio of both bulge components and the thin bar appear approximately constant with $\Upsilon_V \approx 4.4 \pm 0.2 M_\odot L_\odot^{-1}$. The stellar disk at $> 4 \text{ kpc}$ is made of younger stars with an average age of $8.7 \pm 3.3 \text{ Gyr}$ with a minimum of $3\text{-}4 \text{ Gyr}$, with solar value metallicities, and a smaller stellar mass-to-light ratio of $\Upsilon_V=3.0 \pm 0.9 M_\odot L_\odot^{-1}$.

The standard photometric decomposition done for M31 usually includes one Sérsic component for the bulge, one exponential profile for the disc, and a power law or another Sérsic profile for the stellar halo component, where [Courteau et al. \(2011\)](#) estimate in the IRAC $3.6 \mu\text{m}$ for the bulge of M31 an index value of $n=2.2 \pm 0.3$ and effective radius $R_e=1.0 \pm 0.2 \text{ kpc}$ with an ellipticity of $\epsilon_{\text{bulge}} = 0.37 \pm 0.03$, and a dust-free exponential disk with a scale-length of $R_d=5.3 \pm 0.5 \text{ kpc}$ and $\epsilon_{\text{disk}} = 0.73 \pm 0.03$. This approach may lead to an accurate representation of the total light in the galaxy, however it does not represent the substructures present in M31 where ignoring the contribution of the B/P bulge can lead to a lower Sérsic index for the bulge of M31. Later in chapter 3 we present the photometric fit of the classical bulge component alone.

Most dynamical models for the bulge of M31 assume that the bulge has a spherical or an oblate geometry ([Ruiz 1976](#); [Kent 1989](#); [Widrow et al. 2003](#); [Widrow & Dubinski 2005](#); [Block et al. 2006](#); [Hammer et al. 2010](#)), making the mass estimations of the bulge less accurate due to the barred nature of this galaxy. N-body barred galaxy models can represent the bulge and the bar of M31 much better. The M31 bulge mass estimations give a wide range that can vary

up to 50%, due to the different assumptions used for the bulge mass calculations ranging from $2.5 \times 10^{10} M_{\odot}$ (Widrow & Dubinski 2005) up to $4.0 \times 10^{10} M_{\odot}$ (Kent 1989). As the bulge and the bar of M31 are the main topics of this thesis, we present more details and properties in chapters 2 and 3.

1.3.3 The stellar disc

The stellar disc of M31 is seen near edge on with an inclination of ~ 77 deg. Its scale length is $R_d \sim 5.5$ kpc Courteau et al. (2011), more extended than the Milky Way’s disc with $R_d = 2.6 \pm 0.5$ kpc (Bland-Hawthorn & Gerhard 2016). However, in chapter 3 we argue that M31’s disc could present a mild break at ~ 10 kpc showing characteristics of a Type II.o-OLR disc, consisting of a SB break located beyond the bar and related to a ring-like structure near the OLR resonance (Erwin et al. 2008; Kim et al. 2014).

Williams et al. (2017) estimate a stellar mass of $M_{\star}^{\text{Disc}} = 9 \pm 2 \times 10^{10} M_{\odot}$ from stellar evolution models and colour-magnitude diagrams of the Panchromatic Hubble Andromeda Treasury (PHAT), while Tamm et al. (2012) estimate $M_{\star}^{\text{Disc}} = 5.6 \times 10^{10} M_{\odot}$ from modelling the IRAC $3.6 \mu\text{m}$, the spectral energy distribution (SED), and the gas and globular cluster kinematics.

In the centre of the disc within 4 kpc the early disc material was redistributed by the formation of the bar and the B/P bulge changing the kinematic structure within this radius (Blana et al. 2017). Further out Dorman et al. (2015) measures the kinematic properties of M31’s disc with PHAT (Panchromatic Hubble Andromeda Treasury survey) and SPLASH (Spectroscopic and Photometric Landscape of Andromedas Stellar Halo survey). They find a dynamically hot disc, attributing this to a more violent history with minor satellite accretion that heat up the disc. Furthermore, they also find an age-dispersion correlation with the young stars being dynamically colder than the vast majority of the stars that are old, where for example the old stars located at ~ 7 kpc are hot with $\sigma_{\text{old}}^{7 \text{ kpc}} \sim 100 \text{ km s}^{-1}$, while the young stars are $\sigma_{\text{young}}^{7 \text{ kpc}} \sim 40 \text{ km s}^{-1}$; and similarly at ~ 11 kpc old stars dispersion is $\sigma_{\text{old}}^{11 \text{ kpc}} \sim 70 \pm 10 \text{ km s}^{-1}$ and young stars are $\sigma_{\text{young}}^{11 \text{ kpc}} \sim 25 \pm 10 \text{ km s}^{-1}$. Dorman et al. (2013) also find “kicked-up disc stars” which are stars that are dynamically heated reaching the region of the stellar halo.

The disc also presents trailing spiral arms at 5 kpc. In spiral arm theory these substructures appear as density waves travelling through the disk of a galaxy. In N-body simulations Berrier & Sellwood (2016) shows that the swing-amplification mechanism proposed by Toomre (1981) could amplify spiral arms perturbations, where leading spiral waves are reflected at corotation into stronger trailing waves, and the feedback loop mechanism that convert trailing waves into leading waves, can grow triggering an unstable standing wave mode to form a bar structure. In this linear regime, Lindblad resonances could in principle prevent this by reflecting the perturbations not allowing them to travel through the centre shutting down the feedback loop mechanism. However, more recent studies of Sellwood (2012) propose a mechanism to form and develop spiral arms, where particles are scattered by the inner Lindblad resonances, driving the spiral arm production. However, the spiral arms in M31 at 5 kpc spiral arms are probably associated with the bar structure (Blana et al. 2017).

The spiral arms, like bars, can also promote secular evolution. Furthermore, in the over-

density zones produced by the arms, the gas suffers shocks making it to collapse and form stars. This process slows down the gas, making it also to fall into the centre with a rate that goes from a Hubble time to shorter timescales. The arms also transport angular momentum outward the disk. [Gnedin et al. \(1995\)](#) estimate for the spiral galaxy NGC4321 a timescale of this process in the order of ~ 5 to ~ 10 Gyr, but in more weak spiral structured galaxies the timescale could be an order of magnitude longer. This indicates that late-type unbarred spiral galaxies may evolve similarly to barred galaxies, but more slowly.

The most remarkable feature in the disc is the 10 kpc-ring like substructure, seen not only in the stellar maps of the IRAC $3.6 \mu\text{m}$, but also in the dust maps ([Barmby et al. 2006](#)) and in the HI and molecular gas maps ([Nieten et al. 2006](#); [Chemin et al. 2009](#)). [Nieten et al. \(2006\)](#) suggest that the inner 5 kpc arms could be connected with the outer ring. [Block et al. \(2006\)](#); [Dierickx et al. \(2014\)](#) simulations reproduce the ring with a satellite collision. An alternative origin scenario is through a resonant interaction with the bar ([Athanassoula & Beaton 2006](#); [Blana et al. 2017](#)), as is suggested in other barred galaxies ([Kim et al. 2014](#)). [Lewis et al. \(2015\)](#) find evidence supporting the resonance scenario where the ring substructure exhibits the strongest star formation rate with in average $\text{SFR}=0.7 M_{\odot} \text{yr}^{-1}$ and the steady long star formation with over 500 Myr, also finding that the rings position is constant throughout this time. However, a minor collision event may also have taken place, as suggests a global star formation episode 2-4 Gyr ago ([Williams et al. 2015](#)). As we show in chapter 3 the outer Lindblad produced by the bar is located at the radius of the ring ($\sim 11 \pm 1$ kpc).

1.3.4 The stellar halo

Stellar haloes are expected to form in the ΛCDM models due to major merger events and due to minor mergers of tidally disrupted satellites. The stellar halo of M31 dominates in light approximately beyond 9 kpc along the minor axis ([Courteau et al. 2011](#)). [Gilbert et al. \(2012\)](#) use spectroscopically confirmed red giant branch stars with SPLASH to trace the light of the stellar halo further out to ~ 175 kpc. Their best-fitted ellipses to the isophotes in the outer regions have a ratio of $b/a=0.94$ with the major axis of the halo aligned along the disc minor axis, consistent with a mild prolate stellar halo, although within the errors is also consistent with spherical symmetry. They find that the surface-brightness is well fitted by a single power law with an index $\alpha=2.2 \pm 0.2$ with no evidence of a break at large radii, which is consistent with simulations that suggest that the M31 accretion history could have been longer than in the Milky Way ([Deason et al. 2013](#)).

[Dorman et al. \(2012\)](#) measure the kinematics of the inner region of the stellar halo (~ 20 kpc) finding significant spheroid rotation ($v_{\text{rot}} \sim 50 \text{ km s}^{-1}$) beyond $R \sim 5$ kpc, and a velocity dispersion of 140 km s^{-1} at $R=7$ kpc that drops to 120 km s^{-1} at $R=14$ kpc with some dispersion anisotropy.

Significant dynamically cold substructures are detected in the stellar halo out to 90 kpc and beyond, possibly from stellar accreted streams, that when subtracted leave a smoother diffuse halo component that extends to these radii as well ([Gilbert et al. 2012](#)). The Giant Stellar Stream of metal-rich stars found by ([Ibata et al. 2001](#)) could origin by the tidal disruption of dwarf galaxies such as M32 and NGC205.

Ferguson et al. (2002) find several signatures of substructures with spatial density and metallicity variations that can be correlated. Overdensities at large radii close to the southwestern major axis, in the proximity of the very luminous globular cluster G1, and near the northeaster major axis, coinciding with and extending beyond the previously known northern spur. The most prominent metallicity variations are found in the southern half of the halo, where two large substructures with above average stellar density and metallicities are apparent; one of these coincides with the giant stellar stream while the other corresponds to a much lower stellar density and metallicity enhancement.

1.3.5 The gas and dust distribution

M31 has gas and dust distributed in the plane of the stellar disc, and a halo of hot gas. Its interstellar medium contains neutral hydrogen (HI) with a mass of at least $M_{\text{HI}}^{\text{gas}} > 6.7 \times 10^9 M_{\odot}$ measured within 25 kpc, and it also contains molecular hydrogen with a mass of $M_{\text{H}_2}^{\text{gas}} > 3.4 \times 10^8 M_{\odot}$, and $5.4 \times 10^7 M_{\odot}$ of dust (Braun et al. 2009; Draine et al. 2014). Nieten et al. (2006) find a similar value $M_{\text{H}_2}^{\text{gas}} = 3.6 \times 10^8 M_{\odot}$ within 18 kpc and $M_{\text{HI}}^{\text{gas}} = 5.1 \times 10^9 M_{\odot}$ measuring the tracer CO(1-0) line 115GHz (2.6cm) Chemin et al. (2009) estimate within 38 kpc a gas to stellar mass fraction of $M_{\text{HI+He+H}_2}^{38\text{kpc}} / M_{\star}^{38\text{kpc}} = 6.7_{-1.0}^{1.3} \%$.

del Burgo et al. (2000) measured a significant amount of ionised gas (clouds) in the central $R < 125$ pc of the bulge in the form of OIII, H α and NII. They find that the ionisation source could be compatible with post-asymptotic giant branch stars; however, the estimated ionization fluxes exceed to what is expected according to the distribution of planetary nebulae in the bulge of M31. Comparisons with Seyfert galaxies and LINERs (low-ionization nuclear emission-line region galaxies) indicate that the ionisation could instead be produced by ultralow-intensity nuclear activity from the super massive black hole, compatible with the existence of a “dead quasar” in the nucleus of M31. However, more recently Opitsch et al. (2018) also measures the ionised gas OIII in M31’s centre finding high gas velocity motions distributed in streams with a spiral shape, which is consistent with typical streaming motions caused by a bar (see section 1.2.4 and Fig. 1.13), and with a nuclear spiral pattern, which can be also reproduced in simulations that include a super massive black hole in their centre (Kim et al. 2012), concluding that a more likely main ionisation source mechanism are shocks instead of only starburst, which are typical barred galaxies with gas.

Most of the gas in the disc is in the form of atomic hydrogen gas (HI). This gas is cold ($\sim 100\text{K}$) and it traces the circular velocity of the galaxy. Chemin et al. (2009) present full kinematic and flux maps of HI measuring the 21-cm line from the centre of M31 out to 38 kpc, finding several interesting features. In the centre they measure a peak of 340 km s^{-1} , followed by a drop at 4 kpc with 200 km s^{-1} (probably due to the bar’s potential) to then increase up to a flat region of 260 km s^{-1} . Beyond 25 kpc they detect a strong warp of the HI disc, also measured by Corbelli et al. (2010). The most remarkable features are an external arm and two thin HI-spurs in the northern outskirts of the disc. The external arm is 32 kpc long extending on the far side of the galaxy, and has no obvious counterpart on the near side. This could suggest that it is the result of tidal interactions with galaxy companions like NGC 205. They also detect several HI lines

associated with up to five kinematic components where the sum of the smaller components add up to 41% of the total HI mass. They propose some origins such as: (i) unresolved substructures like spiral arms; (ii) geometrical effects due to the high inclination and the presence of the warp; (iii) turbulence and expanding shells induced by shocks and stellar winds of unresolved regions; (iv) gas of the halo infalling onto the disc through fountain mechanism or accretion from the intergalactic medium high; and (v) intermediate velocity clouds. They also do not detect counter rotating gas clouds, which can be produced after a satellite accretion event.

It is expected that the gas spatially correlates with the dust, given that the last forms in star forming regions where the gas is dense. Spitzer Space Telescope observations in the far infrared bands reveal the main dust distribution and many substructures such as the central rings $\sim 1 - 2$ kpc, the spiral arms trailing the bar, and the 10 kpc ring like substructure (Gordon et al. 2006; Barmby et al. 2006).

Star formation history studies estimate current star formation ratios (SFR) between $0.3 M_{\odot} \text{ yr}^{-1}$ and $0.7 M_{\odot} \text{ yr}^{-1}$ (Tabatabaei & Berkhuijsen 2010; Barmby et al. 2006; Kang et al. 2009). Ford et al. (2013) estimate a global $\text{SFR} = 0.25^{+0.06}_{-0.04} M_{\odot} \text{ yr}^{-1}$ from $24 \mu\text{m}$ and far ultraviolet (FUV). Rahmani et al. (2016) estimate a total star formation rate between $0.35 \pm 0.04 M_{\odot} \text{ yr}^{-1}$ and $0.4 \pm 0.04 M_{\odot} \text{ yr}^{-1}$, with most of the star formation localised in the 10 kpc ring (Lewis et al. 2015). Williams et al. (2015) also identify a major global star forming episode 2-4 Gyr ago.

The nearly invisible hot gas halo is estimated to contain at least $\sim 10\%$ of the stellar mass of M31 (Lehner et al. 2017), but distributed in a much larger volume extending to about a million light-years from the centre, almost halfway to the Milky Way which is 2.3 million light years away (0.78 Mpc). The halo is enriched with metals from stellar feedback such as supernovae.

1.3.6 The dark matter and dynamical mass distribution

As explained in section 1.1.2, Λ CDM simulations predict that galaxies like Andromeda are embedded in large and massive dark matter haloes that dominate the dynamics particularly in the outer parts. Andromeda is the most massive galaxy in the LG, although some estimations place the Milky Way as equally or slightly more massive, with $M_{\text{dyn,MW}}^{300 \text{ kpc}} = 0.7 - 3.4 \times 10^{12} M_{\odot}$ (Watkins et al. 2010). The range of estimated dynamical (total) mass of M31 are: $M_{\text{dyn}}^{300 \text{ kpc}} = 1.4 \pm 0.4 \times 10^{12} M_{\odot}$ within 300 kpc for isotropic halo models, or $M_{\text{dyn}}^{300 \text{ kpc}} = 1.3 - 1.6 \times 10^{12} M_{\odot}$ for anisotropic models (Watkins et al. 2010), $M_{\text{dyn}}^{550 \text{ kpc}} = 1.25^{+1.8}_{-0.6} \times 10^{12} M_{\odot}$ within 550 kpc (Evans et al. 2000; Evans & Wilkinson 2000), $M_{\text{VIR}} = 1.5 \pm 0.3 \times 10^{12} M_{\odot}$ within a virial radius of $r_{\text{VIR}} \sim 260$ kpc (Peñarrubia et al. 2014), estimated combining data from planetary nebulae, globular clusters, and galaxy satellites.

Further within the galaxy, Corbelli et al. (2010) use HI kinematics and find within 37 kpc a mass of $M_{\text{dyn}}^{37 \text{ kpc}} = 4.9^{+1.2}_{-1.4} \times 10^{11} M_{\odot}$. Chemin et al. (2009) find a similar value within 38 kpc $M_{\text{dyn}}^{38 \text{ kpc}} = 4.7 \pm 0.5 \times 10^{11} M_{\odot}$, with a dark matter to baryonic mass ratio of $M_{\text{DM}}^{38 \text{ kpc}} / M_{\text{Baryon}}^{38 \text{ kpc}} \sim 3.7$ (79% of dark matter), and a dynamical mass-to-light ratio at this radius is $M_{\text{DM}}^{38 \text{ kpc}} / L_{\text{R}} \sim 6.7 M_{\odot} L_{\odot}^{-1}$, where M_{Baryon} represents the mass of the stars and stellar remnants (M_{\star}), the central black hole and the gas. They estimate a stellar mass of $M_{\star}^{38 \text{ kpc}} = 9.5 \pm 1.7 \times 10^{10} M_{\odot}$, obtained from fit-

ting the HI gas rotation curve and its mass distribution, and the photometric profiles in the R band with different stellar mass-to-light ratios and dark matter haloes. The ratio in percentage between the gas (atomic and molecular HI + He + H₂) and the stellar mass is then $M_{\text{HI+He+H}_2}^{38\text{ kpc}}/M_{\star}^{38\text{ kpc}}=6.7_{-1.0}^{+1.3}\%$. Other stellar mass estimations in the literature are: [Barmby et al. \(2006\)](#) with $M_{\star}=1.1 \times 10^{11} M_{\odot}$, [Williams et al. \(2017\)](#) with $M_{\star}=9 \pm 2 \times 10^{10} M_{\odot}$ for within the disc area, and [Rahmani et al. \(2016\)](#) that estimate $M_{\star}=6.9 \times 10^{10} M_{\odot}$ from the IRAC 3.6 μm ; and in Chapter 2 ([Blana 2018](#)) is estimated a stellar mass within 15 kpc of $M_{\star}^{15\text{ kpc}}=7.5 \times 10^{10} M_{\odot}$. Although all these stellar mass estimations use different methods and tracers, most agree within $\sim 20\%$ where some of the differences may be attributed to the inclusion of the stellar halo in the calculations which has $\sim 4\%$ of the total stellar light ([Courteau et al. 2011](#)).

1.3.7 The satellites of Andromeda

The Andromeda galaxy system has so far 28 detected dwarf satellite galaxies ([Mateo 1998](#); [Watkins et al. 2013](#); [Sanders & Evans 2017](#)). This number is however too low compared to standard ΛCDM simulations where a few hundred are expected, a problem named “the missing satellite problem” ([Cote et al. 2002](#); [Simon & Geha 2007](#)). Current simulations appear to solve or alleviate this disagreement by including other physical processes (stellar feedback, supernovae, magnetic fields, etc), which results in a lower star formation efficiency producing dark matter subhaloes with little or no stars ([Wetzel et al. 2016](#)). These satellites and streams are relics of the hierarchical merger formation scenario that is expected from ΛCDM simulations where stellar haloes and classical bulges are formed in disc galaxies (section 1.1.2). However, other studies consider these dwarf galaxies to be remnants of a galactic collision, perhaps between M31 and MW, forming Tidal Dwarf Galaxies (TDG) as it is suggested by the peculiar flat spatial distribution of the M31 and the MW satellites in two “disc of satellite” (DoS) ([Metz et al. 2007](#); [Metz & Kroupa 2007](#); [Metz et al. 2009](#)).

1.4 Main goals and outline of the thesis

M31 contains a bulge composed of a classical bulge & a box/peanut (B/P) bulge, and a thin bar. There are no M31 models in the literature that quantitatively constrain the main properties of the classical bulge of M31 and the entangled B/P bulge. This thesis’s main goal is to develop rotating triaxial dynamical models considering the barred nature of M31 to constrain the main properties of both bulge components. These are essential to estimate the stellar and dark matter mass in the centre of the galaxy. Chapter 2 describes the development of a large set of N-body simulations where we study the evolution of disc galaxy models with a dark matter halo and classical bulges of different masses and size that evolve in time forming a bar and a box/peanut bulge. Comparing the resulting entangled bulges with infrared photometric properties we find a best N-body model that satisfactorily reproduce M31. In Chapter 3 the previous best N-body model is improved with the made-to-measure method by being directly fitted to photometric and stellar kinematic data. This is done while exploring different values for the stellar mass-to-light ratio, the bar pattern speed and the dark matter mass within the bulge with a large set of M2M, which allows to find

best values. In Chapter 4 we present a discussion on the implications of these results in a larger context, and a summary with the main results. Finally in Chapter 5 is presented the outlook of this project leading to new improved models, potential spin off projects, as well as a better understanding of observations, and the predictions for necessary future observations.

Chapter 2

Andromeda chained to the Box – Dynamical Models for M31: Bulge & Bar

Original publication: Matias Blaña Díaz¹, Christopher Wegg, Ortwin Gerhard, Peter Erwin, Matthieu Portail, Michael Opitsch, Roberto Saglia, Ralf Bender, 2017, MNRAS, 466, 4279 [✉](#)

Abstract

Andromeda is our nearest neighbouring disk galaxy and a prime target for detailed modelling of the evolutionary processes that shape galaxies. We analyse the nature of M31’s triaxial bulge with an extensive set of N-body models, which include Box/Peanut (B/P) bulges as well as initial classical bulges (ICBs). Comparing with IRAC $3.6\ \mu\text{m}$ data, only one model matches simultaneously all the morphological properties of M31’s bulge, and requires an ICB and a B/P bulge with 1/3 and 2/3 of the total bulge mass respectively. We find that our pure B/P bulge models do not show concentrations high enough to match the Sérsic index (n) and the effective radius of M31’s bulge. Instead, the best model requires an ICB component with mass $M^{\text{ICB}}=1.1 \times 10^{10} M_{\odot}$ and three-dimensional half-mass radius $r_{\text{half}}^{\text{ICB}}=0.53\ \text{kpc}$ (140 arcsec). The B/P bulge component has a mass of $M^{\text{B/P}}=2.2 \times 10^{10} M_{\odot}$ and a half-mass radius of $r_{\text{half}}^{\text{B/P}}=1.3\ \text{kpc}$ (340 arcsec). The model’s B/P bulge extends to $r^{\text{B/P}}=3.2\ \text{kpc}$ (840 arcsec) in the plane of the disk, as does M31’s bulge. In this composite bulge model, the ICB component explains the velocity dispersion drop observed in the centre within $R < 190\ \text{pc}$ (50 arcsec), while the B/P bulge component reproduces the observed rapid rotation and the kinematic twist of the observed zero velocity line. This model’s pattern speed is $\Omega_p=38\ \text{km s}^{-1}\ \text{kpc}^{-1}$, placing corotation at $r_{\text{cor}}=5.8\ \text{kpc}$ (1500 arcsec). The outer Lindblad resonance (OLR) is then at $r_{\text{OLR}}=10.4\ \text{kpc}$, near the 10 kpc-ring of M31, suggesting that this structure may be related to the bar’s OLR. By comparison with an earlier snapshot, we estimate that M31’s thin bar extends to $r_{\text{bar}}^{\text{thin}}\sim 4.0\ \text{kpc}$ (1000 arcsec) in the disk plane, and in projection extends to $R_{\text{bar}}^{\text{thin}}\sim 2.3\ \text{kpc}$ (600 arcsec).

2.1 Introduction

The Andromeda galaxy (M31, NGC224) is the nearest spiral galaxy, located at a distance of 785 ± 25 kpc from the Milky Way (MW) (McConnachie et al. 2005), which makes it one of the best cases to study in great detail the structural and evolutionary properties of spiral galaxies. It shows several signs of a hierarchical formation history through its satellites, the Giant Stream and its old stellar halo suggesting a history of minor mergers (Ibata et al. 2001; Tanaka et al. 2010) or also a possible major merger (Hammer et al. 2010; Bekki 2010). It also shows signs of secular evolution such as a massive star forming disk, spiral arms and rings (Gordon et al. 2006; Barmby et al. 2006; Chemin et al. 2009). The massive bulge of Andromeda has commonly been considered in the literature as a classical bulge, or more recently, as a classical bulge with “pseudobulge trimmings” (Mould 2013).

According to theory, classical bulges are considered as elliptical galaxies in the centres of disks, as remnants of a very early formation process, or as remnants of mergers of galaxies occurred during the first gigayears of a violent hierarchical formation (Toomre 1977; Naab & Burkert 2003; Bournaud et al. 2005; Athanassoula et al. 2016). Another proposed mechanism to form early bulges consists of instabilities in the early disk, forming clumps and star clusters that spiral in due to dynamical friction, merging later and forming a bulge (Noguchi 1999; Immeli et al. 2004; Bournaud et al. 2007). The comprehensive review of Kormendy (2013) describes in general how disc galaxies can also develop bulges through secular evolution, referred also as pseudobulges. The term pseudobulge groups disky bulges and box/peanut bulges together. In this scenario pseudobulges are a manifestation of the evolution of the disk, contrary to the classical bulges.

Fisher & Drory (2008); Fabricius et al. (2012) use a sample of spiral galaxies and their photometric and kinematic properties such as the Sérsic index n , the effective radius R_e , and the central dispersion $\sigma_{R_e/10}$ finding that pseudobulges have Sérsic indices $n \lesssim 2$ and classical bulges indices $n \gtrsim 2$.

Simulations of wet mergers by Keselman & Nusser (2012) showed that classical or primordial bulges may also present characteristics of pseudobulges, such as rotation and $n < 2$, which makes even harder to distinguish the origin of its properties. Furthermore, Erwin et al. (2015) showed with observations that classical bulges can coexist with disky pseudobulges and box/peanut bulges, a situation that has also been reproduced in simulations (Athanassoula et al. 2016).

Saha et al. (2012) showed that if a low mass non-rotating classical bulge is present during the formation and evolution of the bar it absorbs angular momentum from the bar (see also Hernquist & Weinberg 1992; Athanassoula 2003), and subsequently the bulge manifests cylindrical rotation like the bar, thereby making the final combined structure with the bar difficult to disentangle. However, more massive classical bulges do not reach cylindrical rotation (Saha et al. 2016).

Observations show that M31’s bulge is triaxial, with a photometric twist relative to the disk (Lindblad 1956; Hodge & Kennicutt 1982; Beaton et al. 2007), and the misalignment of the bulge kinematic major axis and its photometric major axis (Saglia et al. 2010). A known dynamical mechanism to generate a triaxial structure is the buckling instability of the bar, which generates the box/peanut (B/P) bulge in N-body models (Combes et al. 1990; Raha et al. 1991, see Section

2.3.1.2) . Erwin & Debattista (2016) have recently found indications that two barred galaxies (NGC 3227 and NGC 4569) are currently in the buckling phase.

Several hints such as: the kinematics of the bulge, the boxiness of the surface-brightness contours, and the twist of the photometric major axis of the bulge's boxy region and the disk's major axis, suggest that M31 could contain a B/P bulge and therefore may also host a thin bar. The inclination of $\sim 77^\circ$ (Corbelli et al. 2010) of the disk presents challenges, but the proximity of M31 and the excellent available photometric and kinematic data (Barmby et al. 2006; Chemin et al. 2009; Corbelli et al. 2010; Saglia et al. 2010), make it possible to explore this scenario. Courteau et al. (2011) (hereafter Co11) produced photometric models from the IRAC $3.6\mu\text{m}$ data and find a bulge-to-total luminosity ratio of $(B/T)_{3.6\mu\text{m}} \sim 0.3$ a Sérsic index of $n = 2.4 \pm 0.2$, an effective radius $R_e = 1.10 \pm 0.10$ kpc or ≈ 290 arcsec (M31 distance implies a unit conversion of 3.8 pc = 1 arcsec, 1 kpc = 260 arcsec and 13.7 kpc = 1°), and a disk scale length of $R_d = 5.8 \pm 0.1$ kpc, giving a ratio of $R_e/R_d \sim 0.19$. These values would locate M31's bulge just between the classical and the pseudobulges, according to Fisher & Drory (2008). However, the kinematics in the bulge region (Saglia et al. 2010, see the major axis velocity and dispersion profiles in their Fig.3), would classify it among the group of classical bulges (Fabricius et al. 2012), due to the high velocity dispersion at $R_e/10$ of $\sigma_{R_e/10} \gtrsim 150$ km s $^{-1}$ and the rather slow rotation in the bulge region (~ 70 km s $^{-1}$ at R_e).

Another interesting hint of the bulge type of M31 comes from the metallicity analysis and the age estimation of the stars. Saglia et al. (2010) find the presence of a very old stellar population in the central part within 300 arcsec, with an average age of ~ 12 Gyr, which would support the idea of a classical component in the bulge. Meanwhile, from 360 arcsec outwards the mean age of the stellar population drops to < 8 Gyr. This is compatible with the isophotal analysis performed by Beaton et al. (2007), where the authors present strong evidence for the presence and projected extension of the B/P bulge in M31, by quantifying the morphological properties of the isophotes of M31 2MASS 6X images in the J,H,K $_s$ bands. Within ~ 50 arcsec the round isophotes resemble a classical bulge with low ellipticity. Beyond ~ 50 arcsec the boxy isophotes emerge, also increasing the ellipticity, extending until ~ 700 arcsec, where the strongest boxiness is at ~ 300 arcsec. Athanassoula & Beaton (2006, hereafter AB06) used four N-body models of barred galaxies based on Athanassoula (2003), two with a pure B/P bulge and two with a classical bulge combined with a B/P bulge, to compare qualitatively the shape of their isophotes with the isophotes of M31 in the J band, concluding the presence of a dominant B/P bulge and also a classical bulge component in M31.

With the IRAC $3.6\mu\text{m}$ data that are less affected by dust absorption than the 2MASS 6X data and go deeper into the bulge and disk, together with the new kinematic data of Saglia et al. (2010); Chemin et al. (2009); Corbelli et al. (2010) and Opitsch et al. (in preparation), we can quantitatively compare M31 with N-body models. From these observational quantities we can build an understanding of the inner structure of M31's bulge and estimate the contribution of each possible subcomponent *i.e.* a classical bulge, a B/P bulge and a thin bar. The goal of this paper is to explore dynamical models for the bulge of M31 that consist of two components, a classical component and a B/P bulge, and also test pure B/P bulge models.

The paper is ordered as follows: Section 2.2 characterises the observational data, Section 2.3 describes the set-up of the simulations, and our technique to compare the simulations with the

observations. Section 3.3 shows simultaneously the results for M31 and for the simulations. The morphological and photometric analysis are presented in Sections 2.4.2 and 2.4.3. In Section 2.4.5 we present the properties of the best model. In Section 2.5 we discuss properties of triaxial models in the literature, and in Section 3.4 we conclude with a summary of our findings and the implications for M31.

2.2 Observational data: M31 IRAC 3.6 μm image

The imaging data we use for our analysis come from the large-scale IRAC mosaic images of the *Spitzer Space Telescope* (Barmby et al. 2006) – specifically, the 3.6 μm IRAC1 mosaic shown in Fig. 2.2, kindly made available to us by Pauline Barmby. The near side of the disk is in the upper part of the figure, pointing north-west, as evidenced by the dust lanes and reddening maps (Walterbos & Kennicutt, R. C. 1988). Careful inspection of the edges of the mosaic showed extended regions with slightly negative pixel values, suggesting a small oversubtraction of the sky background. Although this has negligible effect on our analysis of the bar and bulge region, we corrected the image by measuring the background in the regions furthest from the galaxy centre along the minor axis. The original IRAC1 mosaic of Barmby et al. (2006) has a pixel scale of 0.863 arcsec/pixel and a size of 16300 \times 7073 pixels (3.89 \times 1.69 degrees), using here for the analysis a resolution of 8.63 arcsec/pixel. We fit ellipses to the 3.6 μm isophotes using the `ellipse` task in the STSDAS package in IRAF; this task is based on the algorithm of Jedrzejewski (1987). The algorithm fits ellipses to isophotes by minimizing the deviations in intensity around a given ellipse; for an ellipse with a given semi-major axis a , this is done by iteratively adjusting the ellipse centre (pixel position in x and y), orientation (position angle PA), and ellipticity ($1 - b/a$ or ϵ , where b is the semi-minor axis of the ellipse). From `ellipse` we obtained the azimuthally average (AZAV) intensity (I) profile. All magnitudes are in the Vega system, and we use the 3.6 μm absolute solar magnitude $M_{\odot}^{3.6} = 3.24$ (Oh et al. 2008). We convert the intensity profile to surface-brightness profile (SB) using the 3.6 μm zero-point calibration 280.9 ± 4.1 Jy (Reach et al. 2005). For each fitted ellipse, the algorithm also expands the residual variations in intensity around the ellipse in a Fourier series:

$$I(\theta) = I_0 \sum_{m=3}^n (\tilde{A}_m \sin m\theta + \tilde{B}_m \cos m\theta), \quad (2.1)$$

where I_0 is the mean intensity along the best-fit ellipse; the $m = 1$ and $m = 2$ components are automatically zero for the best-fit ellipse. In fact, the actual computation divides the $m = 3$ and higher coefficients by the local radial intensity gradient and the ellipse semi-major axis to generate coefficients of radial deviation from a perfect ellipse:

$$\frac{\delta r(\theta)}{r} = I_0 \sum_{m=3}^n (A_m \sin m\theta + B_m \cos m\theta), \quad (2.2)$$

where $r = \sqrt{ab}$. The result is a set of higher-order terms (A_3 , B_3 , etc.) describing how the actual isophote deviates from a perfect ellipse. The most interesting coefficients from our point of view

are A_4 and B_4 . The most well-known of these is B_4 , which is > 0 when the isophotes are “disky” (lemon-shaped) and < 0 when the isophotes have a “boxy” shape. The A_4 term is non-zero when the boxy/disky shape is *rotated* with respect to the fitted ellipse; Erwin & Debattista (2013) (hereafter ED13) discuss how both components are affected by the presence of B/P structures in bars.² We used logarithmic spacing of the semi-major axes for fitted ellipses, to combine high spatial resolution in the central regions and higher S/N at large radii. The `ellipse` profiles obtained for M31 are shown later in Figures 2.3 and 2.4.

2.3 Method

2.3.1 Simulations

We want to explore a scenario where the bulge of M31 is a pure B/P bulge or a combination of a classical bulge and a B/P bulge, and in the last case, to constrain the properties of the classical component. That there are no complete analytical descriptions of B/P bulges that reproduce the vertical complexity of these structures, together with our interest in models which evolve in time and naturally develop the B/P bulge structure in equilibrium with a classical bulge, compels us to proceed with N-body simulations. In N-body models B/P bulges emerge from a disk that forms a bar which later buckles vertically, creating a peanut or boxy structure. This is a non-linear process which involves a redistribution of mass in the inner part of the initial disk, where the potentials of all components are involved *i.e.* the disk, the initial bulge and the dark matter halo. It is not then possible to predict quantitatively the properties of a model after it evolves from its initial conditions. We therefore proceed to make a systematic exploration of the initial parameters with simulations where we change one parameter at the time. We separate here the discussion into the generation of the initial N -body models, and the generation of bars and B/P bulges in those models.

2.3.1.1 N -body models: initial conditions

We use the software NEMO, an array of several independent programs and tools to perform N -body experiments and analysis in stellar dynamics (Teuben 1995). To generate the particle models we select the program MAGALIE (Boily et al. 2001) based on the method proposed by Hernquist (1993) which solves the Jeans equations to generate galaxies close to dynamical equilibrium with several components, e.g. a bulge, a disk and a dark matter halo. The code works in natural units, ergo the gravitational constant is set to $G=1 \text{ u}_v^2 \text{ u}_d \text{ u}_M^{-1}$, and the internal units for the variables are: u_M (mass), u_d (distance), u_t (time) and u_v (velocity). The exact values of the scaling factors for converting internal units into physical units vary between each simulation, as explained later in Section 2.3.2. Typical values are $1 \text{ u}_M \sim 5 \times 10^{10} M_\odot$, $1 \text{ u}_d \sim 2 \text{ kpc}$, $1 \text{ u}_v \sim 300 \text{ km s}^{-1}$ and $1 \text{ u}_t = 1 \text{ u}_d \text{ u}_v^{-1} \text{ Gyr}$ which is $\sim 7.0 \text{ Myr}$. This allows the scaling of the models to M31 by matching velocity and spatial scales independently.

²Note that in the ellipse-fit code of Bender et al. (1988), the $\cos 4\theta$ diskly/boxy term is denoted by a_4 , and is related to B_4 by $a_4/a = \sqrt{b/a} B_4$.

MAGALIE builds N -body dark matter haloes (DMHs) with different mass density profiles, a cored isothermal profile (used by AB06), or a Hernquist profile. Here we chose the latter, as a convenient approximation to a Navarro-Frenk-White (NFW) DMH profile. It has convergent mass at large radii $r \rightarrow \infty$, and mimics the cuspy NFW profile in the inner parts of the halo as both density profiles behave as $\sim r^{-1}$ within their respective scale radius (Springel et al. 2005). It is given by

$$\rho_{\text{halo}}(r) = \frac{M_{\text{H}} (2\pi r_{\text{h}}^3)^{-1}}{r/r_{\text{h}} (1 + r/r_{\text{h}})^3} \quad (2.3)$$

where r is the radius, M_{H} is the mass of the halo at $r \rightarrow \infty$ and r_{h} is the scale length. We truncate the haloes at $r=22 u_{\text{d}}$, which defines the actual halo mass in the simulation $M_{\text{h}}=M(r < 22 u_{\text{d}})$. The density of the DMHs show some evolution in their outer parts at $20 u_{\text{d}}$, but quickly stabilises within $100 u_{\text{t}}$, well before the bar formation, to its final shape.

The initial disk density profile is given by:

$$\rho_{\text{disk}}(\mathbf{R}, z) = M_{\text{d}} (4\pi h^2 z_0)^{-1} \exp(-R/h) \text{sech}^2(z/z_0) \quad (2.4)$$

where R is the cylindrical radius and h is the initial radial scale length of the disk, which is fixed by MAGALIE to be $h=1 u_{\text{d}}$. The scale height of the disk is $z_0=0.18 u_{\text{d}}$ and the mass of the disk is also fixed to $M_{\text{d}}=1.0 u_{\text{M}}$. As we are interested in the bulge we truncate the disk at $r=10 u_{\text{d}}$. The disks have an exponential radial dispersion profile. We choose a Toomre (Toomre 1964) value of $Q_{\text{T}}(R_{Q_{\text{T}}})=1.0$ measured at $R_{Q_{\text{T}}}=2.5 u_{\text{d}}$ which avoids axisymmetric instabilities, but allows non-axisymmetric instabilities to grow. We also modified MAGALIE to generate and test disks with an initial constant $Q_{\text{T}}=1.0$, as explained in Appendix 2.A.

The initial bulges (ICB) are created also with a Hernquist density profile for which, as shown by Hernquist (1990), the projected surface-density profile agrees with a de Vaucouleurs profile (which is a Sérsic profile with index $n=4$), within ≈ 35 per cent for radii in the range $0.06 \lesssim R/R_{\text{e}} \lesssim 14.5$. If integrated, this encloses ≈ 94 per cent of the total light. The density profile and parameters are defined here as:

$$\rho_{\text{bulge}}(r) = \frac{M_{\text{B}} (2\pi r_{\text{b}}^3)^{-1}}{r/r_{\text{b}} (1 + r/r_{\text{b}})^3} \quad (2.5)$$

where r_{b} is the bulge scale length and M_{B} is the mass of the bulge at $r \rightarrow \infty$. We stop the particle sampling at $r=2 u_{\text{d}}$, which defines the actual ICB mass in the simulation $M_{\text{b}}=M(r < 2 u_{\text{d}})$. During the evolution, the ICB density profile near the outer boundary evolves slightly, involving less than 4 per cent of the ICB particles.

2.3.1.2 N -body models: bars & Box/Peanut bulges

Programs like MAGALIE can set up models of disk galaxies, but to study the possible coexistence of a B/P bulge with a classical bulge, we need to evolve the initial models to generate the required structures (Athanasoula 2005). These N -body models generally form a bar that later goes through the buckling instability generating the B/P bulge or thick bar in the centre, which

transitions to the thin bar further out that is aligned with the B/P bulge. Transient material trailing or leading the thin bar, like spiral arms attached to the thin bar ends, are not counted as part of the bar. We reserve the term bar for the whole structure, that includes both the thin bar and the B/P bulge.

We want to generate and explore models with bars that show a wide range of boxy structure, pattern speed, bar length and bar strength among others. Therefore, similarly to [Bureau & Athanassoula \(2005\)](#), we choose different concentrations and masses for the DMHs, leading to models dominated by the mass of the disk (MD models), and models dominated by the halo (MH models). MH models usually develop long thin bars and their B/P bulges have a strong X-shape. MD bars are shorter, the thin bar can be very weak, and the B/P bulge has a more boxy shape. We generate and explore B/P bulge models that also include initial classical bulges, as explained in the next section.

2.3.1.3 *N*-body models: parameter space exploration

We build two sets of models to make a systematic exploration of parameters with a total of 84 simulations. The first set (Set I) contains ICBs combined with B/P bulges and is built from initial models with bulge, disk and DMH components. Here we want to explore how the different ICBs affect the observational parameters. Therefore in this set we vary only the initial mass and size of the ICB component, choosing 12 different masses M_b ranging from $0.05 u_M$ to $0.6 u_M$ with steps at every $0.05 u_M$. For each chosen mass we also explore different sizes for the bulge using 6 values of r_b ranging from $0.1 u_d$ to $0.35 u_d$ with steps at every $0.05 u_d$, ending with a total of 72 simulations for this set. The DMH used in this set has a scale and mass of $r_h=20 u_d$ and $M_h=8 u_M$.

The second set of models (Set II) contains pure B/P bulges and is built from just disk and DMH initial components. Here we try to generate buckled bars with different boxy structures by changing the concentration and the mass of the DMHs. Therefore we use 3 scale lengths r_h of $10 u_d$, $15 u_d$ and $20 u_d$ and for each r_h we explore 4 different masses M_h : $6 u_M$, $7 u_M$, $8 u_M$ and $9 u_M$, making a total of 12 simulations.

In addition to these 84 simulations, we have run 100 simulations with different sets of initial parameters, such as disks with different z_o , others with cored isothermal DMHs, and others with an initial disk with initial constant $Q_T=1.0$, but found that our fiducial choices best reproduced the bulge of M31, and for conciseness we do not give further details of these simulations here.

Due to the difficulty of plotting the results of the analysis of 84 simulations, we proceed to show only three examples in the next sections, Model 1, Model 2 and Model 3, which belong to Set I and therefore they have the same initial DMH and initial disk. Models 1 to 3 have the same ICB scale length of $r_b=0.15 u_d$ and differ only in the mass of the ICBs, which are $0.25 u_M$ (Model 1), $0.05 u_M$ (Model 2) and $0.5 u_M$ (Model 3). We also show Model 0 which is a pure B/P bulge of Set II that has the same initial DMH and disk as the previous models. We will show later that Model 1 is our best model for M31's bulge of all the explored models.

2.3.1.4 *N*-body models: time integration

To evolve the initial models we used a program also contained in NEMO called GYRFALCON (Dehnen 2000). Although this program is not parallelized, it is a fast, momentum-conserving tree-code. It uses the same internal units of MAGALIE. We choose a time step of $t_{\text{step}}=2^{-6} u_t \approx 1.56 \times 10^{-2} u_t$ and we evolve the initial models until $600 u_t$ (~ 4.65 Gyr), analysing all the models this standard time. We also analyse and compare some models at $500 u_t$, $700 u_t$, $800 u_t$ and $1000 u_t$. We choose a tolerance parameter of $\theta_{\text{tol}}=0.5$. For simplicity we use a constant softening parameter of $\epsilon=0.05 u_d$.

The number of particles that we use in both sets for the disk, classical bulge (if present) and DMH are $N_b=10^6$, $N_d=10^6$ and $N_h=2 \times 10^6$ respectively, and therefore the respective particle masses for each component are different, with values for Model 1 of $m_b=1.2 \times 10^4 M_\odot$, $m_d=4.8 \times 10^4 M_\odot$ and $m_h=1.9 \times 10^5 M_\odot$. To examine the effects of force resolution on our main results we have re-run simulations with new softening parameters using a 50 per cent smaller global ϵ and later a 50 per cent larger global ϵ . To test the effects of unequal particle masses we follow the prescription by McMillan & Dehnen (2007): the softening for each particle depends on its mass and on the condition of the maximum force ($F \sim m/\epsilon^2$) allowed between the particles, obtaining for Model 1 the softenings for the bulge, disk and halo $\epsilon_b=0.0125 u_d$ (30 pc), $\epsilon_d=0.025 u_d$ (60 pc) and $\epsilon_h=0.05 u_d$ (120 pc). In the resulting simulation with lower resolution we observed no significant variations, while in the simulations with higher resolution we observed that the bar formation is delayed by roughly $\sim 100 u_t$, but the bar evolution, including the buckling, does not change significantly and therefore the age of the bar remains the same, and the results stay unchanged.

2.3.2 Technique to obtain the best-matching model

In order to compare simulations with observations we also use `ellipse` on images generated from our simulations. From this we obtain semi-major axis (R) profiles of 5 parameters: the position angle (PA) of the fitted ellipse, the Fourier coefficients $A4$ and $B4$ which measure the asymmetry and the boxiness, the ellipticity ϵ and the azimuthally average (AZAV) surface-density profile $\Sigma(R)$ for the simulation images. The position angle is measured anticlockwise with respect to the north celestial pole axis, where $\text{PA}=0^\circ$. We rely on the coefficient $B4$ to quantify the strength of the boxiness (negative $B4$) or diskiness (positive $B4$) of the isophotes. As already mentioned in the Introduction, the Sérsic index is useful to classify bulges as classical bulges ($n > 2$) or pseudobulges ($n < 2$), and therefore we measured this parameter in M31 and in our models. For this we fit a combination of a Sérsic profile (Sersic 1968) and an exponential profile to $I(R)$, obtained from M31, and also to $\Sigma(R)$ from the simulations:

$$\begin{aligned} I(R) &= I_e \exp\left(-b_n \left[(R/R_e)^{1/n} - 1\right]\right) + I_d \exp(-R/R_d) \\ \Sigma(R) &= \Sigma_e \exp\left(-b_n \left[(R/R_e)^{1/n} - 1\right]\right) + \Sigma_d \exp(-R/R_d) \end{aligned} \quad (2.6)$$

where $b_n=1.999 n - 0.3271$ (Capaccioli 1989), R_d is the disk scale length, n the Sérsic Index, and R_e the effective radius which corresponds to the half light (or half mass) radius of the Sérsic

profile. I_e and Σ_e correspond to the half light and half mass of the Sérsic profile. Here we denote by $I_{\text{Sersic}}(R)$ and $\Sigma_{\text{Sersic}}(R)$ the component in Eq.2.6 fitted by the Sérsic profile. The fit of the parameters is performed with a non-linear least squares (NLLS) minimization method using a Levenberg-Marquardt algorithm, where we explore a full suite of Monte Carlo NLLS realizations with a wide range of initial guesses over all fitted parameters, from which we estimate errors from the standard deviations of the solutions around the best values.

We convert the $\Sigma(R)$ of the models to surface-brightness dividing by a stellar mass-to-light ratio (M/L). This is determined after the profiles of Eq.2.6 are fitted to M31 and the models, by scaling $\Sigma_{\text{Sersic}}(R)$ of the models to the intensity of M31 measured at the effective radius of M31 (R_e^{M31}) which is I_e , *i.e.* $\Sigma_{\text{Sersic}}(R_e^{\text{M31}}) = (M/L) I_{\text{Sersic}}(R_e^{\text{M31}}) = (M/L) I_e$.

In order to find a best-matching model for M31 we define 6 observational parameters: (1) $\Delta\text{PA}_{\text{max}}$, corresponding to the difference between the maximum PA (PA_{max}) in the boxy region of the bulge and the PA of the disk PA_{disk} ; (2) $R_{B_4=0}$ that corresponds to the radius where $B_4=0$ and the isophotes stop being boxy and start being disk-like; (3) B_4^{min} that quantifies the maximum boxiness of the boxy bulge; (4) ϵ_{R_e} the ellipticity at R_e ; (5) the Sérsic index n and (6) the effective radius R_e . And finally, we consider an additional parameter, which is the velocity scaling u_v calculated from the line-of-sight maximum velocity dispersion (7) $\sigma_{\text{los}}^{\text{max}}$ measured in M31.

The procedure used to compare the observations with the models is the following:

1. We first project the models on the sky as M31, as shown in Fig.2.1. For this we incline the disk to $i=77^\circ$ (where an edge-on disk is $i=90^\circ$, and a face-on disk is $i=0^\circ$). Then we rotate the projected model around the observer's line-of-sight axis until the projected disk major axis is aligned with the disk major axis of M31, leaving the position angle of the disk major axis like M31 at $\text{PA}_{\text{disk}}=38^\circ$ (de Vaucouleurs 1958), and the near side of the disk in the upper part, pointing north-west like M31. We specify the orientation of the model's bar by an angle θ_{bar} in the plane of the disk, such that for $\theta_{\text{bar}}=0^\circ$ the bar is side-on and its major axis is aligned with the projected disk major axis, and θ_{bar} increases from the side of the disk major axis at $\text{PA}_{\text{disk}}=38^\circ$ in the direction away from the observer until for $\theta_{\text{bar}}=90^\circ$ the bar major axis is almost aligned with the line-of-sight and is seen nearly end on. Then we generate an image for each model, with a pixel size that slightly varies depending on the model, but with typical values of 5 arcsec.
2. We analyse the image of each model with `ellipse` and measure PA_{max} in the boxy region. PA_{max} is estimated as the error weighted mean of 5 PA measurements around the maximal PA value (with errors weights from the `ellipse` fitting), while for the PA_{max} error we use the error weighted standard deviation. This error is larger than the errors estimated by the `ellipse` fitting, and it takes into account the noise that we observe in the `ellipse` fitting profiles.
3. We repeat the previous step for each model, but with different θ_{bar} , ranging from 0° until 74° , until the $\Delta\text{PA}_{\text{max}}$ of each model matches the observed value for M31 which is $\Delta\text{PA}_{\text{max}}^{\text{M31}}=13.3 \pm 1.2$, obtaining a best bar angle $\theta_{\text{bar}}^{\text{best}}$ for each model. This parameter is independent of the size scaling which only determines at what distance $\Delta\text{PA}_{\text{max}}$ is located. To determine the error of the best bar angle we calculate where θ_{bar} matches the upper and the lower errors

of ΔPA_{\max}^{M31} , from which we estimate the $\theta_{\text{bar}}^{\text{best}}$ error as $(\theta_{\text{bar}}^{\text{up}} - \theta_{\text{bar}}^{\text{low}})/2$. As we show later in Fig.2.3, this error is larger than the effects of the noise in the PA profile on the bar angle estimation.

4. We use $\theta_{\text{bar}}^{\text{best}}$ for each model and we obtain the size scale u_d of each model by matching each $R_{B_4=0}$ to the value for M31. We show later in Section2.4.2 that the profile of the B_4 coefficient can successfully quantify the region where the boxy isophotes of M31 end ($B_4=0$), and that our models exhibit a similar behaviour, which makes this value ideal to our interest of restricting the size of the boxy region of M31's bulge and in our models.
5. We measure B_4^{\min} , ϵ_{R_e} , n and R_e in each model.
6. We discard the models that do not match the selected 6 observational parameters of M31 (ΔPA_{\max} , $R_{B_4=0}$, B_4^{\min} , ϵ_{R_e} , n and R_e), until we obtain a best model which simultaneously matches the parameters.
7. We obtain the velocity scale u_v of the best model by matching the maximum value of the line-of-sight dispersion profile along the major axis of the of the model with the value measured from the bulge of M31 by [Saglia et al. \(2010\)](#), *i.e.* $\sigma_{\text{los}}^{M31,\max} = \sigma_{\text{los}}^{\text{model},\max}$.
8. We calculate dispersion and velocity profiles and maps for the best model and compare them with M31 observations.
9. We use the spatial and velocity scaling to obtain the mass scaling and calculate the mass profiles for the best model.

At the end we obtain a model that matches the maximum position angle and the twist of the isophotes, with a boxy region of similar extension and magnitude. And which contains a bulge with similar ellipticity, Sérsic Index, and effective radius. We discuss later the kinematic properties of the best model, which matches the central dispersion and the rotation observed in M31's bulge.

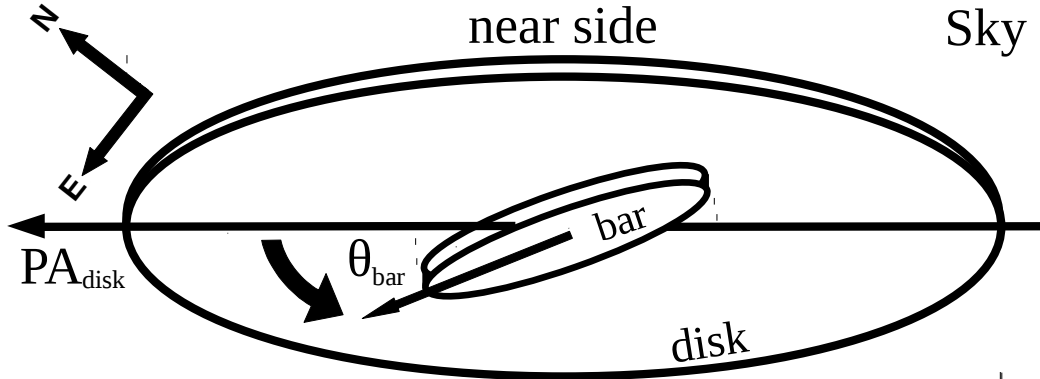


Figure 2.1: Schematic diagram of the orientation of the models. We project the models on the sky as M31, giving an inclination to the disk of $i=77^\circ$, locating the near side of the disk pointing to the north-west, and locating also the position angle of the projected major axis of the disk at $PA_{\text{disk}}=38^\circ$ anticlockwise from the north axis. The bar angle θ_{bar} is measured in the plane of the disk. The straight arrow shows the major axis of the bar that is aligned with the projected disk major axis when $\theta_{\text{bar}}=0^\circ$. The angle θ_{bar} increases anticlockwise, as shown by the curved arrow, until for $\theta_{\text{bar}}=90^\circ$ the bar is seen nearly end-on.

2.4 Results

The results are organized in six subsections. Section 2.4.1 explains how we match the isophotal twist of the bulge using the parameter ΔPA_{max} , to determine the orientation of the bar in three-dimensional space (θ_{bar}). In Section 2.4.2 we show the results of our morphological analysis with `ellipse` on the observations and simulations, determining 3 parameters: B_4^{min} , $R_{B_4=0}$, and ϵ . In Section 2.4.3 we use the surface brightness profile of the observations and the surface mass profile to determine two parameters: the Sérsic index and effective radius. Section 2.4.4 compares the previous mentioned six parameters of the 72 models of Set I, converging in a best matching model. Section 2.4.5 shows in more detail the properties of the best matching model, showing its kinematics, mass profile and others. Finally in Section 2.4.6 we analyse the thin bar and the the spurs in the models and compare them with the observations.

2.4.1 Morphology: bulge isophotal twist & bar angle θ_{bar}

The goal of this step is to match the twist of the isophotes in the boxy region of M31's bulge relative to the disk, as shown in Fig.2.2 (top panel). In external galaxies and in N -body simulations the presence of a classical bulge, and the orientation of the thin and the thick (or B/P bulge) components of the bar determine the shape and twist of the isophotes of the central region (Bettoni & Galletta 1994, AB06, ED13). ED13 compare surface-density contours of N -body barred disk models with isophotes of observed barred disk galaxies using the `ellipse` fitting analysis and identify several substructures that we also find in our models.

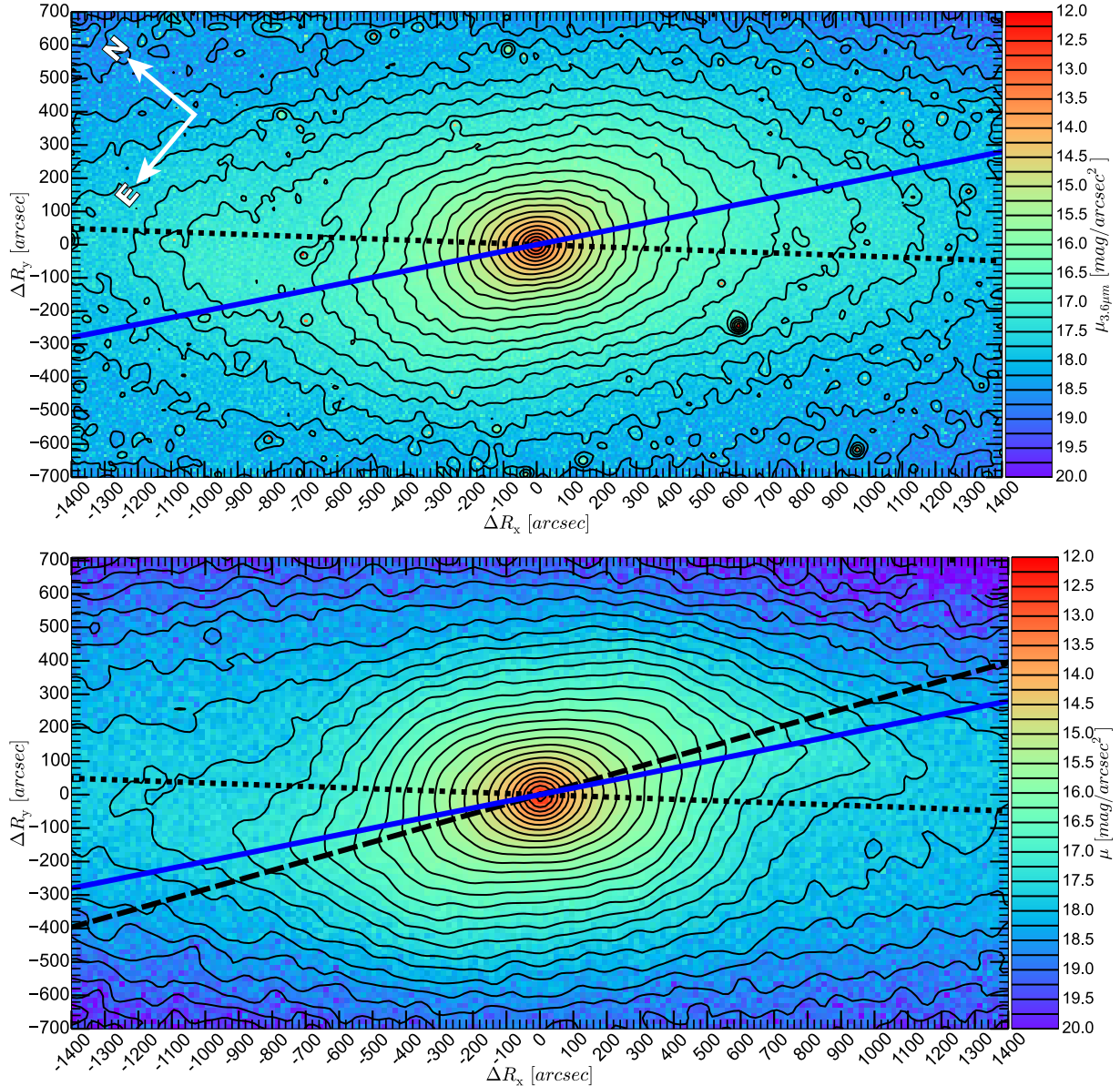


Figure 2.2: *Top panel:* IRAC $3.6\mu\text{m}$ image and isophotes of M31's central region. The position angle of the horizontal axis ΔR_x is $\text{PA}_h=40^\circ$. The dotted line marks the position of the major axis of the disk ($\text{PA}_{\text{disk}}=38^\circ$). The blue solid line marks the maximum position angle determined by the fit of the ellipses, reaching $\text{PA}_{\text{max}}^{\text{M31}}=51.3 \pm 1.2$, and therefore a difference with the disk of $\Delta\text{PA}_{\text{max}}^{\text{M31}}=13.3 \pm 1.2$, quantifying the clear isophotal twist in the central boxy region of the bulge. The near side of the disk is located in the upper part of the panel (Walterbos & Kennicutt, R. C. 1988). *Bottom panel:* Image of the central region of the isophotes of Model 1 at 4.65 Gyr ($600 u_t$). The mass is converted to luminosity dividing by a stellar mass-to-light ratio of $M/L=0.813 M_\odot L_\odot^{-1}$. We reproduce the central twist in the boxy region of the bulge, using the best bar angle of $\theta_{\text{bar}}^{\text{best}}=54.7 \pm 3.8$. The blue line marks the maximum PA of the model which matches $\text{PA}_{\text{max}}^{\text{M31}}$. The dashed line marks the projected bar major axis for the best bar angle $\text{PA}_{\text{bar}}=55.7 \pm 2.5$. The near side of the disk is also located in the upper part of the panel.

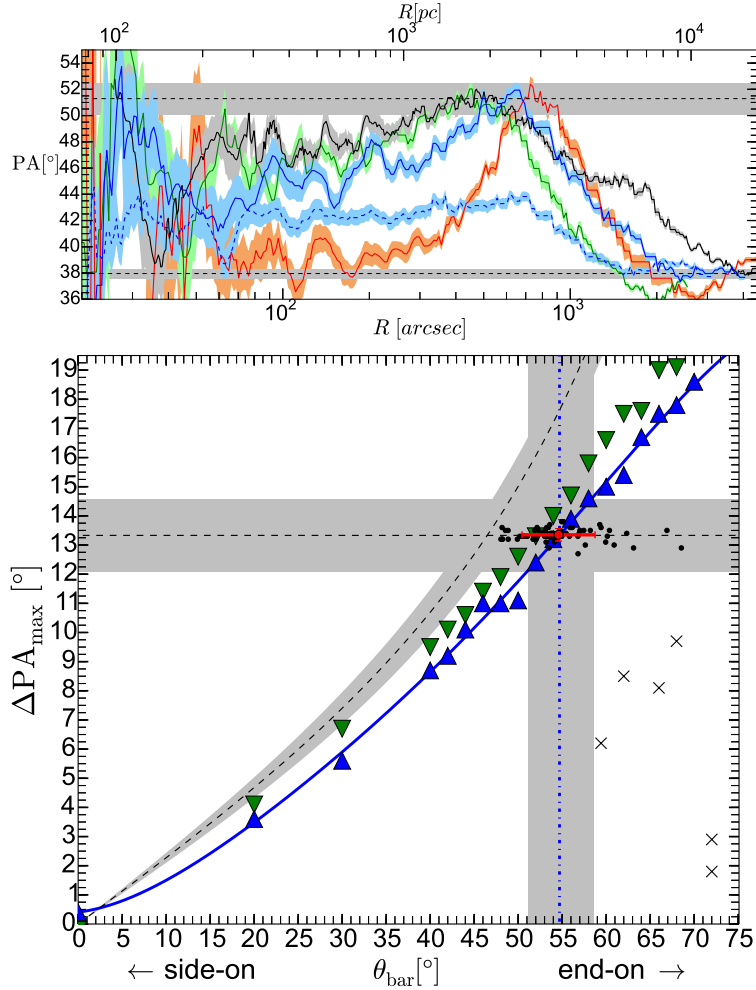


Figure 2.3: *Top panel:* The PA projected semi major-axis profiles determined with `ellipse` for M31 (black), Model 2 ($600 u_t$) (green) with $\theta_{\text{bar}}=52^\circ$ and Model 3 ($600 u_t$) (red) with $\theta_{\text{bar}}=66.9^\circ$, with errors in shaded regions. We show two profiles for Model 1 ($600 u_t$), one where $\theta_{\text{bar}}=30^\circ$ (blue dashed-line), and another where $\theta_{\text{bar}}=54.7^\circ$ (solid blue). The horizontal upper and lower dashed black lines marks the PA peak of M31 $\text{PA}_{\text{max}}^{\text{M31}}=51.3 \pm 1.2$, and the PA of the disk of $\text{PA}_{\text{disk}}=38^\circ$. *Bottom panel:* $\Delta \text{PA}_{\text{max}}$ versus the bar angle θ_{bar} . When $\theta_{\text{bar}}=0^\circ$ the bar is seen side-on, and when $\theta_{\text{bar}}=90^\circ$ it is end-on. The horizontal dashed line marks $\Delta \text{PA}_{\text{max}}^{\text{M31}}$. The dashed curve shows $\theta_{\text{proj}}(\theta_{\text{bar}})$ of Eq.2.7, where the grey area shows the value when $i=77^\circ \pm 1^\circ$. Model 1 $\Delta \text{PA}_{\text{max}}$ values are shown for different θ_{bar} (blue up-side triangles). The blue curve is a polynomial fit to estimate the best θ_{bar} that matches $\Delta \text{PA}_{\text{max}}^{\text{M31}}$ for Model 1. The blue vertical dash-dot line marks Model 1 best bar angle $\theta_{\text{bar}}^{\text{best}}=54.7 \pm 3.8$, where the grey area are the values estimated from the observational errors. The down-side green triangles correspond to Model 2. Dots and crosses correspond to the 72 models of Set I. Dots mark the required $\theta_{\text{bar}}^{\text{best}}$ for each model to match $\Delta \text{PA}_{\text{max}}^{\text{M31}}$. The red cross shows the mean and standard deviation for these best bar angle values: $\langle \theta_{\text{bar}}^{\text{best}} \rangle = 54.5 \pm 4.5$. Black crosses are models that cannot reach $\Delta \text{PA}_{\text{max}}^{\text{M31}}$, due to their concentrated ICBs that generate isophotes with low ϵ .

We quantify the twist in M31 and in the models using the difference between the maximum position angle PA_{max} in the boxy region and the disk $\text{PA}_{\text{disk}}=38^\circ$, obtaining for M31 $\Delta\text{PA}_{\text{max}}^{\text{M31}}=13.3\pm 1.2$. This is close to the measurements of [Beaton et al. \(2007\)](#) using the `ellipse` analysis on the bands J, H and K_s of 2MASS 6X data, obtaining $\Delta\text{PA}_{\text{max}}^{K_s}\sim 10^\circ$.

We measured the $\Delta\text{PA}_{\text{max}}$ of the iso-density contours in each of our models using different angles for the bar θ_{bar} . In Fig.2.3 (top panel) we show the PA profile and the PA_{max} for M31 in the boxy region compared to two PA profiles of Model 1 ($0.25 u_{\text{M}}$) that differ due to the different angles used for the bar, i.e. $\theta_{\text{bar}}=30^\circ$ (blue dash curve) and $\theta_{\text{bar}}=54.7$ (blue solid curve). As shown there, this model requires an angle for the bar of 54.7 to match the $\Delta\text{PA}_{\text{max}}$ observed in M31. We also show Model 3 ($0.5 u_{\text{M}}$) with the more massive ICB which needs an angle of $\theta_{\text{bar}}=66.9$ in order to match PA_{max} .

We show in Fig.2.3 (lower panel) how the bar angle θ_{bar} of a 1D-bar measured in the plane of the disk changes its projection into a plane in the sky, with an inclination angle for the disk of $i=77^\circ$, described by the equations:

$$\theta_{\text{proj}} = \arctan(\tan(\theta_{\text{bar}}) \cos(i)) \quad (2.7)$$

$$\text{PA}_{\text{bar}} = \theta_{\text{proj}}(\theta_{\text{bar}}) + \text{PA}_{\text{disk}} \quad (2.8)$$

where θ_{proj} is the projection of the bar angle θ_{bar} , and PA_{bar} is the *true* position angle of the projected major axis of the bar, that includes the thin bar and the B/P bulge. Therefore if we approximate M31's bulge as a 1D-bar structure, the required angle to match the photometric twist $\Delta\text{PA}_{\text{max}}^{\text{M31}}\sim\theta_{\text{proj}}$ would be $\theta_{\text{bar}}\sim 46.4$. N -body bars and real galaxies are vertically extended and therefore, excluding extreme cases, the difference between the bulge maximum position angle and the position angle of the disk ($\Delta\text{PA}_{\text{max}}$) will usually reach lower values than the infinitesimally thin case ($\Delta\text{PA}_{\text{max}}\leq\Delta\text{PA}_{\text{bar}}$), exactly as we show with our simulations in Fig. 2.3 (lower panel). In the figure we plot $\Delta\text{PA}_{\text{max}}$ versus θ_{bar} for the Models 1 and 2. Using a polynomial fit of order 7 to Model 1 we find that the angle for the bar for which the $\Delta\text{PA}_{\text{max}}$ matches the value observed in M31 is $\theta_{\text{bar}}^{\text{best}}=54.7\pm 3.8$, where the errors are given from the fit using the observational errors, as explained in Section 2.3.2. This angle generates a twist of the isophotes in the boxy region of Model 1, as shown in Fig.2.2 (bottom panel). The projected angle of a 1D-bar given by this best angle is $\theta_{\text{proj}}(\theta_{\text{bar}}^{\text{best}})=17.7\pm 2.5$, with its error calculated from the average of the upper and lower error in $\theta_{\text{bar}}^{\text{best}}$. This locates the PA of the thin bar (and the B/P bulge) at $\text{PA}_{\text{bar}}=\theta_{\text{proj}}(\theta_{\text{bar}}^{\text{best}}) + \text{PA}_{\text{disk}}=55.7\pm 2.5$. Applying the same procedure to Model 2 and Model 3 we recover the best angles $\theta_{\text{bar}}^{\text{best}}=52^\circ$ for Model 2 and $\theta_{\text{bar}}^{\text{best}}=66.9$ for Model 3. Model 1 and 2 recover more similar values for $\theta_{\text{bar}}^{\text{best}}$. Model 3 needs a larger $\theta_{\text{bar}}^{\text{best}}$ to match $\Delta\text{PA}_{\text{max}}$, because this model has a more massive ICB that dominates the morphology in the central region, and therefore the isophotes have lower ϵ and a less boxy shape and shows a low PA. Nonetheless, further out it can reach the observed $\Delta\text{PA}_{\text{max}}$.

Looking carefully at the PA profiles of the models in Fig.2.3 (top panel) clarifies why PA_{max} is chosen to determine the bar angle θ_{bar} . From all the PA values in a profile, PA_{max} is the closest value to the estimation given by Eq. 2.7 ($\Delta\text{PA}_{\text{max}}(\theta_{\text{bar}})\sim\theta_{\text{proj}}(\theta_{\text{bar}})$). The deviation of $\Delta\text{PA}_{\text{max}}(\theta_{\text{bar}})$ from $\theta_{\text{proj}}(\theta_{\text{bar}})$ is shown in Fig.2.3 (bottom panel). This behaviour is observed in all our models with bars and is the reason why we choose PA_{max} as an indicator for the bar angle. We

successfully match the PA_{\max} of M31, although the exact radius of the model's PA_{\max} depends on the morphology and length of the thick and thin bar. As a consequence of this choice, the isophotes of the model show a photometric twist slightly weaker than in M31 within the radius where PA_{\max} matches PA_{\max}^{M31} . Later, in Section 2.4.4.2, we show that our conclusions do not change when we increase θ_{bar} to produce a more pronounced isophotal twist in the inner part of the bulge region of Model 1.

We repeat this process for all the models, obtaining their respective $\theta_{\text{bar}}^{\text{best}}$. The mean and standard deviation of the 72 models of Set I is $\langle\theta_{\text{bar}}^{\text{best}}\rangle=54.5\pm 4.5$ which shows that the angle does not change much from model to model. Furthermore, we see in Fig.2.3 (lower panel) that θ_{proj} of Eq.2.7 is a good predictor as a lower limit for bar angles, because none of the 72 models reach values lower than $\theta_{\text{bar}}^{\text{best}}=46.4$ when they match ΔPA_{\max} . There are some outliers which never match ΔPA_{\max} , reaching always lower values due to the fact that their ICBs have too much mass and/or are too concentrated and their round isophotes dominate.

AB06 used four N-body models with different θ_{bar} and compare the spurs generated by the projection of the thin bar of the models with the spur like features at $R\sim 1000$ arcsec along the major axis of the disk in M31, and concluded that the angle for the bar is between $\theta_{\text{bar}}=20^\circ$ and 30° depending on which model they used. Here instead we use the isophotal twist of the bulge, obtaining $\theta_{\text{bar}}^{\text{best}}=54.7\pm 3.8$, and we argue later in Section 2.4.6 that structures at $R\sim 1000$ arcsec are not simply related to the spurs generated by the thin bar.

2.4.2 Morphology: position angle, boxiness, ellipticity & asymmetry

In this section we compare the morphology of the isophotes of M31 with the N-body models. For this we proceed in a similar way to ED13, with a morphological analysis using `ellipse` on the IRAC $3.6\mu\text{m}$ image shown in Fig.2.2 and on images of our simulations, obtaining four parameters as a function of the major axis R of the fitted ellipses: PA , B_4 , ϵ and A_4 . The resulting profiles for M31 and the models are shown in Fig.2.4. We use these parameters to identify isophotal structures and to define five regions (R1 ... R5) in M31, going from the inner part of the bulge to the disk. Simultaneously, we plot in the figure the morphological profiles of M31 with three models, Model 1, Model 2 and Model 3 measured at $600 u_t$, to compare their properties within these regions. These regions and the profiles are similar to the results obtained for M31's bulge in the bands J, H and K by Beaton et al. (2007), and the morphological properties are also similar to what was found by ED13 for their comparisons between B/P bulges of N-body simulations and other galaxies, using `ellipse`.

- *Region R1*: defined within $R\lesssim 70$ arcsec where $A_4\sim 0$ and $B_4\sim 0$. M31 shows in this region isophotes with a low ellipticity $\epsilon\lesssim 0.2$, symmetric, nearly-round isophotes, which makes the PA uncertain. Model 1 ($0.25 u_M$) shows similar values for ϵ , A_4 and B_4 although the last two parameters indicate slightly more symmetric isophotes than in M31. Model 2 ($0.05 u_M$) has a higher ϵ and a more disk-like shape ($B_4 > 0$) in the inner part ($R\sim 30$ arcsec), but the boxy region starts sooner ($R\sim 45$ arcsec), and is also symmetric $A_4\sim 0$. This highlights the necessity of a more massive ICB component, like the one in Model 1, in order to obtain lower ϵ and a less boxy structure. But if the mass of the ICB is too high like in

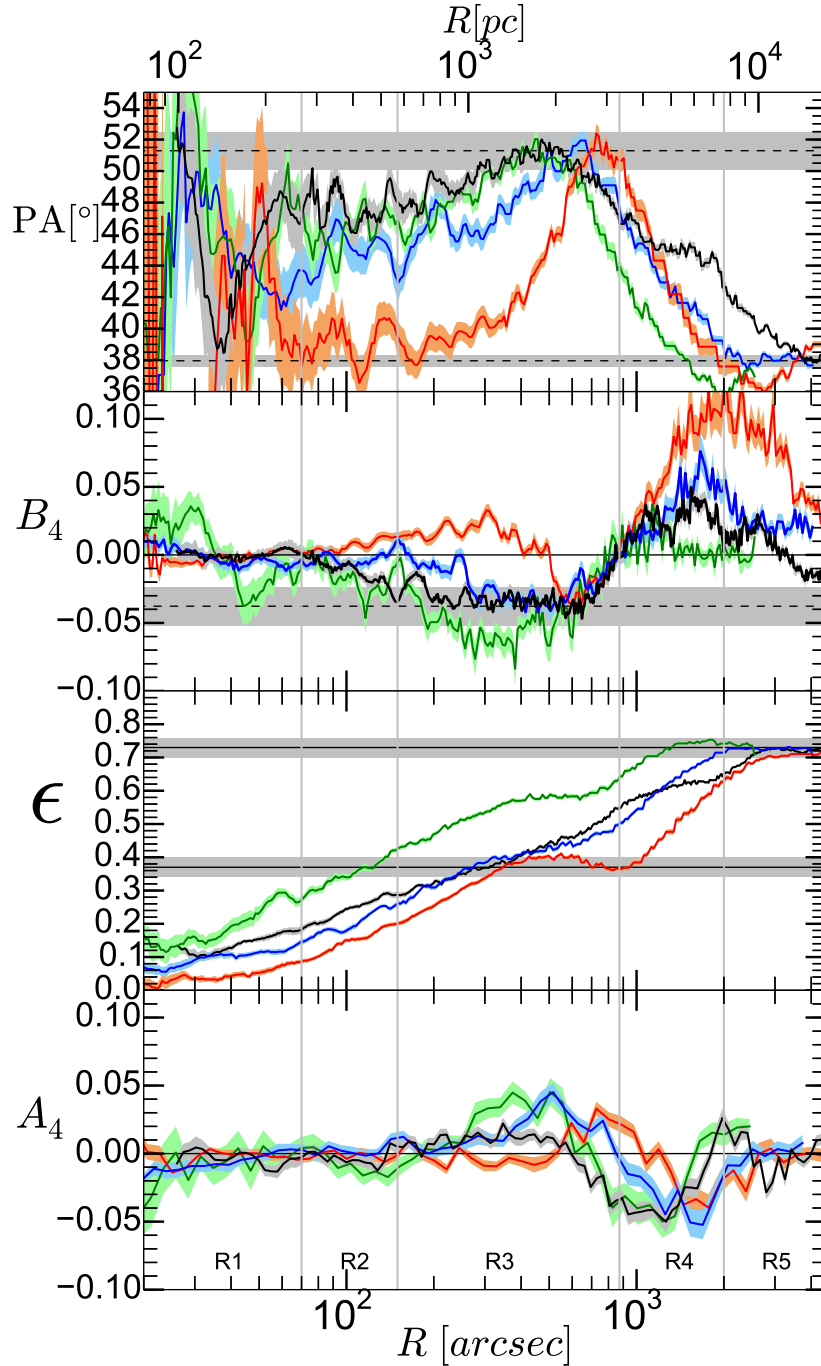


Figure 2.4: Parameters determined with `ellipse` for M31 (black), Model 1 (blue), Model 2 (green), and Model 3 (red) including their errors (shaded areas), within the different regions (vertical lines). The profiles of the models correspond to a snapshot at $600 u_t$. *Top panel:* PA profiles (same as Fig.2.3) The upper and lower horizontal dashed black lines mark PA_{\max}^{M31} , and PA_{disk} . *Second panel:* B_4 profiles. M31 reaches the maximum boxiness $B_4^{\min} \sim -0.037$ at $R \sim 600$ arcsec and its boxy region ends at $R_{B_4=0} = 873$ arcsec. The models are scaled in order to have the same $R_{B_4=0}$, but their isophotes may have stronger or weaker boxiness B_4^{\min} . *Third panel:* ϵ profiles. The upper and lower horizontal lines indicate ϵ for the disk and the bulge respectively by Co11 (see Section 2.4.3) where $\epsilon_{\text{bulge}} = 0.37 \pm 0.03$ and $\epsilon_{\text{disk}} = 0.73 \pm 0.03$. *Bottom panel:* A_4 profiles.

Model 3 ($0.5 u_M$) we observe a very low ϵ due to the massive ICB, with large fluctuations of the PA.

Depending on the scaling parameter u_d of a simulation, region R1 and part of R2 could be within three softening lengths of the centre. Our higher force resolution tests of Model 1 show only small variations of the surface-brightness profile in these regions (see Fig.3.19) and we find that the isophotes and their morphological parameters change only slightly. The small variation is in part because these are line-of-sight projected quantities and therefore the differences are naturally smaller.

- *Region R2*: is the inner boxy region of M31's bulge, $70 \text{ arcsec} \lesssim R \lesssim 150 \text{ arcsec}$, defined by showing boxy isophotes with $B_4 \sim -0.02$, but still roughly symmetric with a low $A_4 \sim 0$. Model 1 is less boxy than M31 in this region, but equally symmetric and with similar ϵ . Model 2 is already more boxy than M31 and its ϵ is much larger than observed, reaching already $\epsilon \sim 0.45$. The models differ again due to the presence of an ICB that dominates in this region, as shown later with the surface density and the mass profiles of Model 1 in Sections 2.4.3 and 2.4.5.4. The PA profiles are better defined, reaching a value of $\sim 48^\circ$ for M31, $\sim 46^\circ$ for Model 1 and $\sim 47^\circ$ for Model 2, but still with some noise. Model 3 still shows a very low PA and has more disk-like isophotes compared to M31, Model 1 and Model 2.
- *Region R3*: is the outer boxy region of M31 with $150 \text{ arcsec} \lesssim R \lesssim 873 \text{ arcsec}$, defined by the radius where the isophotes are boxy and start showing an asymmetry ($A_4 > 0$) and the radius at $R \sim 873 \text{ arcsec}$ where B_4 changes from boxy (negative) to disk-like (positive), indicating the end of the boxy isophotes and the transition to the inner region of the disk, we call this parameter $R_{B_4=0} = 873 \text{ arcsec}$. We also measure $R_{B_4=0}$ in our simulations in internal units u_d and then we use the value of M31 to determine the scaling factor in our models. Therefore all the models end their boxy region at the same place, although they do not necessarily do this in internal units. The maximum boxiness in M31 is $B_4 \sim -0.037$ located between $R \sim 573 \text{ arcsec}$ and 647 arcsec .

Contrary to Region 2 this region shows an asymmetry of the isophotes in M31 given by a positive A_4 of $\sim +0.1$, indicating that the PA is increasing. In our models we see the same features and behaviour of A_4 in this region, where two structures overlap which are the outer boxy bulge and the projected thin bar (that generates spurs). Further out the thin bar dilutes into the inner disk, sometimes with transient trailing or leading spiral structures. An increasing (decreasing) A_4 indicates that the isophotes are asymmetric and deviating anticlockwise (clockwise) from the major axis of fitted ellipse.

In this region we can see the twist of the isophotes in M31's bulge with respect to the isophotes of the disk, as shown in Fig.2.2. This is reflected in the PA profile of the ellipses, which increase until a maximum of $PA_{\text{max}} \sim 51.3^\circ \pm 1.2^\circ$. In the models we also see that the PA reaches a maximum in this region.

The ellipticity of M31 at the effective radius ($R_e^{\text{M31}} \sim 365 \text{ arcsec}$) is ~ 0.37 , which is in agreement with Co11, where $\epsilon_{\text{bulge}} = 0.37 \pm 0.03$. The ϵ profile of Model 1 and ϵ_{R_e} agree quite well

with the observations in this region. In Section 2.4.3 we show for this model that the mass of the B/P bulge dominates over the ICB in this region, which has a strong impact on the shape of the isophotes. The profile of Model 2 shows high ϵ , where ϵ_{R_c} of this model almost doubles the value of M31. Model 3 has generally lower ϵ and more disk-like isophotal shape, and only at $R \sim 500$ arcsec starts showing a boxy shape. At ~ 400 arcsec its ellipticity reaches the value of M31, but remains almost constant until the disk region.

- *Region R4:* This region shows the transition to the disk of M31 at $873 \text{ arcsec} \lesssim R \lesssim 2000 \text{ arcsec}$. The isophotes decrease their PA after reaching PA_{max} . The PA shows a bump $\sim 45^\circ$ between ~ 1000 arcsec and ~ 2000 arcsec which reveals a structure also visible in the isophotes in Fig.2.2. The models shown here do not reproduce this feature, but we offer some possible explanations later in Section 2.4.6. The ellipticity of M31 keeps rising, although near the bump it remains roughly constant, and again this is due to the same structure. The ellipticity of Model 2 is higher than M31 and Model 1, reaching already the value of the outer disk $\epsilon=0.73$. Model 3 has much lower ellipticity than the observations, until 2000 arcsec.
- *Region R5:* the outer part of the disk ($R \gtrsim 2000$ arcsec), where the PA reaches 38° , aligning with the line of nodes of the disk. The ellipticity reaches a maximum of $\epsilon=0.73$ (also consistent with Co11, with $\epsilon_{\text{disk}}=0.73 \pm 0.03$). An infinitesimally thin disk would have an ellipticity of $\epsilon=0.77$ using $i=77^\circ$. Our models have a vertically thick disk and reach $\epsilon=0.73$, as in the observations.

2.4.3 Photometry: M31's surface-brightness – two bulge components?

In Fig.3.19 we show the surface-brightness for M31's bulge region, for Model 0 that is a pure B/P bulge (no ICB), and for Model 1 where we also show its components plotted separately (bottom panel). We also include in the figure our test of Model 1 with a higher force resolution, finding a SB that only differs from the low resolution model by 0.5 per cent within 20 arcsec. We determined the Sérsic index and the effective radius for the models and for M31. We convert the surface density of Model 1 to SB dividing by a stellar mass-to-light ratio calculated as in Section 2.3.2, $M/L=0.813 M_\odot L_\odot^{-1}$ ($\log_{10}(0.813)=-0.09$), which agrees with the range of values estimated by Meidt et al. (2014) for the IRAC $3.6 \mu\text{m}$ band, which goes from $\log_{10}(M/L_{3.6 \mu\text{m}}) \approx -0.4$ to $\log_{10}(M/L_{3.6 \mu\text{m}}) \approx 0.04$ for a Chabrier IMF, depending on the metallicity and the age of the stellar population. The mass-to-light ratio shifts the profile of the models in the vertical axis of Fig.3.19 and is an important value, but not critical at this step of the analysis, as it does not change the shape of the profile.

We see in the figure that the SB of Model 1 agrees quite well with M31 within Region 3 ($R \lesssim 873$ arcsec), where the B/P bulge dominates. Model 0 also shows a similar SB. Within Region 2 ($R \lesssim 150$ arcsec) M31 keeps increasing its SB, while the pure B/P bulge, Model 0, does not. Model 1 matches the observed SB due to the contribution of its ICB. Within Region 1 ($R \lesssim 70$ arcsec) the SB of M31 keeps rising and it is matched by Model 1, where the ICB component now dominates with its cuspy SB over the B/P bulge component that shows a cored SB profile.

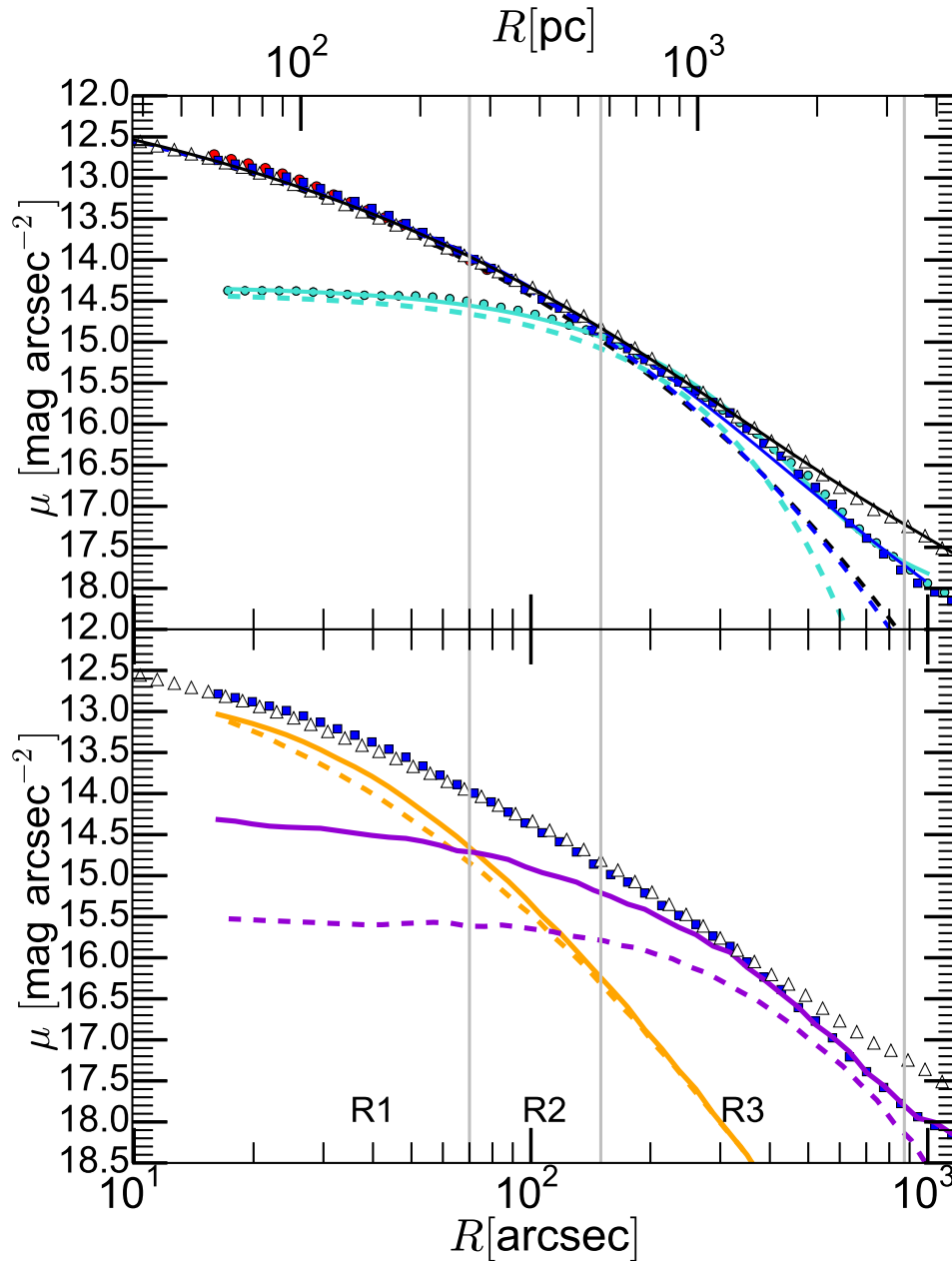


Figure 2.5: *Top panel:* The surface-brightness (SB) profiles of M31 (white triangles), Model 1 (600 u_t) (blue squares) and Model 0 (600 u_t) (cyan circles), within the different regions (vertical lines). We include the inner profile of a re-run of Model 1 with higher force resolution (red circles). The solid curves corresponds to the fit of a Sérsic and an exponential profile, and the dashed curve to the Sérsic component alone. The colours of the curves indicate if the fits belong to M31 (black), Model 1 (blue) or Model 0 (cyan). A stellar mass-to-light ratio of $M/L=0.813 M_{\odot} L_{\odot}^{-1}$ is used in the models to convert $\Sigma(R)$ into SB. *Bottom panel:* SB for M31 (white triangles) and Model 1 (blue squares), and each component of the bulge of Model 1 plotted separately: the disk + B/P bulge (magenta solid curve) and the ICB (orange solid curve). We included also the bulge components of Model 1 at the initial time (dashed curves).

It's interesting that Region 1 was defined with a morphological analysis of the isophotes of M31, and yet we see that this region is exactly where the SB of the classical bulge component dominates in Model 1. Model 0 shows also a cored SB and cannot reach the SB of M31, which highlights the importance of the ICB component and the mass concentration of this component. We also show the SB of the two bulge components of Model 1 at the initial time, before the formation of the bar. The mass redistribution of the initial disk when its material forms the bar increases its SB in the central regions by $\sim 1 \text{ mag arcsec}^{-2}$. The ICB almost does not change its SB despite the dynamical events like the bar formation and buckling, and the subsequent angular momentum transfer between components.

We also show in Fig.3.19 the profiles that we fit to the SB of M31, Model 1 and Model 0. From the fit to M31 we obtain the Sérsic index $n=2.6 \pm 0.8$, the effective radius $R_e=1.4 \pm 0.5$ kpc, and the disk scale length of $R_d=5.7 \pm 2.1$ kpc. I_e and I_d converted to surface-brightness are $\mu_e=16.5 \pm 0.4[\text{mag arcsec}^{-2}]$ and $\mu_d=16.9 \pm 0.4[\text{mag arcsec}^{-2}]$. These values are consistent with the results of Co11, where they used several fitting methods on surface-brightness profiles generated with different fields or cuts of the image, and depending on the masking and the fitting method, finding n values, varying from 1.66 ± 0.03 to 2.4 ± 0.2 , R_e from $\sim 0.618 \pm 0.01$ kpc to $\sim 1.1 \pm 0.1$ kpc and a range of disk scale lengths of $R_d=4.75 \pm 0.01$ kpc to 5.8 ± 0.1 kpc.

We find in our models that after the bar formation the surface-brightness profiles in the disk region shows a broken exponential profile, with two disk scale lengths. In the outer region ($4000 \text{ arcsec} < R$) we find a R_d that is similar to the initial one, while in the inner region ($2000 \text{ arcsec} < R < 4000 \text{ arcsec}$) we find a larger R_d . This is also present and explained by [Debattista et al. \(2006\)](#) as part of the secular evolution due to the mass re-distribution of the disk after the bar formation. Therefore, as we seek models of the bulge region of M31, we choose to leave the disk scale length as a fixed quantity, using $R_d=5.7 \pm 2.1$ kpc, and obtain for M31 a Sérsic index $n=2.59 \pm 0.16$ and an effective radius $R_e^{\text{M31}}=1.4 \pm 0.2$ kpc. We then fit the models in the same way, leaving the parameters of the Sérsic profile $\Sigma_{\text{Sersic}}(R)$ and the central disk intensity (Σ_d) free to vary. In this way we can compare the parameters of the Sérsic component of observations with the simulations alone, which is the component that better quantifies the properties of the bulge's density profile.

We find that Model 0, without a ICB component, has a Sérsic index $n=0.8 \pm 0.2$, lower than M31. On the other hand Model 1, with its ICB, behaves very similarly to M31, with $n=2.37 \pm 0.47$ and $R_e=1.23 \pm 0.47$ kpc. We find that models of Set I that have higher M_b and smaller r_b than Model 1 tend to show n higher than observed. On the other hand, models of Set II, which are pure B/P bulges rarely show n higher than ~ 1 ([Debattista et al. 2006](#)), and therefore this set is ruled out. In the outer parts, beyond Region 3, Model 1 starts to show lower densities than M31's disk. We find that our N-body disk models tend to decrease faster than the observed profile in M31. This disagreement is important, but not critical as our interest in this paper is to find models for M31's bulge.

We also find that the Sérsic index of a model can change with the orientation of the bar. When the bar is side-on ($\theta_{\text{bar}}=0^\circ$) the Sérsic index can be higher, because the ICB has less material of the B/P bulge in the line of sight, emphasizing its steep density profile. And when the bar is end-on ($\theta_{\text{bar}}=90^\circ$) the Sérsic index can be lower, because more material of the B/P bulge is in the line of sight, which has roughly an exponential ($n \sim 1$) profile. Furthermore, the Sérsic index

decreases also in time as the bar and B/P bulge grows incorporating more material, hiding the ICB component (depending also on the orientation).

2.4.4 Parameter space for the ICB

2.4.4.1 Selection of the best model

As explained in Section 2.4.3, the pure B/P bulges do not show high mass concentrations in the centre and therefore their Sérsic indexes are much lower than observed, all with values $n \lesssim 1$, ruling out all models of Set II. Now we investigate the properties of the ICBs of Set I that can simultaneously reproduce all the morphological observables of M31's bulge. The most important initial parameters of the ICB are its mass M_b and its size r_b . We show these two parameters in Fig.2.6 for the 72 models of Set I. The different colours used in the figure identify the four parameters: B_4^{\min} , ϵ_{R_e} , R_e and the Sérsic index n . In order to compare the models and M31 we use the fractional difference between data and model (in percent): $\Delta = 100\% \times (X_{\text{model}} - X_{\text{M31}}) / X_{\text{M31}}$ (where X corresponds to the each of the four parameters). If the circle is fully coloured with one colour it means that this parameter agrees to within $-15\% < \Delta < 15\%$ of the value in M31. Empty circles marked by a solid line (or dashed line) denotes that this parameter is larger than in M31 by $15\% < \Delta$ (or lower than in M31 by $\Delta < -15\%$). The threshold of 15 per cent is chosen for two reasons: (i) typical errors in the parameters are between 10 and 20 per cent, and (ii) it is roughly at this value where is found a unique candidate that *simultaneously* matches all the parameters. By construction the models of Fig.2.6 already match $R_{B_4=0}$ and ΔPA_{\max} (except for a few models marked in the figure with purple circles that have ICBs that are too concentrated to match ΔPA_{\max} , as explained Section 2.4.1). We highlight with a square in the figure the best model, Model 1, which simultaneously reproduces all the parameters.

The Sérsic index gives information about the mass concentration of the models. We explore a reasonable range of sizes and masses for the ICB, which give n as low as 1.13 and as high as 3.23, with an average and standard deviation of $\langle n \rangle = 2.06 \pm 0.49$. As expected the ICB with sizes smaller than $r_b < 0.15 u_d$ are too concentrated, resulting in n too high, with values between 2.52 and 3.23. Fisher & Drory (2008) showed that pseudobulges and classical bulges can be distinguished by the threshold $n \sim 2$. The pure B/P bulge models fail to reproduce M31 surface-brightness, indicating that a classical bulge component is needed, but its mass contribution is limited in order to match n .

The boxiness tends to be weaker in the upper right corner of the figure ($B_4 > -0.037$), where the ICB are more massive and concentrated, which makes the isophotes less boxy. Also, a compact bulge can help to stabilize the buckling instability, therefore making B/P bulge less boxy (Sotnikova & Rodionov 2005). The inverse is also true, as shown by the models with less concentrated ICB and with more strongly boxy structure (or even X-shape) that are located in the bottom left corner of the diagram ($B_4 < -0.037$). The ellipticity behaves similarly to B_4^{\min} , where more compact ICB give round isophotes and therefore low ϵ_{R_e} . We find that the variations of the parameters B_4^{\min} , ϵ_{R_e} and n vary more smoothly in the diagram, contrary to R_e which is more scattered. The boxy structure forms in a non-linear process and its size can show a wide range of values of $R_{B_4=0}$ in internal units (u_d), which in the case of Set I varies from $1.26 u_d$ to $3.74 u_d$.

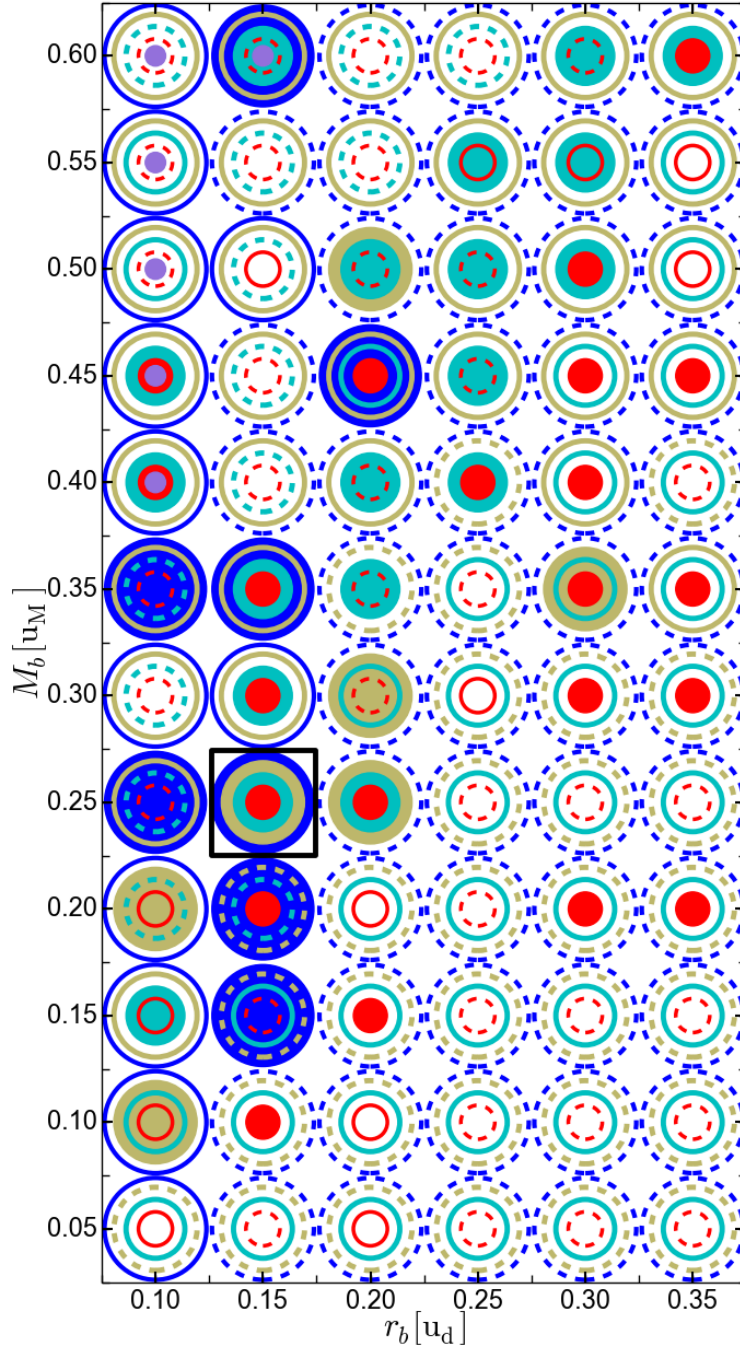


Figure 2.6: Model - M31 comparison in the parameter space of the ICB M_b versus size r_b , for the 72 models of Set I at $600 u_t$. All models already match $R_{B_4=0}$ and ΔPA_{\max} (except for 6 cases shown with a purple filled circle in the upper left corner). Blue, brown, magenta and red represent the parameters n , B_4^{\min} , ϵ_{R_c} and R_c . The parameters of the models that agree well with the parameters of M31 are shown with filled coloured circles, and they have values that are within the range $-15\% < \Delta < 15\%$. Solid thin circles mark models with values larger than the parameters in M31 by $15\% < \Delta$, while dashed circles mark values lower than M31 by $\Delta < -15\%$. Model 1 matches simultaneously all parameters and is the best matching model (square).

Table 2.1: Parameters for M31 and Model 1 at different times.

Variable	M31	Model 1			
Time [u_t] (Gyr)	–	500 (3.8)	600 (4.6)	700 (5.4)	800 (6.2)
$\theta_{\text{bar}}^{\text{best}} [^\circ]$	–	65.86	54.7	53.8	54.5
$\text{PA}_{\text{max}} [^\circ]$	51.3	51.4 (0.8%)	51.3(0%)	51.7 (3.0%)	51.6(2.3%)
$\Delta\text{PA}_{\text{max}} [^\circ]$	13.3	13.4 (0.8%)	13.3 (0%)	13.7 (3.0%)	13.6 (2.3%)
$B_4^{\text{min}} \times 10^{-2}$	–3.79	–4.14 (9.2%)	–3.78 (0.3%)	–3.98 (5.0%)	–3.48 (8.2%)
$\epsilon_{R_e^{\text{M31}}}$	0.37	0.31 (16.0%)	0.38 (5.2%)	0.38 (3.6%)	0.37 (0.1%)
n	2.59	2.25 (12.9%)	2.37 (8.3%)	2.44 (11.5%)	2.39 (12.1%)
R_e [kpc]	1.40	1.31 (5.8%)	1.22 (12.3%)	1.03 (26.4%)	0.90 (36.0%)

Notes: the percentages are the fractional difference between the observational parameters and the model parameters $\Delta=100\% \times (X_{\text{model}} - X_{\text{M31}})/X_{\text{M31}}$ (where X corresponds to the each parameter).

Since R_e is rescaled along with $R_{B_4=0}$, this results in a wide range for R_e as well.

2.4.4.2 Best model parameters & bar angle

In the previous section we analysed and compared the 72 models of Set I with parameters of M31, and at the end of the selection process only one model remains, Model 1. We found that the bar angle $\theta_{\text{bar}}^{\text{best}}=54.7$ best matches the $\Delta\text{PA}_{\text{max}}$ of M31. As shown in Section 2.4.1 matching $\Delta\text{PA}_{\text{max}}$ robustly fixes the bar angle. This generates a twist of the isophotes in the outer part of the boxy region that matches M31. In order to better match the twist in the inner part of the M31's boxy region however, Model 1 would require a larger angle. For this, we also tried $\theta_{\text{bar}}=60^\circ$, and 65° , resulting in a small variation of the parameters by less than $|\Delta| < 15\%$.

Additionally, we tested $\theta_{\text{bar}}=35^\circ$ and 45° , finding that for 45° all parameters are in the range of $|\Delta| < 15\%$. For the most extreme case of 35° , the parameters n , R_e are still in the range of $|\Delta| < 15\%$, while $\epsilon_{R_e^{\text{M31}}}$, B_4^{min} differ by 35 per cent from M31 values. This is expected as at 35° the bar is orientated more side on, showing more elongated isophotes with its B/P bulge appearing slightly less prominent. Of course, with 35° the twist of the isophotes in the bulge region is much weaker than in M31, which is reflected in the low PA profile shown for $\theta_{\text{bar}}=30^\circ$ in Fig. 2.3 (top panel), and therefore we discard such low bar angle values.

2.4.4.3 Best model parameters & time evolution

We analysed the 72 models of Set I at the same internal time of $600 u_t$. We now analyse the temporal evolution of the parameters for Model 1. As we explain later in Section 2.4.5.1, we convert $t=600 u_t$ to $t=4.65$ Gyr, using a time scaling factor of $1 u_t=7.75$ Myr. This model formed the bar at $t \sim 200 u_t \approx 1.55$ Gyr, and therefore the bar has an age of $t_{\text{bar}}^{\text{age}} \approx 400 u_t \approx 3.10$ Gyr at the

moment of our analysis. Following the same procedure we analyse Model 1 at $500 u_t$ (3.87 Gyr), $700 u_t$ (5.43 Gyr) and $800 u_t$ (6.20 Gyr), showing the results in Tab.2.1 along with M31. We find that the snapshot at $500 u_t$ shows slightly larger deviations in the parameters from the values observed in M31, compared to the snapshots at $600 u_t$, $700 u_t$ and $800 u_t$, specially $\epsilon_{R_c^{M31}}$. There are two reasons: (i) at $500 u_t$ the effects of the buckling instability are weak but still present in the bar, as shown later in Fig.2.12, and (ii) at $500 u_t$ $\theta_{\text{bar}}^{\text{best}}$ is slightly increased, changing slightly the orientation of the bar. But at later times the values only slowly change. Only the effective radius shows larger changes, but still within the observational errors estimated from our fit and by Co11. This change is because the bar is slowly growing and in our method we scale the models to the size of the boxy region ($R_{B_4=0}$). Therefore, a larger thick bar implies a smaller R_c .

2.4.5 Best model properties

In Fig.2.7 we show Model 1 at $t=600 u_t$ (4.65 Gyr) seen from different projections. The size scaling of the boxy zone using the parameter $R_{B_4=0}$ gives a factor of $1 u_d=2.314$ kpc. The velocity scaling factor is determined by matching the maximum $\sigma_{\text{los}}^{\text{max}}=173.5 \pm 3.2 \text{ km s}^{-1}$ of M31 along the slit of the photometric major axis of the bulge (PA=48°). The semi-major axis length of the thin bar measured in the plane of the disk from the centre is $r_{\text{bar}}^{\text{thin}}=2.20 u_d=5.1$ kpc. Later, in Section 2.4.6.1, we show that the thin bar in M31 is shorter. The B/P bulge is shorter than the thin bar, extending from the centre in the plane of the disk out to $r^{\text{B/P}}=3.2$ kpc (840 arcsec), and therefore it has a full length of $l^{\text{B/P}}=6.4$ kpc (1680 arcsec). Projecting the model on the sky like M31 ($i=77^\circ$, $\theta_{\text{bar}}=54.7^\circ$), the B/P bulge radius is $R^{\text{B/P}}=1.9$ kpc (510 arcsec) and extends from end to end $L^{\text{B/P}}=3.8$ kpc (1020 arcsec). We determined the B/P bulge 3D size using the prescription of ED13, from the average of the radius where $B_4=0$ ($r_{B_4=0}=1192$ arcsec), and the radius of B_4^{min} ($r_{B_4^{\text{min}}}=487$ arcsec) measured along the disk major axis with $i=60^\circ$ and $\theta_{\text{bar}}=0^\circ$ (bar seen side-on).

2.4.5.1 Kinematics: σ_{los} and v_{los} profiles.

We compare the kinematic properties of Model 1 with the observations of Saglia et al. (2010), who determined the line-of-sight velocity distribution (LOSVD) along multiple slits located in the M31 bulge region. They fit the LOSVD profiles with a Gauss-Hermite expansion following Bender et al. (1994), obtaining the coefficients $H_0=1$, $H_1=0$, $H_2=0$, H_3 , H_4 , $v_{\text{los}}^{\text{fit}}$ and $\sigma_{\text{los}}^{\text{fit}}$, along slits at different PA. Here we show three: one oriented at PA=48°, which is roughly aligned with the photometric major axis of the bulge (or +10° from the major axis of the disk); another at PA=138°, which is aligned with the minor axis of the bulge, and one at PA=108°. Once we project the models (using $\theta_{\text{bar}}^{\text{best}}=54.7^\circ$ and $i=77^\circ$), we use the same orientations of the slits of the observations to calculate for Model 1 and Model 0 the mass weighted line-of-sight velocity profile v_{los} , and the mass weighted line-of-sight velocity dispersion profile σ_{los} , which are the first and the second kinematic moments, using a velocity scaling factor of $1 u_v = 300.8 \text{ km s}^{-1}$. The line-of-sight kinematic profiles for the ICB and the B/P bulge components of Model 1 are shown separately and combined in Fig.2.8, from which we see that they have quite different behaviour. The line-of-sight kinematic profiles of the B/P bulge are only slightly affected by the foreground and background disk material. In Section 2.4.5.4 we define a volume for the B/P

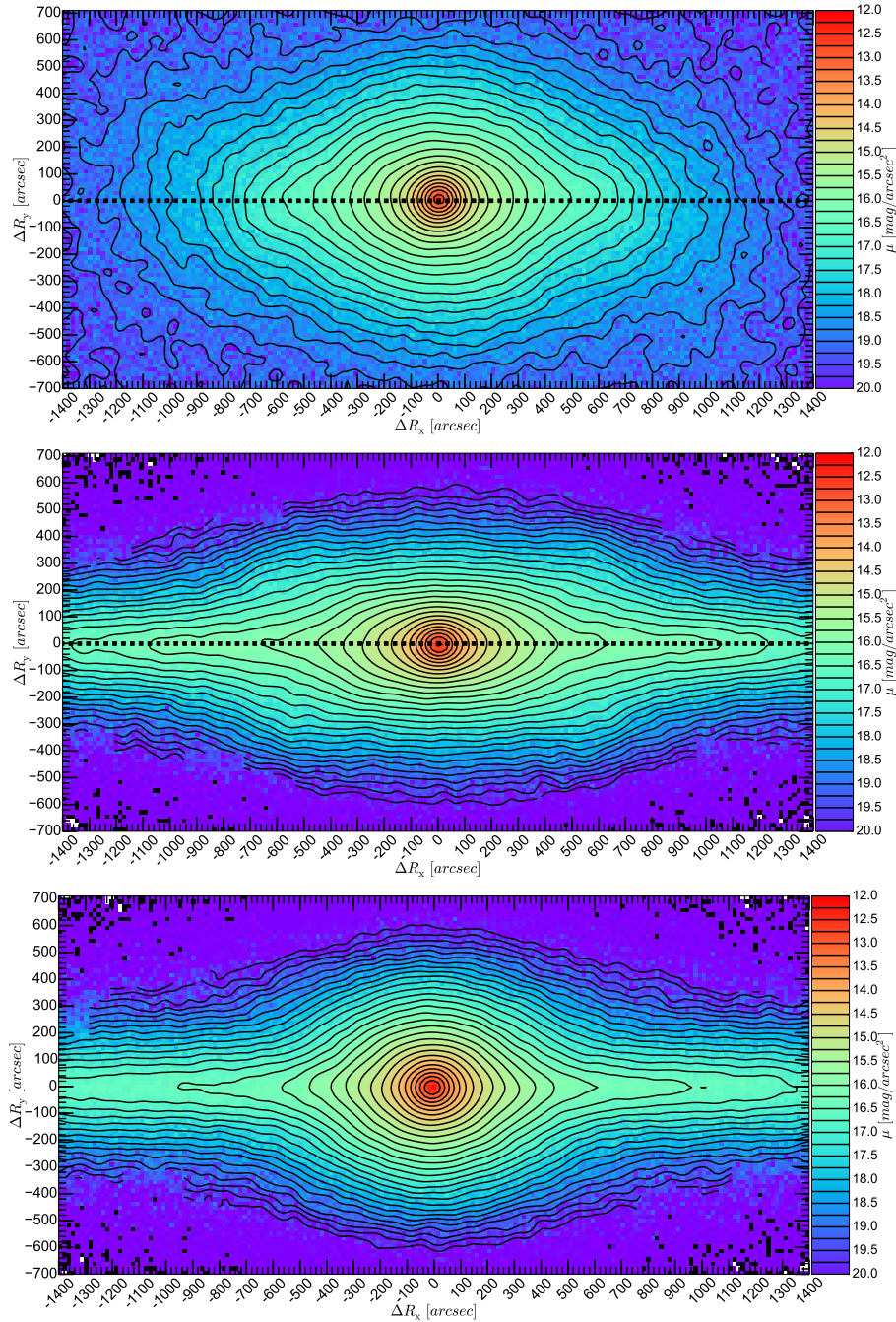


Figure 2.7: Model 1 SB maps at 4.65 Gyr ($600 u_t$) observed with different orientations. *Top panel*: the disk and bar with a face-on view ($i=0^\circ$, $\theta_{\text{bar}}=0^\circ$), where the thin bar extends between $\Delta R_x = -1300$ arcsec and 1300 arcsec. The dotted line shows the bar major axis. *Middle panel*: the disk with a side-on view and the bar is seen edge-on ($i=90^\circ$, $\theta_{\text{bar}}=0^\circ$), where it is possible to observe the boxy isophotes of the B/P bulge, extending from $\Delta R_x = -840$ arcsec to 840 arcsec. *Bottom panel*: the disk is side-on with the bar end-on ($i=90^\circ$, $\theta_{\text{bar}}=90^\circ$).

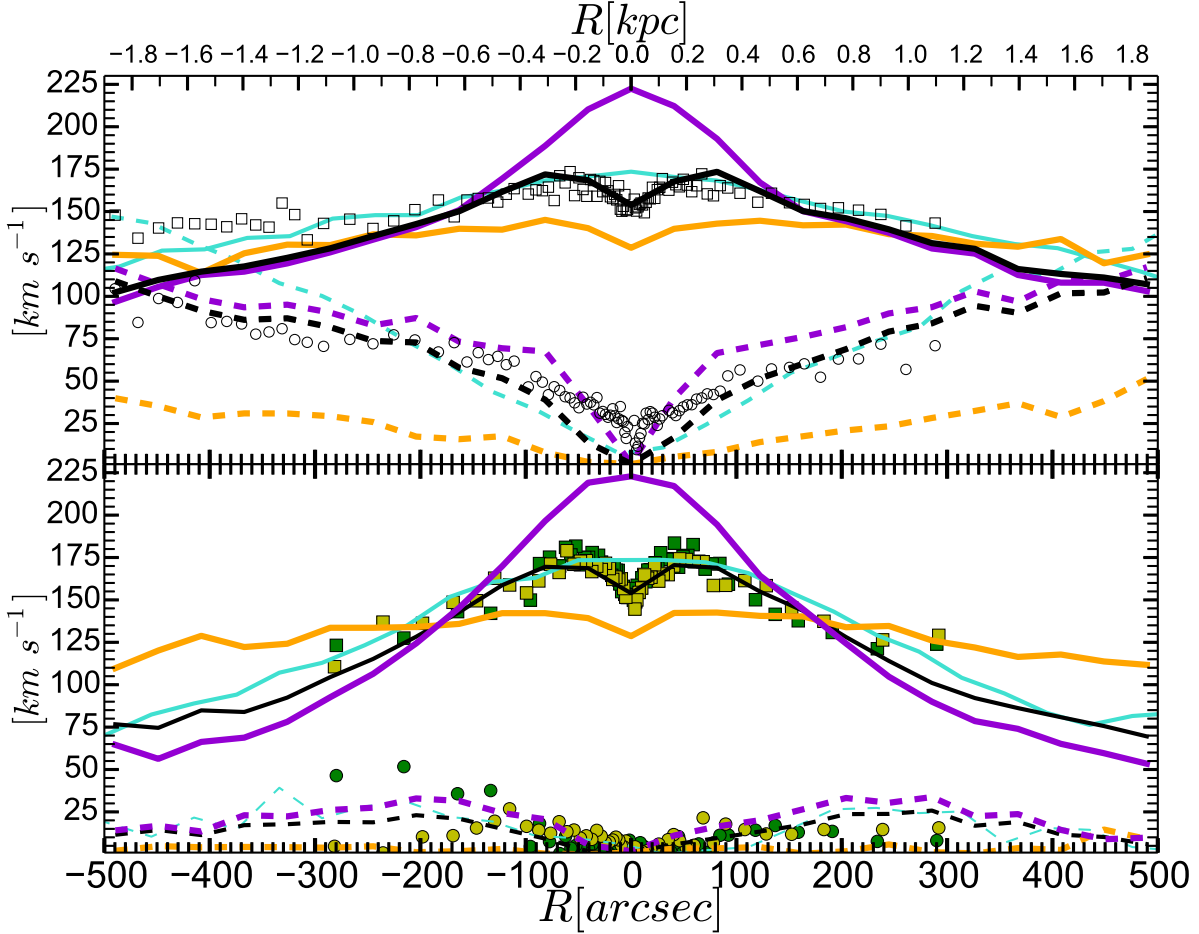


Figure 2.8: Line-of-sight kinematic profiles. We plot $|v_{\text{los}}|$ (dashed curves) and σ_{los} (solid curves), for Model 0 (cyan) and for Model 1 (black) (both at $600 u_t$). We also show the ICB component of Model 1 (orange) and the disk + B/P bulge component (purple). M31's $\sigma_{\text{los}}^{\text{fit}}$ (circles) and $|v_{\text{los}}^{\text{fit}}|$ (squares) for different PA. *Top panel*: M31 values measured along the photometric major axis of the bulge at PA= 48° (Saglia et al. 2010). The kinematic profiles of Model 1 are calculated at the same PA. Positive velocities ($v_{\text{los}} > 0 \text{ km s}^{-1}$) are located at the left side ($R < 0 \text{ arcsec}$) and negative velocities at the right side. *Bottom panel*: M31 values measured at the minor axis of the bulge, at PA= 138° (dark green), and values measured at PA= 108° (light green). Here the kinematic profiles for Model 1 are calculated at PA= 138° .

bulge and use it to calculate the mass in the line-of-sight outside this volume *i.e.* in the disk. We find along the slits at PA=48° and at 138° that on average only 13 per cent and 12 per cent of the stellar mass respectively is outside this volume, while within the effective radius 10 per cent of the stellar mass is outside this volume.

In the inner region ($R < 150 \text{ arcsec} \sim R_e/2$), the B/P bulge component of Model 1 has a very high σ_{los} , reaching a peak of $\sim 220 \text{ km s}^{-1}$ in the centre. This is because the initial disk from which the B/P bulge emerges lives in the potential of the ICB component, and has a high amount of rotational kinetic energy. After the bar instability a large part of this energy in rotation is transformed into random motions (dispersion). In our test models with initial constant Q_T we obtained even higher σ_{los} in the centre for the B/P bulge component. The disk with higher *initial* central dispersion (and therefore lower rotation) leads to a final central dispersion that is lower than it would have been in the disk with a lower *initial* central dispersion (and therefore higher rotation) see Appendix 2.A. The buckling instability also increases the dispersion, but more slightly.

The σ_{los} of the ICB component of Model 1 increases more slowly than the B/P bulge component, until 70 arcsec, where it decreases in an abrupt drop in the centre ($R < 50 \text{ arcsec}$). This is expected from the cuspy density profile. As we shown for the SB profiles, the ICB dominates in the centre, and therefore the combined profile also shows this feature. The σ_{los} measured in M31 also shows a drop in the centre. Model 0, which is a pure B/P bulge, does not show a drop in the centre, which is related to the cored Σ profile previously shown in Fig.3.19.

Further out, at $R > R_e$, the dispersion of the ICB component slowly decreases, while the B/P bulge component decreases faster. The mass of the B/P bulge dominates in this region and therefore the combined profile follows the B/P bulge behaviour.

The velocity profiles behave differently for each component. We can see in the top panel of Fig.2.8, that although the ICB component had no rotation at the beginning, it shows some rotation due to the transfer of angular momentum from the bar, but it rotates much more slowly than the B/P bulge component. In the central region $R < R_e/2$ the rotation of the combined components is slightly lower than in M31, because the ICB dominates in this region, which could be corrected giving some initial rotation to the ICB. At $R > R_e$ the B/P bulge dominates and the combined bulge shows slightly higher v_{los} than in M31. This difference could be caused by some mass missing in the outer part of the bar and/or the disk, either dark matter, or stellar mass, as was also implied by the SB profile of Model 1, which drops slightly faster than that of M31 (Fig.3.19). A second reason could be the difference in the kinematic structure of the bar: Model 1 is slightly more supported by rotation than M31, while its dispersion is lower than in M31. Fig.2.8 (bottom panel) shows that M31 has some rotation along the minor axis of the bulge PA=138°, and shows even lower rotation in the slit at PA=108°. Our model also shows some rotation at 138°, and a lower rotation at 108°, which is related to the twist of the zero line-of-sight velocity curve, as shown in the velocity maps later.

2.4.5.2 Kinematics: σ_{los} , v_{los} , H_3 maps & the zero velocity line twist.

In Fig.3.22 we show σ_{los} and v_{los} maps of Model 1 in projection (using $\theta_{\text{bar}}^{\text{best}}=54.7^\circ$ and $i=77^\circ$), which reflect the same properties as the kinematic profiles of the last section. Additionally, we

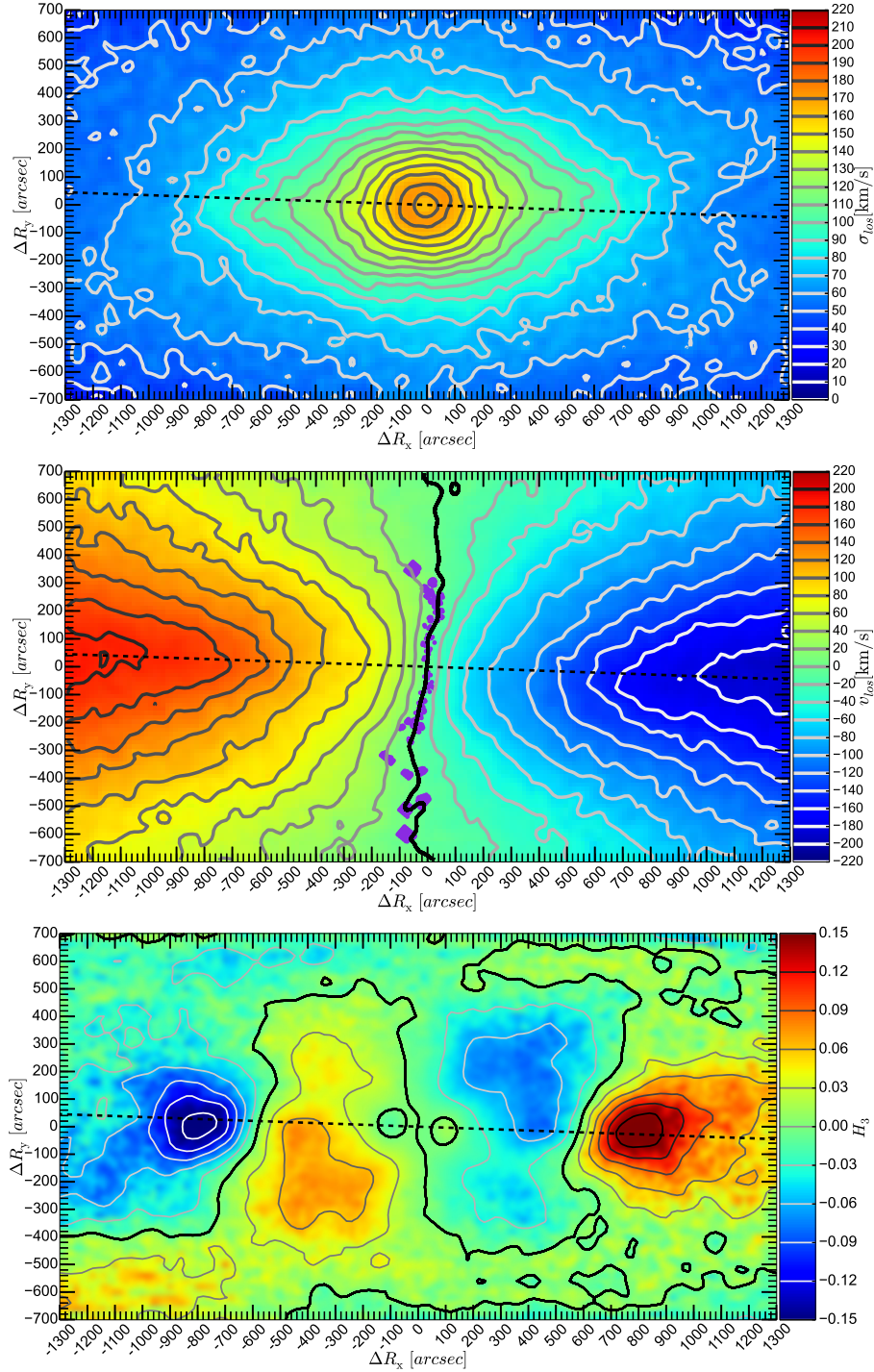


Figure 2.9: Line-of-sight kinematic maps of Model 1 ($600 u_t$), projected as M31 using $i=77^\circ$, $\theta_{\text{bar}}^{\text{best}}=54.7^\circ$ and $\text{PA}_{\text{disk}}=38^\circ$ (dashed lines). The near side of the disk is in the upper part of the panels. *Top panel*: σ_{los} map and contours. *Middle panel*: v_{los} map and contours. The thick black curve marks the zero velocity line ($v_{\text{los}}=0 \text{ km s}^{-1}$) of the model. The purple tracers correspond to the observed zero line-of-sight velocity determined by Opitsch et al. (in prep.). *Bottom panel*: H_3 Gauss-Hermite coefficient map. The thick black curve marks the zero H_3 values.

add in Fig.3.22 the H_3 Gauss-Hermite coefficient map, because it allows to better distinguish the properties of the bar from the disk.

The dispersion map Fig.3.22 (top panel) also manifests a dispersion drop in the central region ($R < 50$ arcsec) due to the ICB component. It is also possible to observe that axis where the dispersion gradient is lower slightly differs from the photometric major axis of the disk. The velocity field and contours exhibit nearly cylindrical rotation within a region of $R < 200$ arcsec. Trying different orientations for the bar (θ_{bar}) we find that this model exhibits a stronger cylindrical rotation when the bar is end-on ($\theta_{\text{bar}}=90^\circ$) and a weaker one when it is side-on ($\theta_{\text{bar}}=0^\circ$), due to the dynamics of a bar and to the presence of the ICB component.

Fig.3.22 (middle panel) shows the zero line-of-sight velocity contour in the central region at $\Delta R_x \sim 0$ arcsec and going from $\Delta R_y = 700$ arcsec to -700 arcsec. At these ΔR_y the disk isophotes dominate, as shown in the photometry in Fig. 2.2. Further inside the zero line-of-sight velocity contour shows twists at $\Delta R_y \sim 300$ arcsec and at -300 arcsec, due to the presence of the B/P bulge and its orientation, as shown also by isophotes in the photometry. In the centre, within $\Delta R_y \sim 100$ arcsec and -100 arcsec the twist becomes weaker due to the presence of the ICB component. We also compare the zero line-of-sight velocity contour of the model with the observed velocities from Opitsch et al. (in preparation). Opitsch et al. observed the central region of M31 with the McDonald Observatory's 2.7-meter Harlan J. Smith Telescope using the VIRUS-W Spectrograph (Fabricius et al. 2012), which has a spectral range of 4850-5480 Angstrom and a resolution of $R \approx 8700$ ($\sigma_{\text{inst}} = 15 \text{ km s}^{-1}$). They were able to completely cover the bulge region and also sample the disk out to one disk scale length (Co11) along six different directions, producing line-of-sight velocity and dispersion maps of the stars and the ionized gas. We plot here only the stellar velocities that are closer than 2 km s^{-1} to the systemic velocity of -300 km s^{-1} (de Vaucouleurs et al. 1991).

We also include in Fig.3.22 (bottom panel) the predictions for the H_3 maps of Model 1. We find that H_3 and v_{los} generally anti-correlate in the disk region, *i.e.* positive v_{los} are found where H_3 is negative, which is visible in the map along the major axis of the disk at ± 700 arcsec and beyond. This can be seen as a consequence of the asymmetric drift. It is also visible in the disk at different times, even in the inner region of the initial disk (within 700 arcsec) before the bar forms. Later, after bar formation, we find that H_3 and v_{los} correlate within 700 arcsec, which is where the bar is located (Bureau & Athanassoula 2005). This direct correlation between H_3 and v_{los} is also observed in M31 along the bulge photometric major axis exactly where the B/P bulge would be located (Saglia et al. 2010). In the left and the right sides of the H_3 map we observe a sharp transition from negative H_3 to positive H_3 exactly where the B/P bulge ends and the disk starts, at $R_x \sim \pm 600$ arcsec along the disk major axis. Also, H_3 is not symmetric with respect to the major axis of the disk, because the bar axis is oriented away from the disk axis, with a $\Delta\text{PA} \sim 13^\circ$. In the B/P bulge region, H_3 reaches extremal values near the photometric major axis of the B/P bulge. The most extreme values in the entire plotted map are present in the disk region. These qualities make H_3 a good parameter to estimate properties of the bar in M31. Furthermore, we find in the central region ($R < 100$ arcsec) where the ICB dominates, that H_3 anti-correlates with v_{los} again, like in the disk, but much more weakly.

2.4.5.3 Kinematics: circular velocity, pattern speed & the Lindblad resonances.

In the top panel Fig.2.10 we show the in plane-azimuthally averaged circular velocity (v_c) curves of the different components of Model 1 and compare them with the rotation curve estimated from HI observations (Chemin et al. 2009). The v_c of the ICB component reaches a maximum circular velocity of 172 km s^{-1} at $\sim 1.0 \text{ kpc}$, dominating over the B/P bulge component within $R \sim 0.5 \text{ kpc}$, and then drops rapidly. The B/P bulge component reaches a maximum of 180 km s^{-1} at $\sim 2.0 \text{ kpc}$, dominating over the ICB. The total circular velocity shows a maximum of 248 km s^{-1} at 1.6 kpc . Beyond 6 kpc the total v_c of the model stays at around $210\text{-}220 \text{ km s}^{-1}$, slightly below the measured $v_c \sim 240 \text{ km s}^{-1}$ (Corbelli et al. 2010). This could be remedied by adjusting the outer disk and halo mass distribution, but we do not attempt this in the present paper, focusing instead on the bulge.

In the bottom panel of Fig.2.10 we show the angular frequency profile (Ω) of Model 1. With the spatial and velocity scaling we calculate the pattern speed of Model 1, $\Omega_p = 0.29 \text{ u}_v \text{ u}_d^{-1}$ in internal units, and $\Omega_p = 38 \text{ km s}^{-1} \text{ kpc}^{-1}$ in physical units. The corotation radius, where $\Omega_p = \Omega$, is located at $r_{\text{cor}} = 5.8 \text{ kpc}$. We also calculate the inner inner and the outer inner Lindblad resonances $\Omega_{\text{ILR}} = \Omega - \kappa/2$ (Lindblad 1956), obtaining $r_{\text{IILR}} = 0.7 \text{ kpc}$ and $r_{\text{OILR}} = 2.2 \text{ kpc}$. The outer Lindblad resonance $\Omega_{\text{OLR}} = \Omega + \kappa/2$ is located at $r_{\text{OLR}} = 10.4 \text{ kpc}$. M31 shows a prominent ring-like structure at $\sim 10 \text{ kpc}$ (Habing et al. 1984; Haas et al. 1998; Gordon et al. 2006; Barmby et al. 2006) (10 kpc-ring), whose origin has been suggested to be due to: (1) a collision with another galaxy (Block et al. 2006; Dierickx et al. 2014), or (2) to a OLR resonance with the bar (AB06). If we assume that: i) the 10 kpc-ring is located near the OLR, and ii) that the circular velocity at OLR is $\sim 240 \text{ km s}^{-1}$ and roughly constant, we estimate a pattern speed of $\Omega_{\text{OLR}} = \Omega (1 + 1/\sqrt{2}) = 240/10(1 + 1/\sqrt{2}) \text{ km s}^{-1} \text{ kpc}^{-1} = \Omega_p = 41.0 \text{ km s}^{-1} \text{ kpc}^{-1}$. The fact that this is within 10 per cent of the value derived from the bulge structure suggests that the ring may indeed be related to the bar's OLR.

2.4.5.4 Bulge mass profile

In Fig.2.11 we show the three-dimensional cumulative radial mass profiles $M(r)$ within the bulge region. The spatial and velocity scaling gives a mass scaling of $1 \text{ u}_M = 4.84 \times 10^{10} \text{ M}_\odot$ for Model 1. The initial mass distribution of the ICB is spherical and it changes in time only slightly, which makes its projected mass distribution almost independent of the spatial orientation. In contrast to the ICB, it is not trivial to define the volume within which to measure the mass of a triaxial structure such as the B/P bulge. Therefore we make two estimations for the B/P bulge stellar mass, using two volumes. In the first estimation we consider all the mass within the B/P bulge spherical radius $r^{\text{B/P}} = 3.2 \text{ kpc}$ (840 arcsec), obtaining a mass $M^{\text{B/P}} = 2.2 \times 10^{10} \text{ M}_\odot$. Within this radius the ICB component mass is $M^{\text{ICB}} = 1.1 \times 10^{10} \text{ M}_\odot$, giving a total stellar mass for the bulge of $M_{\text{Tot}}^{\text{Bulge}} = 3.3 \times 10^{10} \text{ M}_\odot$. If instead we consider the mass within a box³ we obtain

³ The box major axis is $\Delta X = 6.4 \text{ kpc}$ (1680 arcsec), the minor axis $\Delta Y = 2.4 \text{ kpc}$ (630 arcsec) and vertical axis is $\Delta Z = 6.0 \text{ kpc}$ (1580 arcsec), which is perpendicular to the plane of the disk. ΔX major axis is defined based on the B/P bulge major axis ($2 \times r^{\text{B/P}}$). ΔY is chosen to be the distance where the same isophote that intersects the major axis ΔX in the face on view intersect the minor axis ΔY . ΔZ is chosen to be large enough to cover the whole boxy

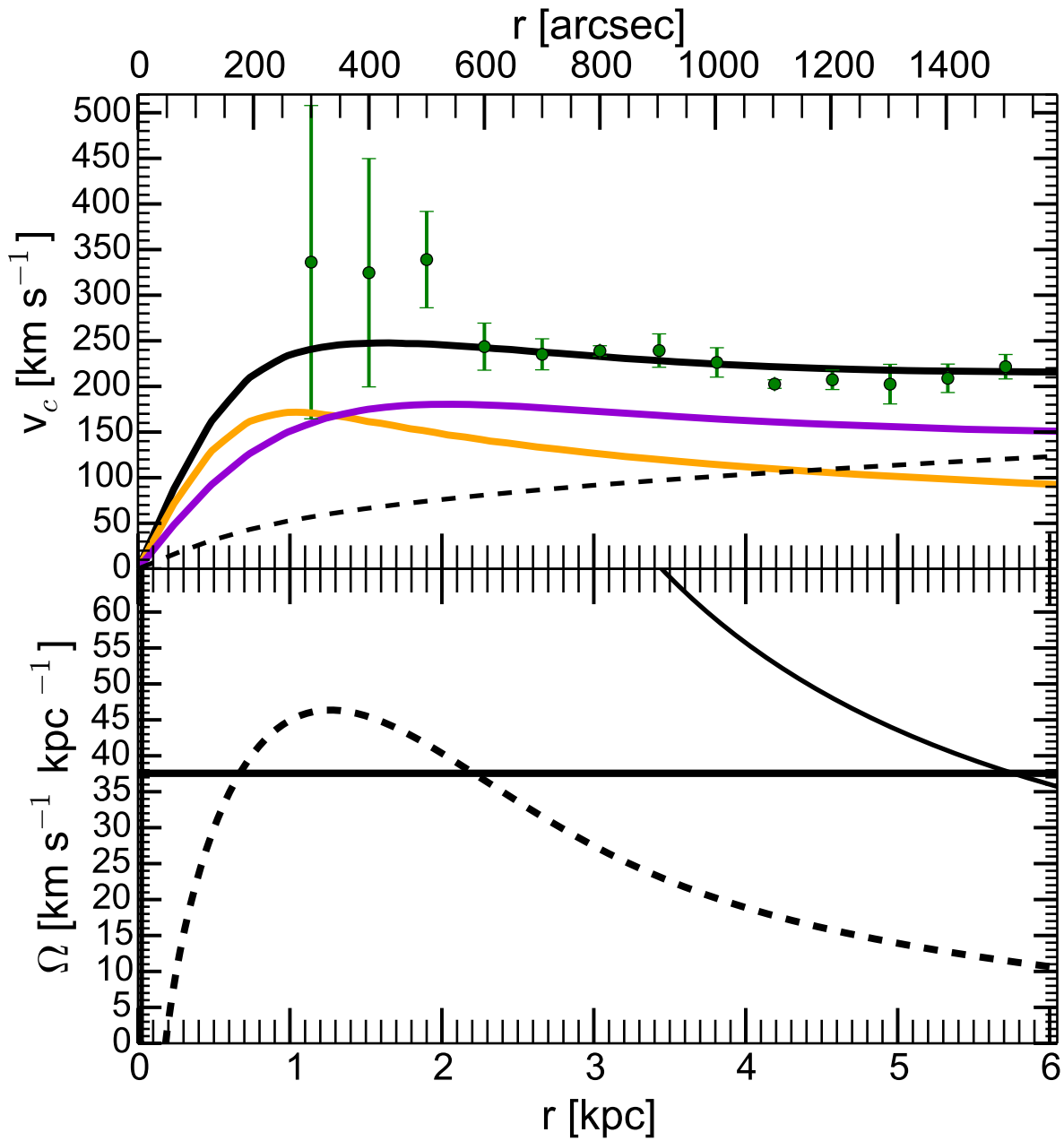


Figure 2.10: *Top panel:* Circular velocities of Model 1 ($600 u_t$) and M31. v_c curves of the different components of Model 1, the ICB (orange), the disk + B/P bulge (purple), the dark matter (dashed curve) and the total v_c (solid black curve). The rotation velocities estimated from HI observations (green dots) (Chemin et al. 2009). *Bottom panel:* The angular frequency profile (Ω) of Model 1 at $600 u_t$ (solid curve), and $\Omega_{\text{ILR}} = \Omega - \kappa/2$ (dashed curve). The pattern speed of the bar is $38 \text{ km s}^{-1} \text{kpc}^{-1}$ (horizontal solid line), locating corotation at 5.8 kpc. The inner inner and the outer inner Lindblad resonances are located at 0.7 kpc and 2.2 kpc .

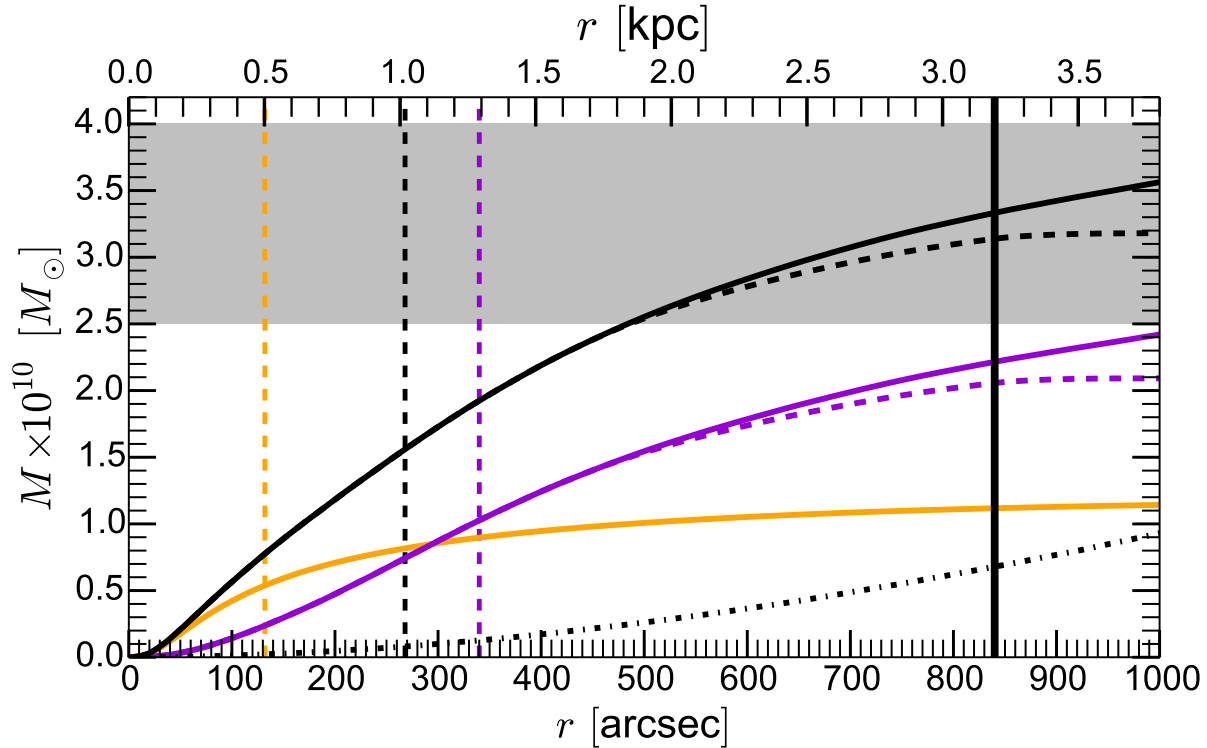


Figure 2.11: Three-dimensional cumulative mass profiles $M(r)$ for Model 1 ($600 u_t$) and its components: ICB (orange curve), disk + B/P bulge (purple curve), disk + B/P bulge within a box-shaped volume (purple dashed curve), the combined bulges within spherical radius (black solid curve), the combined bulges considering a box-shaped volume for the B/P bulge (black dashed curve), and the dark matter halo (dash-dotted curve). The B/P bulge semi-major axis ends at 3.2 kpc (840 arcsec) (solid vertical line). The shaded grey area marks the stellar mass for M31's bulge estimated by Kent (1989) (upper limit) and Widrow & Dubinski (2005) (lower limit). The vertical dot-dash lines mark the deprojected half mass radius for each components.

$M_{\text{Box}}^{\text{B/P}} = 2.06 \times 10^{10} M_{\odot}$, *i.e.* 6 per cent lower than in the spherical volume. This difference is mostly due to the remaining material along the minor axis ΔY between the disk and the B/P bulge. In both cases, the contribution to the total stellar mass of the bulge is $\sim 2/3$ for the B/P bulge and $\sim 1/3$ for the ICB. The DMH mass within the B/P bulge radius is $M^{\text{DMH}}(r^{\text{B/P}}) = 0.7 \times 10^{10} M_{\odot}$, which implies that within this radius the bulge components dominate the dynamics in this region, as is also shown by the circular velocity profiles in Fig. 2.10.

The projected half mass radius of the ICB is $R_{\text{half}}^{\text{ICB}} = 0.4$ kpc (100 arcsec). The deprojected half mass radius of the ICB and the B/P bulge ($M^{\text{B/P}}$) are $r_{\text{half}}^{\text{ICB}} = 0.53$ kpc (140 arcsec) and $r_{\text{half}}^{\text{B/P}} = 1.3$ kpc (340 arcsec), while the combined bulge half mass radius is $r_{\text{half}}^{\text{Bulge}} = 1.02$ kpc (270 arcsec). We find that the ICB dominates within $r < 265$ arcsec ≈ 1.0 kpc in the deprojected case, and $R < 170$ arcsec ≈ 650 pc in the projected case. Beyond this transition region the mass of the B/P bulge dominates, reaching more than double the mass of the ICB component at the end of the B/P bulge.

The combined bulge stellar mass profile already reaches $M(r) = 2.5 \times 10^{10} M_{\odot}$ at $r = 470$ arcsec, which is the mass estimated by [Widrow & Dubinski \(2005\)](#) for M31's bulge, but it does not reach the mass estimate by [Kent \(1989\)](#) of $M = 4.0 \times 10^{10} M_{\odot}$. Using spectral energy distributions and rotation curves, [Tamm et al. \(2012\)](#) estimate even higher values for of M31 bulge mass (which include a stellar halo) ranging $(4.4 - 6.6) \times 10^{10} M_{\odot}$, while [Geehan et al. \(2005\)](#) and [Corbelli et al. \(2010\)](#) estimate lower masses: $3.2 \times 10^{10} M_{\odot}$ and $3.8 \times 10^{10} M_{\odot}$, respectively. It is important to mention that most previous mass estimations for M31's bulge have assumed an axisymmetric or oblate geometry for the bulge, where the mass of the disk strongly contributes within the bulge region. In the models presented here all the stellar mass within the B/P bulge is considered as part of the bulge, its distribution is non-axisymmetric, and no separate massive disk component is present here (the B/P bulge is made from former disk material).

2.4.6 The thin bar of M31

Until now we have focused mostly on the bulge of M31, comparing it with our best model always at the $600 u_t$ snapshot. We now turn to the structure outside the B/P bulge, between $R \sim 500$ and 700 arcsec in projection (Fig. 2.12, top panels), and try to determine the possible presence and properties of the thin bar, which in projection generates so-called *spurs*. While our standard $600 u_t$ snapshot is a good match to the main properties of the B/P bulge as shown above, we describe in this section an earlier snapshot at $500 u_t$ which matches better the isophotal properties of the thin bar in M31, because it has a thin bar shorter than the one at $600 u_t$. Later we turn to the isophotal structures of M31 even further out, between 800 arcsec and 1100 arcsec, which we argue is material trailing the thin bar, that in projection reproduce the *lobe-shaped* isophotes in M31 beyond its triaxial bulge. As we mentioned in Section 2.3.1.2, we define the thin bar as the flat structure that is aligned with the B/P bulge, excluding additional transient material that could be attached to its ends, such as leading or trailing spiral arms.

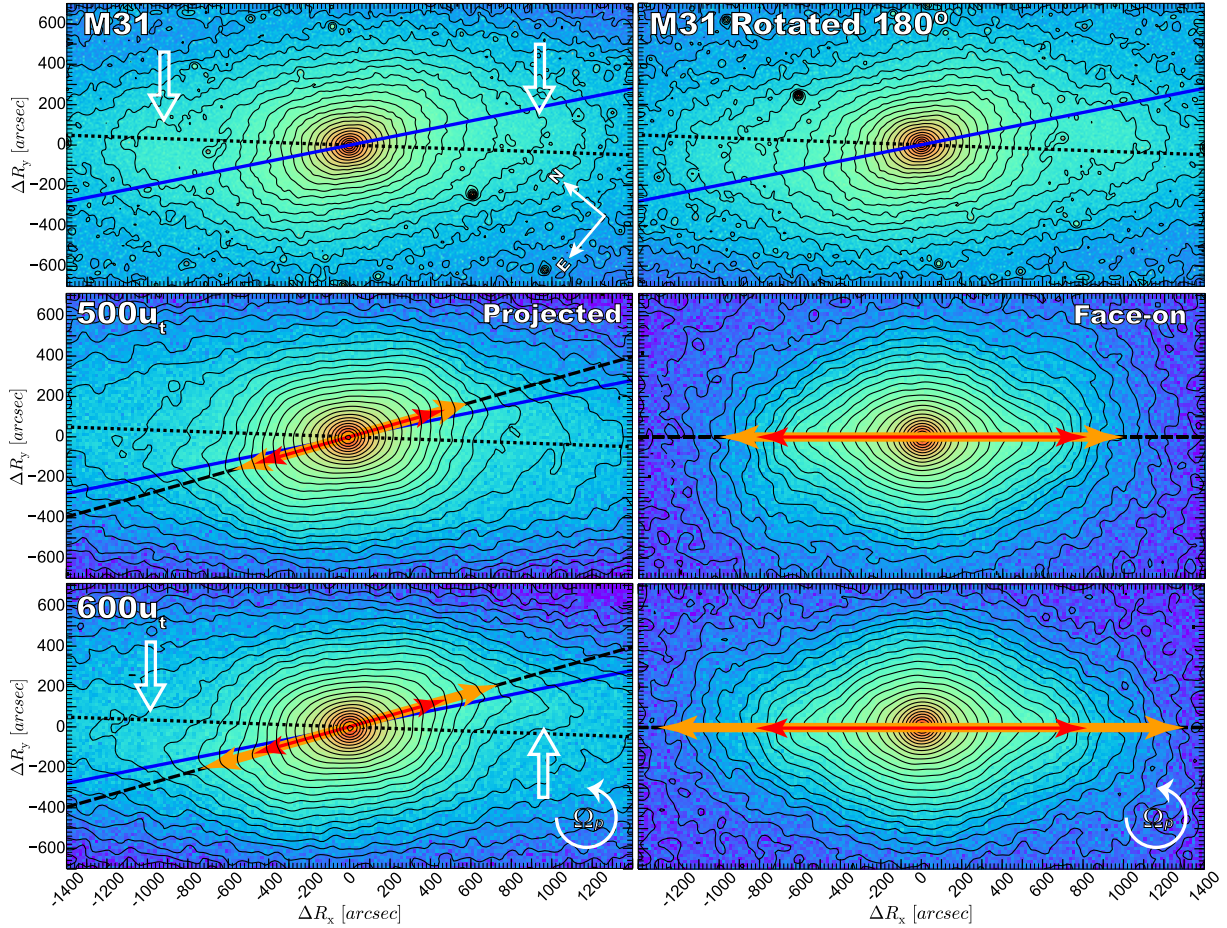


Figure 2.12: SB map of M31 compared with two snapshots of Model 1 projected like M31 ($i=77^\circ$, $\theta_{\text{bar}}=54.7^\circ$), and face-on ($i=0^\circ$, $\theta_{\text{bar}}=0^\circ$), showing the model's thin bar extension (orange arrows) and B/P bulge extension (red arrows). *Top panels*: the left panel shows the M31 IRAC $3.6\mu\text{m}$ image with the near side of the disk in the upper part of the image. We show $\text{PA}_{\text{disk}}=38^\circ$ (dotted line) and $\text{PA}_{\text{max}}^{\text{M31}}=51.3 \pm 1.2$ (blue line). The position angle of the horizontal axis ΔR_x is $\text{PA}_h=40^\circ$. The asymmetric lobe-shaped isophotes are at $\Delta R_x \approx -1000$ arcsec and at 900 arcsec (white arrows). The right panel shows the same image rotated 180° to emphasize the asymmetry of the lobe-shaped structures. *Middle panels*: Model 1 at snapshot $500 u_t$ in projection (left panel) and face-on (right panel) rotating anticlockwise. The PA of the projected major axis of the bar is $\text{PA}_{\text{bar}}=55.7^\circ$ (dashed line in left panels). The thin bar semi-major axis in the plane of the disk is $r_{\text{bar}}^{\text{thin}}=4.0$ kpc (1000 arcsec) (right panel). In projection (left panel) the thin bar appears shorter, extending out only to $\Delta R_x = -580$ arcsec and 580 arcsec (each end of the orange arrow). The B/P bulge semi-major axis is $r^{\text{B/P}}=3.2$ kpc (840 arcsec) (red arrow right panel) and in projection extends only to $R^{\text{B/P}}=1.9$ kpc (510 arcsec) from the centre (red arrow left panel). *Bottom panels*: snapshot at $600 u_t$ projected (left panel) and face-on (right panel) rotating anticlockwise. The thin bar is longer than at $500 u_t$, with $r_{\text{bar}}^{\text{thin}}=5.1$ kpc (1300 arcsec), extending in projection from $\Delta R_x = -740$ arcsec to 740 arcsec. The lobe-shaped isophotes are shown with white arrows. Note that the face-on projections shown in these panels correspond to viewing the model from below relative to our line of sight to M31. Thus the rotation direction indicated in the lower left panel corresponds to the sign of the velocities shown in Fig. 3.22 and to the projected sense of rotation shown in the lower left panel here (curved white arrows).

2.4.6.1 Length of the thin bar & the spurs

In barred disk galaxies viewed at moderate inclination there are often isophotal elongations or so-called spurs extending outside their B/P bulges. These are also visible in N-body models of bars and are the natural projection of the thin bar outside the B/P bulge (ED13; see also AB06). Because they are thinner structures they lie closer to the projected angle of the major axis of the bar than the B/P bulge, which is vertically extended.

When the 600 u_t snapshot of Model 1 is projected with $i=77^\circ$, $\theta_{\text{bar}}=54:7$ and $\text{PA}_{\text{disk}}=38^\circ$ (note that the position angle of the horizontal axis ΔR_x in Fig.2.12 is $\text{PA}_h=40^\circ$), we also observe prominent spurs, as shown in Fig.2.12 (bottom panels). The thin bar semi-major axis in this snapshot is $r_{\text{bar}}^{\text{thin}}=5.1$ kpc (1300 arcsec) in the plane of the disk (bottom right panel). We determine the value $r_{\text{bar}}^{\text{thin}}$ as the point where the ellipticity profile of the model viewed face on drops 15 per cent below its maximum value (Martinez-Valpuesta et al. 2006). Approximating the thin bar as one dimensional locates in projection the ends of the thin bar semi-major axis at:

$$R_{\text{bar}}^{\text{thin}} = \pm r_{\text{bar}}^{\text{thin}} \left[\cos^2(\theta_{\text{bar}}) + \sin^2(\theta_{\text{bar}}) \cos^2(i) \right]^{1/2} \quad (2.9)$$

$$(\Delta R_x, \Delta R_y) = R_{\text{bar}}^{\text{thin}} (\cos(\text{PA}_{\text{bar}} - \text{PA}_h), \sin(\text{PA}_{\text{bar}} - \text{PA}_h)) \quad (2.10)$$

where recalling Eq.2.7 and Eq. 2.8 we have $\theta_{\text{proj}}=17:7$ and the projected major axis of the thin bar at $\text{PA}_{\text{bar}}=55:7 \pm 2:5$ (shown with orange arrows in Fig.2.12). The extension of the thin bar semi-major axis is then $R_{\text{bar}}^{\text{thin}}=\pm 2.9$ kpc (± 770 arcsec) roughly at $(\Delta R_x, \Delta R_y)=(-740, -210)$ arcsec at the left side of the bulge, and at $(\Delta R_x, \Delta R_y)=(740, 210)$ arcsec at the right side of the bulge (bottom left panel). These locations show the end of the thin bar in projection, and beyond this the spur shaped isophotes deviate from the projected bar axis, coming back to the disk major axis. The B/P bulge 3D semi-major axis is $r^{\text{B/P}}=3.2$ kpc (840 arcsec) and in projection extends only to $R^{\text{B/P}}=1.9$ kpc (510 arcsec) from the centre.

However, in M31 the isophotes in this region show no clear corresponding prominent features (Fig.2.12 top panels). As explained in Section 2.4.4.3 the snapshot at 600 u_t was selected to fit the photometry in the bulge of M31. That it fails to match M31 outside this is not unexpected: bars are complex three dimensional structures and is not surprising that this diversity and complexity is not captured completely by a simulation.

To gain insight into which structures project to produce isophotes similar to M31 outside the B/P bulge, we use an earlier snapshot of the same model. We do not claim that M31's thin bar necessarily went through a similar evolution between these two snapshots, but instead we use the morphological structure and mass distribution of the thin bar at different snapshots as a tool to understand the present mass distribution and the morphology of the thin bar in M31.

In Fig.2.12 (middle panels) is shown the earlier snapshot at 500 u_t (3.8 Gyr), when the bar age is $t_{\text{bar}}^{\text{age}}=2.32$ Gyr, and the B/P bulge age since the start of the buckling is $t_{\text{B/P}}^{\text{age}}=1.5$ Gyr. Using the same projection, the B/P bulge at this snapshot is similar to the B/P bulge at 600 u_t , but it manifests less prominent spurs, and is more similar to M31 in the spurs regions. This is the result of the thin bar being shorter, reaching only $r_{\text{bar}}^{\text{thin}}=4.0$ kpc (1000 arcsec) from the

shape of B/P bulge.

centre (in the plane of the disk), as shown in the face on view and therefore the total extension is $l_{\text{bar}}^{\text{thin}}=8$ kpc (2000 arcsec). In projection the thin bar position angle is $\text{PA}_{\text{bar}}=55^\circ.7$ and it extends to $R_{\text{bar}}^{\text{thin}}= \pm 2.3$ kpc (600 arcsec). This locates the ends of the projected thin bar at $(\Delta R_x, \Delta R_y)=(-580, -160)$ arcsec and at $(580, 160)$ arcsec. Beyond these locations the spur shaped isophotes deviate from the projected bar axis similar to the 600 u_t snapshot, but closer to the centre. A shorter thin bar has the consequence that the spurs are weaker and resemble more closely the isophotes outside the M31 bulge at $\Delta R_x= - 570$ arcsec and at 570 arcsec, which we argue are the *real* spurs generated by its thin bar.

Bars are classified as fast if they satisfy the criteria $\mathcal{R}=r_{\text{cor}}/r_{\text{bar}}^{\text{thin}} \leq 1.4$ (Debatista & Sellwood 2000). For Model 1 at 600 u_t , the snapshot that best matches the bulge of M31, the bar pattern speed is $\Omega_p=38$ km s $^{-1}$ kpc $^{-1}$, locating the corotation radius at $r_{\text{cor}}=5.8$ kpc, which combined with the thin bar semi-major axis length at 600 u_t of $r_{\text{bar}}^{\text{thin}}=5.1$ kpc results in a ratio of $\mathcal{R}=1.14$, *i.e.* a fast bar. In the 500 u_t snapshot of Model 1, which best matches the spurs in M31, the bar pattern speed is slightly higher with $\Omega_p=41$ km s $^{-1}$ kpc $^{-1}$, placing the corotation radius at $r_{\text{cor}}=5.3$ kpc, which combined with the thin bar semi-major axis at 500 u_t $r_{\text{bar}}^{\text{thin}}=4.0$ kpc results in a ratio of $\mathcal{R}=1.32$ classifying this also as a fast bar. While the 600 u_t snapshot matches better the main properties of the B/P bulge, as shown in Table 2.1, the 500 u_t snapshot matches better the isophotal properties of the thin bar in M31.

2.4.6.2 Material trailing the thin bar

Now we focus on the structures of M31 located outside the B/P bulge and the thin bar regions. The top left panel in Fig.2.12 shows that M31 has elongated isophotes with *lobe-shaped* structures on both sides of the B/P bulge, which are asymmetric between each other. They are located at $\Delta R_x= - 1000$ arcsec (left side of the bulge) and at $\Delta R_x=900$ arcsec (right side of the bulge), and they are very close to the disk major axis ($\Delta R_y= \pm 100$ arcsec). To show more clearly the asymmetry we also include a rotated image of M31.

In comparison, Model 1 at 600 u_t also presents such lobe-shaped structures beyond the spurs region, as shown in Fig.2.12 (bottom left panel) at $(\Delta R_x, \Delta R_y)=(-1100, -100)$ arcsec and at $(1200, 100)$ arcsec. These features are generated by the material trailing the thin bar, as shown by the face on view (bottom right panel). In the projected view (bottom left panel) we see that this material generates additional isophotal elongated structures beyond the spurs. They have the form of curved isophotes or *lobes* at $\Delta R_x= - 1000$ arcsec (left side of the bulge) and 1000 arcsec (right side) that come back to the disk major axis, and are slightly asymmetric between the left and the right side. The snapshot at 500 u_t also shows this features, but less prominently.

Such lobes are similar to the isophotes observed in M31 at $\Delta R_x=900$ arcsec (right side of the bulge) and even more similar to the side at -1000 arcsec (left side) as shown in Fig.2.12 (top left panel). The notable asymmetry between the left side and the right side argues for the transient nature of these structures. Spiral arms like those seen near the M31 bar region (Gordon et al. 2006; Barmby et al. 2006), bar driven structures (Martinez-Valpuesta & Gerhard 2011), or even the perturbation from a satellite passing near the centre (Block et al. 2006; Dierickx et al. 2014), could trigger transient structures that can change the shape of the isophotes around the thin bar.

AB06 argue that these elongated isophotes in M31 could be the projection of the thin bar,

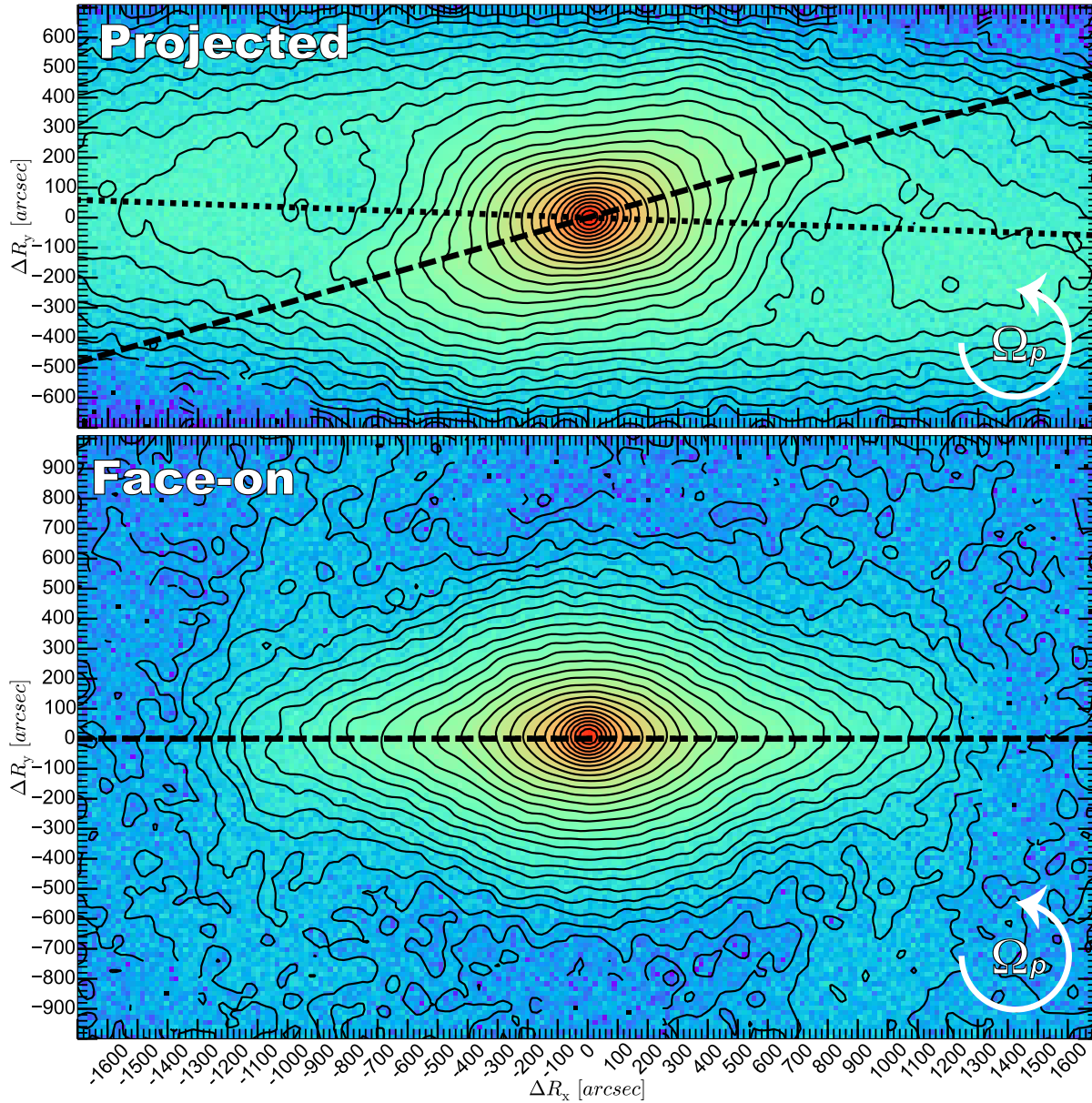


Figure 2.13: SB map of Model 4 at $800 u_t$ rotating anticlockwise. *Top panel*: projection with $i=77^\circ$ and $\theta_{\text{bar}}=54.7^\circ$, showing the disk major axis (dotted line) and the projected bar major axis (dashed line) with a position angle $\text{PA}_{\text{bar}}=55.7^\circ$. The near side of the disk is in the upper part of the panel. *Bottom panel*: face-on view ($i=0^\circ$, $\theta_{\text{bar}}=0^\circ$), with the bar major axis aligned with the horizontal axis (dashed line).

and find bar angles of $\theta_{\text{bar}}=20 - 30^\circ$ by matching these structures with the projected thin bar of their N-body models. However, it would not then be possible to match the orientation of the B/P bulge without requiring a significant misalignment between the B/P bulge and the thin bar of more than 20° in the plane of the disk. In our case we find the bar angle by matching the twist of the boxy bulge, and as a consequence the thin bar generates spurs further away from the disk major axis.

These *lobe-shaped* structures are a common phenomenon in other galaxies, as shows by ED13 with some examples, such as NGC 4725 (their Fig.2), which present trailing spiral arms connected to its thin bar, generating also elongated isophotes that return to the disk major axis. In some galaxies the transient material may be observed in a leading configuration. To demonstrate the effect of material trailing the bar more clearly we show Model 4 in Fig.2.13 with a more unstable disk than the disk of Model 1. Model 4 was built with a constant $Q_T=1.0$ at the initial time and a slightly more massive dark halo, obtaining a B/P bulge with a stronger peanut-shape. Fig.2.13 shows the effect of transient spiral structures behind the bar on the projected isophotes at $\Delta R_x \approx \pm 1200$ arcsec, connecting to the spurs of the thin bar at roughly $\Delta R_x \approx \pm 800$ arcsec. As our models are pure *N*-body systems, the disk is heated in time due to perturbations of the bar and/or the spiral activity, stabilising the disk and weakening in time the transient structures (Sellwood & Carlberg 2014). Only simulations of stellar disks with gas can remain locally unstable for longer times (D’Onghia et al. 2013).

2.5 Triaxial models for the bulge of M31 in the literature.

Historically, the modelling of M31 bulge has been mostly made with axisymmetric or oblate models (Ruiz 1976; Kent 1989; Widrow et al. 2003; Widrow & Dubinski 2005; Block et al. 2006; Hammer et al. 2010). Only few models address the triaxiality of the M31 bulge, either through an analytical approach or N-body simulations, and they differ substantially in their properties.

Following the estimation of $\Delta PA_{\text{max}}=10^\circ$ by Lindblad (1956) between the bulge and the disk major axis, Stark (1977) modelled M31 bulge three dimensional mass density as a triaxial ellipsoid with an apparent axial ratio of $q=0.625$ and using $i=77^\circ$. He obtained a range of bar angles between $\theta_{\text{bar}}=25.3$ and 86.2 , with a prolate solution at 38° . Gerhard (1986) found nearly-prolate solutions for a slightly larger projected axis ratio of $q=0.85$, obtaining a bar angle range between $\theta_{\text{bar}}=38^\circ$ and 88° , and also finding a prolate solution at 38° . If we use $\Delta PA_{\text{max}}=\theta_{\text{proj}}=10^\circ$ and Eq.2.7 for the 1-D bar approximation we obtain a similar result for the bar angle $\theta_{\text{bar}}=38.1$. To constrain the family of solutions, Stark & Binney (1994) compared gas kinematic observations with pseudo-gas models using closed orbit analysis. The bulge was modelled as a spherical component plus a Ferrers bar with 30 per cent of the mass of the spherical component and $\Omega_p=57 \text{ km s}^{-1} \text{ kpc}^{-1}$. Comparing with the observed twist of the velocity iso-contours, they estimate bar angles between $\theta_{\text{bar}}=60^\circ$ and 78° . Berman (2001) and Berman & Loinard (2002) explored full 2D hydrodynamical simulations using a static potential for M31’s stellar and dark matter component, with a triaxial component for the bulge, and compared them with CO observations, estimating a bar angle of $\theta_{\text{bar}}=15^\circ$ and a pattern speed of $\Omega_p=51 - 55 \text{ km s}^{-1} \text{ kpc}^{-1}$.

Besides the present paper, only AB06 have compared full N-body simulations of B/P bulges

combined with classical bulges with the isophotes of M31's bulge. They used two pure B/P bulge models, where one was a weak boxy bulge, and the other a strong X-shaped bulge. They also used two models that combined classical bulges with B/P bulges. They excluded the extreme X-shaped pure B/P bulge model, because it resulted in isophotes that are too pinched in the bulge region. They also excluded the weak pure B/P bulge due to its weak spurs. This left the models with composite bulges as their best candidates, and they concluded that M31 is likely to have a classical bulge component as well as a B/P bulge.

Here we also find a solution with a composite bulge, but with three major differences. The first is our estimated bar angle. While AB06 find angles between $\theta_{\text{bar}}=20^\circ - 30^\circ$ trying to match the lobe-shaped structures in M31 with the projection of the thin bar of their N-body models, we estimate an angle of $\theta_{\text{bar}}=54.7^\circ$ that reproduces the isophotal twist of M31's bulge. This would generate a misalignment of more than 20° between the thin bar major axis and the B/P bulge major axis. Instead, here we find a solution where no misalignment is necessary.

The second difference are the thin bar properties. With the estimated bar angle θ_{bar} the position angle of projection of the thin bar major axis is $\text{PA}_{\text{bar}}=55.7^\circ$. Also, according to our comparison with the $500 u_t$ snapshot of Model 1, the estimated length for the thin bar semi-major axis that matches better the weak spurs observed in M31 is ~ 4 kpc (1000 arcsec) in the plane of the disk, instead of the estimated 1320 arcsec of AB06. If the thin bar were much longer than 1000 arcsec, it would generate spurs much more prominent than observed, as we showed with the thin bar at $600 u_t$ which has a semi-major axis of 5.1 kpc (1300 arcsec) in the plane of the disk.

Finally, the properties of the classical bulge are different. We find a massive, but concentrated ICB component, that combined with the B/P bulge reproduces the surface-brightness profile and the morphology of M31's bulge, and exclude less concentrated solutions for the ICB. The Hernquist ICB mass ranges explored by AB06 are similar to our massive models in the ICB parameter space exploration, but they considered larger scale lengths, with $r_b=0.4 u_d$ and $0.6 u_d$. As shown in Fig. 2.6, this range of scale length results in Sérsic indices lower than is required to match M31. Therefore the surface brightness profile requires a concentrated classical bulge.

2.6 Conclusions

We have presented here a dynamical model that reproduces the main photometric observables of the bulge of the Andromeda galaxy. We explored a large set of N-body models, combining B/P bulges with classical bulges. The B/P bulges are generated in the simulations from the initial disk that naturally forms a bar and buckles generating the boxy structure which evolves together with the ICB, resulting at the end in a system in dynamical equilibrium. We specially focus on exploring the size and mass of the classical bulge component.

By a quantitative comparison of morphological and kinematic properties of M31 with the models, we are able to find a best model. This model requires a classical bulge and a B/P bulge with masses of $1/3$ and $2/3$ of the total stellar mass of the bulge to match the observations. The classical bulge contributes mainly in the centre of the bulge, within ~ 530 pc (140 arcsec), increasing the mass concentration and therefore the Sérsic index. The cuspy density profile is

also reflected in the kinematics, generating a dispersion drop in the centre. On the contrary, the mass contribution of the B/P bulge in the centre is shallow which lowers the Sérsic index of the combined SB profile. Beyond ~ 530 pc (140 arcsec) the B/P bulge dominates, explains the observed rotation, and the boxy shape of the isophotes. We excluded pure B/P bulge models, because they show a Sérsic index too low to reproduce the value observed in M31, and because their central velocity dispersion lacks the drop generated by the ICB component.

From our comparison with the structures outside the B/P bulge, we find that the weak spurs observed in M31 at the end of its boxy bulge suggests that its thin bar is short, with a semi-major axis of $r_{\text{bar}}^{\text{thin}}=4.0$ kpc (1000 arcsec) in the plane of the disk, and in projection extends to $R_{\text{bar}}^{\text{thin}}=2.3$ kpc (600 arcsec) located at a position angle of $\text{PA}_{\text{bar}}=55^\circ.7$. M31 also shows lobe-shaped isophotes further away at $R\sim 3.4$ kpc (950 arcsec) located near the disk major axis. The proximity of these lobe-shaped isophotes to the disk major axis and the asymmetry between the structures at both sides of the bulge suggests the presence of transient structures trailing the thin bar.

The presence of a massive B/P bulge component intertwined with a classical bulge has strong implications for the formation and the secular evolution history of M31. To better understand and quantify the impact of the B/P bulge on the dynamics of the galaxy, we are developing Made-to-Measure models that reproduce simultaneously the thin bar and B/P bulge structures, and also M31's disk mass distribution (Blaña et al. in prep.) using detailed IFU kinematics (Opitsch et al. in preparation).


2.A Initial Conditions and Bar Formation

We modified MAGALIE following the procedure of Athanassoula & Misiriotis (2002) to generate galaxies with a constant Toomre parameter Q_{T} (Toomre 1964). This allows setting disks that are dynamically colder at all radii, than an exponential radial velocity dispersion profile. This is in principle better in the inner regions of the disk, because it respects the epicyclic approximation used by MAGALIE at that radii. A colder disk also is more bar-unstable. As an example, the solutions of the solid body rotator disk (Kalnajs 1965) show that these systems are unstable to bar modes when the ratio (q_{rot}) of rotational kinetic energy to potential energy is $q_{\text{rot}} > 0.1286$ (Binney & Tremaine 2008). Making a disk colder favours bar formation (or in general non-axisymmetric instabilities), because this distributes more kinetic energy in the rotational component of the disk particles than in the random motion component, increasing q_{rot} . We achieve this by choosing a radial velocity dispersion of the form $\sigma_r^{Q_{\text{T}}} = 3.36 Q_{\text{T}} \Sigma \kappa^{-1}$, where κ is the epicyclic frequency, Σ the surface mass density and Q_{T} is the initial value of the Toomre parameter. We choose an initial value of $Q_{\text{T}}=1.0$ to avoid axisymmetric instabilities, although depending on the disk thickness used, this limit can be as low as $Q_{\text{T}}=0.696$, as shown by Behrendt et al. (2015).

In some extreme cases the circular velocity can be very low if the DMH has a low concentration or there is no initial bulge component. This forces the Jeans equations to assign streaming or azimuthal velocities to the particles that would be higher than the circular velocity within a small radius r_{C} . We prevent this by changing the radial velocity dispersion within r_{C} by a profile that also respects the epicyclic approximation and has the form $\sigma_r^{\Sigma} = C \Sigma^{-1/2}$, where C is a constant determined at r_{C} to make a continuous dispersion profile, i.e. $\sigma_r^{Q_{\text{T}}}(r_{\text{C}}) = \sigma_r^{\Sigma}(r_{\text{C}})$.

Chapter 3

Sculpting Andromeda – made-to-measure models for M31’s bar and composite bulge: dynamics, stellar and dark matter mass

Original publication: Matias Blaña Díaz¹, Ortwin Gerhard, Christopher Wegg, Matthieu Portail, Michael Opitsch, Roberto Saglia, Maximilian Fabricius, Peter Erwin, Ralf Bender, 2018, in prep. to MNRAS 

Abstract

The Andromeda galaxy (M31) contains a box/peanut (B/P) bulge entangled to a classical bulge (CB) requiring a triaxial modelling to determine the dynamics, stellar and dark matter mass. We construct made-to-measure models fitting new VIRUS-W IFU kinematic observations, together with IRAC 3.6 μm photometry, and the disc’s HI rotation curve. We explore the parameter space for the 3.6 μm mass-to-light ratio ($\Upsilon_{3.6}$), the pattern speed of the B/P bulge and the thin bar (Ω_p), and the dark matter mass content in the bulge (M_{DM}^{B}) within 3.2 kpc (842 arcsec). Considering Einasto dark matter profiles, we find the best fitting models for $\Upsilon_{3.6} = 0.72 \pm 0.02 \text{ M}_{\odot} \text{ L}_{\odot}^{-1}$, $M_{\text{DM}}^{\text{B}} = 1.2_{-0.4}^{+0.2} \times 10^{10} \text{ M}_{\odot}$ and $\Omega_p = 40 \pm 5 \text{ km s}^{-1} \text{ kpc}^{-1}$. These models have a total dynamical mass within the composite bulge of $M_{\text{dyn}}^{\text{B}} = 4.25_{-0.29}^{+0.10} \times 10^{10} \text{ M}_{\odot}$ including a stellar mass of $M_{\star}^{\text{B}} = 3.09_{-0.12}^{+0.10} \times 10^{10} \text{ M}_{\odot}$ (73%), of which the classical bulge has $M_{\star}^{\text{CB}} = 1.18_{-0.07}^{+0.06} \times 10^{10} \text{ M}_{\odot}$ (28%) and the B/P bulge $M_{\star}^{\text{BP}} = 1.91 \pm 0.06 \times 10^{10} \text{ M}_{\odot}$ (45%). We also explored models with NFW dark matter profiles, finding that while the Einasto models fit the bulge stellar kinematics better than the NFW models, the obtained main parameters agree within the errors. The M_{DM}^{B} values agree with adiabatically contracted cosmological NFW haloes with M31’s virial mass and radius. The best model has two bulge components with completely different kinematics that only together successfully reproduce the M31 photometric and kinematic maps (ν_{los} , σ_{los} , $h3$, $h4$). The modelling includes dust absorption effects that reproduce asymmetric features detected in the kinematic observations. Our results provide new constraints for the early formation history of M31 given the lower mass found for the classical bulge component compared to previous estimates

and the shallow dark matter profile favoured by the kinematic data, as well as the secular evolution history of M31 implied by the massive B/P bulge and thin bar, and its interactions with the classical bulge, the inner stellar halo and the disc through resonances.

3.1 Introduction

The Andromeda galaxy (M31, NGC224) is the closest neighbouring massive spiral galaxy, presenting us a unique opportunity to study in depth the dynamics of disc galaxy substructures, such as classical bulges and bars, the later found in approximately 70 per cent of the disc galaxies in the local Universe (Menendez-Delmestre et al. 2007; Erwin 2017). Historically, M31's triaxial bulge has been mostly addressed as a classical bulge, while generally the bar component has been only qualitatively considered in the modelling of its stellar dynamics. However, an accurate dynamical estimation of the mass distribution of the stellar and the dark matter in the bulge must take into account the barred nature of this galaxy. More recent observations better quantify the triaxiality of the bulge which is produced by its box/peanut (B/P) bulge component (Beaton et al. 2007; Opitsch et al. 2018), a situation similar in many aspects to the Milky Way's B/P bulge (Shen et al. 2010; Wegg & Gerhard 2013; Bland-Hawthorn & Gerhard 2016). The M31 B/P bulge is in addition entangled with a classical bulge component (Athanasoula & Beaton 2006). The classical bulge is much more concentrated than the B/P bulge, with the two components contributing with $\sim 1/3$ and $\sim 2/3$ of the total stellar mass of the bulge respectively, as shown by Blana et al. (2017, hereafter B17).

Each substructure in M31 can potentially teach us about the different mechanisms involved in the formation and the evolution of the whole galaxy. In particular, the properties of the classical bulge component of M31 can give us information about the early formation epoch. Current galaxy formation theories consider classical bulges as remnants of a very early formation process, such as a protogalactic collapse, and/or as remnants of mergers of galaxies that occurred during the first gigayears of violent hierarchical formation (Toomre 1977; Naab & Burkert 2003; Bournaud et al. 2005). On the other hand, the massive B/P bulge of M31 provides us information about the evolution of the disc, as B/P bulges are formed later from the disc material. B/P bulges in N-body models are triaxial structures formed through the buckling instability of the bar, which typically lasts for $\lesssim 1$ Gyr, generating a vertically thick structure (Combes et al. 1990; Raha et al. 1991). Recent observations of two barred galaxies also show evidence of the bar buckling mechanism (Erwin & Debattista 2016). B/P bulges are important being found in 79 per cent of massive barred local galaxies ($\gtrsim 10^{10.4} M_{\odot}$) (Erwin & Debattista 2017). Note that box/peanut bulges are sometimes referred as B/P bulge pseudobulges, however not to be confused with discy pseudobulges, which are formed by gas accreted in the center of galaxies (Kormendy 2013).

Moreover, on even longer time-scales B/P bulges and bars can interact through resonances with the disc and redistribute its material, generating for example surface brightness breaks, as well as ring-like substructures (Buta & Crocker 1991; Debattista et al. 2006; Erwin et al. 2008; Buta 2017). Bars also transfer their angular momentum to the spheroid components, such as classical bulges (Saha et al. 2012, 2016), stellar haloes (Perez-Villegas et al. 2017) and dark mat-

ter haloes (Athanasoula & Misiriotis 2002), changing their dynamical properties. Furthermore, Erwin & Debattista (2016) show also with observations that classical bulges can coexist with discy pseudobulges and B/P bulges, a scenario that has also been reproduced in galaxy formation simulations (Athanasoula et al. 2016).

To understand the formation and the evolution of Andromeda, and to accurately compare it with galaxy formation simulations, it is imperative to first determine the contribution and the properties of each of the substructures, such as their masses and sizes, as well as the dark matter distribution. In the outer disc region the gas kinematics constrain the dark matter distribution (Chemin et al. 2009; Corbelli et al. 2010). However, in the centre, the gas is not in equilibrium due to the triaxial potential generated by the bar. Therefore, we model the stellar kinematics taking into consideration the triaxial structure of the B/P bulge. Opitsch (2016, hereafter O16) and Opitsch et al. (2018, hereafter O18) obtained kinematic observations of exquisite detail using the integral field unit (IFU) VIRUS-W (Fabricius et al. 2012), completely covering the classical bulge, the B/P bulge and most of the projected thin or planar bar. In this paper we use these kinematic observations to fit a wide range of made-to-measure models that allow us to find constraints for the stellar and dark matter mass within the bulge region, as well as other dynamical properties such as the pattern speed of the B/P bulge and the thin bar.

This paper is ordered as follows: Section 3.2 describes the observational data, its implementation, and the made-to-measure modelling of M31. Section 3.3 shows the results of the models that are separated in two main parts. In the first, Section 3.3.1, we present the main results of the parameter search exploration. In the second part, in Section 3.3.2, we present the properties of the best model and we compare it with the M31 observations. In Section 3.4 we conclude with a summary and a discussion of the implications of our findings.

3.2 Modelling the bulge of M31

Most dynamical models for the bulge of M31 assume a spherical or an oblate geometry for the bulge (Ruiz 1976; Kent 1989; Widrow et al. 2003; Widrow & Dubinski 2005; Block et al. 2006; Hammer et al. 2010), making the mass estimations in the centre less accurate due to the barred nature of this galaxy. N-body barred galaxy models can represent the bulge and the bar of M31 much better. However, finding an N-body model that exactly reproduces all the properties of the M31 substructures can be very difficult, because N-body models depend on their initial conditions and also on the bar formation and buckling, evolving in a stochastic way. Therefore, we proceed to use the Made-to-measure (M2M) method to model the bulge of M31 (Syer & Tremaine 1996, hereafter ST96). This method can model triaxial systems and therefore it is the most suitable approach to model M31's bar.

In the following sections we describe our technique that implements the M2M method to fit the kinematic and the photometric observations, which allows us to determine the main dynamical properties of the M31 composite bulge: the pattern speed of the bar (Ω_p), the stellar mass-to-light ratio of the bulge in the $3.6\mu\text{m}$ band ($\Upsilon_{3.6}$) and the dark matter mass within the bulge (M_{DM}^{B}).

3.2.1 Made-to-measure method

We use the program NMAGIC that implements the M2M method (De Lorenzi et al. 2007, 2008; Morganti & Gerhard 2012; Portail et al. 2015a, 2017a). In the original implementation of the M2M method (ST96) the potential and the model observables are calculated from the initial mass distribution of the particles, where their masses are then optimised to match observations, requiring a mass distribution of the particles that is as close to the final model. In the NMAGIC implementation the potential is periodically recomputed to generate a system that is gravitationally self-consistent.

A discrete model observable is define for a system with N particles with phase-space time depending coordinates $\vec{z}_i(t) = (\vec{r}_i, \vec{v}_i)$ as:

$$y(t) = \sum_{i=1}^N K_i(\vec{z}_i(t)) w_i \quad (3.1)$$

where K_i is a known kernel that is used to calculate the distribution moments, w_i is the weight of each particle that contributes to the observable, corresponding here to the particle's mass. We increase the effective number of particles implementing an exponential temporal smoothing with timescale τ_s , obtaining the smoothed observable y_τ .

The observational data is composed by j observations (*e.g.* j number of pixels in an image), and by k different sets of observations; here we work with one set of photometric observations and four sets of kinematic observations. We have in total Y_j^k observations with $Y_{\text{err } j}^k$ errors, and for the model we have $y_{\tau j}^k$ temporally smoothed observables and K_{ij}^k kernels. The deviation between the model observables and the observations is defined by the delta

$$\Delta_j^k(t) = \frac{y_{\tau j}^k(t) - Y_j^k}{Y_{\text{err } j}^k} \quad (3.2)$$

and therefore the sum in time of $(\Delta_j^k)^2$ is the chi-square $\chi^2_j^k$ of the temporal smoothed model observables and the observations.

The heart of the M2M method is the algorithm that determines how the weights of the particles change in time during the iterative fit to the observations. Here we use the ‘‘force-of-change’’ (FOC) defined by ST96 as:

$$\frac{dw_i}{dt} = \epsilon w_i \partial_{w_i} F \quad (3.3)$$

where ϵ is a constant adjusting the strength of the FOC. This relation is a gradient ascent algorithm that maximises F in the space of the weights, defined in NMAGIC as

$$F = -\frac{1}{2}\chi_{\text{tot}}^2 + \mu S \quad (3.4)$$

where the first term is just the total chi-square

$$\chi_{\text{tot}}^2 = \sum_{k,j} \lambda_k \chi_j^{2k} \quad (3.5)$$

where $\chi^2_j = \left(\frac{\Delta_j^k}{\lambda_k}\right)^2$, and λ_k are k constants that balance the contributions between different k sets of observables (Long & Mao 2010; Portail et al. 2015a). The term S is an ‘‘entropy’’ introduced by ST96 that forces the weights of the particle distribution to remain close to their initial distribution, defined here as in Portail et al. (2017a).

$$S = \sum_i w_i \left(1 - \ln \frac{w_i}{\hat{w}_i}\right) \quad (3.6)$$

where \hat{w}_i are the ‘‘priors’’ calculated from the average of the weights of each particle type (classical bulge, B/P bulge and the disc particles, and dark matter particles). The entropy term also forces the model to slowly change its initial 3D mass density distribution. The factor μ balances the contribution between the entropy term and the chi square term (De Lorenzi et al. 2007). Introducing the previous terms in equation 3.3 we have now the FOC equation

$$\frac{dw_i}{dt} = -\epsilon w_i \left[\mu \ln \left(\frac{w_i}{\hat{w}_i}\right) + \sum_k \lambda_k \sum_j \left(K_{ij}^k + w_i \partial_{w_i} K_{ij}^k\right) \frac{\Delta_j^k}{Y_{\text{err } j}^k} \right] \quad (3.7)$$

With the observables that we define later the differential term becomes zero ($\partial_{w_i} K_{ij}^k = 0$).

3.2.2 Inputs to the M2M modelling from B17: initial N-body model and projection angles

The M2M modelling requires an initial particle model that contains sufficient families of orbits to construct a new model that successfully matches the observations. Therefore, we use the best matching particle model for the M31 bulge from B17, *i.e.* Model 1, which comes from a set of 72 N-body models built with a B/P bulge component and a classical bulge component with different masses and scale lengths. These models evolved from a Hernquist density profile for the classical bulge and another for the dark halo with no initial rotation. During these simulations the initial disc forms a bar that later buckles forming a B/P bulge, but leaving bar material in the plane which is the thin bar. The thin bar is aligned with the B/P bulge extending beyond this. We reserve the term bar for whole structure of the thin bar and the B/P bulge together. The bar is entangled with the classical bulge, where both structures evolve due to the transfer of angular momentum from the bar to the classical bulge and the dark matter halo as well, gaining both rotation. The light of the classical bulge and the B/P bulge dominate in the centre, and therefore no stellar halo component is included. The number of particles used for the bulge, disc and halo are $N_{\text{bulge}}=10^6$, $N_{\text{disc}}=10^6$ and $N_{\text{halo}}=2 \times 10^6$.

Model 1 has a concentrated classical bulge and a B/P bulge with a 3D semi-major axis of $r^{\text{BP}}=3.2$ kpc (840 arcsec). Within the radius r^{BP} B17 measure the stellar mass of the bulge of $M_{\star}^{\text{B}}=3.3 \times 10^{10} M_{\odot}$, where the classical bulge and the B/P bulge have $\sim 1/3$ and $\sim 2/3$ of the bulge total stellar mass, respectively. This model has a bar pattern speed of $\Omega_p = 38 \text{ km s}^{-1} \text{ kpc}^{-1}$. They estimate a stellar mass-to-light ratio in the $3.6 \mu\text{m}$ of $\Upsilon_{3.6 \text{ B17}}=0.813 M_{\odot} L_{\odot}^{-1}$.

We test our final results using another model from B17 with $M_{\star}^{\text{CB}}=1.4 \times 10^{10} M_{\odot}$ and $r_{\text{half}}^{\text{CB}}=0.5$ kpc as initial condition for the M2M fits, finding only small differences in the final fitted M2M model.

We also need to project the M2M models on the sky to calculate the model observables defined later in section 3.2.5, requiring then the distance to M31 d_{M31} , the disc inclination angle i , the disc major axis position angle PA_{disk} , and the bar angle θ_{bar} . For this we use the same quantities adopted in B17: $d_{M31}=785 \pm 25$ kpc (McConnachie et al. 2005) (3.8 pc=1 arcsec, 1 kpc=260 arcsec and 13.7 kpc= 1° on the sky), $i=77^\circ$ (Corbelli et al. 2010), $PA_{\text{disk}}=38^\circ$ (de Vaucouleurs 1958), and the bar angle $\theta_{\text{bar}}=54.7 \pm 3.8$ measured in B17. The bar angle is defined in the plane of the disc (where the bar major axis would be aligned with the disc projected major axis for $\theta_{\text{bar}}=0^\circ$, see B17 Figure 1). Projecting θ_{bar} into the sky results in an angle of $\theta_{\text{proj}}=17.7 \pm 2.5$ measured from the line of nodes of the disc major axis, corresponding to a position angle of $PA_{\text{bar}}=55.7 \pm 2.5$. We corroborate later in section 3.3.1.5 that $\theta_{\text{bar}}=54.7 \pm 3.8$ is the angle that best matches the photometry of the bulge reproducing the bulge isophotal twist, also showing that within the bar angle error range we find similar results, not changing our main conclusions.

3.2.3 Fitting the photometry and IFU kinematics

We prepare M31's photometric and kinematic observational data to use it as constraints for the M2M fitting with NMAGIC. The photometric data consist of an image of M31 from the Infrared Array Camera 1 (IRAC 1). The kinematic data correspond to IFU observations of the bulge region of M31, and to HI rotation curves in the disc region. Consistently with the observations, we build model observables that measure and fitted to the equivalent data values. However, as we explain later in Section 3.2.8, to find our range of the best matching models we select a subsample of the fitted observations to compare them with the models. Note that all the model observables y_j^k defined here are temporal smoothed to y_τ^k .

3.2.3.1 Photometry I: IRAC 3.6 μm observations

The imaging data that we use come from the large-scale IRAC mosaic images of M31 of the *Spitzer Space Telescope* (Barmby et al. 2006) kindly made available to us by Pauline Barmby. We use the IRAC 1 band that is in the 3.6 μm wavelength for two reasons: i) it traces well the old stars (bulk of the population) where the light is dominated by giant stars that populate the red giant branch (RGB), and ii) this band has the advantage of being only weakly affected by the dust emission or absorption (Meidt et al. 2014). The IRAC1 mosaic of Barmby et al. (2006) has pixels with size of 0.863 arcsec and covers a region of 3.7×1.6 . We are interested in covering the inner bulge region where the classical bulge dominates within ~ 100 arcsec (0.4 kpc) in the projected radius, also where the B/P bulge is at ~ 700 arcsec (2.7 kpc) in projection. Therefore, we use a resolution of 8.63 arcsec per pixel for the image, which is a convenient scale that shows the light gradients in the central region where the transition between the classical bulge and the B/P bulge is. As we are interested in the scenario where the 10 kpc-ring could be connected to the outer Lindblad resonance, we include the region of the stellar disc out to 3950 arcsec (15 kpc) along the disc projected semi-major axis of an ellipse that is fitted to the isophotes with the `ellipse` task in `iraf` calculating then the ellipticity and position angle at 15 kpc. We mask the pixels of the image that are outside this ellipse at 15 kpc and proceed to fit the image. We also mask hot

pixels in the image, foreground stars, and the dwarf galaxy M32. At the end of the filtering, the total number of photometric observable (pixels) used for the M2M fit is 170651.

The original image pixel values are in intensity I [MJy sr⁻¹]. The surface-brightness figures in the paper that are in mag arcsec⁻² are in the Vega system, and they are transformed from the original units using the 3.6 μ m zero-point calibration 280.9 Jy (Reach et al. 2005). The conversion between the SB in mag arcsec⁻² and the luminosity L_{\odot} is done using the absolute solar magnitude value $M_{\odot}^{3.6}=3.24$ mag (Oh et al. 2008), and multiplying I by the pixel area $A_{\text{pixel}}=8.63 \text{ arcsec} \times 8.63 \text{ arcsec}$.

We also require the photometric error maps for the M2M modelling. Given that the M2M models are a representation of M31 in dynamical equilibrium, they cannot reproduce the observed substructures in M31 that are produced by perturbations such as spiral arms. Therefore, we include these smaller scale deviations between M31 and the models in the errors. For this we combined three types of error maps: the observational error $L_{\text{err}}^{\text{obs}}$, the variability between pixels $L_{\text{err}}^{\text{stdv}}$ and the asymmetry error $L_{\text{err}}^{\text{asym}}$. The first error ($L_{\text{err}}^{\text{obs}}$) is calculated from the square root of the sum in quadrature of the pixel error and the standard deviation for each pixel that comes from the original 0.863 arcsec pixels. The typical $L_{\text{err}}^{\text{obs}}$ errors are between one and 5 per cent of the intensity depending on the pixel location in the image. The second error that we include takes into account the variability observed between contiguous pixels. The surface-brightness image of our M2M models is smoother than the observations. We take into account this variability by including in the photometric error the standard deviation within a radius of one 8.63 arcsec-pixel around each pixel of the image, obtaining the error $L_{\text{err}}^{\text{stdv}}$. Finally we also include the variability observed at kiloparsec scales due to substructures like the spiral arms beyond the bar region, and the 10 kpc-ring. For this we subtract the image with the same image, but rotated 180° around the centre of the bulge, obtaining $L_{\text{err}}^{\text{asym}}$. The bulge is roughly symmetric making this term smaller in the bulge than in the disc region. The combined photometric error per pixel $Y_{\text{err } j}^k$ with $k=0$ is then:

$$Y_{\text{err } j}^{k=0} = L_{\text{err } j} = \left[\left(L_{\text{err } j}^{\text{obs}} \right)^2 + \left(L_{\text{err } j}^{\text{stdv}} \right)^2 + \left(L_{\text{err } j}^{\text{asym}} \right)^2 \right]^{1/2} \quad (3.8)$$

3.2.3.2 Photometry II: model observables and the mass-to-light ratio ($\Upsilon_{3.6}$)

The photometric model observables consist of an array of pixels that extends from the bulge centre out to the disc until 15 kpc along the disc major axis, where each model pixel uniquely corresponds to each observed pixel, with the same pixel size (8.63 arcsec). Each j th pixel measures the stellar masses m_i of N_j particles that pass through each pixel, which are converted to light in the 3.6 μ m band using the stellar mass-to-light ratio $\Upsilon_{3.6}$. The total light per pixel L_j is the photometric model observable y_j^k with $k=0$:

$$y_j^k = L_j = \sum_i^{N_j} l_i = \sum_i^{N_j} \Upsilon_i^{-1} m_i \quad (3.9)$$

where the light per particle (l_i) is just $\Upsilon_i^{-1} m_i$. We define three mass-to-light ratio parameters in the 3.6 μ m band: Υ^{CB} for the classical bulge, Υ^{BP} for the B/P bulge and Υ^{d} for the outer disc,

which are assigned to the particles according to the relation:

$$\Upsilon_i = \begin{cases} \Upsilon^{\text{CB}} & \text{if } i \in \text{CB} \\ \Upsilon^{\text{BP}} & \text{if } i \notin \text{CB} \wedge R_i \leq R_t \\ \left(\Upsilon^{\text{BP}} - \Upsilon^{\text{d}} \right) e^{\frac{-(R_i - R_t)^2}{2R_s^2}} + \Upsilon^{\text{d}} & \text{if } i \notin \text{CB} \wedge R_i > R_t \end{cases} \quad (3.10)$$

where the classical bulge particles are assigned Υ^{CB} everywhere, and the bar and disc particles at the cylindrical radius R_i are assigned Υ^{BP} within R_t , and Υ^{d} if they are outside this radius. The last Gaussian term provides a smooth transition of Υ_i from the value of Υ^{BP} to the value in the disc Υ^{d} , where R_t is the transition radius, and R_s is the scale of the change.

In section 3.2.8 we explain in more detail the different mass-to-light values that we explored, where in most of our fiducial M2M fits we assumed $\Upsilon_{3,6} = \Upsilon^{\text{CB}} = \Upsilon^{\text{BP}} = \Upsilon^{\text{d}}$, with the parameters $R_t = 4 \text{ kpc}$ and $R_s = 1.5 \text{ kpc}$. However, in Section 3.3.1.2 we explore further different values for each component, finding only small differences compared with our range of best models.

From equation 3.9 we have that the photometric kernel ($k=0$) is

$$K_{ij}^{k=0} = \Upsilon_i^{-1} \quad (3.11)$$

3.2.3.3 Kinematics I: M31 Bulge IFU observations

O16 and O18 obtained kinematic IFU observations of the central region of M31 using the McDonald Observatory's 2.7-meter Harlan J. Smith Telescope and the VIRUS-W Spectrograph (Fabricius et al. 2012). They cover the whole bulge and bar region and also sample the disc out to one disc scale length along six different directions, obtaining line-of-sight velocity distribution profiles (LOSVDs). From this they calculate the four Gauss-Hermite expansion coefficient moments (Gerhard 1993; Bender et al. 1994), and obtain kinematic maps for the velocity v_{los} , the velocity dispersion σ_{los} and the kinematic moments $h3$ and $h4$, where by definition the terms $h1$ and $h2$ are zero. The velocity maps are corrected for the systemic velocity of -300 km s^{-1} (de Vaucouleurs et al. 1991). We also define here the light weighted mean line-of-sight velocity $\langle v \rangle_{\text{los}}$ and the light weighted velocity standard deviation (or dispersion) $\langle \sigma \rangle_{\text{los}} = \sqrt{\langle v^2 \rangle_{\text{los}} - \langle v \rangle_{\text{los}}^2}$, that differ from v_{los} and σ_{los} when the LOSVDs deviate from a gaussian distribution ($h3 \neq 0$ or $h4 \neq 0$ or non-zero higher moments).

We re-grid the kinematic observations into new maps with the same spatial resolution of the photometric data. The new values of v_{los} , σ_{los} , $h3$ and $h4$ are calculated from the error weighted average of the original values, obtaining 13400 for each kinematic variable, and therefore 53600 kinematic values in total. The re-gridded observational kinematic errors ($Y_{\text{err}}^{\text{obs } k}_j$, with $k=1, 2, 3, 4$) are calculated from the standard deviation of the error weighted average. Similarly to the photometry, we combined the new observational error and the error due to the variability between different kinematic pixels within one pixel radius ($Y_{\text{err}}^{\text{stdv } k}_j$), obtaining a total kinematic error per observable and per set of:

$$Y_{\text{err } j}^k = \left[\left(Y_{\text{err } j}^{\text{obs } k} \right)^2 + \left(Y_{\text{err } j}^{\text{stdv } k} \right)^2 \right]^{1/2}. \quad (3.12)$$

3.2.3.4 Kinematics II: model observables

Now we proceed to build the kinematic model observables. Given that the kinematic observations are performed in the V band we need to include a dust modelling in our model observables to account for the absorption of the light. The dust is located mostly in the plane of the disk. A further description is given later in section 3.3.2.3. Our dust absorption implementation consists of using M31 dust mass maps (Draine et al. 2014) converted to a V band absorption map, given by the dust model of Draine & Li (2007)

$$A_V^j = 0.74 \left(\frac{\Sigma_{\text{dust}}^j}{10^5 M_\odot \text{ kpc}^{-2}} \right) \text{ mag} \quad (3.13)$$

We convert this to a 3D absorption map p^{AV} , deprojected as

$$p_{i,j}^{AV} = \begin{cases} 10^{-0.4A_V^j} & \text{if } z_i \leq 0 \text{ kpc} \\ 1 & \text{if } z_i > 0 \text{ kpc} \end{cases} \quad (3.14)$$

where for simplicity we assume that the dust is located in the plane of the disk, and therefore any stellar i th particle that is temporarily passing behind the disc at the moment that the kinematic model observable is measured, is then attenuated by the corresponding value of $p_{i,j}^{AV}$ in the j th pixel.

Given that we need kinematic model observables that change linearly with the particle weights, we proceed to fit the Gauss-Hermite moments of the observations, instead of directly fitting σ_{los} and v_{los} . The model kinematic observables are then the light-weighted Gauss-Hermite coefficient moments, calculated as in De Lorenzi et al. (2007), where we additionally included the dust absorption:

$$y_j^k = \text{H}k_j = \sum_i^{N_j} p_{i,j}^{AV} l_i h_{n,i} = \sum_i^{N_j} p_{i,j}^{AV} \Upsilon_i^{-1} m_i 2 \sqrt{\pi} u_k(\beta_i) \quad (3.15)$$

where $k=1, 2, 3, 4$, and $u_k(\beta_i)$ are the dimensionless Gauss-Hermite functions (Gerhard 1993),

$$u_k(\beta_i) = (2^{n+1} \pi n!)^{-1/2} H_k(\beta_i) \exp(-\beta_i^2/2) \quad (3.16)$$

where H_k are the standard Hermite polynomials, with

$$\beta_i = (v_i - v_{\text{los}}) / \sigma_{\text{los}} \quad (3.17)$$

where v_i is the particle's line-of-sight velocity, and the expansion is performed with the observational values of σ_{los} and v_{los} . From this we obtain the light weighted model observables H1, H2, H3, H4. The corresponding kinematic kernel that changes the weights of the particles is

$$K_{i,j}^k = p_{i,j}^{AV} \Upsilon_i^{-1} 2 \sqrt{\pi} u_k(\beta_i) \quad (3.18)$$

Concordantly, the observational data that we fit are the Gauss-Hermite moments $h1=0$, $h2=0$, $h3$ and $h4$, which are light-weighted by the extincted light model observable

$$L_j^{AV} = \sum_i^{N_j} p_{i,j}^{AV} \Upsilon_i^{-1} m_i \quad (3.19)$$

that is then used to light weight the kinematic observations *e.g.* $H1=h1 L^{AV}$, obtaining then the observations that we fit $H1$, $H2$, $H3$, $H4$.

The errors for $h1$ and $h2$ are calculated from the observations v_{los} and σ_{los} as in [van der Marel & Franx \(1993\)](#); [Rix et al. \(1997\)](#).

$$h1_{\text{err}} = \frac{1}{\sqrt{2}} \frac{v_{\text{los, err}}}{\sigma_{\text{los}}}; \quad h2_{\text{err}} = \frac{1}{\sqrt{2}} \frac{\sigma_{\text{los, err}}}{\sigma_{\text{los}}} \quad (3.20)$$

Then, the kinematic errors $h1_{\text{err}}$, $h2_{\text{err}}$, $h3_{\text{err}}$ and $h4_{\text{err}}$ are also light-weighted in the form $H1_{\text{err } j} = h1_{\text{err } j} (L_j)^2 (L_j^{AV})^{-1}$, which gives larger errors to the regions with more light extinction. From this we obtained the light weighted errors $H1_{\text{err}}$, $H2_{\text{err}}$, $H3_{\text{err}}$, $H4_{\text{err}}$. We also test our best model fit considering no dust absorption ($A_V^j=0$ mag) and a constant value $A_V^j=0.5$ mag.

For the actual comparison of the model with the observations, and also for the selection of the range of best models defined in Section 3.2.8, we recover after the M2M fitting the temporal smoothed v_{los} and σ_{los} of the model, using these values to calculate $h3$ and $h4$ of the model. For this we observe the model and calculate $H1$, $H2$, $H3$, $H4$ of the model using equation 3.15, but in equation 3.17 we replace v_{los} and σ_{los} of the observations by the mean velocity $\langle v \rangle_{\text{los}}$ and the velocity standard deviation $\langle \sigma \rangle_{\text{los}}$ of the model. The non-light weighted quantities are recovered dividing by L_j^{AV} , *i.e.* $h1=H1/L_j^{AV}$ and similarly for $h2$, $h3$, $h4$. The parametrisation of the LOSVD with the Gauss-Hermite moments dictates that the variables σ_{los} and v_{los} have values such that the values of $h1$ and $h2$ are zero. If this is not the case we use again the approximation ([van der Marel & Franx 1993](#); [Rix et al. 1997](#)) to correct and replace the old values of the velocity and the dispersion (v_o, σ_o) with the new values (v_n, σ_n) that result in new $h1_n$ and $h2_n$ values closer to zero:

$$v_n = v_o + \sqrt{2} \sigma_o h1_o(v_o, \sigma_o) \quad (3.21a)$$

$$\sigma_n = \sigma_o + \sqrt{2} \sigma_o h2_o(v_o, \sigma_o) \quad (3.21b)$$

We repeat the previous corrections observing the model and calculating the new $h1$, $h2$, $h3$, $h4$ from the new dispersion and velocity using equation 3.15, repeating this iteratively until the terms $h1$ and $h2$ converge to zero or values smaller than the observational errors.

3.2.4 Adjusting the dark matter mass within the bulge (M_{DM}^{B}), and fitting the HI rotation curve

Our goal is to determine the dark matter mass within 3.2 kpc of the bulge M_{DM}^{B} , by exploring a vast range of values given in Section 3.2.8. For this we change the initial dark matter mass

distribution of the input N-body model to match a target analytical profile. As we also want to explore the cusped or cored nature of the dark matter density in the central region, we consider different shapes for the target dark halo, making M2M models with two different target profiles. The Einasto density profile (Einasto 1965) that has a cored profile, parametrise here as:

$$\rho_{\text{DM}}^{\text{EIN}}(m) = \rho_{\text{E}} \exp \left\{ - \left(\frac{2}{\alpha} \right) \left[\left(\frac{m}{m_{\text{E}}} \right)^{\alpha} - 1 \right] \right\} \quad (3.22)$$

where $m = \sqrt{x^2 + y^2 + (z/q)^2}$ is the elliptical radius for a flattening q , m_{E} is the scale length, ρ_{E} is the central density and α is the steepness of the profile. The Navarro-Frenk-White (NFW) dark matter mass density profile, which has a cusped profile (Navarro et al. 1996), parametrised here as

$$\rho_{\text{DM}}^{\text{NFW}}(m) = \frac{\rho_{\text{N}}}{(m/m_{\text{N}}) \left[1 + (m/m_{\text{N}})^2 \right]} \quad (3.23)$$

where ρ_{N} is the central density and m_{N} is the scale length.

The parameters of these target analytical profiles are determined during each M2M run similarly to Portail et al. (2017a), by fitting the dark matter halo profile together with the current stellar mass distribution to match: i) the dark matter mass enclosed within an ellipsoidal volume of the major axis of the bulge ($r^{\text{BP}} = m^{\text{BP}} = 3.2$ kpc) is fixed to the chosen value M_{DM}^{B} , with $M_{\text{DM}}^{\text{B}} = \int dV \rho_{\text{DM}}$ (or $M_{\text{DM}}^{\text{B(p)}}$ from the particles); and ii) that the total circular velocity of the model matches well the disc HI rotation curve data (Corbelli et al. 2010) described in Section 3.2.4.1.

To adjust the particle dark matter distribution to the target analytical dark matter profile we also use the M2M method (De Lorenzi et al. 2007). This is done by expanding the initial dark matter density distribution of the particles and the target analytical dark matter density profile in spherical harmonics, which are then fitted with the M2M scheme. The adaptation of the dark matter particles is performed while the photometric and the stellar kinematic observations are also being fitted.

A change in the dark matter mass profile may significantly change the total circular velocity, particularly in the disc region, affecting the orbits of the particles. This is not desirable for particles in the disc that should remain on near-circular or epicyclic orbits. To alleviate this we measure the circular velocity for a particle before and after the potential update, and then re-scale the velocity of the particle living in the old potential ϕ_{old} to a new velocity given by the new potential ϕ_{new} by multiplying its velocity by the factor $f_{V_{\text{c},i}}$ that is the ratio between the new and the old circular velocities:

$$f_{V_{\text{c},i}} = \sqrt{\vec{A}_i \cdot \vec{\nabla}_{A_i} \phi_{\text{new}} / \vec{A}_i \cdot \vec{\nabla}_{A_i} \phi_{\text{old}}} \quad (3.24)$$

using the spherical radius vector $\vec{A}_i = \vec{r}_i$ for the dark matter and classical bulge particles that have a spheroidal geometric distribution, and the cylindrical radius $\vec{A}_i = \vec{R}_i$ for the disc particles.

3.2.4.1 Kinematics III: HI rotation curve

We use the de-projected azimuthally averaged HI rotation velocity curve estimated by Corbelli et al. (2010) to fit the total circular velocity of our M2M models modifying the dark matter

profile for a given $\Upsilon_{3,6}$ (see section 3.2.4). This data extend from 8.5 kpc out to 50 kpc. We fit the rotation curve out to 20 kpc, for two reasons: i) the contribution of the mass of the HI disc to the circular velocity beyond this radius becomes as important as the stellar disc (Chemin et al. 2009), and ii) the outer disc shows a warp ($R > 27$ kpc) (Newton & Emerson 1977; Henderson 1979; Brinks, E.; Burton 1984; Chemin et al. 2009), changing the inclination with respect to the inner part of the stellar disc that is $\sim 77^\circ$, similar to the inclination of the stellar disc derived by Courteau et al. (2011). This region includes then the 10 kpc-ring and the 15 kpc ring structures Gordon et al. (2006); Barmby et al. (2006).

3.2.5 Bar pattern speed adjustment (Ω_p)

The pattern speed of the bar of the model found in B17 is $\Omega_p = 38 \text{ km s}^{-1} \text{ kpc}^{-1}$. As we want to find constraints for this quantity, we also explore different values (see Section 3.2.8). To change the initial pattern speed, we adiabatically and linearly change its initial value to the desired final value with a certain frequency defined in Section 3.2.7 (see Martinez-Valpuesta 2012; Portail et al. 2017a). The pattern speed change is performed while the kinematic and the photometric observables are fitted and while the potential is frequently recalculated from the new density distribution, resulting at the end of the M2M fit in a self-consistent dynamical system.

3.2.6 Potential solver and orbital integration

As in Portail et al. (2017a), the NMAGIC modelling here uses the hybrid particle-mesh code from Sellwood et al. (2003) to calculate the potential from the particle mass distribution. The potential solver uses a cylindrical mesh Fourier method to calculate the potential for the disc and the bulge components (Sellwood & Valluri 1997). Due to the disc geometry and our interest in resolving the vertical and the in plane distribution, instead of using a spherical softening, we use an oblate softening with 67 pc in the plane and 17 pc in the vertical direction. The potential of the particles of the dark matter component is calculated using a spherical mesh with a spherical harmonics potential solver that extends to 42 kpc and includes terms up to the 16th order (De Lorenzi et al. 2007). The cylindrical mesh extends in the disc plane out to $R=10$ kpc and $z \pm 3$ kpc in the vertical direction, and any stellar mass particle that extends beyond the limits of this mesh is considered during the run in the spherical mesh for the calculation of the potential.

The orbits of the particles are integrated forward in time with an adaptive leap-frog algorithm using the acceleration due to the gravitational potential of all the particles. Given that the bar is rotating, in the NMAGIC M2M implementation the bar is kept fix in the reference frame of the potential by rotating the phase-space coordinates of all the particles around the z -axis at the same rate of the pattern speed of the bar, but opposite in sign (Martinez-Valpuesta 2012; Portail et al. 2015a) (note that the rotated system is still in an inertial frame).

The integration time is measured in iteration units [it], with a time step of [it]=0.23 Myr (see B17). We require that the orbits always have at least 1000 [it], otherwise the orbit is split in smaller time steps.

3.2.7 M2M fitting procedure and parameters

Each M2M fitting done here with NMAGIC takes a total number of iterations of $T_{\text{tot}}=80000$ [it], where each fit is divided in three main phases. The first phase uses $T_{\text{obs}}=5000$ [it], and is when the temporal smoothed measurements of the model observables are made. The temporal smoothing scale is $\tau_s=1600$ [it], and it is chosen to be larger than the period (T_{orbit}) of a circular orbit at 5 kpc with circular velocity V_c , which typically is ~ 1000 [it], *i.e.* $\tau_s=T_{\text{orbit}}/\Delta t_{\text{step}}=2\pi/(V_c \Delta t_{\text{step}})$.

The second phase is when the M2M fitting is performed, and it takes $T_{\text{M2M}}=50000$ [it]. The bar pattern speed is adjusted during this phase, starting at $T_{\text{i}}^{\text{ps}}=10000$ [it] and finishing at $T_{\text{f}}^{\text{ps}}=40000$ [it], with an update of the new value every $T_{\text{up}}^{\text{ps}}=3000$ [it]. During the second phase the total mass of the system may change. Therefore, we recalculate and update the potential from the new mass density distribution every $T_{\text{pot}}=6400$ [it]. These regular potential updates are important to build a system that is gravitationally self-consistent with its density.

The final phase is the stability check that takes $T_{\text{stab}}=25000$ [it], where the M2M fitting stops and the model is only observed. During this phase we recover the values of σ , ν , $h3$ and $h4$ for the model according to equation 3.21 correcting them every $\tau_{\text{corr}}=3 \times \tau_s$.

The FOC parameters ϵ , λ_k and μ of equation 3.7 are chosen sequentially. We first fit only the photometry, leaving the parameters $\lambda_{1\dots 5}$ and μ fixed to zero and varying only ϵ (the parameter $\lambda_{k=0}$, or λ_{phot} , normalises ϵ and for simplicity is set to $\lambda_{\text{phot}}=1$). We measure the reduced chi-square (terms χ^2_j in equation 3.5), for the photometry ($k=0$) in the bulge region finding the relation between χ_n^2 and ϵ shown in Fig.3.1 in the top panel. For too small ϵ the photometry does not have the power to change the model and so the χ_n^2 is large. For too large ϵ the photometry has too much power, changing the particle weights to fit only the local observable (or pixel) that the particle is crossing. And ideal ϵ value allows the weight to change an averaged amount once it crosses all the observables that are along the particle's orbit, converging then its weights to a constant value. We find this optimum value at the minimum χ_n^2 , when $\epsilon=7.0 \times 10^{-9}$.

Secondarily, we find the best λ_k for the IFU kinematic observables (where $k=1 \dots 4$) defined also as λ_{kin} . We use the previous best ϵ and we fit the photometry as well as the IFU kinematics for several values of λ_{kin} . Again, we measure the photometric reduced chi-square in the bulge region, and also the kinematic reduced chi-square in this region, obtaining the relations versus λ_{kin} shown in Fig.3.1 (second panel). The photometric χ_n^2 has smaller values for small λ_{kin} , and it would be the smallest for $\lambda_{\text{kin}}=0$, because the orbits of the model have mostly the constraint of the photometry. As λ_{kin} increases, the kinematic observations have more power tailoring the model towards fitting the kinematics as well, as we see the kinematic χ_n^2 decreasing for larger λ_{kin} , which worsen the photometric χ_n^2 if the kinematics get too much power. Similarly to ϵ if λ_{kin} increases too much, both the photometric and the kinematic χ_n^2 get worse. We find an optimal value of $\lambda_k=2.5 \times 10^{-1}$ for the minimum kinematic χ_n^2 while the photometric χ_n^2 is still small.

To find the best parameter λ_{halo} for the dark matter halo fitting, we fix the previously found parameters ϵ and λ_{kin} and test different values of λ_{halo} versus the reduced chi-square of the dark matter halo density (Figure 3.1 third panel). We find the minimum χ_n^2 at $\lambda_6=10^4$, where we also show that the photometric and the kinematic χ_n^2 remain unchanged.

The entropy magnitude term is $\mu=5 \times 10^3$ (Figure 3.1 bottom panel) that is determine in the same way, fixing the previous parameters and choosing the largest μ that still has small χ^2 values

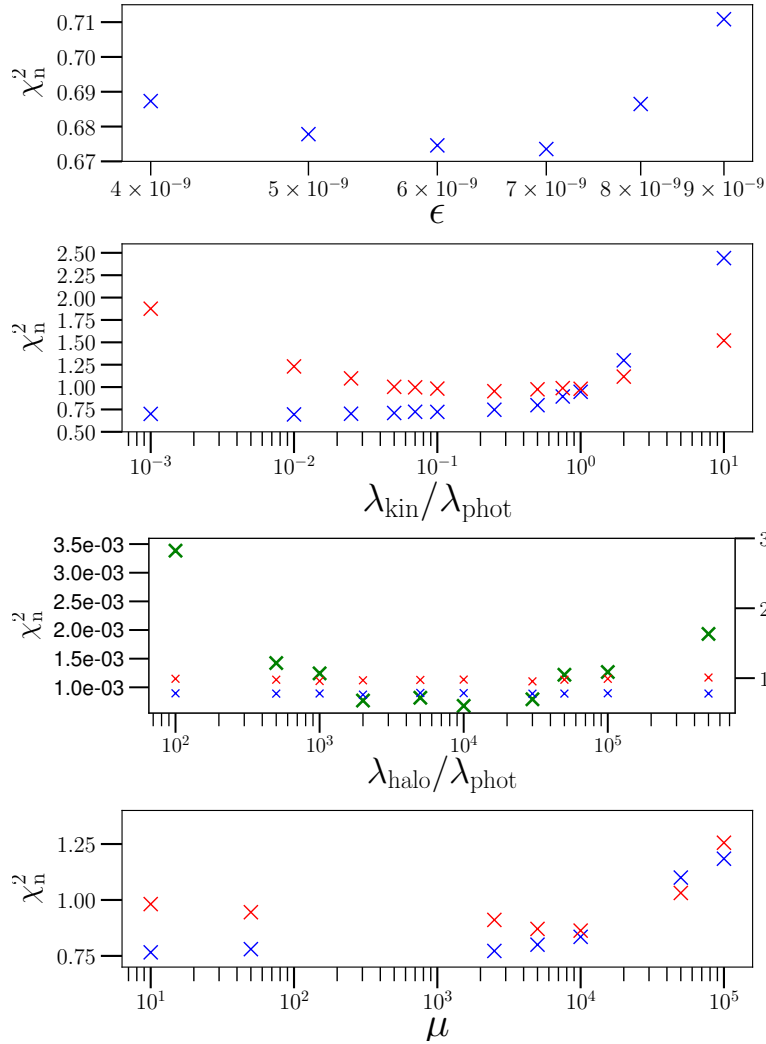


Figure 3.1: Parameters for the FOC equation. Top panel: photometric χ_n^2 values versus ϵ (blue crosses). Second panel: χ_n^2 versus $\lambda_{\text{kin}}/\lambda_{\text{phot}}$ (for $\lambda_{\text{phot}}=1$) for the photometry (blue crosses) and the kinematics (red crosses). Third panel: χ_n^2 versus $\lambda_{\text{kin}}/\lambda_{\text{phot}}$ (also where $\lambda_{\text{phot}}=1$) for the dark matter density (green crosses). We also show the χ_n^2 for the photometry (blue crosses) and the kinematics (red crosses) where the χ_n^2 values are in reference to the right Y-axis numbers. Bottom panel: χ_n^2 versus μ for the photometry (blue crosses) and the kinematics (red crosses).

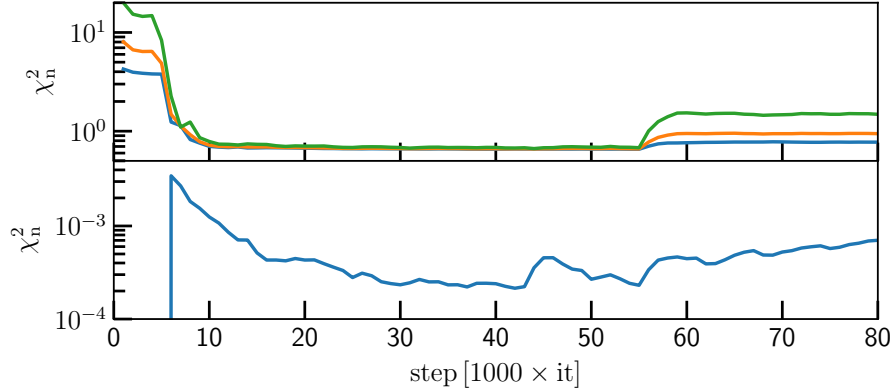


Figure 3.2: Reduced chi-square values as function of time for the M2M fitting of one model as defined in the main text. Top panel: photometry (blue), kinematics (green) and total (yellow) Bottom panel: dark matter halo density.

for the photometry and the kinematics.

After setting the fitting parameters, we run M2M fits showing an example in Figure 3.2, where the reduced chi-squares of the model observables from equation 3.5 are plotted versus time (iterations). In the phase T_{obs} the model temporal smoothed observables are calculated decreasing χ_n^2 at first and then staying constant. Then the fitting phase T_{M2M} starts where χ_n^2 of the photometry, kinematics and the dark matter halo decrease in time. Finally in the stability check phase T_{stab} the values of χ_n^2 increase slightly.

3.2.8 Method to find the best model in the parameter space

B17 finds constraints for the mass ratio between the classical bulge and the B/P bulge while the dark matter distribution and the bar pattern speed are not constrain. Here, we use stellar kinematic and photometric observations as targets to constrain these properties. While the M2M method has the power to change the orbital structure, changing then the model v_{los} , σ_{los} , $h3$, $h4$ and L to match the observations, there are macroscopic parameters that limit the orbital phase space region and therefore a particular fit will have model values as good as these macroscopic parameters allow them to be. Here we have three important dynamical quantities that are inputs to the M2M modelling and that impact the effective potential: the pattern speed of the bar Ω_p , the stellar mass-to-light ratio of the bulge in the $3.6\mu\text{m}$ band $\Upsilon_{3.6}$ which, for a well fitted target observed luminosity, determines the total stellar mass in the bulge M_{\star}^{B} , and the amount of dark matter in the bulge region M_{DM}^{B} . Therefore, we need to apply a method of meta-optimization where each M2M run is an optimisation itself that explores and finds the orbital phase space distribution that best matches the observations for the given potential parameters. Then we manually explore Ω_p , $\Upsilon_{3.6}$, M_{DM}^{B} to find the values that best reproduce all sets of observations. To explore these three global parameters we create one cube of parameters for the Einasto dark matter profile, and a

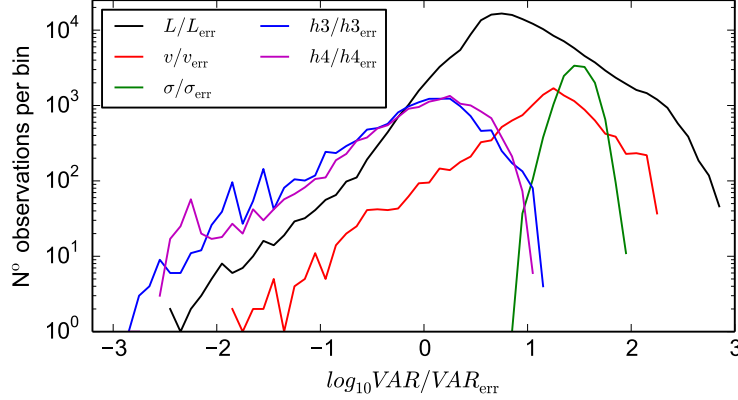


Figure 3.3: Inverse relative errors of the photometric and the kinematic observations. The minimum and maximum errors are: $10^{2.76}$ and $10^{8.05} L_{\odot}$ for the photometry, 0.1 and 15.5 km s^{-1} for the velocity, 1.1 and 15.6 km s^{-1} for the dispersion, 0.6×10^{-3} and 0.7×10^{-1} for $h3$ and 0.7×10^{-3} and 0.6×10^{-1} for $h4$. The median errors are $10^{4.67} L_{\odot}$ for the photometry, 3.6 km s^{-1} for the velocity, 3.8 km s^{-1} for the dispersion, and 0.02 for $h3$ and $h4$.

second cube for the NFW dark matter halo profile, where each model \vec{M} has the coordinates:

$$\vec{M} = (\Upsilon_{3.6}, M_{\text{DM}}^{\text{B}}, \Omega_{\text{p}}) \quad (3.25)$$

For the Einasto cube we explore $\Upsilon_{3.6}$ in the range of 0.5 – $0.85 M_{\odot} L_{\odot}^{-1}$ in steps of $\Delta\Upsilon_{3.6} = 0.05 M_{\odot} L_{\odot}^{-1}$, and including more values between 0.68 – $0.8 M_{\odot} L_{\odot}^{-1}$ in steps of $\Delta\Upsilon_{3.6} = 0.02 M_{\odot} L_{\odot}^{-1}$. For the M_{DM}^{B} we explore 0.6 – $2.4 \times 10^{10} M_{\odot}$ in steps of $\Delta M_{\text{DM}} = 0.2 \times 10^{10} M_{\odot}$. For Ω_{p} we explore the range 20 – $55 \text{ km s}^{-1} \text{ kpc}^{-1}$ in steps of $\Delta\Omega_{\text{p}} = 5 \text{ km s}^{-1} \text{ kpc}^{-1}$, having then a cube of parameters with sizes $13(\Upsilon_{3.6}) \times 10(M_{\text{DM}}^{\text{B}}) \times 8(\Omega_{\text{p}})$, building thus a total of 1040 M2M models with the Einasto dark matter profile.

For the NFW cube we explore $\Upsilon_{3.6}$ in the range 0.62 – $0.8 M_{\odot} L_{\odot}^{-1}$ in steps of $\Delta\Upsilon_{3.6} = 0.02 M_{\odot} L_{\odot}^{-1}$. For M_{DM}^{B} we explore 0.6 – $1.8 \times 10^{10} M_{\odot}$ in steps of $\Delta M_{\text{DM}} = 0.2 \times 10^{10} M_{\odot}$. For Ω_{p} we explore 25 – $50 \text{ km s}^{-1} \text{ kpc}^{-1}$ in steps of $\Delta\Omega_{\text{p}} = 5 \text{ km s}^{-1} \text{ kpc}^{-1}$, having then a cube of parameters with sizes $10(\Upsilon_{3.6}) \times 7(M_{\text{DM}}^{\text{B}}) \times 6(\Omega_{\text{p}})$, having then a total of 420 M2M models for the NFW cube.

Dark matter haloes are expected to be flattened in the central part of disc galaxies due to the influence of the disc gravitational potential. [Widrow et al. \(2003\)](#); [Widrow & Dubinski \(2005\)](#) explored different flattening values for the dark halo of M31, finding reasonable fits between $q \simeq 0.8$ and 1.0 . Here we use a dark halo flattening of $q=0.85$ as our fiducial value for both dark matter density profiles, but we test the effects of different values on the final results, exploring $q=0.7$ and $q=1.0$, finding a similar stellar mass distribution for the disc and the central region of the classical bulge, which we discuss further in section 3.3.1.3.

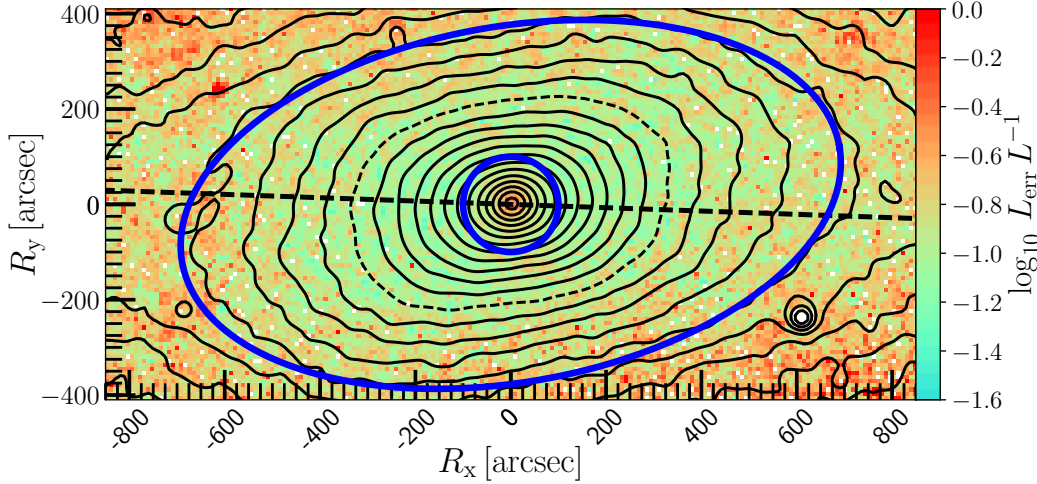


Figure 3.4: The M31 bulge surface luminosity relative error map. We define the region of the classical bulge (RCB) is within the blue circle, and the region of the B/P bulge (RBP) is between the circle and the ellipse, and everything within the ellipse comprehend then the bulge region (RB). The surface-brightness isophotes in the $3.6\ \mu\text{m}$ band are shown spaced with $\Delta\mu_{3.6}=0.25\ [\text{mag arcsec}^{-2}]$. The value $\mu_{3.6}=16\ [\text{mag arcsec}^{-2}]$ is shown with a dashed isophote and the disc major axis at $\text{PA}=38^\circ$ (dash line). In white colour are the masked hot pixels and foreground stars.

3.2.8.1 Building a metric for the comparisons with the observational data: five chi-square subsets

In total, the photometric and the kinematic observations give 224251 data values (photometric and kinematic pixels) and an equal number of χ^2 values. However, these χ^2 values can be substantially different: (i) the typical errors can be different between different variables, like for example the errors of σ_{los} and $h3$, as shown in Figure 3.3, which can lead to different ranges of χ^2 values for each variable. And (ii), for the same variable the errors depend on the spatial regions that we consider, showing for example smaller photometric relative errors in the central part of the bulge than in its outer part, or the disc region, as shown in Figure 3.4.

In consequence, combining linearly the χ^2 values in one total χ^2_{tot} and finding the M2M model in the cube of parameters that has the minimum total reduced chi-square may lead to a model that has a good fit of the B/P bulge region, but an unsatisfactory fit of the smaller central region where the classical bulge is. Also, each observational variable contains different signatures in different locations that are connected with specific physical properties of the system that may be ignored if the chi-square values are combined into a total chi-square.

Therefore, we proceed to define chi-square values for the variables L , ν_{los} , σ_{los} , building five subsets of reduced chi-squares motivated by the properties of the system that we are modelling, which is built with three main substructures that we want to fit *simultaneously* well *i.e.* the classical bulge, the B/P bulge and the disc. Each bulge substructure dominates in different geographi-

cal regions of M31 (Beaton et al. 2007) and (B17): the classical bulge dominates the central light of the M31 bulge, within $R \lesssim 100$ arcsec (380 pc) where we define the region of the classical bulge (RCB) (see Figure 3.4). Further out is the region of the B/P bulge (RBP) where this component dominates in light within ellipses with a semi-major axis of $100 \text{ arcsec} < R_{\text{mj}} < 700 \text{ arcsec}$. The combined regions RCB and RBP enclose then the bulge region (RB). Further out dominates the disc.

We define the five subsets of reduced chi-squares as follows:

- Classical bulge central photometry ($\chi^2_{\mu}^{\text{RCB}}$ or subset 1): we measure the reduced chi-square of the photometry ($L_{3.6\mu\text{m}}$) in the centre of the region RCB, *i.e.* the centre of M31's bulge within a diameter of 40 arcsec (150 pc) that corresponds to approximately one tenth of the M31 bulge Sersic effective radius $R_e/10$. With this we search models from the grid that match the cuspy light profile in the centre of M31's bulge, which reaches a surface-brightness of $\mu_{3.6} \leq 13 \text{ mag arcsec}^{-2}$.
- Classical bulge central dispersion ($\chi^2_{\sigma}^{\text{RCB}}$ or subset 2): the M31 dispersion profile shows two peaks of $\sigma_{\text{los}} \sim 170 \text{ km s}^{-1}$ at $R \sim 50$ arcsec, however in the centre the dispersion drops to $\sigma_{\text{los}} \sim 150 \text{ km s}^{-1}$ (Saglia et al. 2010; Opitsch et al. 2018). Therefore, we also measure the reduced chi-square of the velocity dispersion σ_{los} in the centre within $R_e/10$, to find models of the grid that reproduce this feature.
- B/P bulge photometry ($\chi^2_{\mu}^{\text{RBP}}$ or subset 3): we measure the reduced chi-square of the photometry in the region of the B/P bulge (region RBP delimited in Figure 3.4).
- B/P bulge dispersion ($\chi^2_{\sigma}^{\text{RBP}}$ or subset 4): B17 show that the B/P bulge and the classical bulge of M31 have different kinematic properties. Hence, we calculate the reduced chi-square of the dispersion only in the B/P bulge region RBP. This allows us also to find the dynamical mass within the bulge.
- B/P bulge velocity ($\chi^2_v^{\text{RBP}}$ or subset 5): as shown by Tremaine & Weinberg (1984) the bar pattern speed in disc galaxies can be determined directly from the line-of-sight velocity (v_{los}) and the photometry using the continuity equation. However, the disc inclination and the bar orientation of M31 makes difficult to apply this directly. Therefore, we determine the bar pattern speed indirectly calculating the reduced chi-square of the line-of-sight velocity v_{los} in the bar region RBP, to find the models in the grid that better match this variable.

At the end of the process each model \vec{M} has five additional coordinates with the reduced chi-square parameters $\vec{M}(\Upsilon_{3.6}, M_{\text{DM}}^{\text{B}}, \Omega_p, \vec{\chi}^2)$ where:

$$\vec{\chi}^2 = (\chi^2_{\mu}^{\text{RCB}}, \chi^2_{\sigma}^{\text{RCB}}, \chi^2_{\mu}^{\text{RBP}}, \chi^2_{\sigma}^{\text{RBP}}, \chi^2_v^{\text{RBP}}) \quad (3.26)$$

While the observations in the disc region are fitted in each of the M2M models as well as the Gauss-Hermite coefficients $h3$ and $h4$, we do not include subsets for them in the best model selection; later we show that the best models selected by the five subsets defined above satisfactory reproduce these observations as well.

Table 3.1: Main parameters of the range of acceptable models for the Einasto dark matter profile $\vec{M}_{\text{NBM}}^{\text{EIN}}$. The overall best matching model is Model JR804.

Model	$\Upsilon_{3.6}$	M_{DM}^{B}	Ω_{p}	M_{\star}^{CB}	M_{\star}^{BP}	M_{\star}^{B}	$M_{\text{DM}}^{\text{B(p)}}$	$M_{\text{dyn}}^{\text{B}}$	$\Delta\hat{\chi}_{\mu}^{\text{2RCB}}$	$\Delta\hat{\chi}_{\sigma}^{\text{2RCB}}$	$\Delta\hat{\chi}_{\nu}^{\text{2RBP}}$	$\Delta\hat{\chi}_{\mu}^{\text{2RBP}}$	$\Delta\hat{\chi}_{\sigma}^{\text{2RBP}}$	$\hat{\chi}_{\text{sum}}^2$	$\Delta\hat{\chi}_{\text{sum}}^2$
JR804	0.72	1.2	40	1.18	1.91	3.09	1.16	4.25	0.57	1.27	0.43	1.04	0.61	3.92	0.00
JR803	0.72	1.0	40	1.19	1.89	3.08	0.97	4.05	0.28	1.53	0.98	1.12	0.66	4.58	0.65
JR813	0.74	1.0	40	1.22	1.97	3.19	0.99	4.18	1.67	0.72	0.88	1.31	0.18	4.77	0.84
JR764	0.72	1.2	35	1.15	1.93	3.08	1.18	4.26	0.41	1.17	1.16	0.67	1.68	5.10	1.18
JR763	0.72	1.0	35	1.16	1.91	3.07	0.98	4.05	0.21	0.98	2.24	0.89	1.07	5.39	1.46
JR365	0.70	1.4	40	1.13	1.85	2.98	1.35	4.33	0.26	2.81	0.15	1.08	1.24	5.54	1.61
JR285	0.70	1.4	35	1.11	1.86	2.97	1.38	4.35	0.14	2.32	0.52	0.40	2.31	5.68	1.75
JR812	0.74	0.8	40	1.23	1.95	3.18	0.78	3.96	1.20	0.37	2.07	1.50	0.82	5.95	2.03
JR853	0.74	1.0	45	1.24	1.95	3.19	0.99	4.18	1.58	0.44	0.94	2.64	0.51	6.12	2.19
JR844	0.72	1.2	45	1.20	1.90	3.10	1.18	4.28	0.54	1.39	0.85	2.72	0.77	6.26	2.34
JR284	0.70	1.2	35	1.12	1.85	2.97	1.18	4.15	0.47	2.59	1.23	0.35	1.68	6.32	2.40
B.V.	0.72	1.2	40.0	1.18	1.91	3.09	1.16	4.25							
Δ^+	+0.02 -0.02	+0.2 -0.4	+5.0 -5.0	+0.06 -0.07	+0.06 -0.06	+0.10 -0.12	+0.22 -0.38	+0.10 -0.29							

Notes: M_{\star}^{CB} , M_{\star}^{BP} , M_{DM}^{B} , $M_{\text{DM}}^{\text{B(p)}}$ and $M_{\text{dyn}}^{\text{B}}$ in units of $10^{10} M_{\odot}$. Parameters Ω_{p} and $\Upsilon_{3.6}$ are in units of $\text{km s}^{-1} \text{kpc}^{-1}$ and $M_{\odot} L_{\odot}^{-1}$ respectively.

Table 3.2: Main parameters of the range of acceptable models for the NFW dark matter profile $\vec{M}_{\text{NBM}}^{\text{NFW}}$. The overall best matching model is Model KR241.

Model	$\Upsilon_{3.6}$	M_{DM}^{B}	Ω_{p}	M_{\star}^{CB}	M_{\star}^{BP}	M_{\star}^{B}	$M_{\text{DM}}^{\text{B(p)}}$	$M_{\text{dyn}}^{\text{B}}$	$\Delta\hat{\chi}_{\mu}^{\text{2RCB}}$	$\Delta\hat{\chi}_{\sigma}^{\text{2RCB}}$	$\Delta\hat{\chi}_{\nu}^{\text{2RBP}}$	$\Delta\hat{\chi}_{\mu}^{\text{2RBP}}$	$\Delta\hat{\chi}_{\sigma}^{\text{2RBP}}$	$\hat{\chi}_{\text{sum}}^2$	$\Delta\hat{\chi}_{\text{sum}}^2$
KR241	0.70	1.0	40	1.16	1.82	2.98	0.97	3.95	0.51	1.64	1.76	1.10	1.61	6.61	0.00
KR248	0.72	1.0	40	1.18	1.90	3.08	0.98	4.06	0.80	3.27	1.66	1.16	0.75	7.64	1.03
KR235	0.68	1.2	40	1.12	1.77	2.89	1.17	4.06	1.62	2.97	1.00	0.88	1.45	7.93	1.32
KR171	0.70	1.0	35	1.13	1.85	2.98	0.98	3.96	0.31	1.26	3.87	1.13	1.45	8.03	1.41
KR165	0.68	1.2	35	1.09	1.79	2.88	1.18	4.06	1.19	2.67	2.34	0.56	1.32	8.08	1.47
KR247	0.72	0.8	40	1.20	1.88	3.08	0.78	3.86	0.27	1.35	3.43	1.85	1.99	8.89	2.28
KR242	0.70	1.2	40	1.15	1.84	2.99	1.17	4.16	0.30	6.47	0.83	0.92	0.62	9.14	2.53
KR159	0.66	1.4	35	1.06	1.74	2.80	1.37	4.17	3.34	2.84	1.31	0.20	1.52	9.21	2.60
B.V.	0.70	1.0	40.0	1.16	1.82	2.98	0.97	3.95							
Δ^+	+0.02 -0.04	+0.4 -0.2	+0.0 -5.0	+0.04 -0.10	+0.08 -0.08	+0.10 -0.18	+0.40 -0.19	+0.22 -0.09							

Notes: M_{\star}^{B} , M_{\star}^{CB} , M_{\star}^{BP} , M_{DM}^{B} , $M_{\text{DM}}^{\text{B(p)}}$ and $M_{\text{dyn}}^{\text{B}}$ in units of $10^{10} M_{\odot}$. Parameters Ω_{p} and $\Upsilon_{3.6}$ are in units of $\text{km s}^{-1} \text{kpc}^{-1}$ and $M_{\odot} L_{\odot}^{-1}$ respectively.

3.2.8.2 Selection procedure of the best-matching models

Each of the five subsets defines a volume in the space of the parameters $\Upsilon_{3.6}$, M_{DM}^{B} and Ω_{p} , where it is possible to find a minimum. However, we find that the values of these subsets have stochastic local variations on top of the global variations of the chi-square values, similarly as Morganti et al. (2013) in the two dimensional parametric chi-square analysis of their M2M models. The stochasticity in the M2M modelling dominates the statistical uncertainty, which is not unexpected given the large amount of high quality data fitted.

In order to better determine the global χ^2 minimum in each subset we smooth the chi-square values by averaging each model's reduced chi-square with their $3 \times 3 \times 3 - 1 = 26$ neighbouring models (including the diagonal values), obtaining new smoothed values of χ^2 for each model (see also Gebhardt et al. 2003). We tested averaging with the $3 \times 2 = 6$ neighbouring models finding similar chi-square volumes and the same range of models. Then we find the minimum smoothed

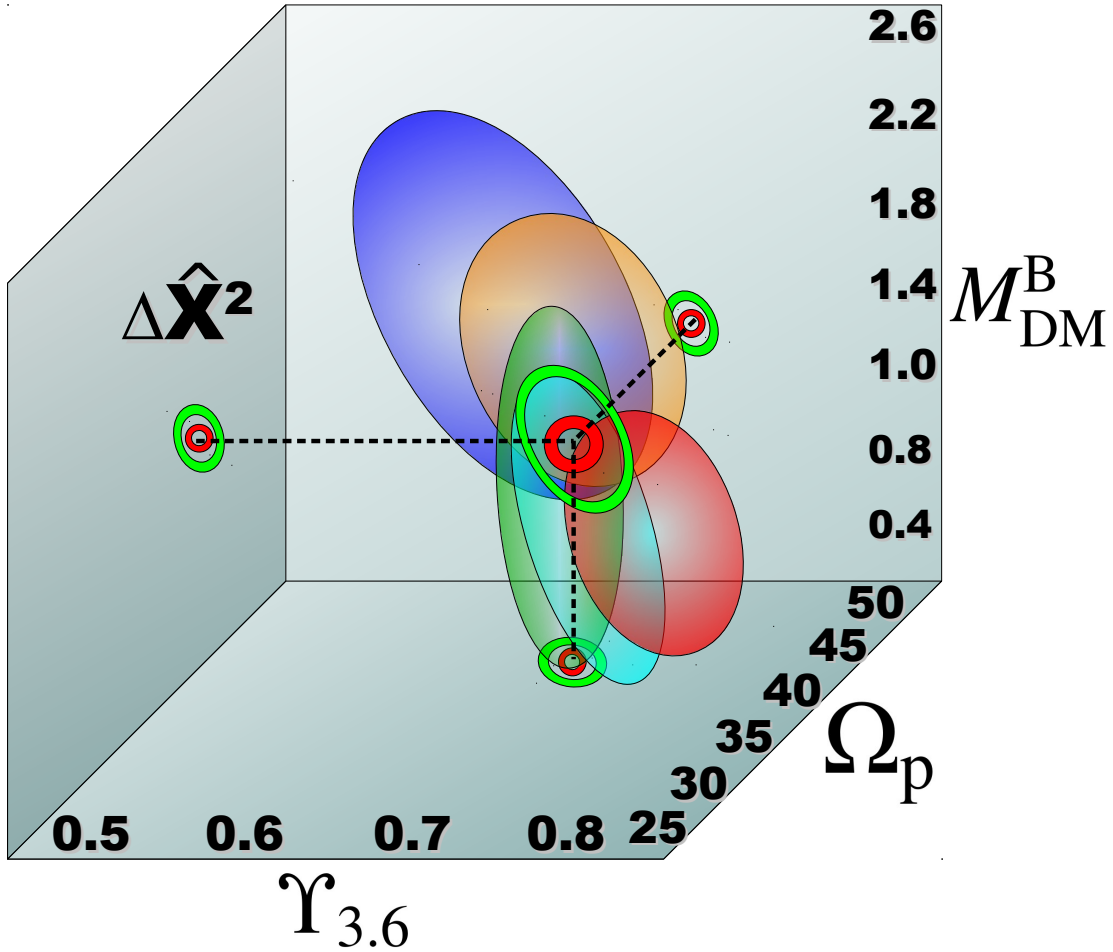


Figure 3.5: Representation of the five chi-square subset volumes in the parameter space of $\Upsilon_{3.6}$, M_{DM}^B and Ω_p . While the models have chi-square values in the whole cube, the coloured ellipses represent volumes where the chi-square values have the lowest values, showing $\Delta\hat{\chi}_\mu^{2\text{RCB}}$ (green), $\Delta\hat{\chi}_\sigma^{2\text{RCB}}$ (blue), $\Delta\hat{\chi}_\mu^{2\text{RBP}}$ (blue), $\Delta\hat{\chi}_\sigma^{2\text{RBP}}$ (red) and $\Delta\hat{\chi}_\nu^{2\text{RBP}}$ (orange). The place where all ellipses intersect is where is located the overall best model \vec{M}_{BM} (red circle). We also show the range of the acceptable models $\vec{M}(\Delta)$ (green ring). The projections of the best model on each of the planes of the parameters are signed with the dashed lines.

chi-square value (χ_{\min}^2) in each of the subsets (which do not necessarily correspond to the same model \vec{M}), obtaining:

$$\vec{\chi}_{\min}^2 = \left(\chi_{\mu \min}^2 \text{RCB}, \chi_{\sigma \min}^2 \text{RCB}, \chi_{\mu \min}^2 \text{RBP}, \chi_{\sigma \min}^2 \text{RBP}, \chi_{\nu \min}^2 \text{RBP} \right) \quad (3.27)$$

where we find the minimum reduced chi-square values in each of the five subsets of the Einasto grid: $\chi_{\mu \min}^2 \text{RCB} = 0.195$, $\chi_{\sigma \min}^2 \text{RCB} = 0.267$, $\chi_{\nu \min}^2 \text{RBP} = 3.544$, $\chi_{\mu \min}^2 \text{RBP} = 0.774$ and $\chi_{\sigma \min}^2 \text{RBP} = 2.717$.

Due to the stochasticity in the original chi-square values there are several models that have values near the minimum in each subset. We quantify the errors introduced by this stochasticity calculating the standard deviation (s) of the original chi-square values of the models neighbouring the model with the minimum smoothed χ^2 that is not in the border of the grid, obtaining for each of the five subsets:

$$\vec{s}(\vec{\chi}_{\min}^2) = \left(s_{\mu}^{\text{RCB}}, s_{\sigma}^{\text{RCB}}, s_{\mu}^{\text{RBP}}, s_{\sigma}^{\text{RBP}}, s_{\nu}^{\text{RBP}} \right) \quad (3.28)$$

finding the values: $s_{\mu}^{\text{RCB}} = 0.062$, $s_{\sigma}^{\text{RCB}} = 0.155$, $s_{\nu}^{\text{RBP}} = 0.370$, $s_{\mu}^{\text{RBP}} = 0.040$ and $s_{\sigma}^{\text{RBP}} = 0.097$. We normalise then each of the subsets by the corresponding standard deviation, subtracting also the respective minimum to obtain normalised reduced delta chi-square values of similar magnitude which allows to compare between different subsets:

$$\Delta \hat{\chi}^2(\text{subset}) = \left(\chi_n^2(\text{subset}) - \chi_{n \min}^2(\text{subset}) \right) / s(\text{subset}) \quad (3.29)$$

obtaining for each model then the coordinates $\vec{M}(\Upsilon_{3.6}, M_{\text{DM}}^{\text{B}}, \Omega_{\text{p}}, \vec{\Delta} \hat{\chi}^2)$ where:

$$\vec{\Delta} \hat{\chi}^2 = \left(\Delta \hat{\chi}_{\mu}^2 \text{RCB}, \Delta \hat{\chi}_{\sigma}^2 \text{RCB}, \Delta \hat{\chi}_{\mu}^2 \text{RBP}, \Delta \hat{\chi}_{\sigma}^2 \text{RBP}, \Delta \hat{\chi}_{\nu}^2 \text{RBP} \right) \quad (3.30)$$

The range of good models in each independent subset is defined by a volume in the space of $\Upsilon_{3.6}$, M_{DM}^{B} and Ω_{p} , with values $\Delta \hat{\chi}^2(\text{subset}) \lesssim 1$, as represented in the diagram in Figure 3.5. The volume where all subsets intersect with small chi-square values, is where all the subsets have *simultaneously* small deviations from the minimum in each subset, and corresponds to the volume of the parameters $\Upsilon_{3.6}$, M_{DM}^{B} and Ω_{p} where the best matching models are found. We quantify the size of this volume of best models, by summing the reduced chi-square of the five subsets ($N_{\text{sub}}=5$) to calculate a total chi-square $\hat{\chi}_{\text{sum}}^2$ and a total delta chi-square $\Delta \hat{\chi}_{\text{sum}}^2$ for each model:

$$\hat{\chi}_{\text{sum}}^2 = \sum_i^{N_{\text{sub}}} \Delta \hat{\chi}_i^2 \quad (3.31)$$

$$\Delta \hat{\chi}_{\text{sum}}^2 = \left(\hat{\chi}_{\text{sum}}^2 - \hat{\chi}_{\text{sum, min}}^2 \right) \quad (3.32)$$

where $\hat{\chi}_{\text{sum, min}}^2$ is the minimum value of $\hat{\chi}_{\text{sum}}^2$. This defines a new parameter for each model $\vec{M}(\Upsilon_{3.6}, M_{\text{DM}}^{\text{B}}, \Omega_{\text{p}}, \Delta \hat{\chi}_{\text{sum}}^2)$, which ranks the models from the best fitting model for the minimum value $\hat{\chi}_{\text{sum, min}}^2 = 3.92$, up to the worst fitting model of the grid with $\hat{\chi}_{\text{sum}}^2 = 954$. Sorting the models by the variable $\hat{\chi}_{\text{sum}}^2$ results in the Table 3.1 for the Einasto grid, where we show just the range of

acceptable models. The first model (JR804) has the minimum total chi-square and corresponds to the overall best matching model \vec{M}_{BM} , which determines the best values (B.V.) of the parameters $\Upsilon_{3.6}$, M_{DM}^{B} and Ω_{p} . The model \vec{M}_{BM} does not have necessarily the minimum reduced chi-square in each subset, but it has the minimum of the sum of the subsets, making it the best compromise that best match *simultaneously* all the observational subsets (see also [Portail et al. 2017a](#)).

The error range of the parameters $\Upsilon_{3.6}$, M_{DM}^{B} and Ω_{p} are estimated from the maximum and the minimum values from the range of acceptable models \vec{M}_{AM} , which fulfil the selection criteria:

$$\vec{M}_{\text{AM}} = \left\{ \forall \vec{M} \mid \Delta \hat{\chi}_{\text{sum}}^2 \leq \Delta \right\} \quad (3.33)$$

where we choose $\Delta=2.706$, obtaining the range of models of the Table 3.1 that ends up with model JR284 with $\hat{\chi}_{\text{sum}}^2=6.32$ (where the worst fitting model of the grid has $\hat{\chi}_{\text{sum}}^2=954$). While the exact value of this threshold is arbitrary, the inspection of the models listed within this limit satisfactory reproduce the bulge stellar kinematics. We find that the models within $\Delta=1.18$ have a good fit in the individual subsets as well, which show values below 2, and have a similar range of the parameters $\Upsilon_{3.6}$, M_{DM}^{B} and Ω_{p} . For $\Delta=2.706$ no individual subset has a value larger than 3 and the included models increase the range of parameters $\Upsilon_{3.6}$, M_{DM}^{B} and Ω_{p} adding four new values. The range of models that have values between $\Delta \hat{\chi}_{\text{sum}}^2=2.706$ and 4 only add one new value of M_{DM}^{B} while the other models have the same parameter range (in different combinations). However, the individual subset values within this $\Delta \hat{\chi}_{\text{sum}}^2$ get much worse, which is confirmed by inspecting these models. Therefore we choose $\Delta=2.706$ as the fiducial threshold, as within this range the subsets still have simultaneously small values. Moreover, if these chi-square values would follow a chi-square distribution, then a delta of $\Delta \hat{\chi}_{\text{sum}}^2=2.706$ would correspond to the 90 per cent of the distribution.

Furthermore, we also tested a different selection criteria to find the range of acceptable models, by selecting models where each subset has a maximum allowed deviation from the minimum in each subset, finding a similar range of models \vec{M}_{AM} and consequently, a similar error range for the parameters $\Upsilon_{3.6}$, M_{DM}^{B} and Ω_{p} .

We applied the same procedure for the grid of NFW models finding a similar range of parameters $\Upsilon_{3.6}$, M_{DM}^{B} and Ω_{p} . However, the chi-square comparisons of the subset values and $\hat{\chi}_{\text{sum}}^2$ between the Einasto and the NFW models indicate that the Einasto dark matter profile provides generally a better fit to the observations. The NFW grid has similar normalisation values ($\vec{s}(\hat{\chi}_{\text{min}}^2)$), therefore here we normalise them by the Einasto normalisation values to compare and relate both grids with each other. The range of the acceptable models with the NFW dark matter profiles $\vec{M}_{\text{NBM}}^{\text{NFW}}$ are shown in Table 3.2. and the overall best model ($\vec{M}_{\text{BM}}^{\text{NFW}}$) is model KR241.

3.3 Results

The results are organised in two main subsections. In the in first part, section 3.3.1, we present the main results of our parameter space exploration for both model grids. In the second part, in section 3.3.2, we compare the M31 photometric and kinematic maps and profiles with our best matching model.

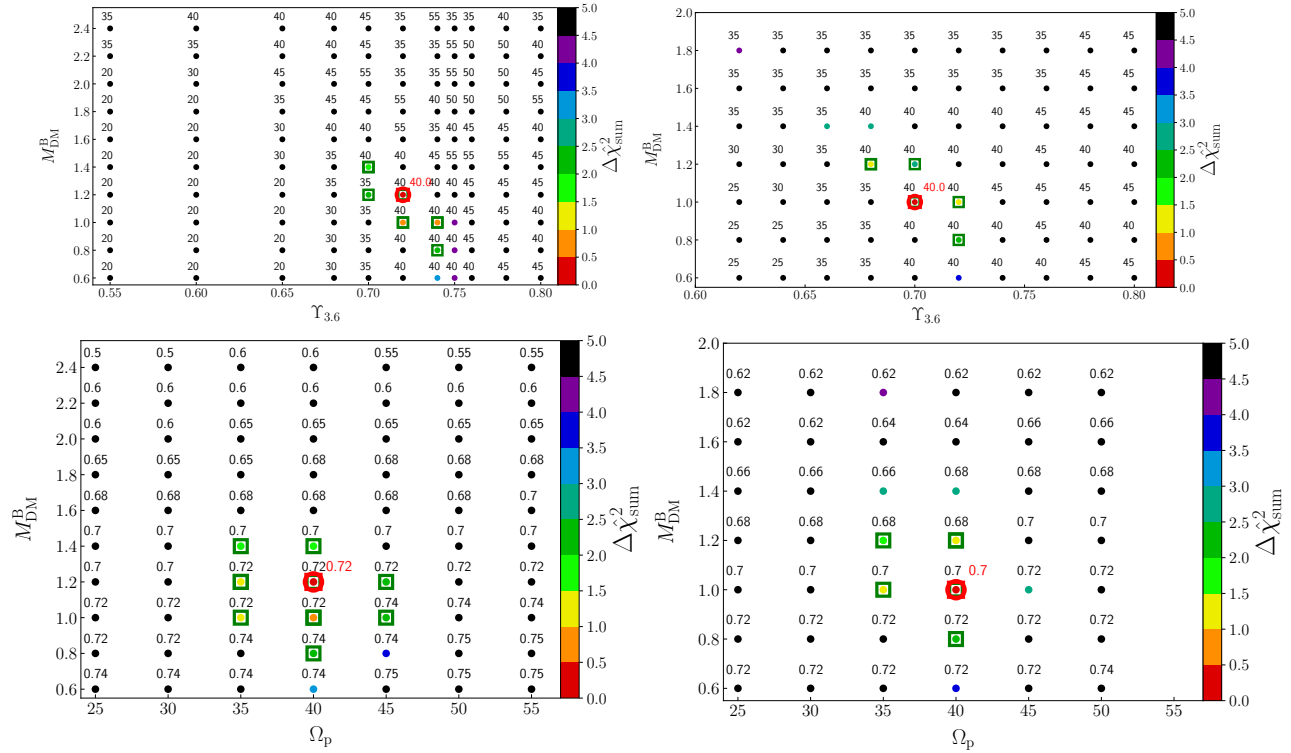


Figure 3.6: Range of acceptable models defined by the variable $\Delta\hat{\chi}_{\text{sum}}^2$, showing the results for the Einasto grid of models (left column), and the NFW halo (right column), as function of projections of the parameters $\Upsilon_{3.6}$ and Ω_p . The green squares mark the range of acceptable models, with the red circles marking the overall best matching model for each grid, model JR804 (right column) and model KR241 (right column). Top panels: $\Delta\hat{\chi}_{\text{sum}}^2$ as function of $\Upsilon_{3.6}$ and M_{DM}^{B} selecting the minimum value along the parameter Ω_p axis. Bottom panels: $\Delta\hat{\chi}_{\text{sum}}^2$ as function of Ω_p and M_{DM}^{B} selecting the minimum value along the parameter $\Upsilon_{3.6}$ axis. In black are values that can also be much larger than 5 ($\Delta\hat{\chi}_{\text{sum}}^2 \gtrsim 5$), with the largest value $\hat{\chi}_{\text{sum}}^2 = 954.7$.

3.3.1 Parameter space: the best M2M models

Following our selection procedure explained in section 3.2.8.2 we find the range of parameters $\Upsilon_{3.6}$, M_{DM}^{B} and Ω_p for the grids of models with the Einasto and the NFW dark matter profiles that best match the observations, obtaining a similar range for both grids, as we show in tables 3.1 and 3.2 with their main properties.

The best parameters for the Einasto grid are a stellar mass-to-light ratio in the $3.6\ \mu\text{m}$ band of $\Upsilon_{3.6} = 0.72 \pm 0.02\ \text{M}_{\odot}\ \text{L}_{\odot}^{-1}$, a dark matter mass within the bulge of $M_{\text{DM}}^{\text{B}} = 1.2^{+0.2}_{-0.4} \times 10^{10}\ \text{M}_{\odot}$ and a bar pattern speed of $\Omega_p = 40 \pm 5\ \text{km}\ \text{s}^{-1}\ \text{kpc}^{-1}$, while for the NFW grid we obtain the best parameters $\Upsilon_{3.6} = 0.70^{+0.02}_{-0.04}\ \text{M}_{\odot}\ \text{L}_{\odot}^{-1}$, $M_{\text{DM}}^{\text{B}} = 1.0^{+0.4}_{-0.2} \times 10^{10}\ \text{M}_{\odot}$ and $\Omega_p = 40 \pm 5\ \text{km}\ \text{s}^{-1}\ \text{kpc}^{-1}$. In both cases the best model is the central value and the errors are the range of acceptable models.

In Figure 3.6 we show $\Delta\hat{\chi}_{\text{sum}}^2$ as function of the parameters $\Upsilon_{3.6}$, M_{DM}^{B} and Ω_p for both

grids of models (Einasto and NFW). Both ranges of models are close in parameter space however, the NFW acceptable models are more extendedly distributed along the parameters $\Upsilon_{3.6}$ and M_{DM}^{B} than the results of the Einasto grid. This is because for the same value of M_{DM}^{B} the more concentrated NFW profile has more mass within the bulge than the Einasto profile, increasing then the degeneracy between $\Upsilon_{3.6}$ and M_{DM}^{B} .

We find that the Einasto grid of models provide a better fit than the NFW grid, shown by smaller values of the variable $\hat{\chi}_{\text{sum}}^2$ of the Einasto grid (Table 3.1) compared to the NFW models (Table 3.2), where the best Einasto model has $\hat{\chi}_{\text{sum}}^2=3.92$, while the best NFW model has $\hat{\chi}_{\text{sum}}^2=6.61$, meaning that the best matching models of the NFW grid is already outside the range of acceptable models of the Einasto grid.

In the next section we show how each individual subset provides a signature in their chi-square values that is connected to the physical parameters $\Upsilon_{3.6}$, M_{DM}^{B} and Ω_{p} , allowing us to, for example, break the degeneracy between the stellar mass and the dark matter mass in the bulge.

3.3.1.1 Parameters $\Upsilon_{3.6}$ and M_{DM}^{B}

The first part of our parameter exploration of the Einasto grid of models is shown in Figure 3.7, and the equivalent for the NFW grid of models is shown in the appendix in Figure 3.28. In the figure we show the classical bulge photometry and dispersion variables $\Delta\hat{\chi}_{\mu}^{2\text{RCB}}$, $\Delta\hat{\chi}_{\sigma}^{2\text{RCB}}$, and the B/P bulge photometry and dispersion $\Delta\hat{\chi}_{\mu}^{2\text{RBP}}$ and $\Delta\hat{\chi}_{\sigma}^{2\text{RBP}}$ as function of the stellar mass-to-light and the dark matter mass. We discuss the variable $\Delta\hat{\chi}_{\nu}^{2\text{RBP}}$ and the pattern speed in section 3.3.1.4. The full results comprehend five cubes with the values of the five subsets of variables, each with sides $\Upsilon_{3.6}$, M_{DM}^{B} and Ω_{p} having a chi-square distribution as the diagram of Figure 3.5. For simplicity, in Figure 3.7 we show only $\Upsilon_{3.6}$ and M_{DM}^{B} , making projections selecting the lowest value along the parameter Ω_{p} axis. Figure 3.7 shows that while the lowest chi-square values for each subset have slightly different locations in the space of $\Upsilon_{3.6}$ and M_{DM}^{B} , the region of acceptable models overlap.

The classical bulge region (RCB): we find that the parameter $\Upsilon_{3.6}$ is strongly constraint by the dynamical properties of the classical bulge of M31, where $\Delta\hat{\chi}_{\mu}^{2\text{RCB}}$ and $\Delta\hat{\chi}_{\sigma}^{2\text{RCB}}$ have very confined regions of low chi-square in the $\Upsilon_{3.6}$ and M_{DM}^{B} space. We show later that this is expected given that in the very centre of the bulge the dynamics is governed mainly by the stellar mass, while the dark matter matters more in the outer part of the bulge, where the B/P bulge is. The models that best match the photometry in the centre of the RCB region are in the range $\Upsilon_{3.6}=0.70 - 0.74 M_{\odot} L_{\odot}^{-1}$ where the lowest values of $\Delta\hat{\chi}_{\mu}^{2\text{RCB}}$ are located. Similarly, the models that better match the central velocity dispersion in the RCB region are within $\Upsilon_{3.6}=0.70 - 0.75 M_{\odot} L_{\odot}^{-1}$, showing the lowest values of $\Delta\hat{\chi}_{\sigma}^{2\text{RCB}}$. The variables $\Delta\hat{\chi}_{\mu}^{2\text{RCB}}$ and $\Delta\hat{\chi}_{\sigma}^{2\text{RCB}}$ constrain the dark matter mass to be within $M_{\text{DM}}^{\text{B}} \leq 1.4 \times 10^{10} M_{\odot}$, while the pattern speed has only a small effect in the region of the classical bulge, which translates into having low values of $\Delta\hat{\chi}_{\mu}^{2\text{RCB}}$, $\Delta\hat{\chi}_{\sigma}^{2\text{RCB}}$ for a wide range of values of Ω_{p} .

The B/P bulge region (RBP): $\Delta\hat{\chi}_{\mu}^{2\text{RBP}}$ is less constraining with low values that are more extensively distributed in $\Upsilon_{3.6}$ and M_{DM}^{B} , with the best models located at $\Upsilon_{3.6} \lesssim 0.74 M_{\odot} L_{\odot}^{-1}$ and $M_{\text{DM}}^{\text{B}} \gtrsim 0.8 \times 10^{10} M_{\odot}$. The variable $\Delta\hat{\chi}_{\sigma}^{2\text{RBP}}$ has a constrained region of low chi-square values in the range $\Upsilon_{3.6}=0.70 - 0.78 M_{\odot} L_{\odot}^{-1}$ and $M_{\text{DM}}^{\text{B}} \leq 1.4 \times 10^{10} M_{\odot}$, (and unlike the variables $\Delta\hat{\chi}_{\mu}^{2\text{RCB}}$

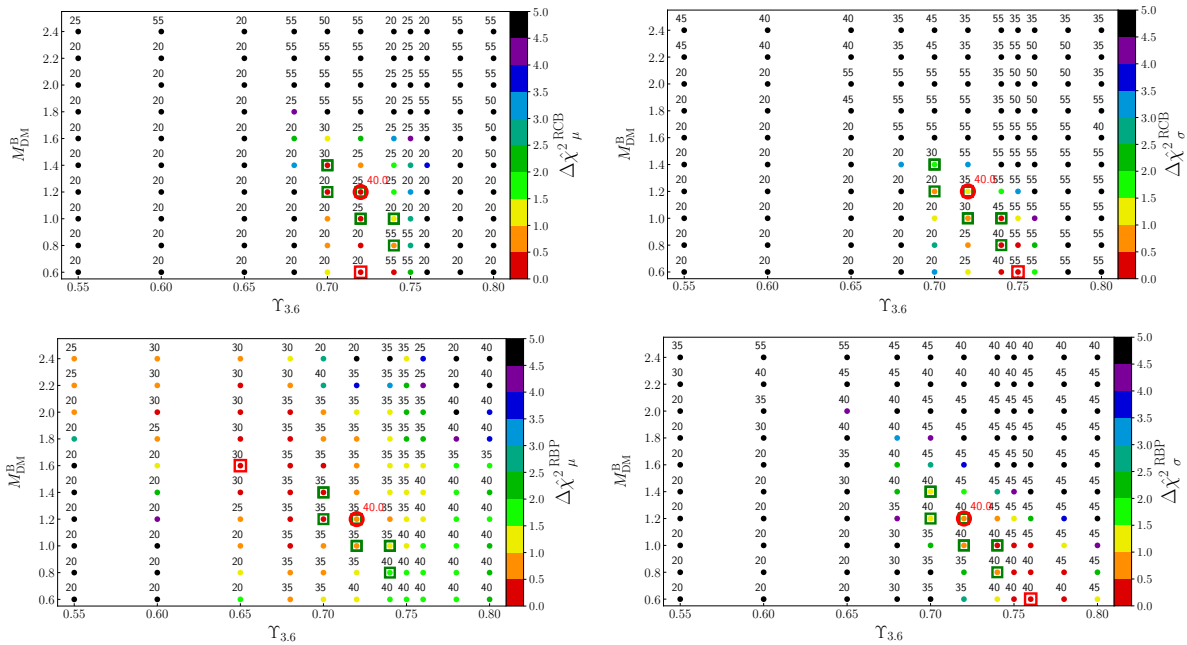


Figure 3.7: Breaking the degeneracy of $\Upsilon_{3.6}$ and M_{DM}^B with different data sets. Results of the Einasto grid of models the subsets: $\Delta\chi^2_{\mu}^{RCB}$ (top left), $\Delta\chi^2_{\sigma}^{RCB}$ (top right), $\Delta\chi^2_{\mu}^{RBP}$ (bottom left) and $\Delta\chi^2_{\sigma}^{RBP}$ (bottom right) as function of the parameters $\Upsilon_{3.6}$ and M_{DM}^B , selecting the minimum value along the Ω_p axis. We do not plot in the figure the whole range of explored values for better clarity, leaving only the range of higher interest. With coloured points are shown the values of each subset. The number corresponds to the Ω_p with the lowest chi-square. We mark the best model JR804 (red circle), the models with the minimum values in each subset (red squares), and the range of acceptable models \vec{M}_{NBM}^{EIN} (green squares). The green squares do not necessarily agree with the pattern speed shown.

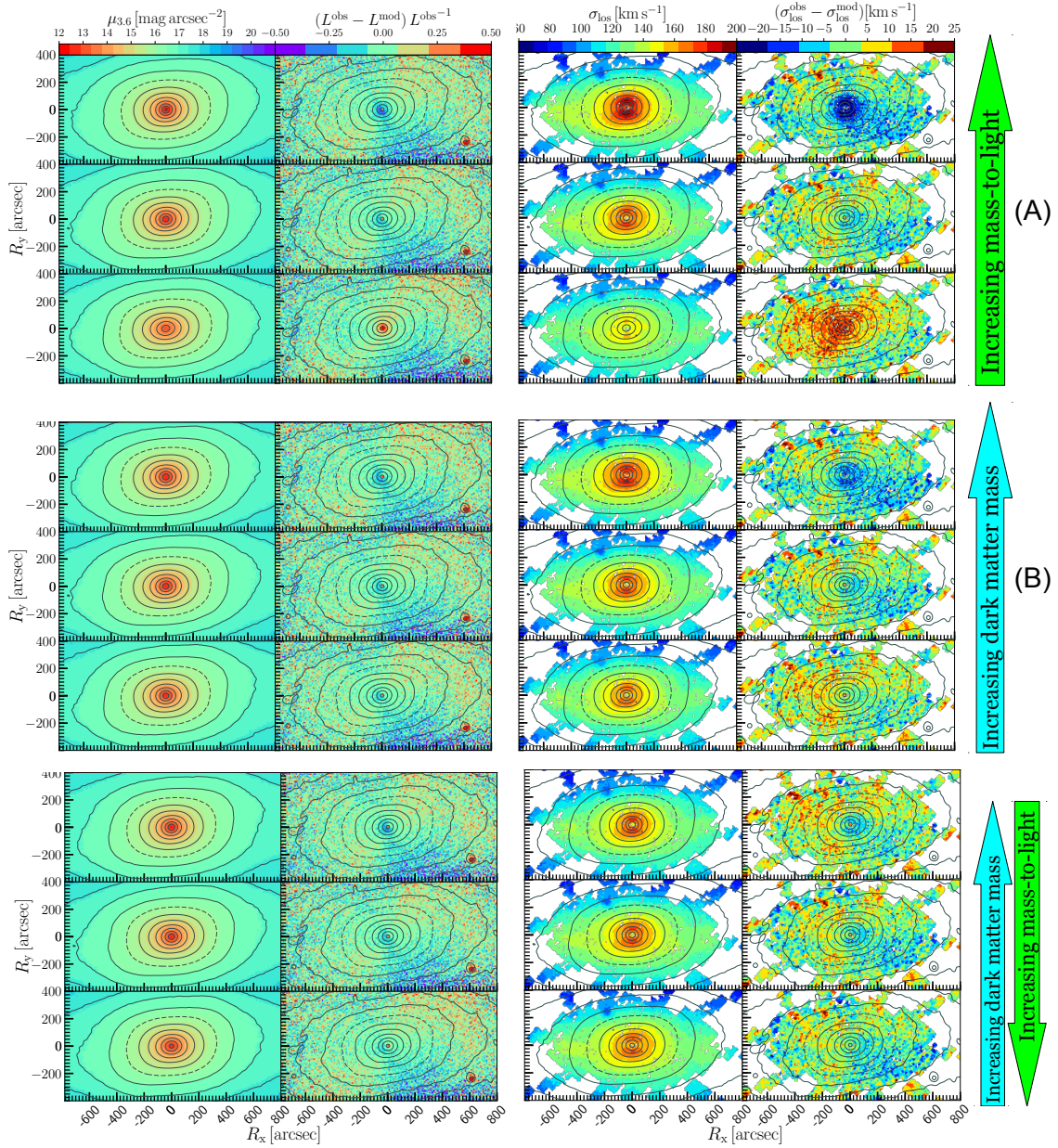


Figure 3.8: Model maps and their residuals with the observations for the surface-brightness (1st, 2nd columns) and the dispersion and residual (3rd and 4th columns). Case A with variation only in $\Upsilon_{3,6}$ showing a model with $\Upsilon_{3,6} = 0.80 M_{\odot} L_{\odot}^{-1}$ (1st row), the best model with $\Upsilon_{3,6} = 0.72 M_{\odot} L_{\odot}^{-1}$ (2nd row) and a model with $\Upsilon_{3,6} = 0.65 M_{\odot} L_{\odot}^{-1}$ (3rd row). Case B with variation only in M_{DM}^{B} showing a model with $M_{\text{DM}}^{\text{B}} = 1.6 \times 10^{10} M_{\odot}$ (4th row), the best model with $M_{\text{DM}}^{\text{B}} = 1.2 \times 10^{10} M_{\odot}$ (5th row) and a model with $M_{\text{DM}}^{\text{B}} = 0.8 \times 10^{10} M_{\odot}$ (5th row). Case C with variation of $\Upsilon_{3,6}$ and M_{DM}^{B} showing a model with $\Upsilon_{3,6} = 0.75 M_{\odot} L_{\odot}^{-1}$ and $M_{\text{DM}}^{\text{B}} = 0.8 \times 10^{10} M_{\odot}$ (6th row), the best model (7th row), and a model with $\Upsilon_{3,6} = 0.68 M_{\odot} L_{\odot}^{-1}$ and $M_{\text{DM}}^{\text{B}} = 1.6 \times 10^{10} M_{\odot}$ (8th row). We show the isophotes of the models (1st and 3rd column) and M31 (2nd and 4th column) spaced with $\Delta\mu_{3,6} = 0.5 \text{ [mag arcsec}^{-2}]$ and the value $\mu_{3,6} = 16 \text{ [mag arcsec}^{-2}]$ is shown with a dashed isophote.

and $\Delta\hat{\chi}_{\sigma}^{2\text{RCB}}$, we show later in Figure 3.13 that the pattern speed is also constrained by $\Delta\hat{\chi}_{\sigma}^{2\text{RBP}}$.

The most important result shown by Figure 3.7 is that the expected degeneracy between the stellar mass-to-light ratio and the dark matter is broken by combining the different subsets, particularly the classical bulge photometry ($\Delta\hat{\chi}_{\mu}^{2\text{RCB}}$) and dispersion ($\Delta\hat{\chi}_{\sigma}^{2\text{RCB}}$) which are sensitive to $\Upsilon_{3.6}$, allowing a narrow range of values, which then constrain the dark matter via $\Delta\hat{\chi}_{\sigma}^{2\text{RBP}}$ and $\Delta\hat{\chi}_{\sigma}^{2\text{RCB}}$, which measure how well the B/P bulge region is fitted.

As we show now with velocity dispersion maps, for a given luminosity distribution and pattern speed, the gradient of the dispersion is determined by the steepness of gravitational potential that depends on two remaining quantities: the stellar mass in the central bulge region and the dynamical mass in the outskirts of the bulge. For example, models that have too much dark matter mass within the bulge and low mass-to-light ratios can result in a dispersion profile that is too flat, matching the data in the outer part of the B/P bulge, but too low in the central part where the classical bulge is. This effect is stronger in the Einasto grid of models than in the grid of models with NFW profiles, which have more concentrated dark matter mass profiles that generate a deeper central potential (see 3.3.1.3). And the opposite scenario also occurs, where too large mass-to-light ratios end up with too high dispersion in the centre.

In Figure 3.8 we present photometric and kinematic maps of the best model ($\vec{M}_{\text{BM}}^{\text{EIN}}$) and compare them with the maps of other models with different values of $\Upsilon_{3.6}$ and M_{DM}^{B} to show how these physical parameters are connected with the observed quantities L and σ_{los} , and by extension to the variables $\Delta\hat{\chi}_{\mu}^{2\text{RCB}}$, $\Delta\hat{\chi}_{\sigma}^{2\text{RCB}}$, $\Delta\hat{\chi}_{\mu}^{2\text{RBP}}$ and $\Delta\hat{\chi}_{\sigma}^{2\text{RBP}}$. For this we consider three main cases: (A) variations of only the mass-to-light ratio ($\Delta\Upsilon_{3.6}$), (B) variations of only the dark matter ($\Delta M_{\text{DM}}^{\text{B}}$), and (C) varying both simultaneously ($\Delta\Upsilon_{3.6}$, $\Delta M_{\text{DM}}^{\text{B}}$) to show how the degeneracy between these parameters is constrained:

- (A) In the top panels in Figure 3.8 we show the best model compared to two models with the same dark matter mass and pattern speed, but with different mass-to-light ratios. The model with a larger $\Upsilon_{3.6}$ has a slightly worse fit to the photometry in the B/P bulge region (RBP) (larger $\Delta\hat{\chi}_{\mu}^{2\text{RBP}}$), and a worse fit to the dispersion, which is higher in the model than in the data (larger $\Delta\hat{\chi}_{\sigma}^{2\text{RBP}}$). The high $\Upsilon_{3.6}$ results in too much mass in the centre of the bulge, which has the consequence of a velocity dispersion that is higher than the observations. What occurs during the M2M fit in this case is that the masses of the particles are increased to fit the luminosity in the centre, making the gravitational potential deeper, which results in a velocity dispersion too high compared to the observations. For the model with lower $\Upsilon_{3.6}$ (3rd row) the effects are the opposite. The most important result here is that the mass-to-light ratio has the strongest effect in the central region where the classical bulge is, showing the important signature of the variables $\Delta\hat{\chi}_{\mu}^{2\text{RCB}}$ and $\Delta\hat{\chi}_{\sigma}^{2\text{RCB}}$.
- (B) If we change only the dark matter mass within the bulge, we obtain effects similar to the previous case. In the middle panels of Figure 3.8 we show the best model and two models that have the same $\Upsilon_{3.6}$ and Ω_{p} , but different dark matter masses. Both models give in general a worse fit to the observed dispersion map than the best model. In the B/P bulge region the mass of the dark matter is comparable to the stellar mass within the volume of the bulge (25 per cent of the stellar mass depending on the model) and therefore the total mass is what is connected to the dispersion. However, the stellar mass is determined

by $\Upsilon_{3.6}$ (for well-fitted photometry), which is a parameter that is constrained from the central region of the bulge, while $\Delta\hat{\chi}_{\mu}^{2\text{RBP}}$ and $\Delta\hat{\chi}_{\sigma}^{2\text{RBP}}$ constrain the dynamical mass, and by extension the dark matter mass M_{DM}^{B} .

- (C) Finally, considering the case of $\Upsilon_{3.6} - M_{\text{DM}}^{\text{B}}$ jointly: what happens if we decrease (increase) the mass-to-light ratio, but we also increase (decrease) the dark matter mass content? Using our selection criteria in section 3.2.8.2 we find range of values for the parameters $\Upsilon_{3.6}$ and M_{DM}^{B} that fit the observations well with: $\Upsilon_{3.6} = 0.72 \pm 0.02 M_{\odot} L_{\odot}^{-1}$ and $M_{\text{DM}}^{\text{B}} = 1.2_{-0.4}^{+0.2} \times 10^{10} M_{\odot}$. The best values of $\Upsilon_{3.6}$ are determined by the photometry and the kinematics of the classical bulge region ($\Delta\hat{\chi}_{\mu}^{2\text{RCB}}$ and $\Delta\hat{\chi}_{\sigma}^{2\text{RCB}}$) where the stellar mass dominates, while the dark matter is determined by the photometry and the kinematics of the B/P bulge. Here we show models just outside the range of acceptable models, and so these differences are subtle in the maps.

3.3.1.2 Parameter $\Upsilon_{3.6}$: two bulge components

We find for the Einasto grid of models that the best range of values for the stellar mass-to-light ratio in the $3.6 \mu\text{m}$ band is $\Upsilon_{3.6} = 0.72 \pm 0.02 M_{\odot} L_{\odot}^{-1}$. Given that the bulge of M31 has two components: a classical bulge that likely formed very early from a hierarchical process, and a B/P bulge formed by the redistribution of a disc component, we might expect different values of $\Upsilon_{3.6}$ for each component. However, we now show that due to their measured metallicities and ages, their mass-to-light ratios in the $3.6 \mu\text{m}$ band are rather similar and that the best value represents well both bulge components.

In Figure 3.9 we show the stellar mass-to-light in the $3.6 \mu\text{m}$ band as function of metallicity and age computed by Meidt et al. (2014)² using a stellar population analysis. We also show the ranges of metallicity and age within the bulge of M31 measured by Opitsch (2016) who found that the bulge is uniformly old with mean age of 11.4 ± 1.2 Gyr and has a metallicity $-0.15 < [Z/H] < 0.3$ over the whole bulge, with $0.05 < [Z/H] < 0.2$ in the classical bulge alone. These values assume a Chabrier initial mass function (IMF). Analysis of mass dependent absorption features in high signal-to-noise spectra by Zieleniewski et al. (2015) indicate that the IMF is consistent with Chabrier across the bulge.

Considering then stellar populations with the metallicities and averaged ages estimated in the M31 bulge, our range of best values for the mass-to-light ratios are in good agreement with what is expected.

An important characteristic of the relation between metallicity, age and mass-to-light ratio in the $3.6 \mu\text{m}$ band shown in the figure is that an old and slightly more metal-rich population could have a mass-to-light similar to that of a slightly younger and less metal-rich population. Elliptical galaxies and classical bulges show metallicity gradients with the most metal rich part in their centres (Koleva et al. 2011). We also expect the material of the B/P bulge to be comparably old, even if the bar formed dynamically more recently, the material from the former disc would be old.

²values taken directly from their Figure 2

Table 3.3: Bulge components with different $\Upsilon_{3.6}$ values.

$\Upsilon_{3.6}$	$M_{\odot} L_{\odot}^{-1}$	case i)	case ii)	case iii)	case iv)	case v)
Υ^{CB}		0.72	0.72	0.72	0.72	0.72
Υ^{BP}		0.70	0.68	0.72	0.72	0.72
Υ^{d}		0.70	0.68	0.65	0.55	0.80

Consequently, our assumption of a unique value of $\Upsilon_{3.6}$ for both bulge components is not unexpected and is sufficient to reproduce the most important dynamical properties of the M31 bulge, and the narrow range of valid values suggest that the combination of two different values for each bulge component must be limited. Certainly in the outer disc region, beyond the bar, younger stars can strongly decrease the mass-to-light ratio. Colour gradients also suggest a metallicity gradient between the more metal rich bulge and the outer disc (Courteau et al. 2011). To test these assumptions we also performed M2M fits with different $\Upsilon_{3.6}$ values for the bulge components and the disc, considering five cases shown in Table 3.3. We only find small changes in the dynamical properties of the model within the bulge region. As we show in the next section, even in the outer part of the disc ($R > 10$ kpc) for lower $\Upsilon_{3.6}$ in the outer disc we require small variations of ~ 10 per cent of dark matter mass at that radius in order to match the HI rotation curve.

3.3.1.3 Stellar and dark matter mass distribution

In the previous section we found the range of $3.6 \mu\text{m}$ mass-to-light ratios and dark matter masses within the bulge that best reproduce the observations, obtaining then the range of stellar masses for each bulge component. Table 3.1 contains the resulting masses within 3.2 kpc for the range of acceptable models with the Einasto dark matter haloes $\vec{M}_{\text{NBM}}^{\text{EIN}}$, with the best values being: $M_{\star}^{\text{CB}} = 1.18_{-0.07}^{+0.06} \times 10^{10} M_{\odot}$ for the classical bulge, $M_{\star}^{\text{BP}} = 1.91 \pm 0.06 \times 10^{10} M_{\odot}$ for the B/P bulge, making a total bulge stellar mass of $M_{\star}^{\text{B}} = 3.09_{-0.12}^{+0.10} \times 10^{10} M_{\odot}$. Including the bulge dark matter mass $M_{\text{DM}}^{\text{B}} = 1.2_{-0.4}^{+0.2} \times 10^{10} M_{\odot}$ we have a total dynamical mass within the bulge of $M_{\text{dyn}}^{\text{B}} = 4.25_{-0.29}^{+0.10} \times 10^{10} M_{\odot}$. Integrating the mass of the classical bulge out to 10 kpc we obtain $M_{\star}^{\text{CB}, 10 \text{ kpc}} = 1.71_{-0.09}^{+0.10} \times 10^{10} M_{\odot}$. Other bulge mass estimations in the literature neglect the composite nature of M31's bulge, and therefore they recover similar values to our bulge total stellar mass ($M_{\star}^{\text{B}} = 4 \times 10^{10} M_{\odot}$; Kent 1989), ($M_{\star}^{\text{B}} = 2.5 \times 10^{10} M_{\odot}$; Widrow et al. 2003). Our classical bulge value is the lowest value in the literature for M31, and it has important implications for the early formation history of M31.

The models with NFW haloes result in a similar range of values (Table 3.2), with $M_{\star}^{\text{CB}} = 1.16_{-0.10}^{+0.04} \times 10^{10} M_{\odot}$ and $M_{\star}^{\text{BP}} = 1.82 \pm 0.08 \times 10^{10} M_{\odot}$, and a total stellar mass of $M_{\star}^{\text{B}} = 2.98_{-0.18}^{+0.10} \times 10^{10} M_{\odot}$. The dark matter is $M_{\text{DM}}^{\text{B}} = 1.0_{-0.2}^{+0.4} \times 10^{10} M_{\odot}$ with the total mass within the bulge being $M_{\text{dyn}}^{\text{B}} = 3.95_{-0.09}^{+0.22} \times 10^{10} M_{\odot}$.

In Figure 3.10 we present the cumulative mass profiles of the best models and the acceptable

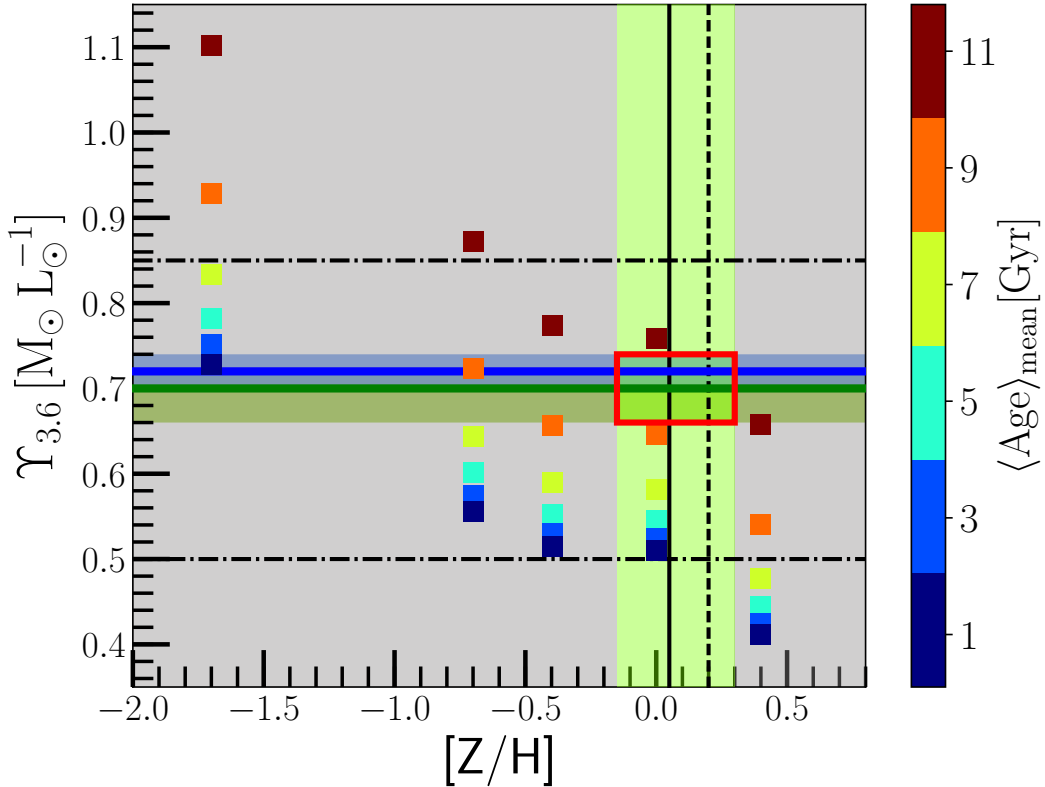


Figure 3.9: Stellar mass-to-light ratio in the $3.6\mu\text{m}$ band as function of the metallicity. The best values are $\Upsilon_{3.6} = 0.72 \pm 0.02 M_{\odot} L_{\odot}^{-1}$ (blue line) for the Einasto grid of models, and $\Upsilon_{3.6} = 0.70^{+0.02}_{-0.04} M_{\odot} L_{\odot}^{-1}$ for the NFW grid (green line), and the range of explored values of $\Upsilon_{3.6}$ (dotted dashed horizontal lines). The vertical lines correspond to averaged $[Z/H]$ of the bar (solid line) and the bulge region (dashed line) of M31 from O16, and the shaded vertical green area marks the minimum and maximum values measured in the bulge and bar region. Meidt et al. (2014) estimate from stellar population evolution analysis predictions, relations for $\Upsilon_{3.6}$, the metallicity and the mean stellar age (squares). The red rectangle indicates the region of $\Upsilon_{3.6}$ values that we expect to intersect with the values from the stellar populations analysis, given the metallicities measured within the M31 bulge.

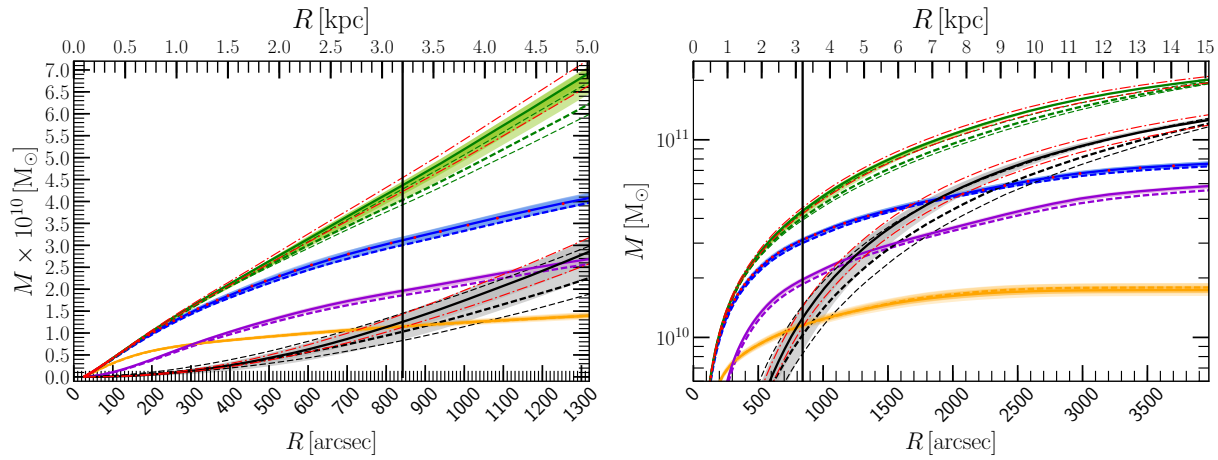


Figure 3.10: Cumulative mass profiles within 5 kpc and (left panel) 15 kpc (right panel) for the best model (JR804) of the grid with the Einasto dark matter profile (solid curves) and the best model (KR241) of the NFW grid (thick dashed curves), for the different components: classical bulge (orange), B/P bulge and disc (purple), total stellar (blue), dark matter (black) and total dynamical mass (green). The range of acceptable models of the Einasto grid $\vec{M}_{\text{NBM}}^{\text{EIN}}$ is shown in shaded regions. The most extreme values of M_{DM}^{B} from the range of the models $\vec{M}_{\text{NBM}}^{\text{NFW}}$ are shown with the thin dashed curves. The end of the deprojected B/P bulge is at 3.2 kpc (vertical black solid). The test of the extreme variations of the flattening have masses within the bulge that lay within the range of models for $q=1.0$ (lower red line) and 0.7 (upper red line), and the stellar component in red dots. The profiles are function of the cylindrical radius R summing the mass within a spheroidal volume with our fiducial flattening of $q=0.85$.

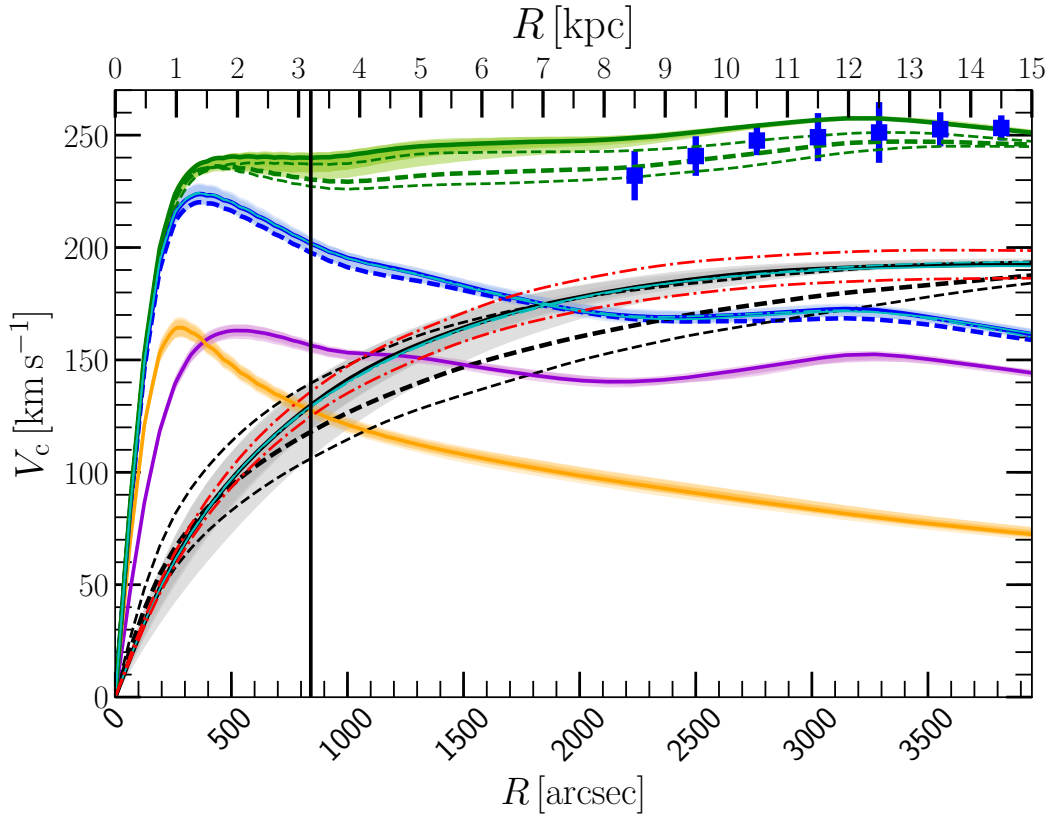


Figure 3.11: Azimuthally averaged circular velocity in the plane of the disc of the model JR804 (solid curves) and model KR241 (dashed curves) for the CB (orange), the B/P bulge and the disc (purple), total stellar mass (blue curve), the dark matter (black curve), and the total circular velocity (green curve). The HI data of Corbelli et al. (2010) is shown out 15 kpc (blue squares). The shaded regions correspond to the models with the Einasto profile $\vec{M}_{\text{NBM}}^{\text{EIN}}$ and the NFW profile $\vec{M}_{\text{NBM}}^{\text{NFW}}$ (green shade). The dotted dashed curve indicate the profile of the models with the maximum and the minimum M_{DM}^{B} of the models $\vec{M}_{\text{NBM}}^{\text{NFW}}$. We show the $Y_{3.6}$ variations of the disc with $Y_{\text{d}}=0.8 M_{\odot} L_{\odot}^{-1}$ (cyan solid) and $Y_{\text{d}}=0.55 M_{\odot} L_{\odot}^{-1}$ (cyan dot dashed line), which may overlap in some regions. The test of the different flattening for $q=1.0$ (lower red dot dash line) and 0.7 (upper red dot dash line), and the stellar component in red dots.

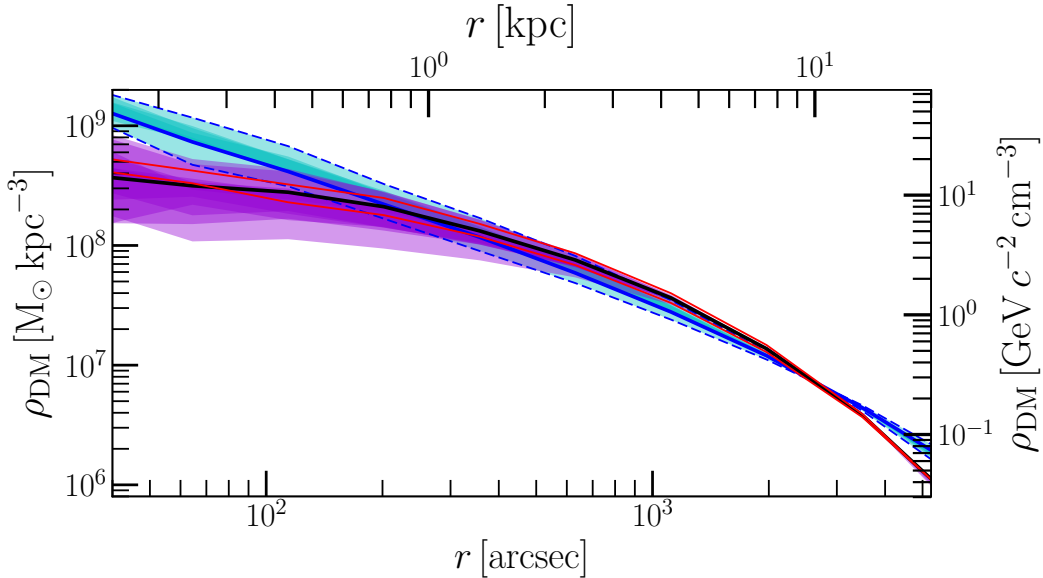


Figure 3.12: Dark matter density profiles of the best matching Einasto model (black curve) and the best NFW model (blue curve). The shaded regions correspond to the models with the Einasto profile $\vec{M}_{\text{NBM}}^{\text{EIN}}$ (violet shade) and the NFW profile $\vec{M}_{\text{NBM}}^{\text{NFW}}$ (cyan shade). The dotted blue dashed curve indicate the profile of the models with the maximum and the minimum M_{DM}^{B} of the models $\vec{M}_{\text{NBM}}^{\text{NFW}}$.

range models of the Einasto grid ($\vec{M}_{\text{NBM}}^{\text{EIN}}$) and the NFW grid ($\vec{M}_{\text{NBM}}^{\text{NFW}}$). The resulting range of models have very similar stellar mass profiles, and most of the total mass variation is due to the dark matter. The classical bulge dominates the centre reaching the same mass of the B/P bulge at 1.2 kpc (300 arcsec). Further out the B/P bulge dominates the stellar mass, almost double the mass of the classical bulge at the end of the B/P bulge. Interestingly, the profiles show that the dark matter masses reach a similar value to the classical bulge at end of the B/P bulge at 3.2 kpc (850 arcsec). The best values of the Einasto grid of models are similar within the errors to the best NFW models, with the best matching NFW models requiring slightly lower masses within 3.2 kpc. This is explained by the more cuspy density profile of the NFW profile: for the same mass at the end of the bulge (3.2 kpc) the NFW models have more dark matter distributed in the very centre than the Einasto models, as is shown by the density profiles in Figure 3.12.

We show in Figure 3.11 the circular velocity profiles of the models $\vec{M}_{\text{BM}}^{\text{EIN}}$ and $\vec{M}_{\text{BM}}^{\text{NFW}}$ within 15 kpc *i.e.* the radius where we fit the photometry. While the total dark matter within the bulge is fixed to a value M_{DM}^{B} during each M2M fit, where we select the values that best reproduce the photometry and the stellar kinematic observations, the dark matter in the disc region is determined during each run by fitting the HI rotation curve. We find that for the Einasto profile the range of dark matter masses and the resulting circular velocity values are more constrained than the range of values of the NFW profile.

We include in the mass profile and in the circular velocity figures our variations of model JR804 with a flattening $q=1.0$ and 0.7 , having dark matter mass and circular velocity values

within the range of the acceptable models. As expected the dark matter mass profile deviates for different flattening values; however, the stellar mass profile remains within the range of the acceptable models. We also include the circular velocity figure our tests with different $\Upsilon_{3.6}$ values for the disc from Table 3.3, showing that even the extreme values $\Upsilon^d=0.55 M_\odot L_\odot^{-1}$ and $\Upsilon^d=0.80 M_\odot L_\odot^{-1}$ remain within the range of the acceptable models. The variation of the circular velocity in the disc region at ~ 10 kpc is small because most of the stellar mass is contained within this radius and the dark matter dominates at this distances, making the local variation of the stellar mass at ~ 10 kpc only a small contribution to the total circular velocity.

In Figure 3.12 we present the particle dark matter density profiles of the best models of the Einasto and the NFW grids, and the range of acceptable models. Fitting equation 3.22 to the Einasto density we recover the parameters $\rho_E=1.29 \pm 0.05 \times 10^7 M_\odot \text{ kpc}^{-3}$, $m_E=7.8 \pm 0.1$ kpc and $\alpha=0.51 \pm 0.01$ (or $n_{\text{Ein}}=\alpha^{-1}=1.95 \pm 0.02$) Similarly, a fit from equation 3.23 recovers the NFW profile values $\rho_{\text{NFW}}=1.54 \pm 0.05 \times 10^7 M_\odot \text{ kpc}^{-3}$, and $m_{\text{NFW}}=10.4 \pm 0.1$ kpc.

We find a dark matter mass of $M_{\text{DM}}^B = 1.2_{-0.4}^{+0.2} \times 10^{10} M_\odot$ within 3.2 kpc for the Einasto grid of models and $M_{\text{DM}}^B = 1.0_{-0.2}^{+0.4} \times 10^{10} M_\odot$ for the NFW models, where the bulge stellar kinematics favours the cored Einasto profile. We find that the central dark matter masses are in agreement with cosmologically motivated haloes. Haloes with the virial mass M31 of $M_{\text{DM}200}=1.04 \times 10^{12} M_\odot$ (Tamm et al. 2012) in cosmological simulation are expected to have a concentration of $c_{200}=8.8$ and virial radius of $R_{200}=277$ kpc (Correa et al. 2015a,b, with Planck cosmology (Planck Collaboration et al. 2013)). For such halo, the expected mass within 3.2 kpc for a pure NFW halo is $M_{\text{DM}200}^{3.2 \text{ kpc}}=0.34 \times 10^{10} M_\odot$, lower than our measurement. However, the baryonic mass accretion can cause an adiabatic contraction of the halo that increases the central dark matter mass up to $M_{\text{DM}200}^{3.2 \text{ kpc}}=1.88 \times 10^{10} M_\odot$ in the more extreme case (Blumenthal et al. 1986), or a lower value of $M_{\text{DM}200}^{3.2 \text{ kpc}}=0.97 \times 10^{10} M_\odot$, as more recent hydrodynamical cosmological simulations show less contraction ($\nu=0.4$) (Dutton et al. 2011; Abadi et al. 2010). Our results then agree with a moderate adiabatic contraction in the centre of the halo, but also favour a cored nature of the halo's central distribution.

3.3.1.4 Parameter Ω_p : B/P bulge and thin bar pattern speed.

The bar of M31 consists of a vertically thick structure that is the B/P bulge component, and the thin bar component that is mostly concentrated in the disc's plane where both structures are aligned and rotate at the same pattern speed. Most estimations of the M31 bar pattern speed are based on comparisons with gas kinematics, finding typically $\Omega_p \approx 50 - 60 \text{ km s}^{-1} \text{ kpc}^{-1}$ (Stark & Binney 1994; Berman 2001; Berman & Loinard 2002).

Tremaine & Weinberg (1984) derived a relation from the continuity equation to determine the pattern speed of a two dimensional bar in disc galaxies directly from the observations using the information of the line-of-sight velocity (v_{los}) and the photometry ($L_{3.6}$). Here we have the unique possibility to use new IFU stellar kinematics of the M31 bulge from O18 to determine the bar pattern speed. However, the disc inclination is too high to robustly determine it directly from the data. Therefore, we proceed to use this relation indirectly by comparing with models that have been fitted to the photometric and IFU observations, which have different pattern speed values. Then, we select the models with a good match of the velocity field in the bar region

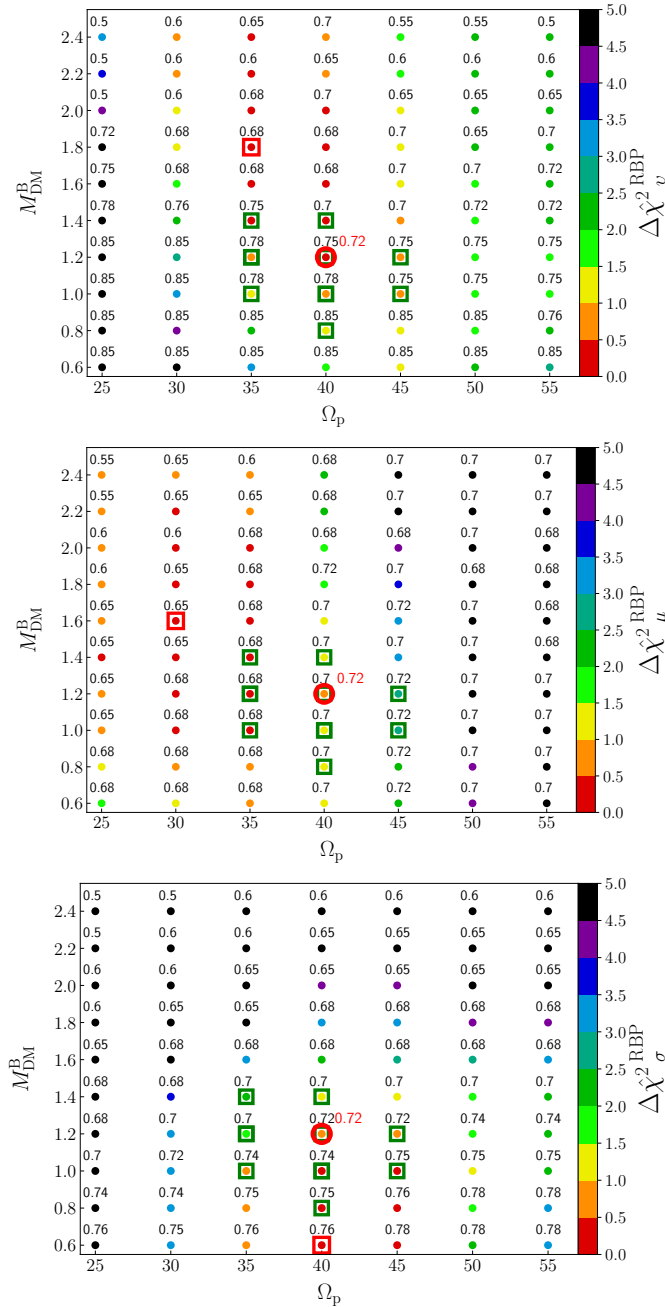


Figure 3.13: Results of the grid of models for the Einasto dark matter halo for the subsets 3,4 and 5: $\Delta\hat{\chi}^2_{\nu}^{\text{RBP}}$ (top), $\Delta\hat{\chi}^2_{\mu}^{\text{RBP}}$ (middle) and $\Delta\hat{\chi}^2_{\mu}^{\text{RBP}}$ (bottom) and $\Delta\hat{\chi}^2_{\sigma}^{\text{RBP}}$ (bottom right) as function of the parameters Ω_p and M_{DM}^{B} selecting the lowest value along the axis of the parameter $\Upsilon_{3,6}$. The values of each subset are the points that are coded in the coloured bar, and the number corresponds to the selected $\Upsilon_{3,6}$. We mark the best model JR804 (red circle), the models with the minimum values in each subset (red squares), and the range of acceptable models $\vec{M}_{\text{NBM}}^{\text{EIN}}$ (green squares). The green squares do not necessarily agree with the shown $\Upsilon_{3,6}$.

($\Delta\hat{\chi}_\nu^{2\text{RBP}}$), and the surface luminosity density ($\Delta\hat{\chi}_\mu^{2\text{RBP}}$). Furthermore, the velocity dispersion (σ_{los}) is also connected to the velocity through the total kinetic energy ($\sigma_{\text{los}}^2 + v_{\text{los}}^2$), and therefore it also constrains the bar pattern speed. And so, combining these two variables with the variables $\Delta\hat{\chi}_\mu^{2\text{RCB}}$, $\Delta\hat{\chi}_\sigma^{2\text{RCB}}$ and $\Delta\hat{\chi}_\sigma^{2\text{RBP}}$ we are able to finding the range of best matching models that also reproduce the velocity field in M31's bulge. From the explored range of $\Omega_p = 20\text{--}55 \text{ km s}^{-1} \text{ kpc}^{-1}$, we find $\Omega_p = 40 \pm 5 \text{ km s}^{-1} \text{ kpc}^{-1}$ for both grids of Einasto and NFW models (tables 3.1 and 3.2).

In Figure 3.13 we show the results for $\Delta\hat{\chi}_\nu^{2\text{RBP}}$, $\Delta\hat{\chi}_\sigma^{2\text{RBP}}$, and $\Delta\hat{\chi}_\mu^{2\text{RBP}}$ as function of Ω_p and M_{DM}^{B} for the Einasto grid of models, with the best model located at $M_{\text{DM}}^{\text{B}} = 1.2 \times 10^{10} M_\odot$ and $\Omega_p = 40 \text{ km s}^{-1} \text{ kpc}^{-1}$ (NFW grid results in Figure 3.29). The variable $\Delta\hat{\chi}_\nu^{2\text{RBP}}$ has low values in the range of $\Omega_p = 30\text{--}45 \text{ km s}^{-1} \text{ kpc}^{-1}$ and for $M_{\text{DM}}^{\text{B}} \geq 1.0 \times 10^{10} M_\odot$. $\Delta\hat{\chi}_\mu^{2\text{RBP}}$ has low values within $\Omega_p = 25\text{--}40 \text{ km s}^{-1} \text{ kpc}^{-1}$ and within $\Upsilon_{3,6} = 0.55\text{--}0.75 M_\odot L_\odot^{-1}$. The variable $\Delta\hat{\chi}_\sigma^{2\text{RBP}}$ has low values within $\Omega_p = 35\text{--}50 \text{ km s}^{-1} \text{ kpc}^{-1}$ and $M_{\text{DM}}^{\text{B}} \leq 1.2 \times 10^{10} M_\odot$. Taking into account the restrictions given by the variables $\Delta\hat{\chi}_\mu^{2\text{RCB}}$, $\Delta\hat{\chi}_\sigma^{2\text{RCB}}$ and $\Delta\hat{\chi}_\sigma^{2\text{RBP}}$ that constrain the best values for the mass-to-light ratio and the dark matter mass to be $\Upsilon_{3,6} = 0.72 M_\odot L_\odot^{-1}$ and $M_{\text{DM}}^{\text{B}} = 1.2 \times 10^{10} M_\odot$, we find that the best value for the bar pattern speed is $\Omega_p = 40 \text{ km s}^{-1} \text{ kpc}^{-1}$.

In order to show the effects of changing the bar pattern speed we present in Figure 3.14 the isophotes, the velocity maps and velocity residual maps of the best model ($\vec{M}_{\text{BM}}^{\text{EIN}}$) and compare them with maps of two models with the same $\Upsilon_{3,6}$ and M_{DM}^{B} , but with $\Omega_p = 25 \text{ km s}^{-1} \text{ kpc}^{-1}$ and $\Omega_p = 55 \text{ km s}^{-1} \text{ kpc}^{-1}$. The best model shows smaller residuals than the other two models. The isophotes slightly change in the outer parts of the B/P bulge in response to the change of Ω_p , where the model with $\Omega_p = 25 \text{ km s}^{-1} \text{ kpc}^{-1}$ shows slightly more boxy isophotes than the model with $\Omega_p = 55 \text{ km s}^{-1} \text{ kpc}^{-1}$.

Could the M31 bulge be a triaxial elliptical galaxy? Classical bulges are often considered to be akin to elliptical galaxies sitting in the centres of disc galaxies (Kormendy 2013). Triaxial elliptical galaxies can also show rotation, but contrary to B/P bulges, they show very little or no configuration rotation or pattern speed. The historic consideration of the M31 bulge as a classical bulge implies that the bulge has no pattern speed. Many studies estimate the pattern speed of M31' bulge (Stark & Binney 1994; Berman 2001; Berman & Loinard 2002). The recent kinematic analysis of O18 (see their section 5.3.) estimates several signatures directly from the data, such as the bulge cylindrical rotation, which favours the barred nature of the M31 bulge over the triaxial elliptical galaxy bulge scenario. We compared our best matching model with the extreme case of a model with a slowly rotating bar $\Omega_p = 15 \text{ km s}^{-1} \text{ kpc}^{-1}$ and another with $\Omega_p = 0 \text{ km s}^{-1} \text{ kpc}^{-1}$, which is fundamentally a triaxial ‘‘elliptical’’ galaxy. The resulting models have indeed a central triaxial structure; however, the fits are much worse in all the five subsets, comparing with the models with higher pattern speeds. Furthermore, also the $h3$ and $h4$ fit are worse, and the $h3 - v_{\text{los}}$ correlation observed in the bar region cannot be well reproduced, favouring then the barred nature of M31's bulge.

3.3.1.5 Parameter θ_{bar} : bar angle

Here we show that the fiducial bar angle value chosen for the Einasto and NFW grid of models of $\theta_{\text{bar}} = 55^\circ$ gives the best photometric fits in the B/P bulge region compared to other values of θ_{bar} .

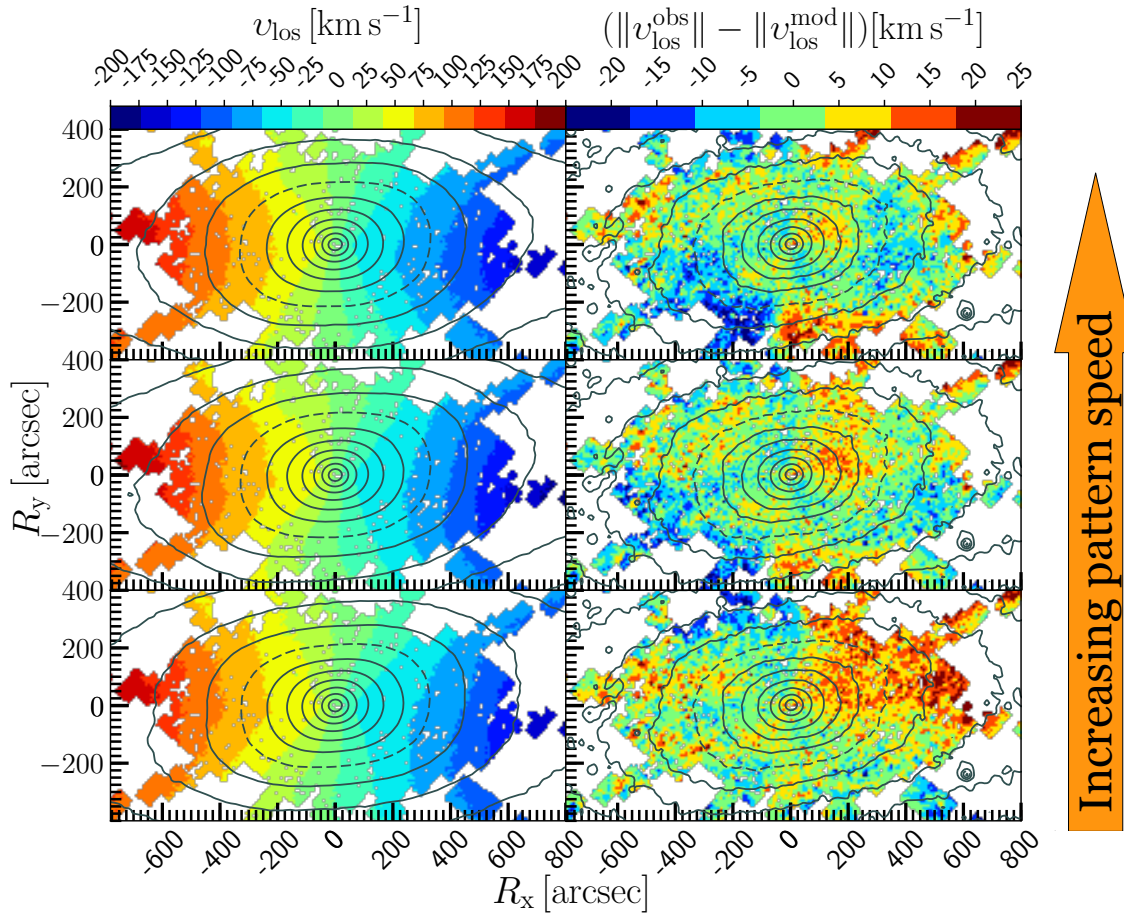


Figure 3.14: Model velocity maps (left column) and velocity residual with the observations (right column) for models with $\Upsilon_{3.6} = 0.72 M_{\odot} L_{\odot}^{-1}$ and $M_{\text{DM}}^{\text{B}} = 1.0 \times 10^{10} M_{\odot}$ with different pattern speeds, with 55 (top), 40 (middle) and 25 km s⁻¹ kpc⁻¹ (bottom). We show the isophotes of the models (first column) and M31 (second column) spaced with $\Delta\mu_{3.6} = 0.5$ [mag arcsec⁻²] and the value $\mu_{3.6} = 16$ [mag arcsec⁻²] is shown with a dashed isophote.

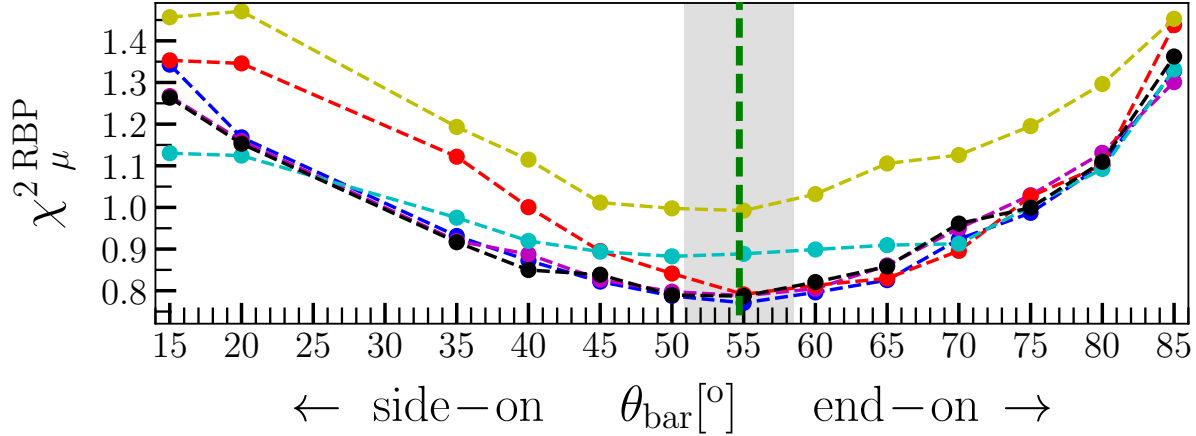


Figure 3.15: Variable $\chi^2_{\mu}^{\text{RBP}}$ (chi-square of the photometry in the B/P bulge region) for six different M2M models fitted with different bar angle values: the best model JR804 (black), model JR355 (red), model JR813 (magenta), model JR364 (blue), model JR683 (cyan) and model JR923 (yellow). Their properties are given in the main text. The fiducial value for our runs is $\theta_{\text{bar}}=54.7 \pm 3.8$ (vertical green line) from B17, which matches within errors with the minimum in all the tested models.

In Figure 3.15 we show different values of the bar angle versus $\chi^2_{\mu}^{\text{RBP}}$ for the best matching model JR804, showing that our fiducial value $\theta_{\text{bar}}=54.7 \pm 3.8$ (section 3.2.2) from B17 best matches within errors with the minimum value. The minimum value $\chi^2_{\mu}^{\text{RBP}}$ depends on the bar angle to reproduced the observed twist of the bulge isophotes with respect to the projected major axis of the isophotes in the disk region, while the allowed range of angles is given by the flexibility of the made-to-measure technique to adapt the orbital distribution to match the twist. Furthermore, we also consider models with very different dynamical properties such as model JR355 with $(\Upsilon_{3.6}, M_{\text{DM}}^{\text{B}}, \Omega_{\text{p}}) = (0.65, 1.4, 40)^3$, and models neighbouring the best model in variations of the mass-to-light ratio, such as model JR813 with $(\Upsilon_{3.6}, M_{\text{DM}}^{\text{B}}, \Omega_{\text{p}}) = (0.70, 1.0, 40)$, model JR364 with $(\Upsilon_{3.6}, M_{\text{DM}}^{\text{B}}, \Omega_{\text{p}}) = (0.74, 1.0, 40)$, and variations of the bar pattern speed, like model JR683 with $(\Upsilon_{3.6}, M_{\text{DM}}^{\text{B}}, \Omega_{\text{p}}) = (0.72, 1.0, 25)$ and model JR923 with $(\Upsilon_{3.6}, M_{\text{DM}}^{\text{B}}, \Omega_{\text{p}}) = (0.72, 1.0, 55)$, finding that these models also have a minimum values of $\chi^2_{\mu}^{\text{RBP}}$ at $\theta_{\text{bar}} \approx 55^\circ$, confirming therefore that the fiducial bar angle value found by B17 is located in a global chi square minimum, making unnecessary to vary the bar angle during our parameter search exploration.

3.3.2 Properties of the best M2M model

In the following section we compare the photometric and kinematic properties of M31 with the best model from the Einasto grid of models (JR804), showing the contribution of the classical bulge and the B/P bulge components separately as well.

³ $\Upsilon_{3.6}$, M_{DM}^{B} and Ω_{p} in units of $M_{\odot} L_{\odot}^{-1}$, $10^{10} M_{\odot}$ and $\text{km s}^{-1} \text{kpc}^{-1}$

3.3.2.1 Surface-brightness maps

We present our entire photometric M2M fitted map of the best model in Figure 3.16, where we show the bulge and the disc region, as well as M31 in the $3.6\ \mu\text{m}$ band, and a close-up of the bulge in Figure 3.17. The disc of the model fits in general well, where the model is a system in dynamical equilibrium and it has a symmetric structure (to 180° rotations) and hence the larger differences arise where the substructures are observed such as the spiral arms at $\sim 5\ \text{kpc}$ ($1300\ \text{arcsec}$) and the ring at $\sim 10\ \text{kpc}$ ($2600\ \text{arcsec}$). The M31 bulge is also not entirely symmetric, showing asymmetries between the near side (upper) of the bulge and the far side (bottom), where the near side has slightly higher luminosity than the far side, more noticeable for the isophotes with $\mu_{3.6} \geq 16\ \text{mag arcsec}^{-2}$. The dust light extinction is too weak in the $3.6\ \mu\text{m}$ band to cause this asymmetry, with typical V band extinction in the bulge of $A_V \approx 1\ \text{mag}$ (Draine et al. 2014) that corresponds to a $3.6\ \mu\text{m}$ band extinction of $A_{3.6} \sim 0.07\ \text{mag}$ (Schlafly & Finkbeiner 2011). Moreover, the expected dust extinction effect is the opposite of what is observed, where the luminosity in the far side should be systematically higher than in the near side, unlike what is observed in the map of Figure 3.17. The $3.6\ \mu\text{m}$ photometric asymmetry also does not show a spatial correlation with high dust density regions (Figure 3.21) where the dust could have more emission. Another possibility is a minor instability in progress in the outer parts of the B/P bulge, perhaps related to transient material in the disc, or even a possible passage of a satellite galaxy near its centre (Block et al. 2006; Dierickx et al. 2014).

In Figure 3.18 we show separately the classical bulge component and the B/P bulge component of model JR804. As we show with the surface-brightness profile in section 3.3.2.2, the classical bulge dominates in light and mass in the centre. Within $R \lesssim 100\ \text{arcsec}$ it has roundish ellipses isophotes with their major axis roughly aligned with the disc major axis. The B/P bulge is more extended and it has boxy isophotes that give to the combined bulge a twist of the isophotes as observed in M31, shifted away from the disc major axis by $\Delta\text{PA} \sim 13^\circ$ (B17). The classical bulge has a more oblate shape and therefore it cannot reproduce the triaxial structure and the twist.

3.3.2.2 Surface-brightness profiles

In Figure 3.19 we show the azimuthally averaged (AZAV) surface-brightness profiles of the best model and M31 in the $3.6\ \mu\text{m}$ band calculated with `ellipse-IRAF` (Jedrzejewski 1987) directly from the images shown in Figure 3.16. We also plot separately the B/P bulge component and the classical bulge component. We fit the total AZAV surface-brightness profiles of the best M2M model JR804 and M31 with a Sérsic profile (Sérsic 1968; Capaccioli 1989) and an exponential profile out to $15\ \text{kpc}$ using a non-linear least squares (NLLS) minimization method, obtaining the parameters in Table 3.4. We also fit the model components separately, fitting the B/P bulge and the disc with a Sérsic profile and an exponential profile and the classical bulge component alone with a Sérsic profile. We also fit the classical bulge component alone with a Sérsic profile.

We also use `imfit` (Erwin 2015) to perform a 2D fit to the image of the classical bulge component (Figure 3.18 bottom panel) with a Sérsic profile, finding values similar to the 1D

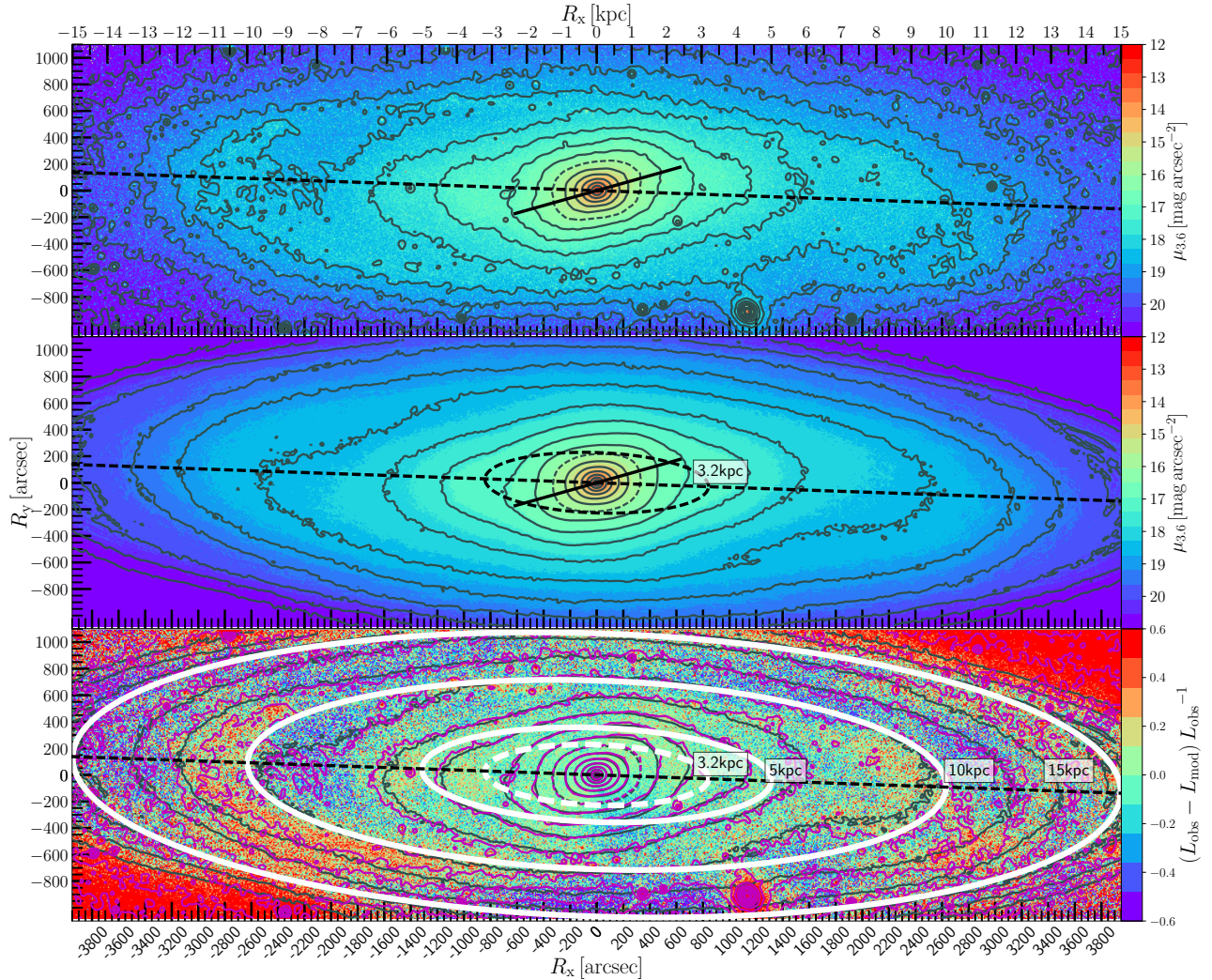


Figure 3.16: Surface-brightness $3.6\mu\text{m}$ band maps and isophotes spaced with $\Delta\mu_{3.6}=0.5 [\text{mag arcsec}^{-2}]$ and the value $\mu_{3.6}=16 [\text{mag arcsec}^{-2}]$ is shown with a dashed isophote. Top panel: M31 with the disc projected major axis at $\text{PA}_{\text{disc}}=38^\circ$ (dash line) and the projected bar major axis at $\text{PA}_{\text{bar}}=55^\circ.7$ (solid line). The north-east and the near side of the disc are in the top part of the panel (positive R_y). Some foreground stars are visible as well as M32 in the bottom at $R_x\sim 1100$ arcsec. Middle panel: Model JR804 with the disc major axis (dash line). We indicating the end of the B/P bulge with a circle projected in the plane of the disk with $i=77^\circ$ at the radii 3.2 kpc (840 arcsec) (black ellipse). Bottom panel: fractional difference normalised by the observations with the isophotes of M31 (magenta) and model JR804 (black). We show with circles projected into the disc the different substructures observed in M31 where the largest deviations occur, where the spiral arms are located 5 kpc (1300 arcsec), the ring-like structures at 10 kpc (2600 arcsec) and at 15 kpc (3950 arcsec) (white ellipses).

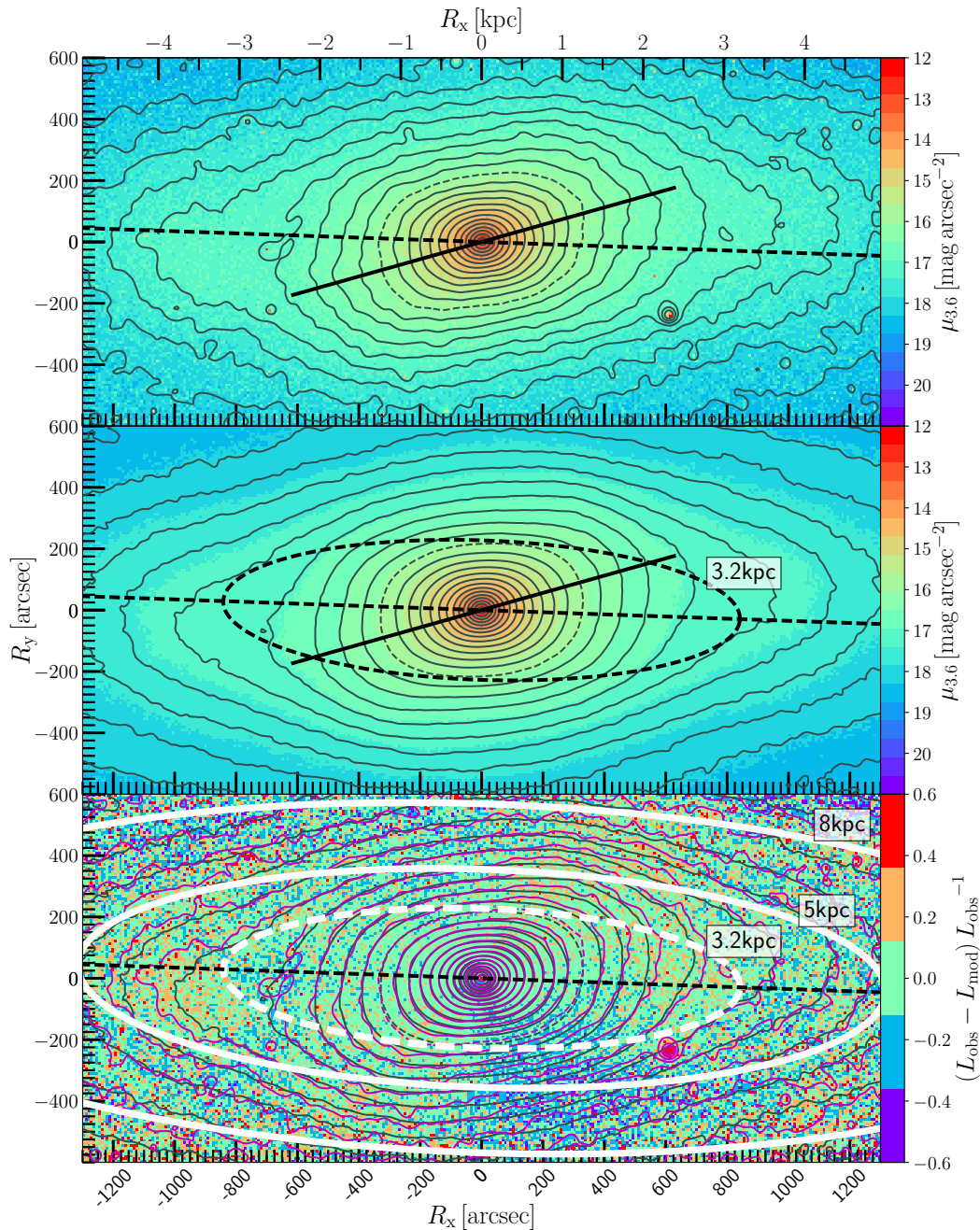


Figure 3.17: Bulge surface-brightness $3.6\mu\text{m}$ band maps and isophotes spaced with $\Delta\mu_{3.6}=0.25[\text{mag arcsec}^{-2}]$ and the value $\mu_{3.6}=16[\text{mag arcsec}^{-2}]$ is shown with a dashed isophote. Top panel: M31 with the disc projected major axis at $\text{PA}=38^\circ$ (dash line). The north-east and the near side of the disc are in the top part of the panel (positive R_y). Middle panel: Model JR804 with the disc major axis (dash line) and the projected bar major axis ($\text{PA}=55.7^\circ$). We show circles in the plane of the disk projected for an inclination of $i=77^\circ$ at the radii 3.2 kpc (840 arcsec), 5 kpc (1300 arcsec) and 8 kpc (2100 arcsec) (red ellipses). Bottom panel: fractional difference normalised by the observations with the isophotes of M31 (magenta) and the model (black), and the projected circles (red ellipses)

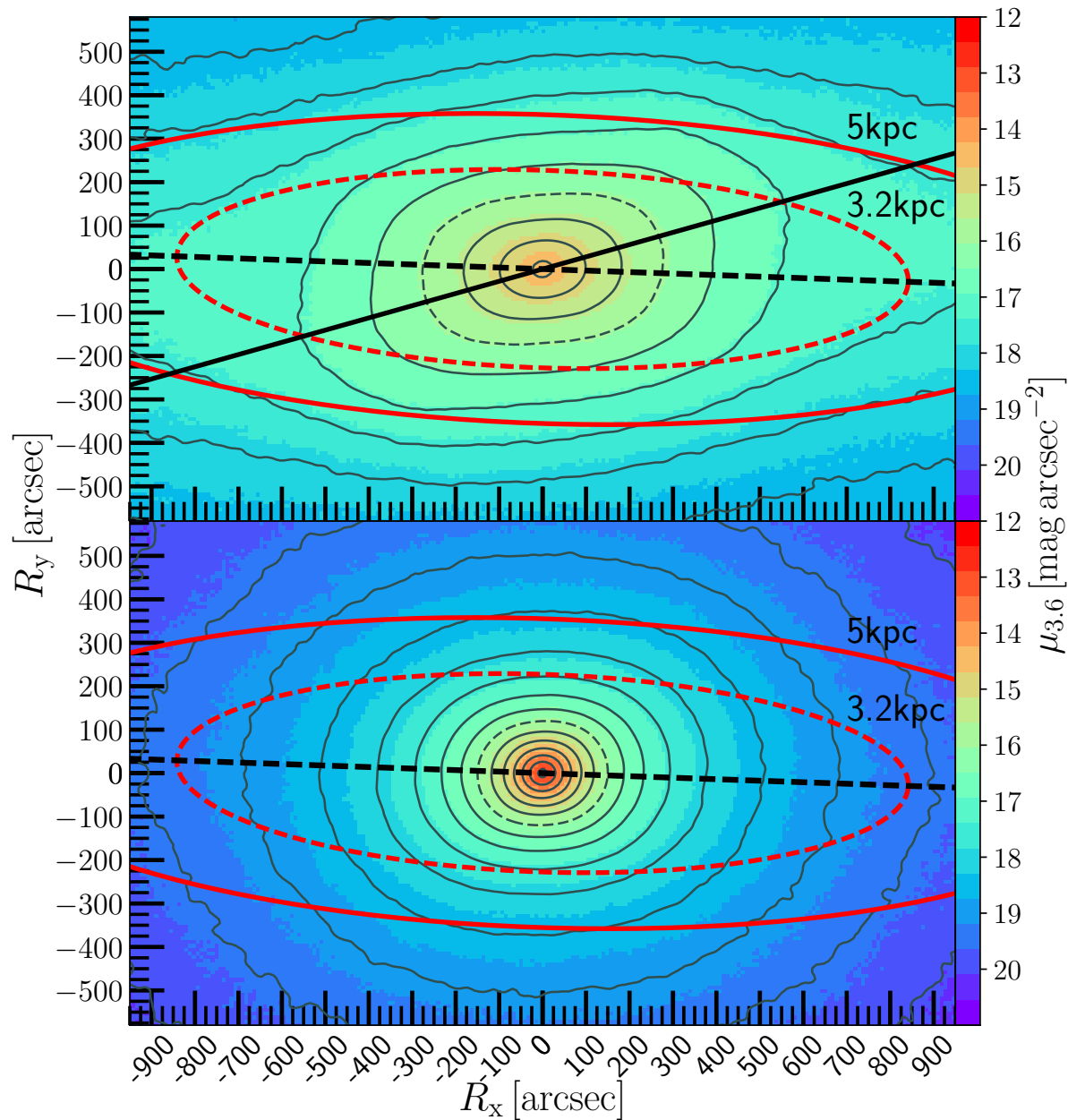


Figure 3.18: Surface-brightness maps of the B/P bulge component (top panel) and the classical bulge component (bottom panel). showing also their isophotes, spaced with $\Delta\mu_{3.6}=0.5$ [mag arcsec $^{-2}$] and the value $\mu_{3.6}=16$ [mag arcsec $^{-2}$] is shown with a dashed isophote. We show circles at the radii 3.2, 5 and 8 kpc in the plane of the disk projected for an inclination of $i=77^\circ$ (red ellipses). The projected bar major axis is shown at PA=55 $^\circ$.7 (solid black line)

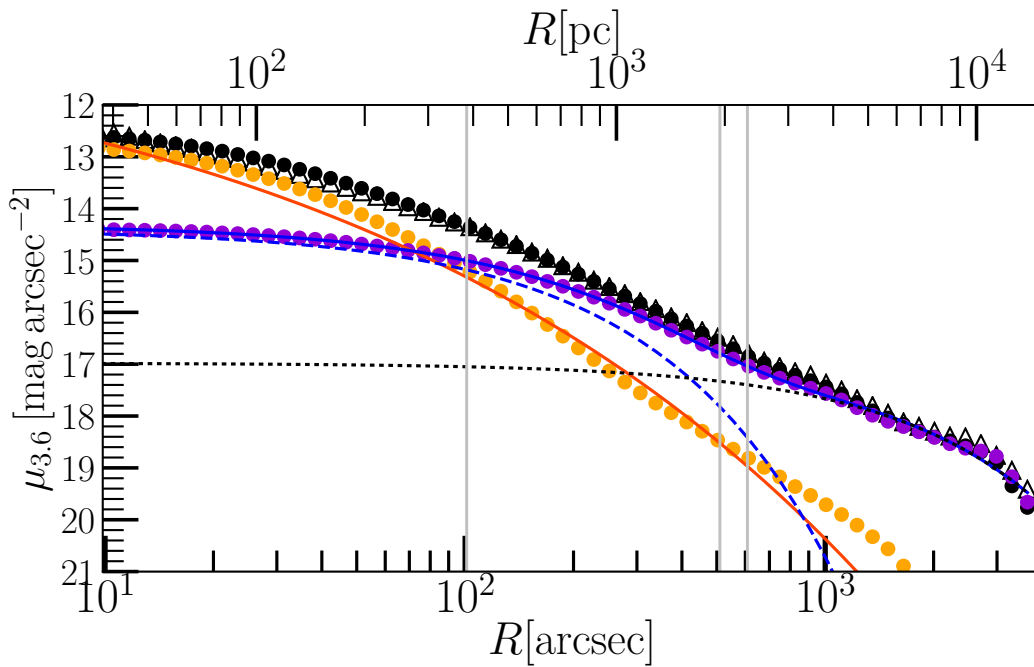


Figure 3.19: Azimuthally averaged surface-brightness profiles in the $3.6\ \mu\text{m}$ band from ellipses fitted to the images of Figure 3.16 as function of the ellipse major axis for M31 (white triangles) and model JR804 (black circles) plotted out to 15 kpc. We also plot separately the classical bulge component (orange circles) with its Sérsic fit (red curve) and the B/P bulge and disc component (purple circles), with its Sérsic fit (dash blue curve), an exponential fit (black dotted curve), and the combined (solid blue curve). The vertical line at 100 arcsec marks the end of region RCB. The vertical lines at 510 arcsec and 600 arcsec mark the end of the projected major axis of the B/P bulge and the thin bar (B17). Region RBP ends at 700 arcsec.

Table 3.4: Photometric profile fit parameters for the azimuthally averaged surface-brightness in the $3.6\ \mu\text{m}$ band for M31 and the best model.

Parameter	M31	CB+BP+disc	BP+disc	CB
n	2.58 ± 0.04	2.24 ± 0.04	1.10 ± 0.01	4.3 ± 0.2
μ_e	16.50 ± 0.04	15.96 ± 0.04	16.42 ± 0.01	17.4 ± 0.1
R_e [kpc]	1.38 ± 0.04	0.98 ± 0.03	1.09 ± 0.02	1.22 ± 0.06
ϵ_{R_e}	0.37 ± 0.01	0.33 ± 0.01	0.40 ± 0.01	0.25 ± 0.02
μ_o [a]	16.94 ± 0.03	16.80 ± 0.03	16.98 ± 0.02	-
R_d [kpc]	5.71 ± 0.08	5.31 ± 0.07	6.02 ± 0.08	-

Notes: parameters from top to bottom are the Sérsic profile parameters: index n , surface-brightness μ_e in units of mag arcsec^{-2} , effective radius R_e and ellipticity ϵ_{R_e} ; and the exponential profile parameters: the surface-brightness μ_o and the disc scale length R_d . Each parameter error is calculated from the range of solutions taking 90 per cent of the chi-square distribution.

fit, with $R_e=273.3$ arcsec, $\mu_e=17.1$ mag arcsec^{-2} and a Sersic index of $n=3.4$. If we neglect the contribution of the B/P bulge in the centre, the resulting Sersic index from the usual photometric decomposition of a Sersic profile and an exponential profile component is $n \approx 2$ as shown by Courteau et al. (2011) and also B17. Fisher & Drory (2008) show that the Sersic index value of $n \sim 2$ is a threshold that can distinguish galaxies with pseudobulges or classical bulges, the later typically showing values larger than 2. However, in our scenario we have a composite bulge with a classical bulge with a high Sérsic index $n^{\text{CB}} \sim 4$ and a B/P bulge with a lower value $n^{\text{BP}} \lesssim 1$, that when fitted with a single Sérsic and an exponential for the disc results in an intermediate value of 2.

The most important properties revealed in the figure are: i) the classical bulge dominates in the central region $R \lesssim 100$ arcsec, and it is required in order to reproduce the central light concentration in M31, and as we show later in more detail in section 3.3.2.4, this component also reproduces the central dispersion profile observed in M31; ii) the end of the B/P bulge and the thin bar in projection are at $R^{\text{BP}}=510$ arcsec and $R^{\text{thin}}=600$ arcsec; ii) the surface-brightness bump at $R \sim 1000 - 1300$ arcsec (4 – 5 kpc) caused by material trailing the bar and spiral arms, reproduced in the model by an increased disc density; and iv) the surface-brightness profile also reveals a second “bump” at 10 kpc (Barmby et al. 2006; Courteau et al. 2011) from which point the surface brightness decreases at a faster rate. This is generally attributed to an additional contribution of the 10 kpc-ring structure, however it is also possible to attribute this to a change in the SB profile, as in the scenario presented here, M31 is a barred galaxy, which are systems that typically develop such a break by process of secular evolution that is related to the Lindblad resonances and the angular momentum transfer, and the redistribution of the disc material by the bar formation (Debattista et al. 2006). As we show later in section 3.3.2.5, we find that the outer Lindblad resonance is indeed located at 11 ± 1 kpc, supporting this scenario. This indicates that the disc of M31 could be a mild Type II.o-OLR disc, consisting of a SB break at ~ 10 kpc and

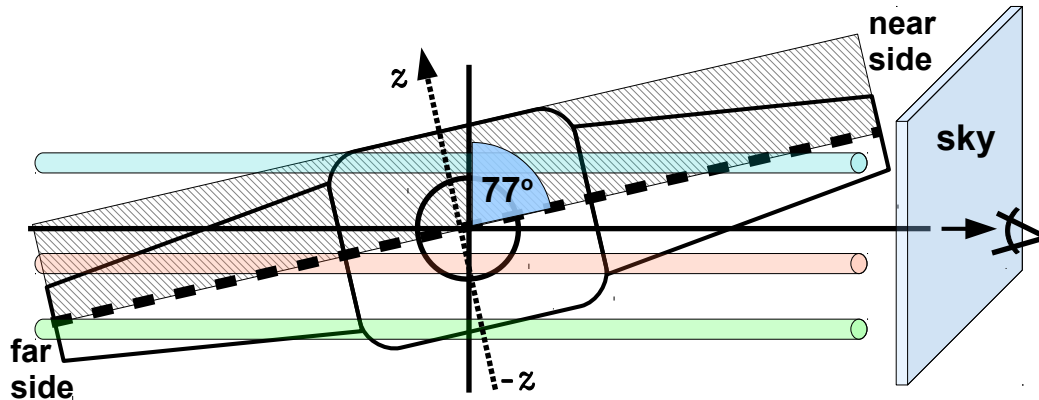


Figure 3.20: Diagram of M31 asymmetric projection effects due to the dust and the geometrical orientation with a disc inclination $i=77^\circ$. Without extinction M31 projects into an image where the near and the far side are symmetric to the observer (right). However, if the light has a strong extinction by the dust located in the plane of the disc (dashed line) the observer detects an asymmetry. With strong extinction the light integrated along the near side of the disc (blue tube) will be dominated by the outer and younger part of the disk, while the material within the dashed area will be obscured by the dust in the plane of the disc. The opposite occurs in the far side of the disk, where the inner part of the disk dominates (green tube). The bulge also projects asymmetrically and as a consequence the region where most of the light of the bulge is detected is slightly shifted to the far side (bottom) from the bulge centre (red tube), being then the deepest part of the bulge.

related to a ring-like structure near the OLR resonance (Erwin et al. 2008; Kim et al. 2014), like the galaxy NGC3504, but more difficult to detect due to the high disc inclination. This would imply that a broken profile would be better suited for the photometric parametrisation of the outer M31 stellar disc, rather than the standard with only one exponential profile component.

3.3.2.3 Dust extinction effects on the observed kinematics

Given that the IFU M31 bulge kinematic observations (O18) are in the V band, we include the effects of the dust extinction in our modelling implemented according to section 3.2.3.4. The diagram in Figure 3.20 qualitatively shows that when some of the light of the galaxy is absorbed by the dust located in the plane of the disc, the projected image can have an asymmetry between the near side of the disc and the far side. These asymmetries are strongly reflected in the kinematics. The line-of-sight to the far side of the disc penetrates more deeply into the galaxy than the near side. Thus, for example, the deepest region in the bulge is located slightly towards the far side from the bulge centre. This effect has been also detected in the reddening of RGB stars (Dalcanton et al. 2015).

We observe the model without dust extinction to fit the image in the $3.6\mu\text{m}$ band calculating the model light observable L , and we also observe the model through an extinction map shown in Figure 3.21 (top panel) calculating L^{AV} . Without dust both sides are symmetric, as shown

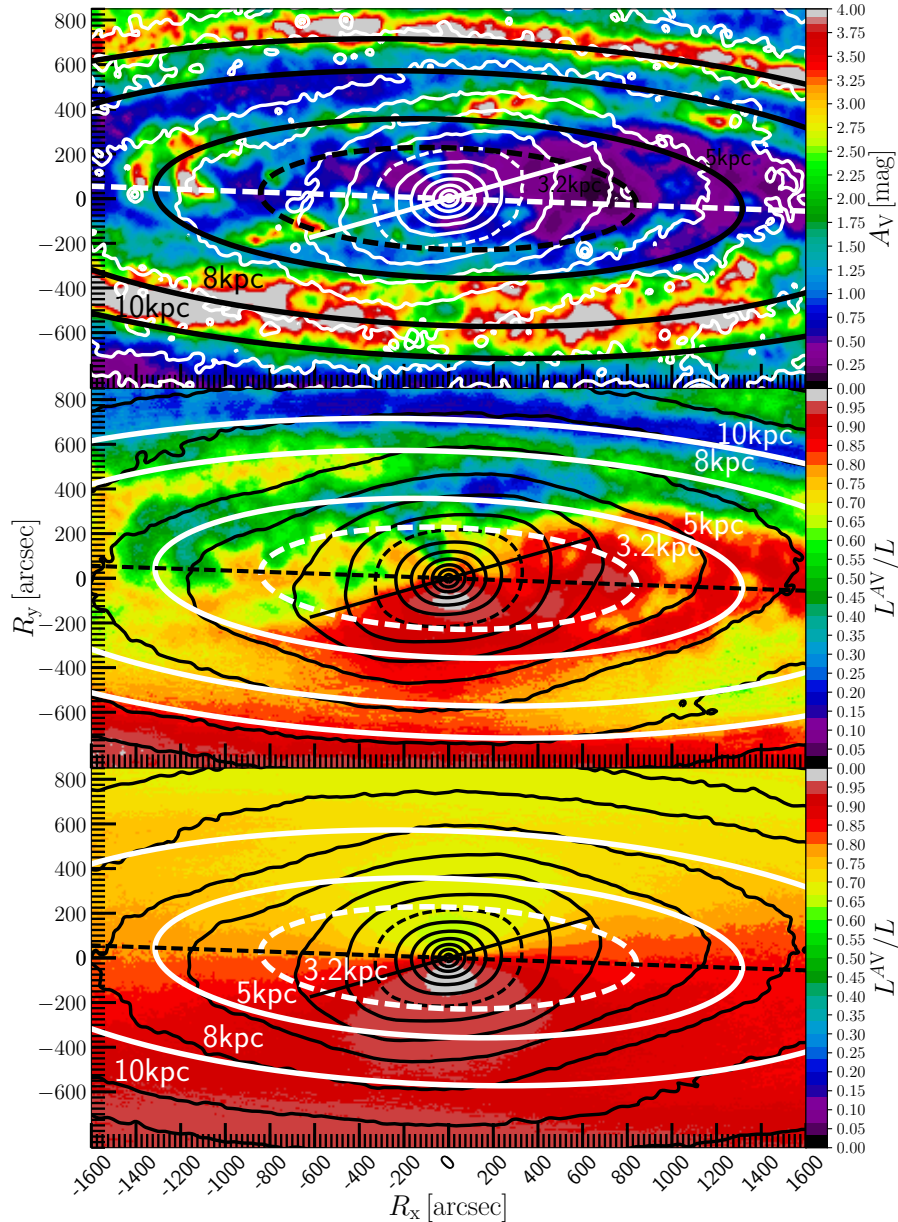


Figure 3.21: Top panel: M31 absorption map in the V band calculated from equation 3.13 and the dust surface mass map (Draine et al. 2014). The disc projected major axis (dash line) with the near side of the disc is in the upper part of the figure (positive R_y). The M31 isophotes in the $3.6\ \mu\text{m}$ band (white contours) are shown spaced with $\Delta\mu_{3.6}=0.5\ [\text{mag arcsec}^{-2}]$ and the value $\mu_{3.6}=16\ [\text{mag arcsec}^{-2}]$ is shown with a dashed isophote. Middle panel: model JR804 luminosity ratio between the light absorbed model observable L^{AV} and the light un-absorbed model observable L . The model isophotes (black contours) are shown spaced with $\Delta\mu_{3.6}=0.5\ [\text{mag arcsec}^{-2}]$ and the value $\mu_{3.6}=16\ [\text{mag arcsec}^{-2}]$ is shown with a dashed isophote. We show circles at the radii 3.2, 5 and 8 kpc in the plane of the disk projected for an inclination of $i=77^\circ$ (white ellipses). The projected bar major axis is shown with a black solid line. Note the white region near the bulge centre where effects of the extinction in the V band are minimal. Bottom pane: L^{AV} and L ratio and isophotes for a model with the parameters of JR804, but observed and fitted through a dust map with a constant absorption of $A_V=0.5\ \text{mag}$

in Figure 3.17, however with light extinction the model produces the asymmetry between the near side of the disc and the far side, as shown in Figure 3.21 (middle panel) with the ratio $f_{AV}=L^{AV} L^{-1}$, where for the region of the map with the value of $f_{AV}=1$ means that all the light is detected, while for a ratio of zero it is completely absorbed. Note that the ratio f_{AV} is proportional to the ratio between the light in the V band and the $3.6\mu\text{m}$ band.

The map reveals interesting features that are caused not only by the dust absorption itself, but also by the geometrical orientation of M31 with its disc inclination $i=77^\circ$ and its bar angle $\theta_{\text{bar}}=54^\circ.7$. The least absorbed (or deepest) region in the M31 bulge is shifted to the far side of the disc (white region at $R_y \sim -100$ arcsec), as expected from the diagram in Figure 3.20, and the most extreme effect of extinction near the M31 bulge is in the near side of the disc between $R_y \sim 200$ arcsec and 400 arcsec (blue regions) due to the dust accumulated in the spiral arms. And regions with large amounts of dust can have lower effects of light extinction like the far side at $R_y \sim -500$ arcsec where the outer ring is with a large dust lane.

In the bottom panel of Figure 3.21 we show a fit where we used a constant light absorption of $A_V=0.5$ mag to estimate how the heterogeneity of the M31 dust map (Draine et al. 2014) affects the ratio $L^{AV} L^{-1}$, finding that the general features and the asymmetry are also reproduced. Dalcanton et al. (2015) finds lower absorption values in M31 than Draine (2014), for which we reduced the absorption values of the dust map by 50 per cent, finding a model with properties similar to the overall best model, where the asymmetries are also reproduced, but are weaker.

We conclude that the most important consequence of the dust extinction for the kinematics in the V band is that kinematic asymmetries are also generated between the near side of the disc and the far side, because the light integrated along the line-of-sight can be dominated by different structures with different intrinsic kinematic properties. An example of this is shown by Baes & Dejonghe (1999) for elliptical galaxies. Furthermore, it is important to consider that neither the near side of the disc, nor the far side, have the complete signature along the line of sight, although the far side is much less affected by light extinction.

3.3.2.4 Stellar kinematics

In this section we present the bulge kinematics of the best model and compare them with the IFU kinematic measurements of O18.

For a better qualitative comparison we show kinematic maps in Figure 3.22, presenting the velocity, the dispersion, $h3$ and $h4$ of M31, the best model JR804 and the residuals. In Figure 3.23 we show separately the classical bulge component and the B/P bulge component of the best model. For an easier quantitative comparison we also show kinematic profiles along the disc major axis in Figure 3.24, and along the bar projected major and minor axis in Figure 3.25.

I) *The line-of-sight dispersion (σ_{los}):* it has three important features that are reproduced by the model:

- i) Within $R < 100$ arcsec the velocity dispersion of M31 shows two peaks of $\sigma_{\text{los}}^{\text{max},\text{M31}} \sim 170 \text{ km s}^{-1}$ along the bulge minor axis (O18), with a drop of σ_{los} in the centre. We find that this is produced by the concentrated classical bulge that dominates in the centre, as shown in

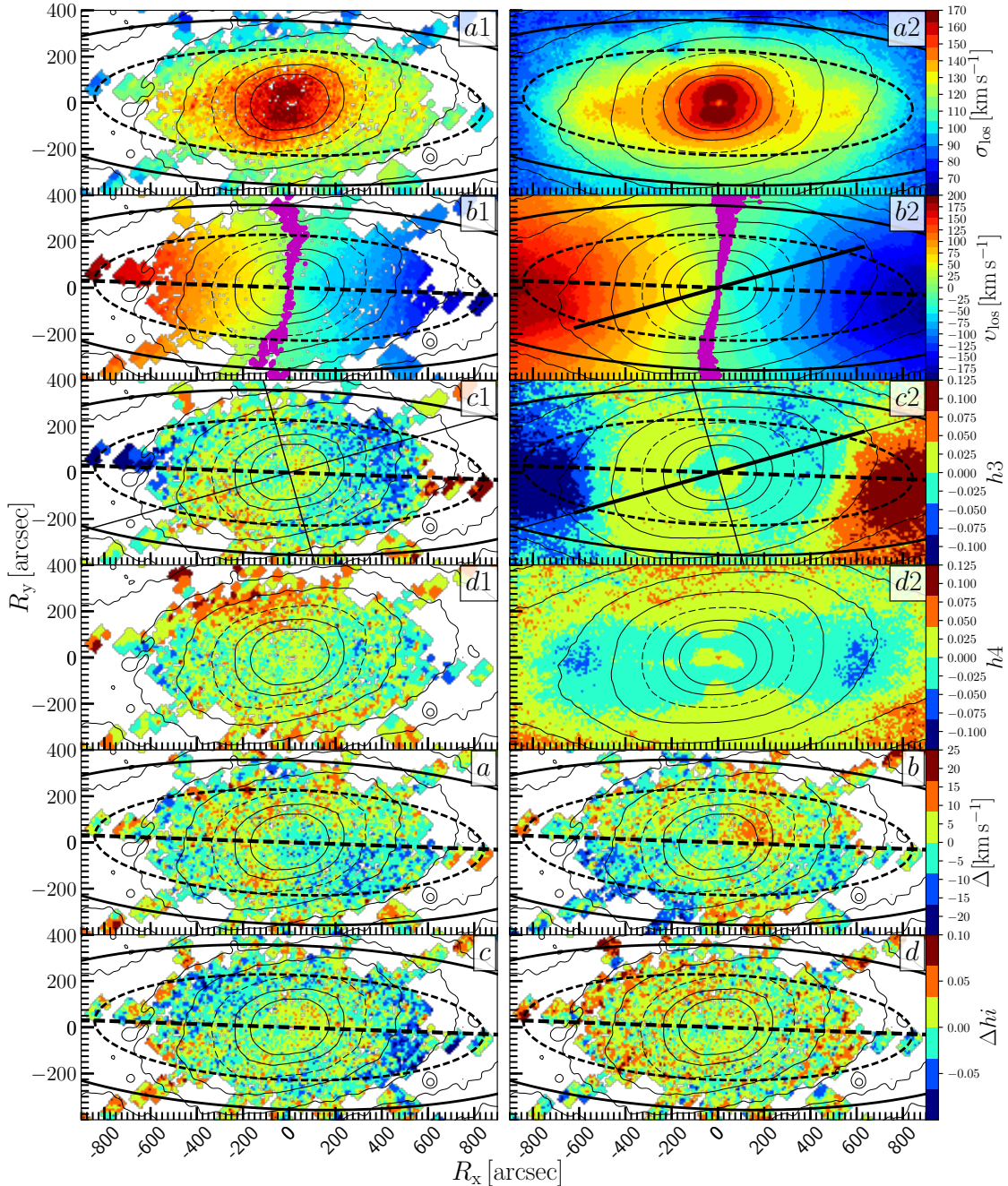


Figure 3.22: Kinematic maps of σ_{los} , v_{los} , $h3$, $h4$ and isophotes of M31 (O18) (a1, b1, c1, d1) and model JR804 (panels a2, b2, c2, d2), showing isophotes spaced every $\Delta\mu_{3,6}=0.5$ [mag arcsec $^{-2}$] and $\mu_{3,6}=16$ [mag arcsec $^{-2}$] (dashed isophote). We exclude the central isophotes to better reveal the kinematic features. Some panels display two circles projected on the disc's plane with $i=77^\circ$ at 3.2 kpc (black dashed ellipse) and 8 kpc (solid black ellipse), the projected disk major axis (dash black line), and the projected bar major axis (black line at $\text{PA}=55^\circ.7$) and minor axis (black line at $\text{PA}=145^\circ.7$). The differences between the observations and the model are shown in panel (a) with $\Delta=\sigma_{\text{los}}^{\text{obs}} - \sigma_{\text{los}}^{\text{model}}$, (b) with $\Delta=||v_{\text{los}}^{\text{obs}}|| - ||v_{\text{los}}^{\text{model}}||$, (c) with $\Delta h3=h3^{\text{obs}} - h3^{\text{model}}$, and panel (d) with $\Delta h4=h4^{\text{obs}} - h4^{\text{model}}$. We show the zero velocity values within a range $v_{\text{los}}=0 \pm 5$ km s $^{-1}$ (magenta) in panels b1 and b2.

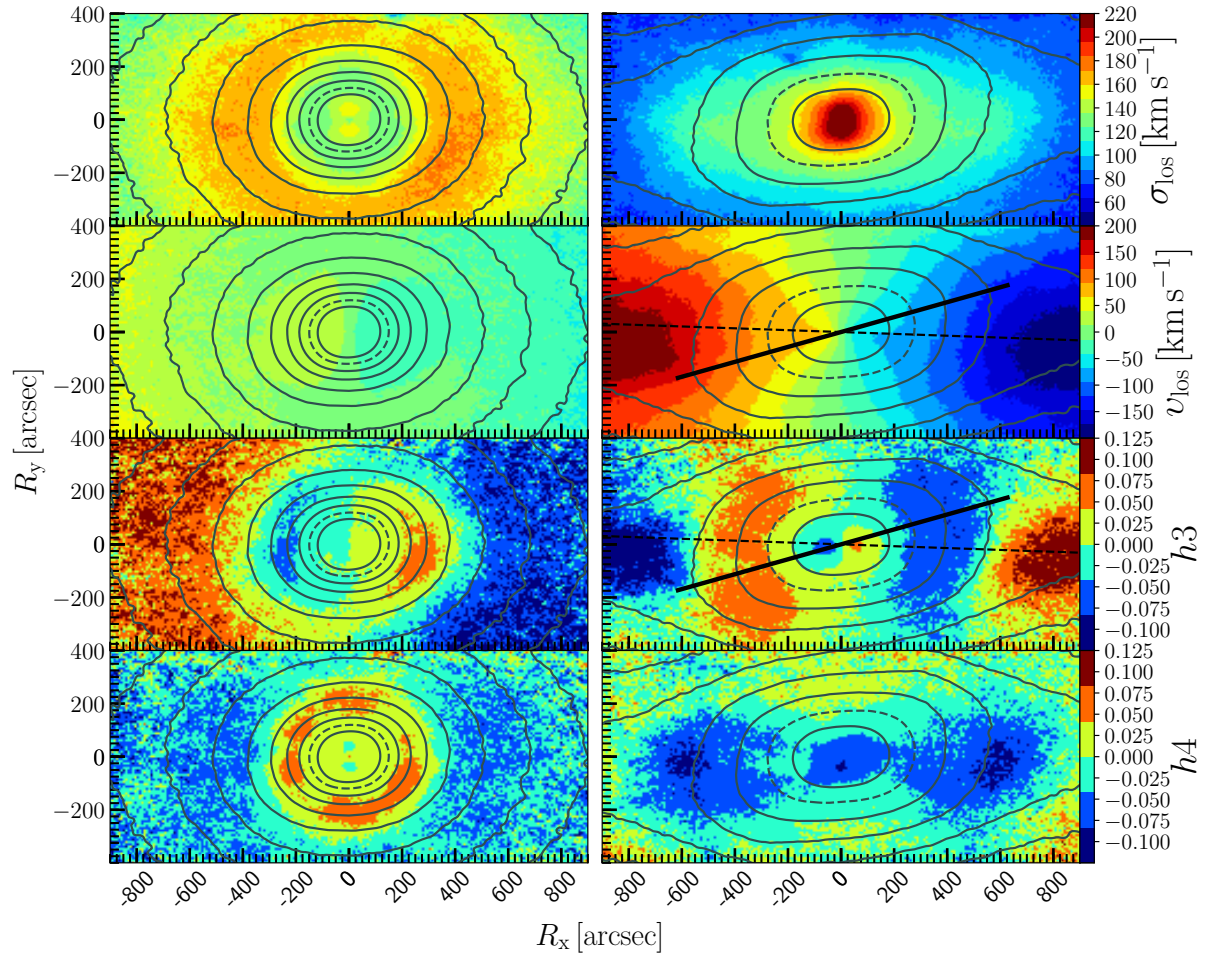


Figure 3.23: Kinematic maps and isophotes of model JR804 for the classical bulge particles (left column) and the B/P bulge and disc particles (right column). The isophotes are spaced every $\Delta\mu_{3,6}=0.5$ [mag arcsec $^{-2}$] and the value $\mu_{3,6}=16$ [mag arcsec $^{-2}$] is shown with a dashed isophote. We exclude the isophotes in the centre to better reveal the central kinematic structures of each bulge component.

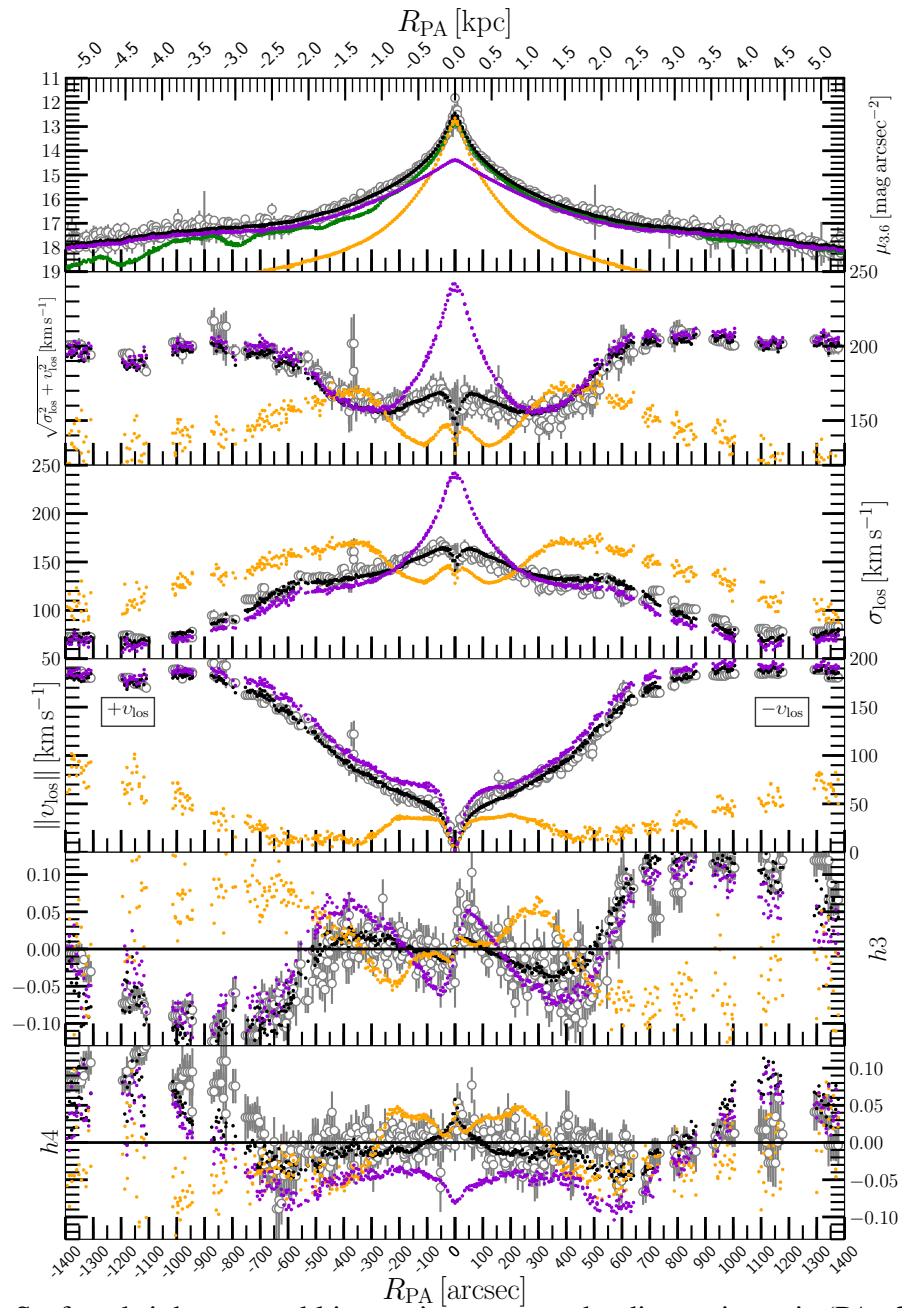


Figure 3.24: Surface-brightness and kinematic cuts near the disc major axis ($PA=33^\circ$) of model JR804 (black dots) with its components, the classical bulge (orange) and the B/P bulge (purple), and of M31 (white circles). We also plot the extinguished surface-brightness of the model observable L^{AV} (μ_{AV} , green line). Positive R_{PA} extends into the far side of the disc.

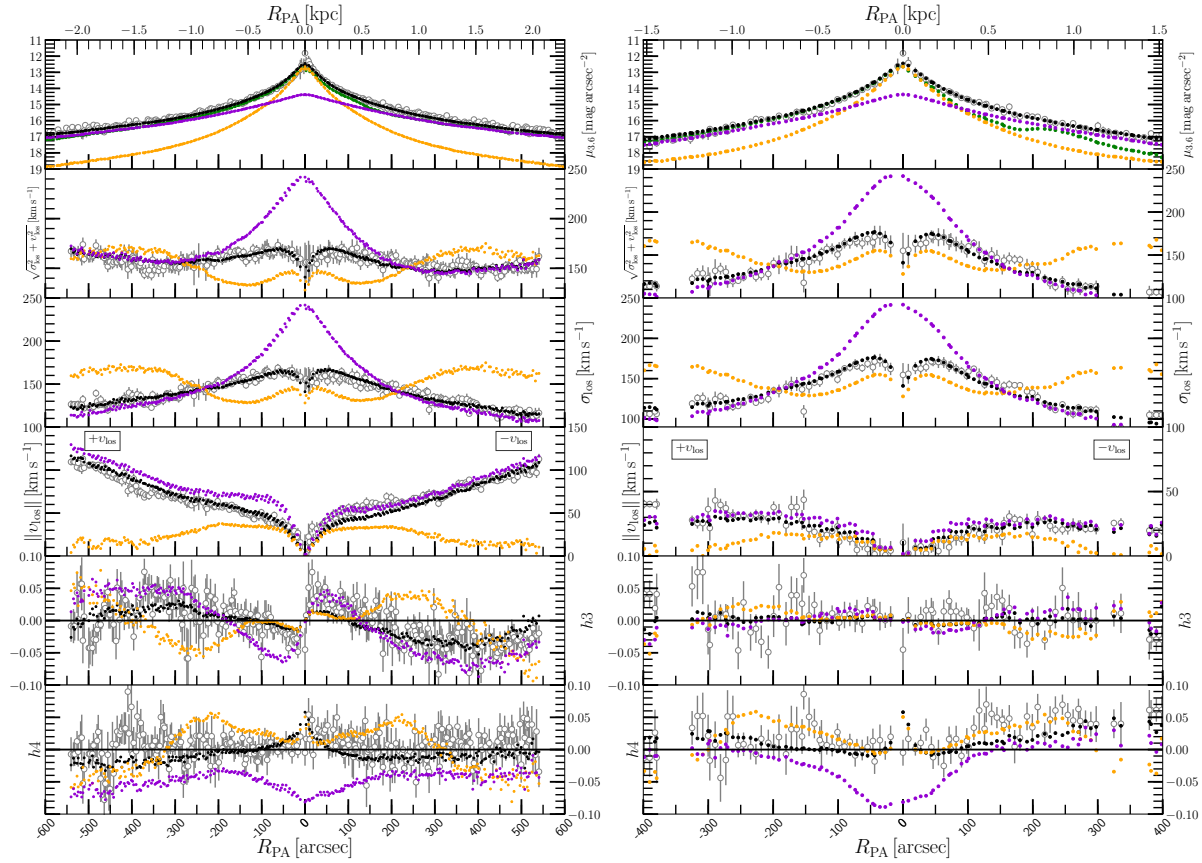


Figure 3.25: Surface-brightness and kinematic cuts along the projected bar major axis (PA=55.7°) in the left column and the bar minor axis (PA=145.7°) in the right column of model JR804 (black dots) with its components, the classical bulge (orange) and the B/P bulge (purple), and of M31 (white circles). We also plot the extinguished surface-brightness of the model observable L^{AV} (μ_{AV} , green line). Positive R_{PA} extends into the near side of the disc.

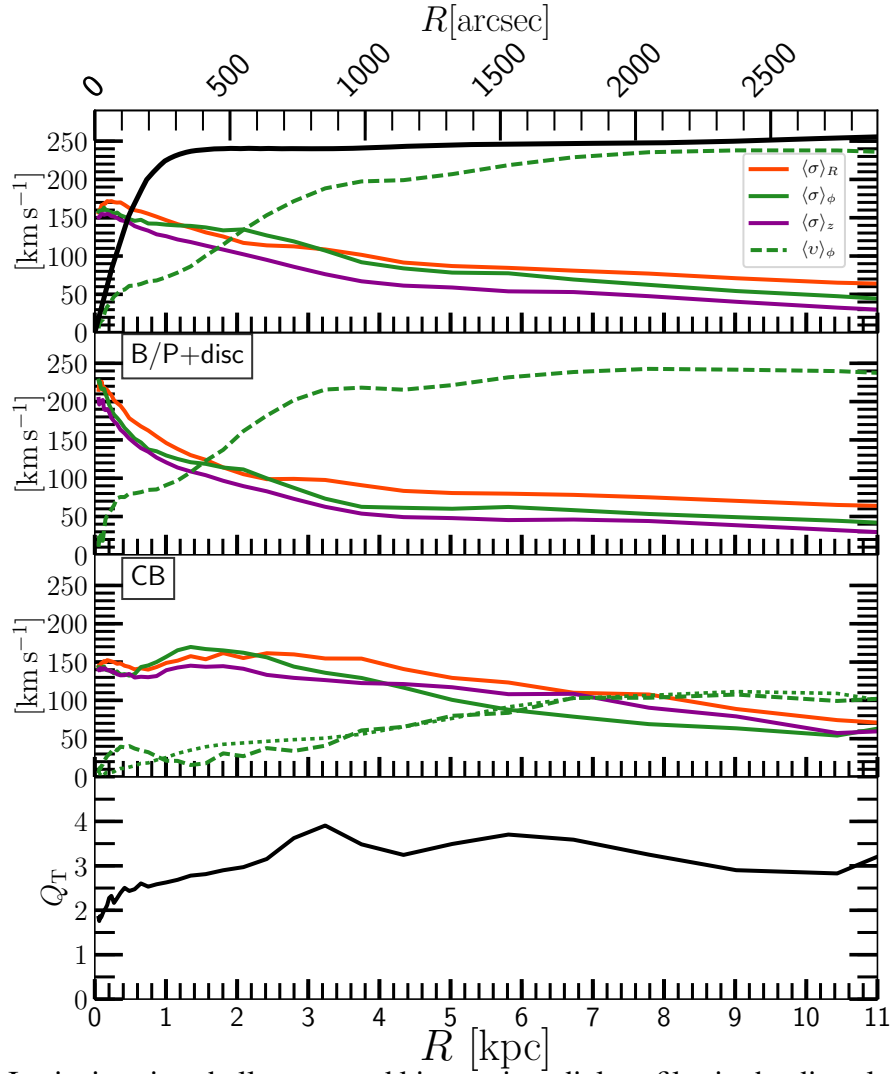


Figure 3.26: Intrinsic azimuthally averaged kinematic radial profiles in the disc plane for the best Einasto model for the total stellar components (top panel), B/P bulge and disc (second panel), CB component (third panel), and the Toomre parameter Q_T (bottom panel). The dispersion profiles are shown in the first three panels in solid line for the coordinates $\langle\sigma\rangle_R$ (red), $\langle\sigma\rangle_\phi$ (green) and $\langle\sigma\rangle_z$ (magenta), and the streaming velocity $\langle v\rangle_\phi$ is shown with a dashed green line. We also show $\langle v\rangle_\phi$ of the classical bulge of Model 1 (dots green line). The total circular velocity is shown in the first panel (black line).

B17, which is revealed with the dispersion maps of each component in Fig 3.23, and in the σ_{los} profiles of Figure 3.24 and 3.25. The classical bulge mass profile is similar to a Hernquist model, where the material in the centre requires much lower kinetic energy to remain confined in gravitational equilibrium, leading to a dispersion drop. The two dispersion peaks, and partially the dispersion drop, can also be attributed to CB particles in circular orbits near the centre, as Hernquist (1990) shows for the Hernquist model. When plotted separately, the maximum central velocity dispersion of the classical bulge alone is $\sigma_{\text{los}}^{\text{max,CB}} \sim 150 \text{ km s}^{-1}$, which combined with the high maximum central dispersion of the B/P bulge with a peak of $\sigma_{\text{los}}^{\text{max,BP}} \sim 240 \text{ km s}^{-1}$, reproduce the central dispersion in M31. A very important characteristic of the B/P bulge is that its high central velocity dispersion is caused by the deep gravitational potential of the classical bulge component, which due to its high mass concentration increases the central circular velocity. This results in particles orbiting the B/P bulge and the thin bar that have high velocities when passing the centre.

- ii) Our model also reproduces the two elongated high σ_{los} plateaus in the bulge noted by O18 within $R_x = \pm 600 \text{ arcsec}$ shown in Figures 3.22 and 3.25. This features are reproduced in the model by the B/P bulge that dominates here over the classical bulge. At the end of the B/P bulge along the projected bar major axis, or at the projected disc major axis at $R_x \sim -600 \text{ arcsec}$, the B/P bulge surface-brightness is $\mu_{3,6} \sim 17 \text{ mag arcsec}^{-2}$, while the classical bulge is much fainter, with $\mu_{3,6} \sim 18.5 \text{ mag arcsec}^{-2}$. The dispersion of the classical bulge component in the outer part rises again. Further out the two σ_{los} plateaus end at $R_x \sim 600 \text{ arcsec}$, decreasing along the major axis (Figure 3.22 to $\sigma_{\text{los}} \sim 70 \text{ km s}^{-1}$ in the disc.
- iii) Along the disc minor axis and at the near side of the disc (positive R_y) the dispersion is systematically lower than the far side of the disc (negative R_y) as shown by the maps (Figure 3.22) and the profiles (Figure 3.25). This feature is also reproduced in the model, and caused by the dust absorption. This can be understood from Figure 3.20, and the dust extinction map in Figure 3.21: the light of the near side of the bulge that is behind the dust plane is strongly extinguished by the dust, leaving mostly the light of the foreground disc that has a dispersion lower than the bulge. In contrast, at negative R_y , most of the light of the bulge is transmitted, while part of the light of the kinematically cooler disc material, which is now behind the bulge is absorbed, resulting in dispersions slightly higher than if the disc would be fully included. The dust also causes the observed asymmetry between the two σ_{los} plateaus, where for the side of $R_x < 0 \text{ arcsec}$ the dispersion is higher than at the side of $R_x > 0 \text{ arcsec}$.

II) *The line-of-sight velocity (v_{los}):* We also find that the combination of both bulge components reproduces different characteristics of the M31 bulge velocity field, listing three of them below:

- i) In the very centre ($R < 50 \text{ arcsec}$) and near the disc major axis (PA=33°) (Figure 3.24) both bulge components show similar rotation ($v_{\text{los}} \sim 30 \text{ km s}^{-1}$). However, at $R \sim 100 \text{ arcsec}$ the B/P bulge rotates much faster, reaching already $\sim 70 \text{ km s}^{-1}$, while the classical bulge component has $\sim 35 \text{ km s}^{-1}$, which then combined reproduce the total velocity of M31 with $\sim 50 \text{ km s}^{-1}$. Between 100 arcsec and 600 arcsec along the disc major axis, the B/P bulge

dominates the light and the rotation increases with a constant slope, reaching a roughly constant value of $v_{\text{los}} \sim \pm 200 \text{ km s}^{-1}$ in the disc region.

- ii) Analysing the difference in velocity between the model and the observations in the panel *b* of Figure 3.22, we find a region in the observations at $(R_x, R_y) = (200 \text{ arcsec}, 100 \text{ arcsec})$ that has a velocity $\sim 10 \text{ km s}^{-1}$ higher than the model. This is an asymmetry in the M31 observations that is not reproduced by our dust modelling. CO observations in this region (Melchior & Combes 2011) indicate that the molecular gas kinematics is complex and maybe tilted in this region, and so it may be that our dust modelling is too simple here. As the bar major axis v_{los} profile shows (Figure 3.25), the B/P bulge velocities match the observations well, suggesting that classical bulge light contribution could be much weaker in this particular region.
- iii) The velocity map (Figure 3.22) shows in the centre a twist in the zero velocity values that reproduces the velocity twist observed in M31. The twist is weaker in the very centre (within 100 arcsec) due to the classical bulge component, which has a more oblate structure (Figure 3.23).

III) The Gauss-Hermite coefficients $h3$ and $h4$:

- i) The $h3$ maps (Figure 3.22) and profiles (Figure 3.25) show that the $h3$ values in the disc region beyond $(R_x > 700 \text{ arcsec})$ are anti-correlated with the velocity v_{los} , changing when we enter the region of the bar, with $h3$ then correlated with the velocity, as expected (Bureau & Athanassoula 2005; Iannuzzi & Athanassoula 2015). However, the central region of M31's bulge has a second change of sign in $h3$, which is also reproduced by the model (*i.e.* $h3$ and v_{los} are again anti-correlated for isophotes with $\mu \leq 16.5 \text{ mag arcsec}^{-2}$). This central $h3 - v_{\text{los}}$ anti-correlation feature is produced by both bulge components, and it is driven by the near axisymmetric density distribution, similar to the way that the asymmetric drift causes the $h3 - v_{\text{los}}$ anti-correlation in the axisymmetric disc. The dust extinction also generates an asymmetry between the $h3$ at the left and the right side of the bar that is reproduced by the model (Figure 3.22). In particular, the $h3 - v_{\text{los}}$ correlation in the bar region is more extended along the R_x axis in the positive side of R_x . This is because the light from the bar at negative R_x is more strongly absorbed, leaving the disc component more visible.
- ii) The M31 $h4$ map in Figure 3.22 reveals in the centre a positive region, while at the end of the B/P bulge ($R_x \sim \pm 600 \text{ arcsec}$) the $h4$ map shows negative values. In the model the B/P bulge $h4$ map in Figure 3.23 shows mostly negative values, and the central positive $h4$ region is reproduced by the classical bulge that shows strong positive $h4$ (except where the two σ_{los} peaks are detected, where the classical bulge $h4$ is negative). Along the disc minor axis $h4$ has positive values at $R_y = \pm 400 \text{ arcsec}$, with larger positive values in the near side of the disc, which is where the dust extinction effects are stronger. Our $h4$ maps also agree with the results for other B/P bulge models (Iannuzzi & Athanassoula 2015), where $h4$ depends on the bar angle for bars with strong B/P bulges, while bars with weak or without a B/P bulge show a weaker dependence.

IV) *Stellar kinematics in the outer disc and the inner spheroid:*

In Figure 3.26 we show the de-projected kinematic profiles of the best Einasto model. We also show the Toomre parameter $Q_T = \kappa \langle \sigma \rangle_r (3.36 G \Sigma(R))^{-1}$ (Toomre 1964) calculated using the epicycle frequency κ from the total circular velocity, the surface mass density $\Sigma(R)$ and the radial velocity dispersion $\langle \sigma \rangle_r$ from the disc particles. The stellar disc is stable and dynamically hot with a radially averaged value and standard deviation of $\langle Q_T \rangle = 2.6 \pm 0.6$. This is consistent with Dorman et al. (2015, see their Figure 16) who finds a dynamically hot stellar disc.

The intrinsic kinematic profiles in Figure 3.26 also shows that in the outer parts the classical bulge increases its rotation to $\sim 70 \text{ km s}^{-1}$ at 5 kpc, similar to the values estimated for the inner spheroidal component at that radius (Dorman et al. 2012), reaching $\sim 100 \text{ km s}^{-1}$ at 10 kpc. The outer rotation of the classical bulge is similar to the Model 1 of B17, which obtained all its rotation from the angular momentum transfer from the bar (Saha et al. 2016). The increase of the rotation of the inner spheroid at this radius is not unexpected, as for example it is also observed in the Milky Way's inner stellar halo (Ness et al. 2013; Perez-Villegas et al. 2017).

V) *Stellar and globular cluster kinematics:*

Given that the kinematic properties of each bulge component are different, is there a signature to identify each stellar component observationally? Morrison et al. (2011) obtained velocities and metallicities of a sample of old star clusters near the M31 centre, finding that the metal-rich clusters near the disc have velocities similar to the M31 surrounding field stars ($\sim 200 \text{ km s}^{-1}$), but within the B/P bulge region ($R < 2 \text{ kpc}$), the clusters reach higher velocities ($\sim 300 \text{ km s}^{-1}$) similar to the B/P bulge dispersion profile presented here. Given that they assumed that the bar is roughly edge on ($\theta_{\text{bar}} \sim 20^\circ$) they associate the metal-rich component with the x_2 orbits that are perpendicular to the bar. However, here we find $\theta_{\text{bar}} \sim 55^\circ$ with the end of the thin bar in projection at $R = 2.3 \text{ kpc}$ (600 arcsec) approximately the location where the metal-rich star clusters velocity change. The more metal-poor clusters show less co-rotation with the field stars with a more broad velocity distribution, similar to our classical bulge kinematic properties. Therefore, given the scenario presented here, the star clusters could be associated with different bulge components.

3.3.2.5 Kinematics: circular velocity & the Lindblad resonances.

In Figure 3.27 we show the total circular velocity V_c profile of the best model JR804 with its different components. The classical bulge component reaches a maximum circular velocity of $V_c^{\text{CB,max}} = 165 \text{ km s}^{-1}$ at 1.0 kpc, dominating over the B/P bulge component within $R \leq 0.5 \text{ kpc}$, and then drops rapidly. The B/P bulge component reaches a maximum of $V_c^{\text{BP,max}} = 160 \text{ km s}^{-1}$ at 2.0 kpc, where it dominates over the classical bulge, which has 140 km s^{-1} at that radius. The total circular velocity increases fast due to the classical bulge contribution, reaching $V_{c,o} = 235 \text{ km s}^{-1}$ at 1.6 kpc where it stays roughly flat reaching a maximum of $V_{c,\text{max}} = 255 \text{ km s}^{-1}$ at $\sim 12.5 \text{ kpc}$. We also show the HI rotation curve of Corbelli et al. (2010) that is used to fit the dark matter density profile, which is in general well fitted. The authors neglect the inner $R < 8.5 \text{ kpc}$, arguing

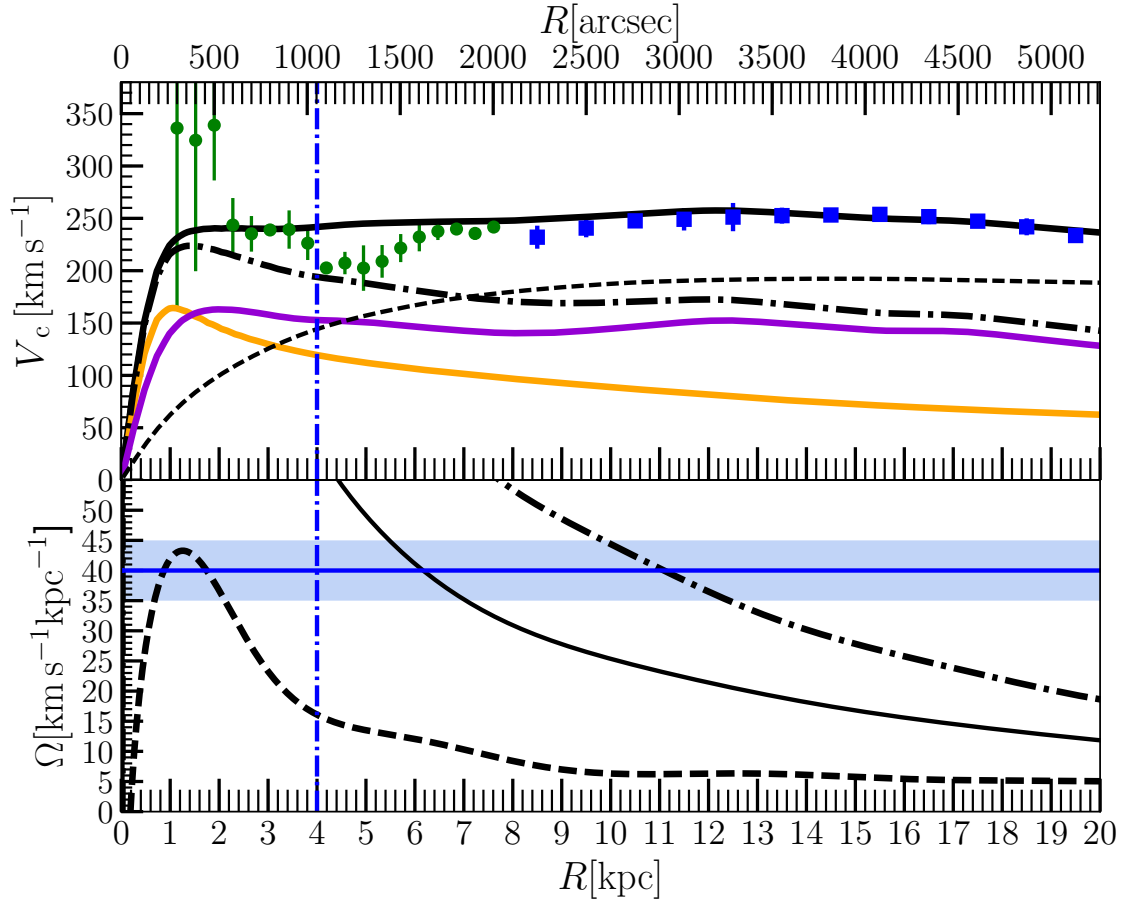


Figure 3.27: Top panel: azimuthally averaged circular velocity in the plane of the disc of the model JR804 with the different components: the classical bulge (orange), the B/P bulge and the stellar disc (purple), the total stellar component (dot dashed line), the dark matter (dash) and the total circular velocity (solid black). The HI data of [Corbelli et al. \(2010\)](#) is shown out 26 kpc (blue squares) that is fitted out to 21 kpc. We also show the HI data of [Chemin et al. \(2009\)](#) within 8 kpc (green squares). Bottom panel: the angular frequency profile Ω (solid curve), $\Omega_{\text{ILR}} = \Omega - \kappa/2$ (dash curve), and $\Omega_{\text{OLR}} = \Omega + \kappa/2$ of the model JR804 with a bar pattern speed $\Omega_p = 40 \pm 5 \text{ km s}^{-1} \text{ kpc}^{-1}$ (horizontal line). The corotation radius, the Lindblad resonances inner inner, the outer inner, and the outer are located at $r_{\text{cor}} = 6.5 \pm 1.0 \text{ kpc}$, $r_{\text{ILR}} = 1.0 \text{ kpc}$, $r_{\text{OILR}} = 1.8 \text{ kpc}$ and $r_{\text{OLR}} = 11.2 \pm 1.0 \text{ kpc}$.

the presence of an inner warp and the non-circular motion of the gas. For comparison we also show the inner $R < 8$ kpc of the HI rotation curve from Chemin et al. (2009).

In the bottom panel of Figure 3.27 we show the angular frequency profile (Ω) of the best model, with the range of best bar pattern speed $\Omega_p = 40 \pm 5 \text{ km s}^{-1} \text{ kpc}^{-1}$. The corotation radius, where $\Omega_p = \Omega$, is located at $r_{\text{cor}} = 6.5 \pm 1.0$ kpc. The isophotal comparison of the M31 bulge with N-body models in B17 suggests that the thin bar length of M31 is $r_{\text{bar}}^{\text{thin}} \sim 4.0$ kpc, which would classify M31's bar as a slow bar with $\mathcal{R} = 1.6 \pm 0.2$, where Debattista & Sellwood (2000) define slow bars when $\mathcal{R} = r_{\text{cor}}/r_{\text{bar}}^{\text{thin}} \leq 1.4$. The inner inner and the outer inner Lindblad resonances $\Omega_{\text{ILR}} = \Omega - \kappa/2$ Lindblad (1956), in this model are located at $r_{\text{ILR}} = 1.0$ kpc and $r_{\text{OILR}} = 1.8$ kpc. The outer Lindblad resonance $\Omega_{\text{OLR}} = \Omega + \kappa/2$ is then at $r_{\text{OLR}} = 11 \pm 1$ kpc.

The gas kinematics and its distribution in M31 shows many substructures that are consistent with the typical properties observed in other barred galaxies. In the centre of the bulge between ~ 1 kpc (260 arcsec) and ~ 2 kpc (500 arcsec) the gas velocity measured by Chemin et al. (2009) reaches $\sim 340 \text{ km s}^{-1}$, higher than the circular velocity $V_c \sim 230 \text{ km s}^{-1}$. However, this difference is expected in barred galaxies where the gas has a non-circular motion with infalling streams of gas, as shown by Kim et al. (2012, see their Figure 5) (Li et al. 2015). Such streams are typically located near the inner Lindblad resonances, which in this model are at $r_{\text{ILR}} = 1.0$ kpc (260 arcsec) and $r_{\text{OILR}} = 1.8$ kpc (470 arcsec), almost exactly where O18 also detects the presence of high velocity streams of gas with $\sim \pm 300 \text{ km s}^{-1}$.

A second signature is that the HI gas velocity drops in the transition between the bar and the disc, as observed between 4 kpc and 6 kpc. This again is typically produced in barred galaxy simulations due to the non circular motion of the gas in a non axisymmetric potential produced by the bar.

Finally, there is the 10 kpc ring-like substructure (Habing et al. 1984; Gordon et al. 2006; Barmby et al. 2006). This is made of stars, gas and dust and it is where most of the current star formation occurs (Ford et al. 2013; Rahmani et al. 2016), with a star formation timescale longer than 500 Myr (Lewis et al. 2015). This is longer than the characteristic time scale, making an ephemeral collision origin unlikely, as proposed by Block et al. (2006); Dierickx et al. (2014) (see however Hammer et al. 2018). Assuming that this structure is located at 10 kpc and that it is related to a resonance with the bar, B17 predict a bar pattern speed of $\Omega_p = 41 \text{ km s}^{-1} \text{ kpc}^{-1}$. Here we use the bulge stellar kinematics as fitting constraints, finding $\Omega_p = 40 \pm 5 \text{ km s}^{-1} \text{ kpc}^{-1}$, placing the outer Lindblad resonance at $r_{\text{OLR}} = 11 \pm 1$ kpc near the ring structure. This suggests that the OLR could be related to the formation of the ring, as also observed in other galaxies (Buta & Crocker 1991; Buta 2017).

3.4 Conclusions

We explored a large range of stellar mass-to-light ratios in the $3.6 \mu\text{m}$ band, dark matter masses within the bulge of M31, and pattern speeds for the B/P bulge and the bar, finding a constrained range of values that best match *simultaneously* the $3.6 \mu\text{m}$ band photometry (Barmby et al. 2006) and the IFU bulge kinematics (O18), with $\Upsilon_{3.6} = 0.72 M_{\odot} L_{\odot}^{-1}$, $M_{\text{DM}}^{\text{B}} = 1.2 \times 10^{10} M_{\odot}$, and $\Omega_p = 40 \text{ km s}^{-1} \text{ kpc}^{-1}$.

The best model has a classical bulge component with a stellar mass $M_{\star}^{\text{CB}} = 1.8 \times 10^{10} M_{\odot}$ with a 3D half mass radius of $r_{\text{h}}^{\text{CB}} = \text{kpc}$

The models that best reproduce the data require a total dynamical mass of $M_{\text{dyn}}^{\text{B}} = 4.0 \pm 0.3 \times 10^{10} M_{\odot}$ within the bulge. The stellar mass within the composite bulge is $M_{\star}^{\text{B}} = 3.0 \pm 0.2 \times 10^{10} M_{\odot}$, having the classical bulge $M_{\star}^{\text{CB}} = 1.2 \pm 0.1 \times 10^{10} M_{\odot}$ and the B/P bulge $M_{\star}^{\text{BP}} = 1.9 \pm 0.1 \times 10^{10} M_{\odot}$. We also explored a grid of models with the NFW dark matter profile, finding that while the Einasto models fit generally better than the NFW profile, we obtain similar values for the main parameters, having for the dark matter within the bulge $M_{\text{DM}}^{\text{B}} = 1.0_{-0.2}^{+0.4} \times 10^{10} M_{\odot}$, slightly lower mass-to-light ratio and the same bar pattern speed. Our best model has two bulge components with completely different kinematic structures that together successfully reproduced detailed properties of the kinematic and the photometric maps. Our modelling includes dust absorption effects that can reproduce the kinematic asymmetries in the observations.

A further discussion of these results is given in the following Chapter 4.

3.A Cube of parameters

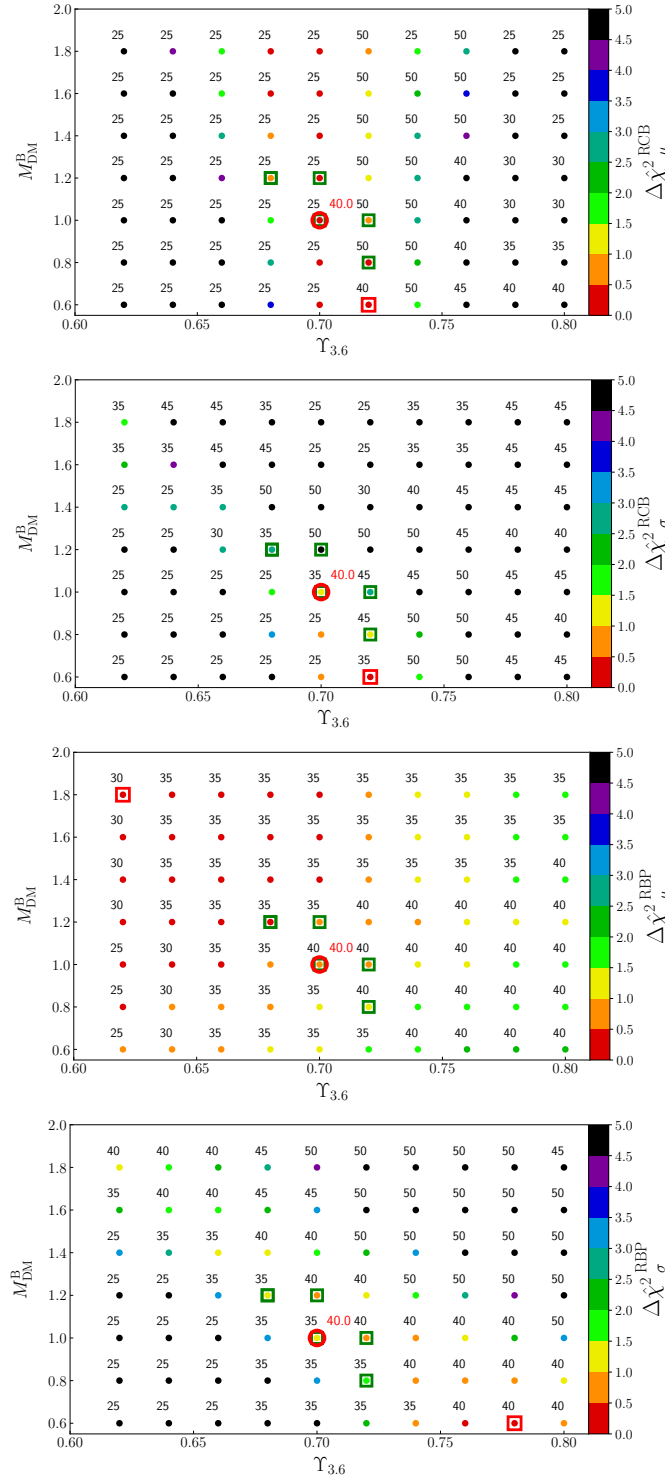


Figure 3.28: Results of the grid of models for the NFW dark matter halo for the first four subsets: $\Delta\hat{\chi}^2_{\mu}^{RCB}$ (top left), $\Delta\hat{\chi}^2_{\sigma}^{RCB}$ (top right), $\Delta\hat{\chi}^2_{\mu}^{RBP}$ (bottom left) and $\Delta\hat{\chi}^2_{\sigma}^{RBP}$ (bottom right) as function of the parameters $\Upsilon_{3.6}$ and M_{DM}^B marginalising along the axis of the parameter Ω_p . The values of each subset are the points that are coded in the coloured bar, and the number corresponds to the selected Ω_p . We mark the best model KR241 (red circle), the models with the minimum values in each subset (red squares), and the range of the neighbouring best models \vec{M}_{NBM}^{NFW} (green squares). The green squares do not necessarily agree with the pattern speed shown.

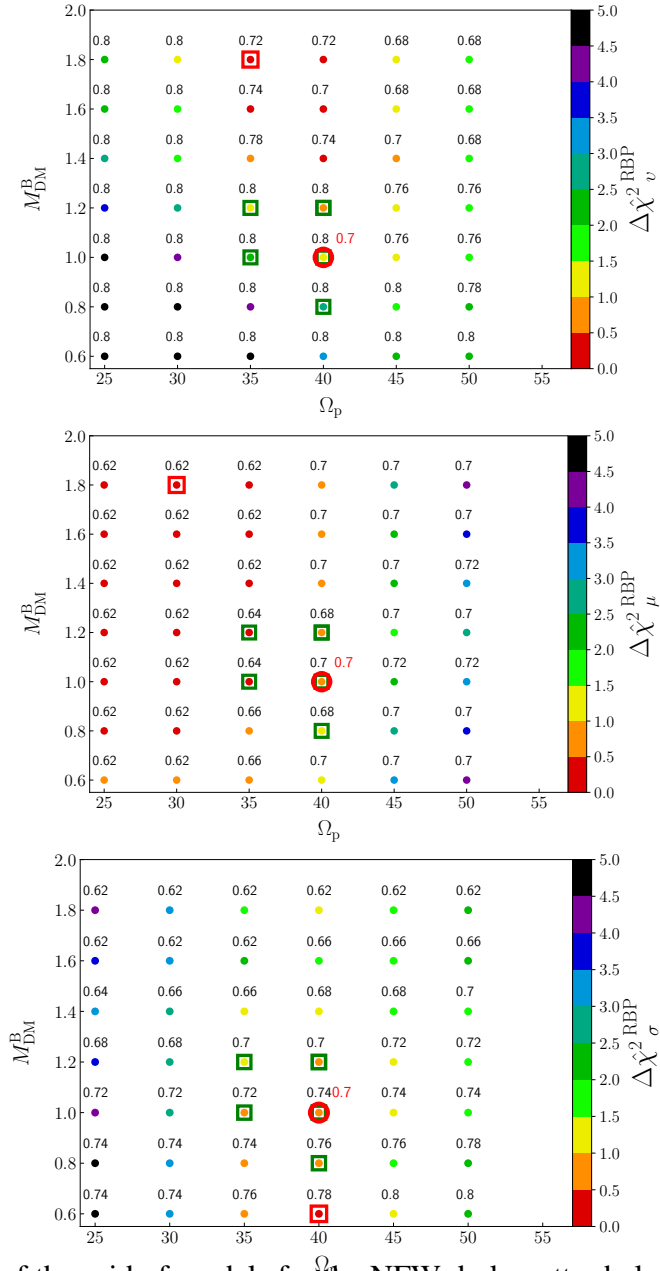


Figure 3.29: Results of the grid of models for the NFW dark matter halo for the subsets 3,4 and 5: $\Delta\hat{\chi}^2_{\nu}^{\text{RBP}}$ (top), $\Delta\hat{\chi}^2_{\mu}^{\text{RBP}}$ (middle) and $\Delta\hat{\chi}^2_{\sigma}^{\text{RBP}}$ (bottom) and $\Delta\hat{\chi}^2_{\mu}^{\text{RBP}}$ (bottom right) as function of the parameters Ω_p and M_{DM}^{B} marginalising along the axis of the parameter $\Upsilon_{3,6}$. The values of each subset are the points that are coded in the coloured bar, and the number corresponds to the selected $\Upsilon_{3,6}$. We mark the best model JR804 (red circle), the models with the minimum values in each subset (red squares), and the range of the neighbouring best models $\vec{M}_{\text{NBM}}^{\text{NFW}}$ (green squares). The green squares do not necessarily agree with the shown $\Upsilon_{3,6}$.

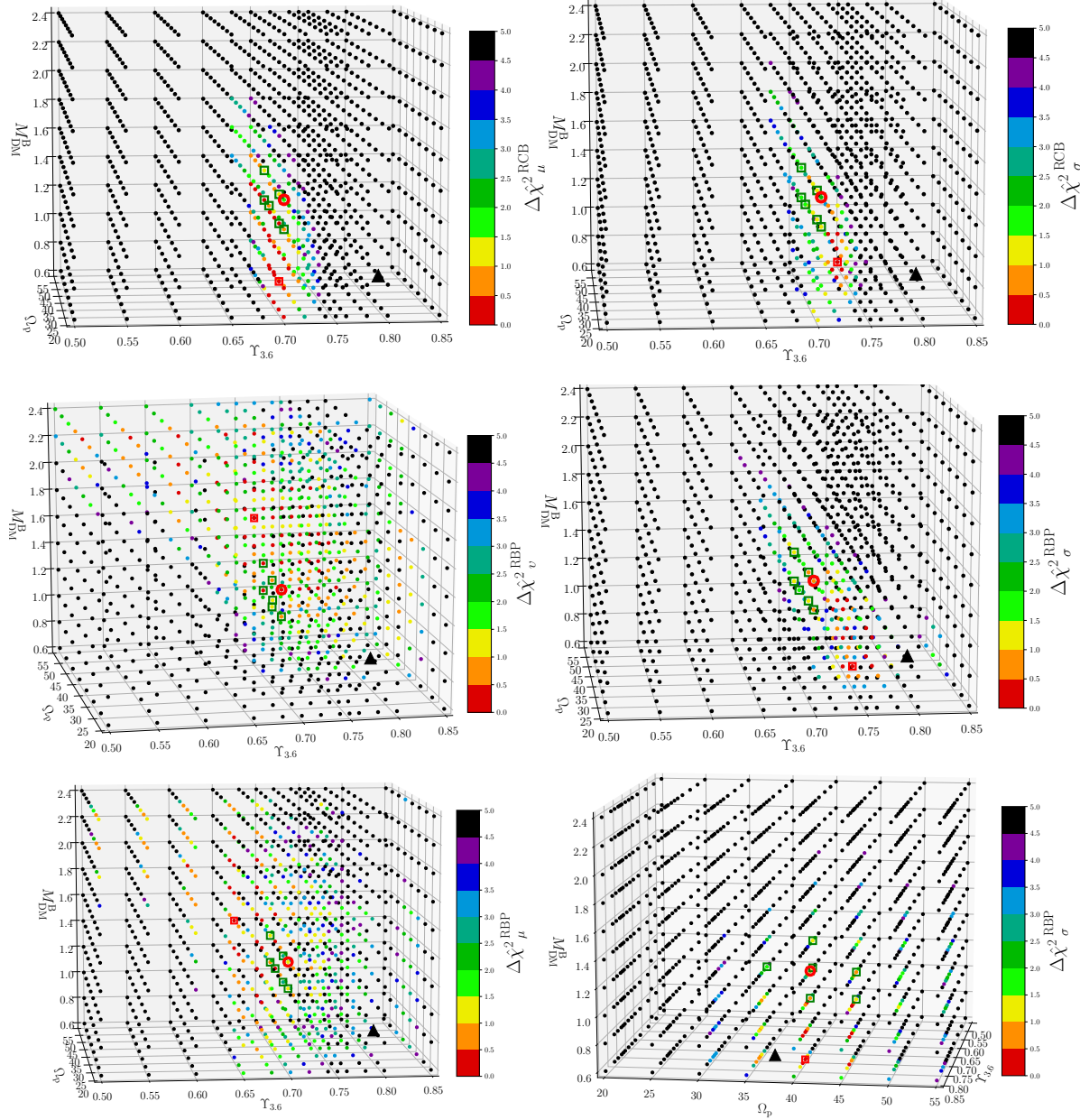


Figure 3.30: Results of the normalised chi-squares of the five subsets for the Einasto grid of models as function of the parameters $\Upsilon_{3.6}$, M_{DM}^B and Ω_p . We show the best matching model \vec{M}_{BM}^{EIN} JR804 (red circle), the neighbouring best models \vec{M}_{NBM}^{EIN} (green squares), and the initial model is shown with the black triangle.

Chapter 4

Final summary

In this thesis I have presented the first mass estimations in the literature for the box/peanut bulge component and the classical bulge component of the Andromeda galaxy, as well as the central dark matter mass considering the triaxial structure of the bulge. For this are built self-consistent dynamical models that reproduce photometric and stellar kinematic observations that allows to determine the stellar and dark matter mass distribution within the bulge, as well as the bar pattern speed. The main results of each project are summarised below:

In the first project, in Chapter 2, is shown with idealised pure N-body simulations that it is possible to form a composite bulge with properties similar to M31's triaxial bulge. The B/P bulges are generated in the simulations from an initial disk that naturally forms a bar. This bar then buckles generating the boxy structure which evolves together with the classical bulge, resulting in a system in approximate dynamical equilibrium. In order to constrain the properties of the M31 bulge a set of N-body models is explored, with pure B/P bulges and also combining B/P bulges with classical bulges components of different sizes and masses, which then are compared with morphological properties of M31 using the IRAC 3.6 μm band (Barmby et al. 2006), finding a best matching N-body model (Model 1). The main results are the following:

- I) The best matching model has a classical bulge and a B/P bulge with masses of $\sim 1/3$ and $\sim 2/3$ of the total stellar mass of the bulge.
- II) The classical bulge contributes mainly in the centre of the bulge, within ~ 530 pc (140 arcsec), increasing the total light concentration and therefore increasing the Sérsic index n , while central light contribution of the B/P bulge is shallow which lowers the Sérsic index of the combined surface-brightness profile. Only combining both bulge components can the central surface-brightness of the M31 bulge be successfully reproduced.
- III) Pure B/P bulge models are excluded, as they show a Sérsic indices too low to reproduce the value in M31, and their central velocity dispersion also lacks the drop generated by the classical bulge component.
- IV) The cuspy density profile of the classical bulge generates the velocity dispersion drop observed in the centre of M31.

- V) Beyond ~ 530 pc (140 arcsec) the B/P bulge dominates which reproduces the observed rapid rotation, the twist of the zero line-of-sight velocity ($v_{\text{los}}=0$ km s $^{-1}$), the correlation of $h3 - v_{\text{los}}$ in the B/P bulge and the bar region, and the boxy shape of the isophotes.

The best N-body model is a good morphological match to M31's bulge, however in the outer parts of the B/P bulge the surface-brightness and the velocity dispersion show lower values than in M31, suggesting that more mass is required, in the form of dark matter or stellar mass, which is solved in the second project.

In the second project, Chapter 3, the best model of the first part (Model 1) is improved with the M2M method by directly fitting the IRAC $3.6 \mu\text{m}$ photometric data and the VIRUS-W stellar kinematic observations (Opitsch et al. 2018). By exploring and comparing with ~ 2000 M2M models with different values of the bar pattern speed Ω_p , the bulge stellar mass-to-light ratio in the $3.6 \mu\text{m}$ band $\Upsilon_{3.6}$, and the mass and density of the dark matter within the bulge M_{DM}^{B} , we find a range of models that best fit the kinematic and photometric observations. The main results are:

- I) The range of parameters that best reproduce all the observations simultaneously are:
 $\Upsilon_{3.6} = 0.72 \pm 0.02 M_{\odot} L_{\odot}^{-1}$, $\Omega_p = 40 \pm 5 \text{ km s}^{-1} \text{ kpc}^{-1}$ and $M_{\text{DM}}^{\text{B}} = 1.2^{+0.2}_{-0.4} \times 10^{10} M_{\odot}$, using an Einasto dark matter profile. These models have a total dynamical mass within the composite bulge of $M_{\text{dyn}}^{\text{B}} = 4.25^{+0.10}_{-0.29} \times 10^{10} M_{\odot}$ with of a stellar mass of $M_{\star}^{\text{B}} = 3.09^{+0.10}_{-0.12} \times 10^{10} M_{\odot}$ (73%). The classical bulge mass is $M_{\star}^{\text{CB}} = 1.18^{+0.06}_{-0.07} \times 10^{10} M_{\odot}$ (28%) and the B/P bulge is $M_{\star}^{\text{BP}} = 1.91 \pm 0.06 \times 10^{10} M_{\odot}$ (45%).
- II) The best models with the NFW dark matter density profiles result in similar masses than the Einasto models, with $M_{\text{DM}}^{\text{B}} = 1.0^{+0.4}_{-0.2} \times 10^{10} M_{\odot}$; however, the more shallow density profiles of the Einasto models give better fits to the stellar kinematics of the bulge than the cuspy NFW haloes.
- III) Our best model has two bulge components with completely different kinematics that only together can successfully reproduce the properties of the photometric and the kinematic maps of M31, such as the dispersion drop in the centre due to the classical bulge, or the $h3 - v_{\text{los}}$ correlation in the bar region.
- IV) Furthermore, our modelling includes dust absorption effects that can reproduce σ_{los} asymmetries in the observations. The model, for example, reproduces the lower dispersion of the near side of the galaxy compared to the far side.
- V) Our estimations of the M31 bar properties place this bar within slow bars with $\mathcal{R} = 1.6 \pm 0.2$. This is within the range of recent measurements of \mathcal{R} of barred galaxies, finding $\mathcal{R} = 1.41 \pm 0.26$ (Spitzer with gas kinematics Font et al. 2017) and $\mathcal{R} = 1.0^{+0.7}_{-0.4}$ (CALIFA survey Aguerri et al. 2015).
- VI) The bar pattern speed places the inner Lindblad resonances near the gas rings and streams observed within the bulge (Opitsch et al. 2018), and the outer Lindblad resonance near the

10 kpc ring, which could explain its origin and persisting star forming activity (Lewis et al. 2015).

How does the best N-body model (Model 1) compares with the best M2M model? Both models have similar main properties, finding a similar mass and luminosity for the classical bulge. While both B/P bulge models have a similar luminosity, the B/P bulge of the N-body model has a mass 15% higher than the M2M B/P bulge, which is due to a slightly larger stellar mass-to-light ratio. The N-body model kinematic maps qualitatively match several features observed in M31, however the best M2M model highly improves the match quantitatively. For example, the M2M model reproduces now the velocity dispersion in the outer parts of the B/P bulge due to a more massive dark matter halo.

4.1 M31 context and implications

As I describe in the main introduction, barred galaxies can show a wide range of morphologies, which can also have a B/P bulge substructure. In this section are presented some implications for the formation and evolution of M31, in relation to the properties discovered for the classical bulge and the B/P bulge of M31.

- 1) Our results present new constraints on the early formation of M31 given the lower mass found for the classical bulge component compared to previous estimations in the literature. One implication is on the relation between bulges and central super massive black holes (SMBH). SMBH masses show correlations with classical bulges and not pseudobulges (Saglia et al. 2016). Using the $M_{\bullet} - M_{\text{bulge}}$ ¹ relation from Saglia et al. (2016) for the classical bulge component alone with a mass of $M_{\star}^{\text{CB}, 10 \text{ kpc}} = 1.71 \times 10^{10} M_{\odot}$ predicts a SMBH mass of $M_{\bullet} = 0.7^{+0.7}_{-0.3} \times 10^8 M_{\odot}$, where the errors are the intrinsic scatter in the relation. This is somewhat lower than the measured $M_{\bullet} = 1.4^{+0.9}_{-0.3} \times 10^8 M_{\odot}$ (Bender et al. 2005), but lies within the intrinsic scatter. Using the $M_{\bullet} - M_{\text{bulge}} - \sigma^2$ relation with $\sigma_{\text{max}}^{\text{CB}} \sim 130 - 150 \text{ km s}^{-1}$ predicts a mass of $M_{\bullet} = 1.7^{+2.2}_{-0.9} - 2.7^{+3.5}_{-1.5} \times 10^8 M_{\odot}$, that is closer to the measured value in M31.
- 2) The tightly constrained stellar mass-to-light ratio value of $\Upsilon_{3,6} = 0.72 \pm 0.02 M_{\odot} L_{\odot}^{-1}$ is in agreement with the expected values from stellar populations with a Chabrier IMF (Meidt et al. 2014), with the metallicities and ages measured in M31's bulge and bar (Opitsch 2016; Saglia et al. 2018). Considering the classical bulge alone a Chabrier IMF would be consistent with Cappellari et al. (2012) (using $\Upsilon_r \sim 4 M_{\odot} L_{\odot}^{-1}$ and $\sigma_{\text{CB}} \sim 150 \text{ km s}^{-1}$). It is however inconsistent with the Salpeter IMF found for more massive classical bulges measured by Dutton et al. (2013, SWELLS survey).
- 3) Our findings agree with the photometric (Fisher & Drory 2008) and kinematic (Fabricius et al. 2012) bulge classification criteria using the Sersic index (n) and the central kinematics to distinguish classical bulges ($n > 2$) from pseudobulges ($n < 2$). As Fisher & Drory (2008)

¹for the sample CorePowerEClassnoBars

²for the sample CorePowerEClassPC

mentions and [Erwin et al. \(2015\)](#) investigate further, composite bulges can have an effect on the bulge selection criteria, and they can manifest both bulge type properties. Here we find that M31's composite bulge Sersic index is at the boundary with $n_{M31} \sim 2$ and it shows kinematic properties of both bulge types. Moreover, considering the classical bulge alone we find $n_{CB} \sim 4$, a classical bulge to total mass ratio $B/T=0.21$, half mass radius $r_{h,CB} \sim 1$ kpc, and central dispersion $\sigma_{CB} \sim 150$ km s⁻¹, which also agree with the criteria for classical bulge types.

Here we present two properties of a composite bulge that could improve the selection criteria: i) a composite bulge with $n \approx 2$ can host a classical bulge with a high Sersic index, where the composite bulge has a value lowered by the presence of a B/P bulge, and ii) the presence of a classical bulge can increase the total central dispersion by increasing the B/P bulge dispersion that lives within the classical bulge potential. This could suggest that other observed bulges with low Sersic values ($n \lesssim 2$), but with high central dispersion could be hosting a compact classical bulge.

- 4) The range of dark matter masses found within the bulge is in agreement with what is expected for a slightly adiabatically contracted cosmological simulated NFW halo with a virial mass like M31 of $M_{DM200} = 1.04 \times 10^{12} M_{\odot}$ ([Tamm et al. 2012](#)), which depending on the degree of adiabatic contraction can be $M_{DM200}^{3.2kpc} = 1.88 \times 10^{10} M_{\odot}$ in the more extreme case, or with less contraction $M_{DM200}^{3.2kpc} = 0.97 \times 10^{10} M_{\odot}$ ($\nu=0.4$) ([Dutton et al. 2011](#); [Abadi et al. 2010](#)), while for no contraction is $M_{DM200}^{3.2kpc} = 0.34 \times 10^{10} M_{\odot}$.
- 5) The best Einasto models fit the bulge stellar kinematics generally better than the models with NFW haloes, favouring a shallow central dark matter halo distribution, similar to that found in the Milky Way ([Portail et al. 2017a](#)). This also reveals the importance of kinematic data with high spectral and spatial resolution, and the appropriate modelling to accurately determine the central dark matter mass distribution in galaxies.
- 6) Our best M31's bar pattern speed is $\Omega_p = 40 \pm 5$ km s⁻¹ kpc⁻¹ which results in a ratio of $\mathcal{R} = 1.3 - 1.8$ placing this bar at the limit of a slow bars, and within the average of samples of barred galaxies with $\mathcal{R} = 1.41 \pm 0.26$ (*Spitzer* with gas kinematics [Font et al. 2017](#)) and $\mathcal{R} = 1.0_{-0.4}^{+0.7}$ (CALIFA survey [Aguerri et al. 2015](#)).
- 7) In the scenario presented in this thesis, the Andromeda galaxy has a composite bulge made of a classical bulge and a bar with a B/P bulge substructure. These results are consistent with the scenario provided from the stellar population analysis of ([Opitsch 2016](#); [Opitsch et al. 2018](#)) and [Saglia et al. \(2018\)](#), that suggests that the classical bulge formed first, and coexists now with a B/P bulge and a thin bar that would have formed from the inner disc after the classical bulge.
- 8) Also within this scenario, the bar would be a main responsible for the secular evolution of M31. Our range of pattern speed places the inner Lindblad resonances at $r_{OILR} = 0.9 \pm 0.1$ kpc and $r_{IILR} = 1.9 \pm 0.2$ kpc, near the high velocity gas streams within the bar detected by ([Opitsch et al. 2018](#)), suggesting that the bar can also promote and determine the gas accretion process in the centre, as expected in barred galaxies ([Kim et al. 2012](#)). And the outer Lindblad resonance is at $r_{OLR} = 11 \pm 1$ kpc near the 10 kpc ring, which could explain its origin and persisting

star forming activity ([Lewis et al. 2015](#)). The bar dynamics could also be related to the spiral arms at 5 kpc, and the mild break in the disc surface-brightness profile at 10 kpc as seen in Type II.o-OLR disc galaxies ([Erwin et al. 2008](#); [Kim et al. 2014](#)).

Chapter 5

Outlook and Future Work

The new dynamical models presented in this thesis will allow now to explore new aspects of the the formation and the evolution of the Andromeda galaxy, as well as galaxies in general. In the next section are presented five possible projects derived from the research developed here.

5.1 Chemodynamical modelling of M31

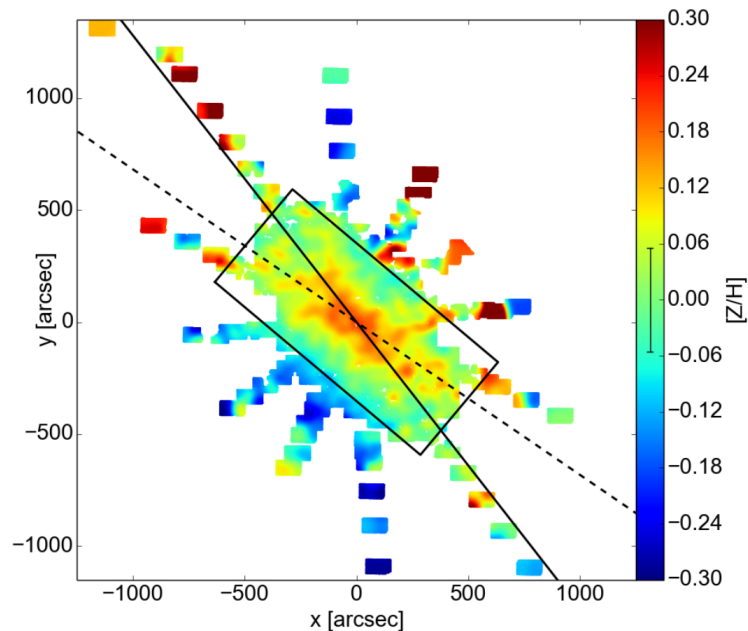


Figure 5.1: Taken from [Opitsch \(2016\)](#). Metallicity map of M31. Disc major axis (solid line) and bar major axis (dash line).

In the last years large spectroscopic campaigns have allowed to cover whole galaxies to obtain not only kinematic maps of these systems, but also maps of the chemical elements in their

stars. It is observed that galaxies present metallicity and α -elements abundances with radial gradients. From stellar population and galaxy formation theory, and also from chemodynamical galaxy formation simulations (Kobayashi & Nakasato 2011) we expect that the stars with different element abundances may have different spatial distributions, and therefore different orbits, connecting the kinematic and the spatial properties with different chemical properties that allows to dissect galaxies by their orbital structure. Furthermore, this information could reveal fossil signatures from their progenitors. Powerful methods such as the Made-to-measure method (Syer & Tremaine 1996; De Lorenzi et al. 2007) or the Schwarzschild modelling (Schwarzschild 1979; Cretton et al. 1999; Thomas et al. 2004) allow the construction of stellar dynamical systems in equilibrium from orbits, which need to fit now not only dynamical quantities, but also chemical properties. With the M2M method we fitted the $3.6\ \mu\text{m}$ image from the centre out to 15 kpc covering the bulge and the disc as well as IFU observations fitting the Gauss-Hermite coefficients maps observables, and the HI rotation curve out to 15 kpc. Furthermore, the M31 bulge IFU observations also measured valuable chemical maps of the metallicity (Figure 5.1) and the α -elements abundances (Opitsch 2016; Saglia et al. 2018), which can provide information on the formation of galactic substructures when this information is combined with chemodynamical models, in a similar way than for the Milky Way (Portail et al. 2017b).

In order to reach this goal a sequence of intermediate steps can be done: i) incorporate into the M2M modelling the fitting of chemical elements such as metallicity distributions as well as α -elements abundances, developing the modules for the model observables designed to fit IFU observations or individual stars measurements, by assigning and adapting chemical weights to the library of orbits. ii) Recovering intrinsic chemical properties: how well can we recover stellar populations with different kinematic signatures? mock data is created using N-body models in dynamical equilibrium of barred galaxy models (also best models of Paper I and II) with multiple stellar populations with different kinematic properties, and using the M2M modelling to recover the chemodynamical signatures. iii) applying the chemodynamical technology developed before to M31 chemical maps, and use it to, for example, dissect the thin bar structure from the B/P bulge, and to determine the metallicity gradient of the classical bulge component.

5.2 Improved M2M models for M31: substructures

The new dynamical models presented here are an excellent starting point to study other M31 substructures in much more detail, and depending on the goals, several improvements can be done. For example, here we find that M31 has a classical bulge with a mass that is 50% lower compared with other estimations in the literature. However, the extension of this and its connection with the outer stellar halo is not clear. For example Dorman et al. (2012) finds that at 5 kpc the inner halo has significant rotation ($\sim 50\ \text{km s}^{-1}$). An extended classical bulge or a stellar halo component could be added in the M2M modelling that connects the inner classical bulge with the outer halo, using for example kinematic PNe data from Merrett et al. (2006) that covers from ~ 1 kpc out to 20 kpc.

Furthermore, Dorman et al. (2015) also finds that the disc of M31 is dynamically hotter than expected, encountering kick up disc stars living in the stellar halo region. This can be also

incorporated in the modelling using two disc components, *i.e.* a thin and a thick disc.

5.3 Future spectroscopic observations of M31 and the dust modelling

The effects of dust extinction in M31 is particularly important in the V-band (Draine et al. 2014), affecting the kinematics that are measured in that band, *e.g.* the stellar kinematics that are determined from the 5150Å Magnesium line, and the gas kinematics calculated with the doublet of forbidden lines of doubly ionized oxygen [OIII] $\lambda\lambda 4959\text{\AA}$, 5007Å. The dust and the orientation of M31 result in asymmetric features in the stellar kinematic maps, as shown in Section 3.3.2.3. Dalcanton et al. (2015) estimate that the V-band dust extinction is weaker than the estimations from Draine et al 2014, suggesting that a further dust modelling may be required.

Furthermore, more spectroscopic observations in the red band, or (near-)infrared bands can be less sensitive to dust extinction, such as the CALIFA survey (0.43–0.70 μm) and the SPLASH survey using the Keck/DEIMOS (0.645 – 0.915 μm) to observe the Ca II triplet (8498Å, 8542Å and 8662Å) absorption feature present in RGB stars (Dorman et al. 2012), or also APOGEE (Apache Point Observatory Galactic Evolution Experiment) (Majewski et al. 2015), as demonstrated by star cluster campaigns in M31 (Schiavon et al. 2013; Sakari et al. 2016)

However, the dust modelling can also be quite revealing, given that the asymmetries generated by the dust could potentially better constraint the three dimensional structure of M31.

5.4 Gas dynamics in M31: outer ring and inner streams

Bars in disc galaxies are “engines” that promote the secular evolution of galaxies. Not only the stellar dynamics is affected by the resonances with the bar, but also the gas is strongly affected by the presence of the rotating triaxial potential generated by the bar. In the central region, within the bar, the gas can form ring-like substructures, as Kim et al. (2012) show (Figure 1.13), which can trigger star formation episodes. The Spitzer and Herschel dust observations show similar ring-like substructures in the bulge and bar region of M31, which could be similarly explained by M31’s bar. This is the case for studies of the MW central region, where the bar generate gas rings and streams falling within the galaxy (Li et al. 2016).

In the outer region of the disc, the gas can also react to the barred potential and the outer Lindblad resonance, forming rings and large spiral arms (Schwarz 1981; Buta & Combes 1996; Rautiainen & Salo 2000). As we summarise in the introduction, M31 presents a prominent star forming ring-like structure at ~ 10 kpc, which we find is likely to be related to the OLR of the bar (Athanasoula & Beaton 2006; Blana et al. 2017) (Chapter 3). Being the most important current star forming region in M31, it would be interesting to study if such structure can indeed be generated by the bar. A preliminary example is shown in Figure 5.2 with a simulation of a gas distribution reacting to an analytical disc potential and a triaxial barred potential set with a pattern speed of $\Omega_p = 40 \text{ km s}^{-1} \text{ kpc}^{-1}$ and a half bar major axis of 4 kpc. The gas is isothermal with a temperature of $T_{\text{gas}} = 10^4 \text{ K}$. We produced the simulation with the sph code PHANTOM (Price

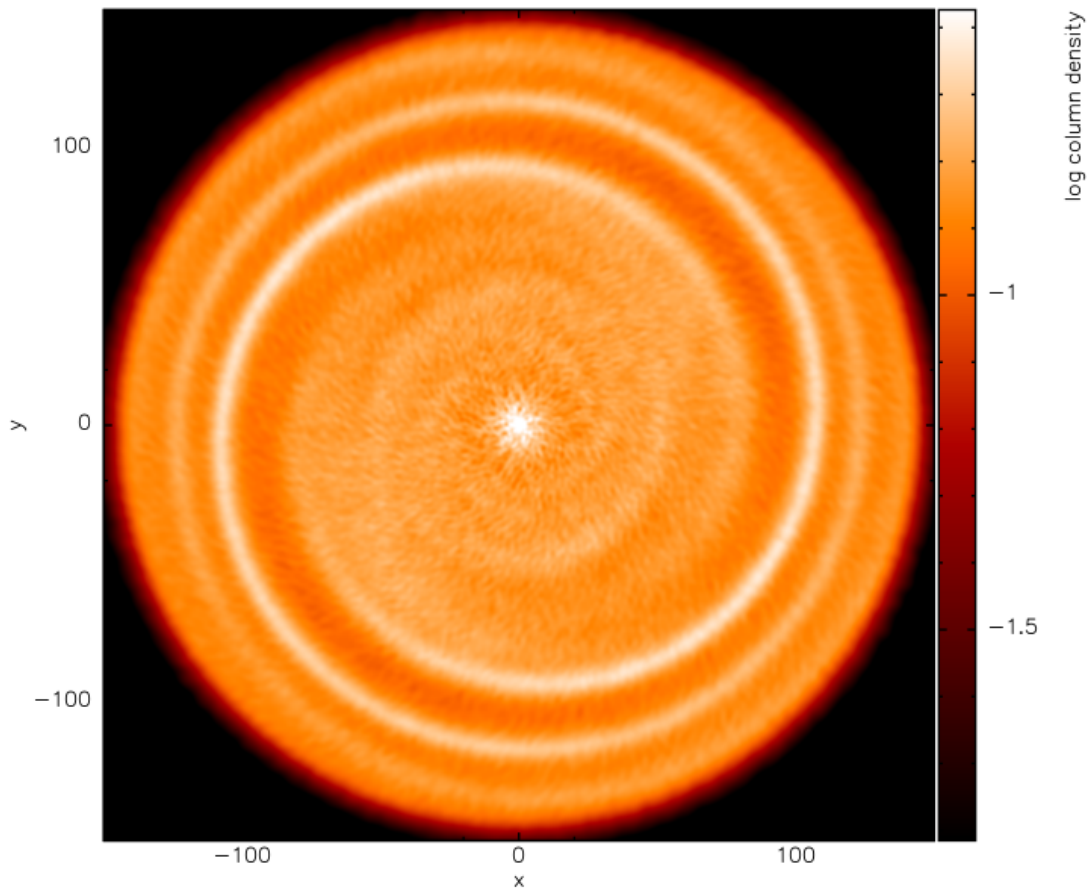


Figure 5.2: Our gas simulation using analytical potentials for the disc and the bar with $r_{\text{bar}}=4$ kpc and $\Omega_p=40$ km s $^{-1}$ kpc $^{-1}$. (x, y) in 10^{-1} kpc. Sph simulations performed with PHANTOM (Price et al. 2017).

et al. 2017) using 1 million particles. There is a clear ring-like or spiral pattern in the gas in response to the triaxial potential that has a long life time. In a next step the analytical potential can be replaced by the best M2M models, and to model not only the outer region, but also the inner region of the bar to reproduce the inner ring-like substructures.

5.5 Microlensing modelling of M31

Massive Astrophysical Compact Halo Objects (MACHOs) were originally proposed as a material with baryonic origin to explain the dark matter in galaxies (Griest 1991). MACHOs include black holes or neutron stars as well as brown dwarfs and unassociated planets, and therefore they emit little or no radiation making them difficult to detect. These MACHOs objects can act as a gravitational lens deflecting and concentrating the light coming from a distant star between

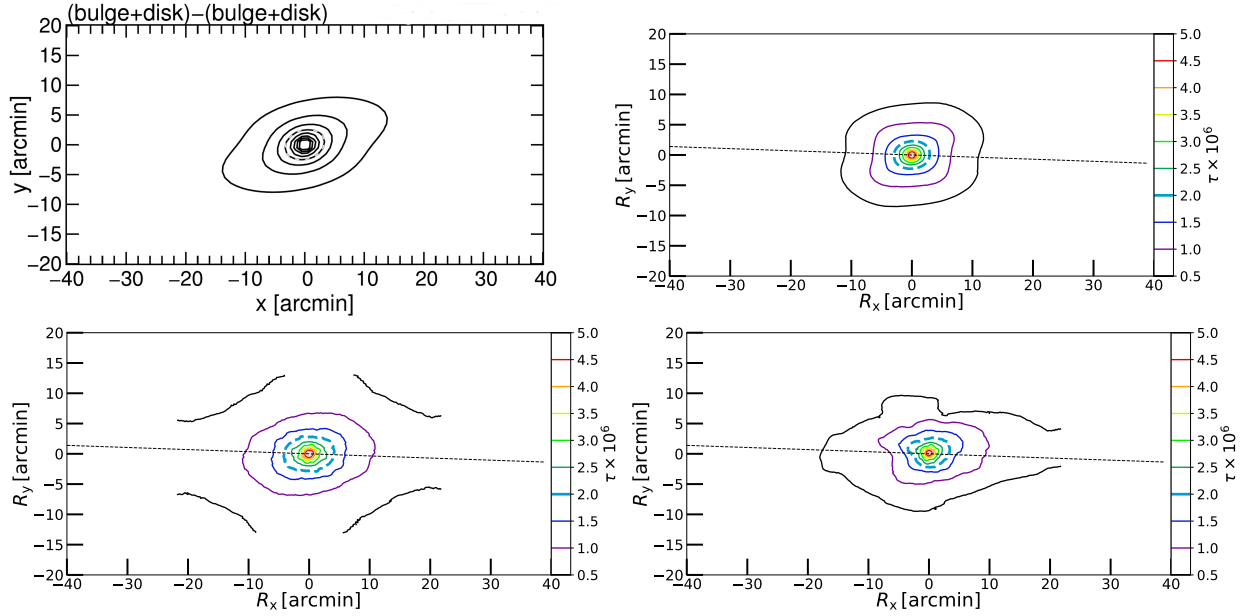


Figure 5.3: Contours of the averaged line-of-sight optical depth $\langle\tau\rangle$ for the M31 models. Top left: taken from Riffeser et al. (2006) with the M31 bulge model of Kent (1989). Top right: the best N-body model (Model 1) from B17, using the code from Wegg et al. (2016). Bottom left: the best M2M model (JR804). Bottom right: the best M2M model where the sources have been attenuated by the dust extinction (A_V), generating an asymmetry. The disc major axis (black dash line) with the near side of the disc in the upper part of the panels. The spacing between adjacent contours is $\Delta\langle\tau\rangle=0.5 \times 10^{-6}$, with the value $\langle\tau\rangle=2 \times 10^{-6}$ in cyan dashed contours.

the gravitational lens and the observer (Einstein 1936); a process called a microlensing event. Campaigns of microlensing survey have been observing M31, such as PLAN (Pixel Lensing Andromeda; Calchi Novati et al. 2014), PAndromeda (Pan-STARRS 1; Lee et al. 2012) and WeCAPP (Wendelstein Calar Alto Pixel-lensing Project; Lee et al. 2015), where 56 events were detected. These events are not necessarily produced by MACHOs, they can also occur by other stars and stellar remnants in M31, a process named self-lensing (Riffeser et al. 2006). Stellar components of a galaxy produce stellar remnants similar to the MACHO material however, they have the same phase-space density distribution of the luminous matter, and their lensing contribution is taken within the self-lensing component, and in the dynamics and the stellar populations, their contribution is considered in the stellar mass-light-ratio and the present day stellar mass function, respectively. Therefore, to have an accurate estimation of self-lensing events, so we can better constraint the MACHOs in the halo, it is necessary to have an accurate three dimensional stellar mass (stars and remnants) distribution of substructures such as the bulge and the disc.

Current micro-lensing models for M31 (Riffeser et al. 2006) use oblate models for the bulge of M31 (Kent 1989). Our new barred models of M31 are fitted directly to $3.6 \mu\text{m}$ photometric im-

ages and to kinematic observations resulting in an improved three dimensional mass distribution. This allows better predictions and comparisons with micro-lensing observations, in particular the predictions for bulge self-lensing events in M31, which will allow to measure the amount of dark matter in the bulge of M31 and to constraint its IMF, both fundamentally important astronomical properties to understand the formation and evolution of M31 and galaxies in general.

Microlensing events can be estimated with the optical depth (τ), which is the probability or the fraction of stars (sources) that can be significantly lensed by an object (lens) that lies along a line-of-sight tube with an Einstein radius size. In Fig.5.3 we show the optical depth for micro (self-)lensing events averaged within a small region calculated by Riffeser et al. (2006) using the oblate bulge model, compared with the optical depth of Model 1 of Paper I and the best M2M model (JR804), calculated with the code from Wegg et al. (2016). In the central 5 arcmin the optical depth does not show large differences, while further out the distribution of the iso-contours is less elongated. We also include the effects of the dust absorption (A_V) in the best M2M model, which generate asymmetries, which shows that the dust modelling needs to be included in the micro-lensing predictions.

Preliminary results with the code of Riffeser et al. (2006) for micro-lensing predictions show that for a minimum signal to noise of $S/N=10$, the Kent model predicts an event rate of 7.4 ev/yr in the central region of the bulge ($8\text{arcmin} \times 8\text{arcmin}$), while for Model 1 (best N-body model) the prediction is slightly lower, with 6.8 ev/yr. This is expected, given the lower stellar mass found for the bulge that is $\sim 83\%$ of the mass found by Kent (1989). New upcoming calculations with the M2M models will soon improve the prediction of self-lensing events for the M31 bulge.

Bibliography

- Abadi M. G., Navarro J. F., Fardal M., Babul A., Steinmetz M., 2010, [MNRAS](#), 407, 435
cited on pages 104 and 136
- Aguerri J. A. L., Sánchez S. F., Husemann B., Mast D., 2015, [A&A](#), 576, 102
cited on pages 134 and 136
- Angulo R. E., Springel V., White S. D. M., Jenkins A., Baugh C. M., Frenk C. S., 2012, [Mon. Not. R. Astron. Soc. Vol. 426, Issue 3, pp. 2046-2062.](#), 426, 2046
cited on pages 6
- Athanassoula E., 1992, [Mon. Not. R. ...](#), 259, 345
cited on pages 18
- Athanassoula E., 2003, [MNRAS](#), 341, 1179
cited on pages 32 and 33
- Athanassoula E., 2005, [MNRAS](#), 358, 1477
cited on pages 36
- Athanassoula E., 2012, [arXiv Prepr. arXiv1211.6752](#), pp 1–47
cited on pages 17
- Athanassoula E., Beaton R. L., 2006, [MNRAS](#), 370, 1499
cited on pages 22, 25, 33, 72, and 141
- Athanassoula E., Misiriotis A., 2002, [MNRAS](#), 330, 35
cited on pages 70 and 73
- Athanassoula E., Rodionov S. A., Peschken N., Lambert J. C., 2016, [ApJ](#), 821
cited on pages 32 and 73
- Baes M., Dejonghe H., 1999, [MNRAS](#), 313, 153
cited on pages 117
- Barmby P., et al., 2006, [ApJ](#), 650, L45
cited on pages 25, 27, 28, 32, 33, 34, 60, 66, 76, 82, 114, 127, and 133
- Beaton R. L., et al., 2007, [ApJ](#), 658, L91
cited on pages 22, 32, 33, 44, 45, 72, and 88
- Behrendt M., Burkert A., Scharfmann M., 2015, [MNRAS](#), 448, 1007
cited on pages 70
- Bekki K., 2010, [MNRAS](#), 401, L58
cited on pages 32
- Bender R., Doebereiner S., Moellenhoff C., 1988, [Astron. Astrophys. Suppl. Ser. \(ISSN 0365-0138\)](#), 74, 385
cited on pages 35

- Bender R., Saglia R. P., Gerhard O. E., 1994, *MNRAS*, 269 *cited on pages 54 and 78*
- Bender R., et al., 2005, *ApJ*, 631, 280 *cited on pages 21, 22, and 135*
- Berman S., 2001, *A&A*, 371, 476 *cited on pages 68, 104, and 106*
- Berman S., Loinard L., 2002, *MNRAS*, 336, 477 *cited on pages 68, 104, and 106*
- Berrier J. C., Sellwood J. A., 2016, *ApJ*, 831, 1 *cited on pages 24*
- Bettoni D., Galletta G., 1994, *Astron. Astrophys. (ISSN 0004-6361)*, 281, 1 *cited on pages 41*
- Binney J., Merrifield M., 1998, *Galact. Astron. / James Binney Michael Merrifield. Princeton, NJ Princet. Univ. Press. 1998. (princet. Ser. Astrophys. QB857 .B522 1998*
cited on pages 162
- Binney J., Tremaine S., 2008, *Phys. Today*, 62, 56 *cited on pages 17 and 70*
- Blana M., 2018, *Sculpting Andromeda from a box - Made-to-measure models for M31's bar and bulge: dark matter within the compound bulge* *cited on pages 28*
- Blana M., Wegg C., Gerhard O., Erwin P., Portail M., Opitsch M., Saglia R., Bender R., 2017, *MNRAS*, 466, 4279 *cited on pages viii, 18, 21, 22, 23, 24, 25, 72, 75, 76, 82, 85, 88, 108, 109, 113, 114, 123, 125, 127, 141, and 143*
- Bland-Hawthorn J., Gerhard O., 2016, *Annu. Rev. Astron. Astrophys.*, 54, 529 *cited on pages 24 and 72*
- Block D. L., Wainscoat R. J., 1991, *Nature*, 353, 48 *cited on pages 13*
- Block D. L., et al., 2006, *Nature*, 443, 832 *cited on pages 23, 25, 60, 66, 68, 73, 109, and 127*
- Blumenthal G. R., Faber S. M., Flores R., Primack J. R., 1986, pp 27–34 *cited on pages 104*
- Boily C. M., Kroupa P., Peñarrubia-Garrido J., 2001, *New Astron.*, 6, 27 *cited on pages 35*
- Bournaud F., Jog C. J., Combes F., 2005, *A&A*, 437, 69 *cited on pages 6, 32, and 72*
- Bournaud F., Elmegreen B. G., Elmegreen D. M., 2007, *ApJ*, 670, 237 *cited on pages 9 and 32*
- Boylan-Kolchin M., Springel V., White S. D. M., Jenkins A., Lemson G., 2009, *Mon. Not. R. Astron. Soc. Vol. 398, Issue 3, pp. 1150-1164.*, 398, 1150 *cited on pages 6*
- Braun R., Thilker D. A., Waltherbos R. A., Corbelli E., 2009, *ApJ*, 695, 937 *cited on pages 26*
- Brinks, E.; Burton W. B., 1984, *A&A*, 141, 195 *cited on pages 82*
- Bureau M., Athanassoula E., 2005, *ApJ*, 626, 159 *cited on pages 6, 23, 37, 59, and 124*
- Buta R. J., 2017,] 10.1093/mnras/stx1392, 3849, 3819 *cited on pages 72 and 127*

- Buta R., Combes F., 1996, *Fundam. Cosm. Physics*, Vol. 17, pp. 95-281., 17, 95
cited on pages 15 and 141
- Buta R., Crocker D. A., 1991, *Astron. J.*, 102, 1715
cited on pages 72 and 127
- Calchi Novati S., et al., 2014, *ApJ*, 783
cited on pages 143
- Capaccioli M., 1989, 1989, world galaxies; Proc. Conf. New York Springer-Verlag, 208, eds
Corwin Jr. H.G. Bottinelli L.
cited on pages 38, 109, and 161
- Cappellari M., et al., 2012, *Nature*, 484, 485
cited on pages 135
- Carollo C. M., Stiavelli M., de Zeeuw P. T., Mack J., 1997, *Astron. J.*, 114, 2366
cited on pages 3
- Carollo C. M., Stiavelli M., Mack J., 1998, *Astron. J.*, 116, 68
cited on pages 3
- Chemin L., Carignan C., Foster T., 2009, *ApJ*, 705, 1395
cited on pages 25, 26, 27, 32, 33, 60, 61, 73, 82, 126, and 127
- Combes F., Sanders R. H., 1981, *Astron. Astrophys.* vol. 96, no. 1-2, Mar. 1981, p. 164-173., 96,
164
cited on pages 17
- Combes F., Debbasch F., Friedli D., Pfenniger D., 1990, *Astron. Astrophys.* (ISSN 0004-6361),
233, 82
cited on pages 32 and 72
- Contopoulos G., 1980, *A&A*, 81, 198
cited on pages 15
- Corbelli E., Lorenzoni S., Walterbos R., Braun R., Thilker D., 2010, *A&A*, 511, A89
cited on pages 21, 26, 27, 33, 60, 63, 73, 76, 81, 102, 125, and 126
- Correa C. A., Wyithe J. S. B., Schaye J., Duffy A. R., 2015a, *MNRAS*, 450, 1514
cited on pages 104
- Correa C. A., Stuart J., Wyithe B., Schaye J., Duffy A. R., 2015b, *MNRAS*, 452, 1217
cited on pages 104
- Cote P., West M. J., Marzke R. O., 2002, *ApJ*, 567, 853
cited on pages 28
- Courteau S., Widrow L. M., McDonald M., Guhathakurta P., Gilbert K. M., Zhu Y., Beaton R. L.,
Majewski S. R., 2011, *ApJ*, 739, 20
cited on pages 20, 21, 23, 24, 25, 28, 33, 82, 99, and 114
- Cretton N., de Zeeuw P. T., van der Marel R. P., Rix H.-W., 1999, *Astrophys. J. Suppl. Ser.*, 124,
383
cited on pages 140
- D'Onghia E., Vogelsberger M., Hernquist L., 2013, *ApJ*, 766, 34
cited on pages 68
- Dalcanton J. J., et al., 2015, *ApJ*, 814, 47
cited on pages 115, 117, and 141

- De Lorenzi F., Debattista V. P., Gerhard O., Sambhus N., 2007, *MNRAS*, 376, 71
cited on pages 74, 75, 79, 81, 82, and 140
- De Lorenzi F., Gerhard O., Saglia R. P., Sambhus N., Debattista V. P., Pannella M., Méndez R. H., 2008, *MNRAS*, 385, 1729
cited on pages 74
- Deason A. J., Belokurov V., Evans N. W., Johnston K. V., 2013, *ApJ*, 763
cited on pages 25
- Debattista V. P., Sellwood J. A., 2000, *ApJ*, 543, 704
cited on pages 17, 66, and 127
- Debattista V. P., Mayer L., Carollo C. M., Moore B., Wadsley J., Quinn T., 2006, *ApJ*, 645, 209
cited on pages 50, 72, and 114
- Dehnen W., 2000, *Astrophys. J. Suppl. Ser.*, 536, L39
cited on pages 38
- Diemand J., Kuhlen M., Madau P., 2007, *Astrophys. Journal*, Vol. 657, Issue 1, pp. 262-270., 657, 262
cited on pages 6
- Diemand J., Kuhlen M., Madau P., Zemp M., Moore B., Potter D., Stadel J., 2008, *Nature*, 454, 735
cited on pages 6 and 11
- Dierickx M., Blecha L., Loeb A., 2014, *ApJ*, 788, L38
cited on pages 25, 60, 66, 109, and 127
- Djorgovski S., Davis M., 1987, *ApJ*, 313, 59
cited on pages 5
- Dorman C. E., et al., 2012, *ApJ*, 752, 147
cited on pages 25, 125, 140, and 141
- Dorman C. E., et al., 2013, *ApJ*, 779, 103
cited on pages 24
- Dorman C. E., et al., 2015, *ApJ*, 803, 24
cited on pages 24, 125, and 140
- Draine B. T., Li A., 2007, *ApJ*, 657, 810
cited on pages 79
- Draine B. T., et al., 2014, *ApJ*, 780, 172
cited on pages 26, 79, 109, 116, 117, and 141
- Dutton A. A., 2009, *MNRAS*, 396, 121
cited on pages 8
- Dutton A. A., et al., 2011, *MNRAS*, 416, 322
cited on pages 104 and 136
- Dutton A. A., et al., 2013, *MNRAS*, 428, 3183
cited on pages 135
- Eggen O. J., Lynden-Bell D., Sandage A. R., 1962, *ApJ*, 136, 748
cited on pages 8
- Einasto J., 1965, *Tr. Astrofiz. Instituta Alma-Ata*, Vol. 5, p. 87-100, 1965, 5, 87
cited on pages 81
- Einstein A., 1936, *Science (80-.)*, 84, 506
cited on pages 143
- Elmegreen B. G., Elmegreen D. M., 1985, *ApJ*, 288, 438
cited on pages 18

- Elmegreen B. G., Elmegreen D. M., Hirst A. C., 2004, *Astrophys. Journal*, Vol. 612, Issue 1, pp. 191-201., 612, 191 *cited on pages 13*
- Erwin P. M. P. I. f. e. P., 2015, *ApJ*, 799, 26 *cited on pages 109*
- Erwin P., 2017, *MNRAS*, 474, 5372 *cited on pages 72*
- Erwin P., Debattista V. P., 2013, *MNRAS*, 431, 3060 *cited on pages 35*
- Erwin P., Debattista V. P., 2016, *Astrophys. J. Lett.*, 825, L30 *cited on pages 33, 72, and 73*
- Erwin P., Debattista V. P., 2017, *MNRAS*, 468, 2058 *cited on pages 72*
- Erwin P., Pohlen M., Beckman J. E., 2008, *Astron. J.*, 135, 20 *cited on pages 24, 72, 115, and 137*
- Erwin P., et al., 2015, *MNRAS*, 446, 4039 *cited on pages 5, 32, and 136*
- Evans N. W., Wilkinson M. I., 2000, *Mon. Not. R. Astron. Soc. Vol. 316*, Issue 4, pp. 929-942., 316, 929 *cited on pages 27*
- Evans N. W., Wilkinson M. I., Guhathakurta P., Grebel E. K., Vogt S. S., 2000, *Astrophys. Journal*, Vol. 540, Issue 1, pp. L9-L12., 540, L9 *cited on pages 27*
- Faber S. M., Jackson R. E., 1976, *ApJ*, 204, 668 *cited on pages 5*
- Fabricius M. H., Saglia R. P., Fisher D. B., Drory N., Bender R., Hopp U., 2012, *ApJ*, 754, 67 *cited on pages 4, 5, 32, 33, 59, 73, 78, and 135*
- Ferguson A. M. N., Irwin M. J., Ibata R. A., Tanvir N. R., Lewis G. F., Tanvir N. R., 2002, *Astron. J.*, 124, 1452 *cited on pages 25*
- Fisher D. B., Drory N., 2008, *Astron. J.*, 136, 773 *cited on pages 4, 5, 8, 32, 33, 51, 114, and 135*
- Font J., et al., 2017, *ApJ*, 835, 1 *cited on pages 134 and 136*
- Ford G. P., et al., 2013, *ApJ*, 769, 55 *cited on pages 27 and 127*
- Gavazzi G., et al., 2015, *A&A*, 580, A116 *cited on pages 13*
- Gebhardt K., et al., 2003, *ApJ*, 583, 92 *cited on pages 89*
- Geehan J. J., Fardal M. A., Babul A., Guhathakurta P., 2005, *Mon. Not. R. Astron. Soc. Vol. 366*, Issue 3, pp. 996-1011., 366, 996 *cited on pages 63*
- Gerhard O. E., 1986, *MNRAS*, 219, 373 *cited on pages 68*
- Gerhard O. E., 1993, *MNRAS*, 265 *cited on pages 78 and 79*
- Gilbert K. M., et al., 2012, *ApJ*, 760, 76 *cited on pages 25*

- Gnedin O. Y., Goodman J., Frei Z., 1995, *Astron. J.* v.110, p.1105, 110, 1105 *cited on pages 25*
- Gordon K. D., et al., 2006, *ApJ*, 638, L87 *cited on pages 27, 32, 60, 66, 82, and 127*
- Governato F., et al., 2010, *Nature*, 463, 203 *cited on pages 8*
- Griest K., 1991, *ApJ*, 366, 412 *cited on pages 142*
- Haas M., Lemke D., Stickel M., Hippelein H., Kunkel M., Herbstmeier U., Mattila K., 1998, *A&A*, 338, L33 *cited on pages 60*
- Habing H. J., et al., 1984, *ApJ*, 278, L59 *cited on pages 60 and 127*
- Hammer F., Yang Y. B., Wang J. L., Puech M., Flores H., Fouquet S., 2010, *ApJ*, 725, 542 *cited on pages 23, 32, 68, and 73*
- Hammer F., Yang Y. B., Wang J. L., Ibata R., Flores H., Puech M., 2018, *Mon. Not. R. Astron. Soc.* *cited on pages 127*
- Hasan H., Norman C., 1990, *ApJ*, 361, 69 *cited on pages 17*
- Henderson A. P., 1979, *A&A*, 75, 311 *cited on pages 82*
- Hernquist L., 1990, *ApJ*, 356, 359 *cited on pages 36 and 123*
- Hernquist L., 1993, *Astrophys. J. Suppl. Ser.*, 86, 389 *cited on pages 35*
- Hernquist L., Weinberg M. D., 1992, *ApJ*, 400, 80 *cited on pages 32*
- Hodge P. W., Kennicutt R. C., 1982, *Astron. J.*, 87, 264 *cited on pages 32*
- Iannuzzi F., Athanassoula E., 2015, *MNRAS*, 450, 2514 *cited on pages 124*
- Ibata R., Irwin M., Lewis G., Ferguson A. M., Tanvir N., 2001, *Nature*, 412, 49 *cited on pages 25 and 32*
- Immeli A., Samland M., Gerhard O., Westera P., 2004, *A&A*, 413, 547 *cited on pages 9 and 32*
- Jedrzejewski R. I., 1987, *MNRAS*, 226, 747 *cited on pages 34 and 109*
- Kalnajs A. J., 1965, The Stability of Highly Flattened Galaxies. *cited on pages 70*
- Kalnajs A. J., 1970, Spiral Struct. our Galaxy *cited on pages 16*
- Kang Y., Bianchi L., Rey S.-C., 2009, *Astrophys. Journal*, Vol. 703, Issue 1, pp. 614-627 (2009)., 703, 614 *cited on pages 27*
- Kent S. M., 1989, *Astron. J.*, 97, 1614 *cited on pages 23, 24, 62, 63, 68, 73, 99, 143, and 144*
- Keselman J. A., Nusser A., 2012, *MNRAS*, 424, 1232 *cited on pages 8 and 32*

- Kim W.-T., Seo W.-Y., Stone J. M., Yoon D., Teuben P. J., 2012, *ApJ*, 747, 60
cited on pages 18, 19, 26, 127, 136, and 141
- Kim T., et al., 2014, *ApJ*, 782, 64
cited on pages 24, 25, 115, and 137
- Kobayashi C., Nakasato N., 2011, *ApJ*, 729
cited on pages 140
- Koleva M., Prugniel P., De Rijcke S., Zeilinger W. W., 2011, *MNRAS*, 417, 1643
cited on pages 98
- Kormendy J., 2013, Cambridge Univ. Press. p.1, eds. J. Falcon-Barroso J. H. Knapen
cited on pages 3, 6, 7, 9, 13, 15, 16, 19, 32, 72, and 106
- Kormendy J., Illingworth G., 1982, *ApJ*, 256, 460
cited on pages 18
- Kormendy J., Kennicutt R. C., 2004, *Annu. Rev. Astron. Astrophys.*, 42, 603
cited on pages 3, 5, and 8
- Lauer T. R., Bender R., Kormendy J., Rosenfield P., Green R. F., 2012, *ApJ*, 745
cited on pages 21
- Lee C. H., et al., 2012, *Astron. J.*, 143
cited on pages 143
- Lee C.-H., Riffeser A., Seitz S., Bender R., Koppenhoefer J., 2015, *ApJ*, 806, 161
cited on pages 143
- Lehner N., Howk J. C., Wakker B. P., 2017, *ApJ*, 848, 71
cited on pages 27
- Lewis G. F., et al., 2013, *ApJ*, 763, 4
cited on pages 20
- Lewis A. R., et al., 2015, *ApJ*, 805
cited on pages 25, 27, 127, 135, and 137
- Li Z., Shen J., Kim W.-T., 2015, *ApJ*, 806, 150
cited on pages 127
- Li Z., Gerhard O., Shen J., Portail M., Wegg C., 2016, *Astrophys. Journal*, Vol. 824, Issue 1, *Artic. id. 13, pp. (2016).*, 824
cited on pages 141
- Lindblad B., 1956, *Stock. Obs. Ann.*, 19, 2
cited on pages 22, 32, 60, 68, and 127
- Long R. J., Mao S., 2010, *MNRAS*, 405, 301
cited on pages 75
- Majewski S. R., et al., 2015, *Astron. Journal*, Vol. 154, Issue 3, *Artic. id. 94, 46 pp. (2017).*, 154
cited on pages 141
- Martinez-Valpuesta I., 2012, *Dyn. Meets Kinematic Tracers*, Online
<http://mpia.de/~dynamics/ringberg/?view=program>, id.12
cited on pages 82
- Martinez-Valpuesta I., Gerhard O., 2011, *ApJ*, 734, L20
cited on pages 66

- Martinez-Valpuesta I., Shlosman I., Heller C., 2006, *ApJ*, 637, 214 *cited on pages 65*
- Martinez-Valpuesta I., Aguerri J. A. L., González-García A. C., Vecchia C. D., Stringer M., 2016, *Mon. Not. R. Astron. Soc. Vol. 464, Issue 2, p.1502-1511*, 464, 1502 *cited on pages 16*
- Mateo M. L., 1998, *Annu. Rev. Astron. Astrophys.*, 36, 435 *cited on pages 28*
- McConnachie A. W., Irwin M. J., Ferguson A. M. N., Ibata R. A., Lewis G. F., Tanvir N., 2005, *MNRAS*, 356, 979 *cited on pages 1, 19, 21, 32, and 76*
- McMillan P. J., Dehnen W., 2007, *MNRAS*, 378, 541 *cited on pages 38*
- Meidt S. E., et al., 2014, *ApJ*, 788, 144 *cited on pages 48, 76, 98, 100, and 135*
- Melchior A.-L., Combes F., 2011, *A&A*, 536, 19 *cited on pages 124*
- Menendez-Delmestre K., Sheth K., Schinnerer E., Jarrett T. H., Scoville N. Z., 2007, *ApJ*, 657, 790 *cited on pages 13 and 72*
- Merrett H. R., et al., 2006, *MNRAS*, 369, 120 *cited on pages 140*
- Merritt D., 1999, *Phys. Rep.*, 333-334, 10 *cited on pages 5*
- Merritt D., 2013, Dynamics and Evolution of Galactic Nuclei. <http://openlibrary.org/works/OL16802359W/Dynamics{ }and{ }Evolution{ }of{ }Galactic{ }Nuclei> *cited on pages 21*
- Metz M., Kroupa P., 2007, *MNRAS*, 376, 387 *cited on pages 28*
- Metz M., Kroupa P., Jerjen H., 2007, *MNRAS*, 374, 1125 *cited on pages 28*
- Metz M., Kroupa P., Jerjen H., 2009, *MNRAS*, 394, 2223 *cited on pages 28*
- Molaeinezhad A., Falcón-Barroso J., Martínez-Valpuesta I., Khosroshahi H. G., Balcells M., Peletier R. F., 2016, *MNRAS*, 456, 692 *cited on pages 23*
- Morganti L., Gerhard O., 2012, *MNRAS*, 422, 1571 *cited on pages 74*
- Morganti L., Gerhard O., Coccato L., Martinez-Valpuesta I., Arnaboldi M., 2013, *MNRAS*, 431, 3570 *cited on pages 89*
- Morrison H., Caldwell N., Schiavon R. P., Athanassoula E., Romanowsky A. J., Harding P., 2011, *ApJ*, 726, L9 *cited on pages 125*
- Mould J., 2013, *Publ. Astron. Soc. Aust.*, 30, e027 *cited on pages 22 and 32*
- Naab T., Burkert A., 2003, *ApJ*, 597, 893 *cited on pages 6, 32, and 72*

- Navarro J. F., Frenk C. S., White S. D. M., 1996, *ApJ*, 462, 563 *cited on pages 81*
- Ness M., et al., 2013, *MNRAS*, 432, 2092 *cited on pages 125*
- Newton K., Emerson D. T., 1977, *MNRAS*, 181, 573 *cited on pages 82*
- Nieten C., Neininger N., Guélin M., Ungerechts H., Lucas R., Berkhuijsen E. M., Beck R., Wielebinski R., 2006, *A&A*, 453, 459 *cited on pages 25 and 26*
- Noguchi M., 1999, *ApJ*, 514, 77 *cited on pages 9 and 32*
- Oh S.-H., de Blok W. J. G., Walter F., Brinks E., Kennicutt R. C., 2008, *Astron. J.*, 136, 2761 *cited on pages 34, 77, and 162*
- Opitsch M., 2016, PhD thesis, LMU München, <https://edoc.ub.uni-muenchen.de/20107/> *cited on pages 73, 78, 98, 100, 135, 136, 139, and 140*
- Opitsch M., Fabricius M., Saglia R., Bender R., Blaña M., Gerhard O., 2018, *A&A*, 611 *cited on pages 22, 23, 26, 72, 73, 78, 88, 104, 106, 115, 117, 118, 123, 127, 134, and 136*
- Patsis P. A., Katsanikas M., 2014a, *MNRAS*, 445, 3525 *cited on pages 17*
- Patsis P. A., Katsanikas M., 2014b, *MNRAS*, 445, 3546 *cited on pages 16*
- Peñarrubia J., Ma Y. Z., Walker M. G., McConnachie A., 2014, *MNRAS*, 443, 2204 *cited on pages 27*
- Perez-Villegas A., Portail M., Gerhard O., 2017, *MNRAS*, 464, L80 *cited on pages 72 and 125*
- Planck Collaboration et al., 2013, *Astron. Astrophys. Vol. 571, id.A16, 66 pp.*, 571 *cited on pages 104*
- Portail M., Wegg C., Gerhard O., Martinez-Valpuesta I., 2015a, *MNRAS*, 448, 713 *cited on pages 22, 74, 75, and 82*
- Portail M., Wegg C., Gerhard O., 2015b, *MNRAS*, 450, L66 *cited on pages 17*
- Portail M., Gerhard O., Wegg C., Ness M., 2017a, *MNRAS*, 465, 1621 *cited on pages 74, 75, 81, 82, 92, and 136*
- Portail M., Wegg C., Gerhard O., Ness M., 2017b, *MNRAS*, 470, 1233 *cited on pages 140*
- Prendergast K. H., 1983, in Athanassoula E., ed., Vol. 100, Intern. Kinemat. Dyn. galaxies; Proc. Symp. Besancon, Fr. August 9-13, 1982 (A83-49201 24-89). Dordrecht, D. Reidel Publ. Co., 1983, p. 215-220.. Dordrecht, D. Reidel Publishing Co., Besancon, pp 215–220, doi:1983IAUS..100..215P, <http://adsabs.harvard.edu/abs/1983IAUS..100..215P> *cited on pages 18*
- Price D. J., et al., 2017, *Publ. Astron. Soc. Aust.* *cited on pages 141 and 142*

- Raha N., Sellwood J. A., James R. A., Kahn F. D., 1991, *Nature*, 352, 411
cited on pages 9, 16, 32, and 72
- Rahmani S., Lianou S., Barmby P., 2016, *MNRAS*, 456, 4128 *cited on pages 27, 28, and 127*
- Rautiainen P., Salo H., 2000, *A&A*, 362, 465 *cited on pages 15 and 141*
- Reach W. T., et al., 2005, *Publ. Astron. Soc. Pacific*, 117, 978 *cited on pages 34 and 77*
- Riffeser A., Fliri J., Seitz S., Bender R., 2006, *Astrophys. J. Suppl. Ser.*, 163, 225
cited on pages 143 and 144
- Rix H.-W., de Zeeuw P. T., Cretton N., van der Marel R. P., Carollo C. M., 1997, *ApJ*, 488, 702
cited on pages 80
- Ruiz M. T., 1976, *ApJ*, 207, 382 *cited on pages 23, 68, and 73*
- Saglia R. P., et al., 2010, *A&A*, 509, A61 *cited on pages 22, 32, 33, 40, 54, 56, 59, and 88*
- Saglia R. P., et al., 2016, *ApJ*, 818, 69 *cited on pages 22 and 135*
- Saglia R. P., Opitsch M., Fabricius M. H., Bender R., Blaña M., Gerhard O., 2018, *Submitt. to A&A*
cited on pages 22, 135, 136, and 140
- Saha K., Gerhard O., 2013, *MNRAS*, 430, 2039 *cited on pages 23*
- Saha K., Martinez-Valpuesta I., Gerhard O., 2012, *MNRAS*, 421, 333
cited on pages 5, 32, and 72
- Saha K., Gerhard O., Martinez-Valpuesta I., 2016, *A&A*, 588, A42
cited on pages 32, 72, and 125
- Sakari C. M., et al., 2016, *ApJ*, 829, 116 *cited on pages 141*
- Sanders J. L., Evans N. W., 2017, *Mon. Not. R. Astron. Soc. vol. 472, issue 3, pp. 2670-2685, 472, 2670*
cited on pages 28
- Sanders R. H., Tubbs A. D., 1980, *ApJ*, 235, 803 *cited on pages 13*
- Schiavon R. P., Caldwell N., Conroy C., Graves G. J., Strader J., Macarthur L. A., Courteau S., Harding P., 2013, *Astrophys. J. Lett.*, 776
cited on pages 141
- Schlafly E. F., Finkbeiner D. P., 2011, *ApJ*, 737, 103 *cited on pages 109*
- Schwarz M. P., 1981, *ApJ*, 247, 77 *cited on pages 15 and 141*
- Schwarzschild M., 1979, *ApJ*, 232, 236 *cited on pages 140*
- Sellwood J. A., 1996, *Barred galaxies. Astron. Soc. Pacific Conf. Ser.*, 91 *cited on pages 16*

- Sellwood J. A., 2012, *ApJ*, 751, 44 *cited on pages 24*
- Sellwood J. A., Carlberg R. G., 2014, *ApJ*, 785, 137 *cited on pages 68*
- Sellwood J. A., Valluri M., 1997, *MNRAS*, 287, 124 *cited on pages 82*
- Sellwood J. A., et al., 2003, *ApJ*, 587, 638 *cited on pages 82*
- Sersic J., 1968, Atlas galaxias australes, Cordoba, Argentina Obs. Astron.
cited on pages 38 and 109
- Shen J., Sellwood J. A., 2004, *ApJ*, 604, 614 *cited on pages 18*
- Shen J., Rich R. M., Kormendy J., Howard C. D., De Propris R., Kunder A., 2010, *Astrophys. J. Lett.*, 720, L72 *cited on pages 72*
- Sheth K., et al., 2008 *cited on pages 13*
- Simon J. D., Geha M., 2007, *ApJ*, 670, 313 *cited on pages 28*
- Skokos C., Patsis P. A., Athanassoula E., 2002a, *Mon. Not. R. Astron. Soc. Vol. 333, Issue 4, pp. 847-860.*, 333, 847 *cited on pages 16*
- Skokos C., Patsis P. A., Athanassoula E., 2002b, *Mon. Not. R. Astron. Soc. Vol. 333, Issue 4, pp. 861-870.*, 333, 861 *cited on pages 16*
- Sotnikova N. Y., Rodionov S. A., 2005, *Astron. Lett.*, 31, 15 *cited on pages 51*
- Springel V., Di Matteo T., Hernquist L., 2005, *MNRAS*, 361, 776 *cited on pages 6 and 36*
- Springel V., et al., 2008, *MNRAS*, 391, 1685 *cited on pages 6 and 11*
- Stark A. A., 1977, *ApJ*, 213, 368 *cited on pages 68*
- Stark A. A., Binney J., 1994, *ApJ*, 426, L31 *cited on pages 68, 104, and 106*
- Syer D., Tremaine S., 1996, *MNRAS*, 282, 223 *cited on pages 73, 74, 75, and 140*
- Tabatabaei F. S., Berkhuijsen E. M., 2010, *A&A*, 517, A77 *cited on pages 27*
- Tamm a., Tempel E., Tenjes P., Tihhonova O., Tuvikene T., 2012, *A&A*, 546, A4
cited on pages 24, 63, 104, and 136
- Tanaka M., Chiba M., Komiyama Y., Guhathakurta P., Kalirai J. S., Iye M., 2010, *ApJ*, 708, 1168
cited on pages 32
- Teuben P., 1995, *Astron. Data Anal. Softw. Syst. IV, ASP Conf. Ser. eds. R.A. Shaw, H.E. Payne, J.J.E. Hayes.*, 77 *cited on pages 35*

- Thomas J., Saglia R. P., Bender R., Thomas D., Gebhardt K., Magorrian J., Richstone D., 2004, *MNRAS*, 353, 391 *cited on pages 22 and 140*
- Toomre a., 1964, *ApJ*, 139, 1217 *cited on pages 36, 70, and 125*
- Toomre A., 1977, *Evol. Galaxies Stellar Popul. Proc. a Conf. Yale Univ.* eds Beatrice M. Tinsley Richard B. Larson. New Haven Yale Univ. Obs. *cited on pages 6, 32, and 72*
- Toomre A., 1981, *Struct. Evol. Norm. galaxies; Proc. Adv. Study Inst.*, pp 111–136 *cited on pages 24*
- Tremaine S., 1995, 110, 628 *cited on pages 21*
- Tremaine S., Ostriker J. P., 1982, *ApJ*, 256, 435 *cited on pages 22*
- Tremaine S., Weinberg M. D., 1984, *ApJ*, 282, L5 *cited on pages 88 and 104*
- Vogelsberger M., et al., 2014a, *Mon. Not. R. Astron. Soc. Vol. 444, Issue 2*, p.1518-1547, 444, 1518 *cited on pages 6*
- Vogelsberger M., et al., 2014b, *Nature, Vol. 509, Issue 7499*, pp. 177-182 (2014)., 509, 177 *cited on pages 6*
- Walterbos R. A. M., Kennicutt, R. C. J., 1988, *A&A*, 198 *cited on pages 34 and 42*
- Watkins L. L., Evans N. W., An J. H., 2010, *MNRAS*, 406, 264 *cited on pages 27*
- Watkins L. L., Evans N. W., Van de ven G., 2013, *MNRAS*, 430, 971 *cited on pages 28*
- Wegg C., Gerhard O., 2013, *MNRAS*, 435, 1874 *cited on pages 22 and 72*
- Wegg C., Gerhard O., Portail M., 2016, *MNRAS*, 463, 557 *cited on pages 143 and 144*
- Wetzel A. R., et al., 2016, *ApJ*, 827, L23 *cited on pages 28*
- Widrow L. M., Dubinski J., 2005, *ApJ*, 631, 838 *cited on pages 23, 24, 62, 63, 68, 73, and 86*
- Widrow L., Perrett K., Suyu S., 2003, *ApJ*, pp 311–325 *cited on pages 23, 68, 73, 86, and 99*
- Williams B. F., et al., 2015, *ApJ*, 806, 48 *cited on pages 25 and 27*
- Williams B. F., et al., 2017,] 10.3847/1538-4357/aa862a, 145 *cited on pages 24 and 28*
- Zieleniewski S., Houghton R. C. W., Thatte N., Davies R. L., 2015, *MNRAS*, 452, 597 *cited on pages 98*
- de Vaucouleurs G., 1958, *ApJ*, 128, 465 *cited on pages 21, 39, and 76*

- de Vaucouleurs G., de Vaucouleurs A., Corwin, H. G. J., Buta R. J., Paturel G., Fouqué P., 1991, Third Ref. Cat. Bright Galaxies. Vol. I Explan. Ref. Vol. II Data galaxies between 0h 12h. Vol. III Data galaxies between 12h 24h. *cited on pages 21, 59, and 78*
- del Burgo C., Mediavilla E., Arribas S., 2000, [ApJ](#), 540, 741 *cited on pages 26*
- van der Marel R. P., Franx M., 1993, [ApJ](#), 407, 525 *cited on pages 80*

Appendix

5.6 Constants and units

$$G = 4.3 \times 10^{-6} \left(\frac{\text{kpc}}{M_{\odot}} \right) \left(\frac{\text{km}}{\text{s}} \right)^2 = 4.49842 \times 10^{-12} \left(\frac{\text{kpc}}{M_{\odot}} \right) \left(\frac{\text{kpc}}{\text{Myr}} \right)^2 \quad (5.1)$$

$$G = 39.16 \left(\frac{\text{AU}}{M_{\odot}} \right) \left(\frac{\text{AU}}{\text{yr}} \right)^2 = 6.67428 \times 10^{-11} \left(\frac{\text{m}}{\text{kg}} \right) \left(\frac{\text{m}}{\text{s}} \right)^2 \quad (5.2)$$

$$h = 6.62606957 \times 10^{-34} \text{ (m}^2 \text{ kg/s)} \quad (5.3)$$

$$1 \text{ (km/s)} = 1.022(69 - 73) \text{ (kpc/Gyr)} \quad (5.4)$$

$$1 \text{ (AU)} = 1.5 \times 10^8 \text{ (km)} \quad (5.5)$$

$$1 \text{ (pc)} = 3.261 \text{ (Lyr)} = 3.09 \times 10^{13} \text{ (km)} = 205712.0166 \text{ (AU)} \quad (5.6)$$

$$1 L_{\odot} = 3.889 \times 10^{26} \text{ (W)} \quad (5.7)$$

$$1 M_{\odot} = (1.98855 \pm 0.00025) \times 10^{30} \text{ kg} \quad (5.8)$$

$$1 R_{\odot} = 6.955 \times 10^8 \text{ m} = 0.0046491 \text{ AU} \quad (5.9)$$

5.7 Basic relations

$$F_{\text{band}} = L_{\text{band}} / (4\pi D^2) \quad (5.10)$$

$$m_1 - m_2 = -2.5 \log_{10} (F_1/F_2) \quad (5.11)$$

$$m_{\text{band}} - M_{\text{band}} = 5 \log_{10} (D/(10 \text{ pc})) \quad (5.12)$$

$$M_{\text{band}} = M_{\text{band}}^{\text{sun}} - 2.5 \log_{10} (L_{\text{band}}/L_{\odot}) \quad (5.13)$$

$$L_{\text{band}} (1 \text{ arcsec}^2) = I_{\text{band}} D^2 \delta\theta_0^2 \quad (5.14)$$

$$\delta\theta_0 = 1 \text{ arcsec} = 1/206265 [\text{rad}] \quad (5.15)$$

$$\mu_{\text{band}} = m_{\text{band}} (1 \text{ arcsec}^2) \quad (5.16)$$

$$\mu_{\text{band}} [\text{mag/arcsec}^2] = M_{\text{band}}^{\text{sun}} + 21.572 - 2.5 \log_{10} (I_{\text{band}}/(L_{\odot}/\text{pc}^2)) \quad (5.17)$$

5.8 Stellar dynamics

Plummer profile

$$\rho_p(r) = \frac{3}{4\pi} \frac{M_{\text{Pl}}}{r_{\text{Pl}}^3} \frac{1}{\left(1 + (r/r_{\text{Pl}})^2\right)^{5/2}} \quad M_p(r) = M_{\text{Pl}} \left(\frac{r^2/r_{\text{Pl}}^2}{1 + (r/r_{\text{Pl}})^2} \right)^{3/2} \quad (5.18)$$

$$\Sigma_p(R) = \frac{1}{\pi} \frac{M_{\text{Pl}}}{r_{\text{Pl}}} \frac{1}{\left(1 + R^2/r_{\text{Pl}}^2\right)^2} \quad \phi_p(r) = \frac{-G M_{\text{Pl}}}{\left(r^2 + r_{\text{Pl}}^2\right)^{1/2}} \quad (5.19)$$

$$\nabla\phi_p(r) = \frac{G M_{\text{Pl}}}{\left(r^2 + r_{\text{Pl}}^2\right)^{3/2}} \vec{r} \quad \sigma(r) = \sqrt{\frac{G M_{\text{Pl}}}{6 r_{\text{Pl}}}} \frac{1}{\left(1 + r^2/r_{\text{Pl}}^2\right)^{1/4}} \quad (5.20)$$

$$\sigma_{\text{LOS}}(R) = \sqrt{\frac{3\pi G M_{\text{Pl}}}{64 r_{\text{Pl}}}} \frac{1}{\left(1 + R^2/r_{\text{Pl}}^2\right)^{1/4}} \quad (5.21)$$

Hernquist profile

$$\rho_h(r) = \frac{1}{2\pi} \frac{M_{\text{H}}}{r_{\text{H}}^3} \frac{1}{r/r_{\text{H}}} \frac{1}{\left(1 + r/r_{\text{H}}\right)^3} \quad M_h(r) = M_{\text{H}} \left(\frac{r/r_{\text{H}}}{1 + r/r_{\text{H}}} \right)^2 \quad (5.22)$$

$$\phi_h(r) = \frac{-G M_{\text{H}}}{r + r_{\text{H}}} \quad \nabla\phi_h(r) = \frac{G M_{\text{H}}}{\left(r + r_{\text{H}}\right)^2} \hat{r} \quad (5.23)$$

$$r_{1/2} = \left(1 + \sqrt{2}\right) r_{\text{H}} \quad (5.24)$$

Isothermal profile

$$\rho_{\text{iso}}(r) = \frac{\exp(-r^2/r_c^2)}{r^2 + \gamma^2} \quad (5.25)$$

Miyamoto Nagai disk profile

$$\phi_{\text{disk}}(R, z) = \frac{-G M_{\text{d}}}{\sqrt{R^2 + \left[b + \sqrt{z^2 + c^2}\right]^2}} \quad (5.26)$$

Navarro Frank White (NFW) profile

$$\rho_{\text{NFW}} = \frac{\rho_o}{(r/r_s)(1+r/r_s)^2} \quad (5.27)$$

$$M_{\text{NFW}} = 4\pi\rho_o r_s^3 \left(\ln(1+r/r_s) - \frac{r/r_s}{1+r/r_s} \right) \quad (5.28)$$

$$\phi_{\text{NFW}} = -4\pi\rho_o r_s^3 \left(\frac{\ln(1+r/r_s)}{r} - \frac{1}{r_c+r_s} \right) \quad (5.29)$$

Einasto profile (3D Sersic with $\alpha = 1/n$)

$$\rho_E(m) = \rho_o \exp \left\{ -\frac{2}{\alpha} \left[\left(\frac{m}{m_o} \right)^\alpha - 1 \right] \right\}; m^2 = x^2 + y^2 + (z/q)^2 \quad (5.30)$$

Sérsic profile

$$\Sigma(R) = \Sigma_c \exp \left(-b_n \left[(R/R_c)^{1/n} - 1 \right] \right); b_n = 1.999n - 0.3271 \quad (5.31)$$

(Capaccioli 1989)

De Vaucouleurs profile (n=4)

$$\Sigma(R) = \Sigma_c \exp \left(-7.669 \left[(R/R_c)^{1/4} - 1 \right] \right) \quad (5.32)$$

(Capaccioli 1989)

Jaffe profile

$$\rho_J(r) = \frac{1}{4\pi} \frac{M_J}{r_J^3} \frac{1}{(r/r_J)^2} \frac{1}{(1+r/r_J)^2} \quad \phi_J(r) = \frac{-GM_J}{r_J} \ln \left(\frac{r}{r+r_J} \right) \quad (5.33)$$

Dispersion profile

$$\sigma_r^2(r) = \frac{1}{\rho(r)} \int_r^\infty \rho(r') \frac{GM(r')}{r'^2} dr' \quad (5.34)$$

5.9 Tables

Table 5.1: Solar absolute magnitudes in different bands ($M_{\text{band}}^{\text{sun}} [mag/ \text{arcsec}^2]$).

$M_{\text{bol}}^{\text{sun}}$	$M_{\text{U}}^{\text{sun}}$	$M_{\text{B}}^{\text{sun}}$	$M_{\text{V}}^{\text{sun}}$	$M_{\text{R}}^{\text{sun}}$	$M_{\text{I}}^{\text{sun}}$	$M_{\text{J}}^{\text{sun}}$	$M_{\text{H}}^{\text{sun}}$	$M_{\text{K}}^{\text{sun}}$	$M_{3.6\mu\text{m}}^{\text{sun}}$	$M_{4.5\mu\text{m}}^{\text{sun}}$
4.74 ⁽¹⁾	5.61 ⁽¹⁾	5.48 ⁽¹⁾	4.83 ⁽¹⁾	4.42 ⁽¹⁾	4.08 ⁽¹⁾	3.64 ⁽¹⁾	3.32 ⁽¹⁾	3.28 ⁽¹⁾	3.24 ⁽²⁾	3.27 ⁽²⁾

Notes: (1) values from [Binney & Merrifield \(1998\)](#), (2) values from [Oh et al. \(2008\)](#) for the bands 3.6 and 4.5 μm ; also available here <https://www.astro.umd.edu/ssm/ASTR620/mags.html>

Table 5.2: Spectral types of stars.

Type	$M [M_{\odot}]$	$L [L_{\odot}]$	$R [R_{\odot}]$	$N [\%](^*)$	$T [\text{K}]$	$\tau_{\text{life}} [\text{Myr}]$
O	≥ 16	$\sim 3 \times 10^4$	6.6	3×10^{-5}	3.3×10^4	< 10
B	2.1 - 16	25 - 3×10^4	1.8 - 6.6	0.13	10^4 - 3.3×10^4	10 - 20
A	1.4 - 2.1	5 - 25	1.4 - 1.8	0.6	0.75×10^4 - 10^4	

Notes: (*) for a Kroupa IMF.

Table 5.3: Redshift, age and time conversion.

z	0	0.1	0.2	0.5	1	2	5	10	100	1000	1100
$t [\text{Gyr}]$	0	1.310	2.451	5.093	7.817	10.404	12.469	13.721	13.721	13.721	13.721
Age [Gyr]	13.721	12.411	11.270	8.628	5.903	3.316	1.186	0.478	0.016633	4.34×10^{-4}	3.7×10^{-4}
(since the Big Bang)										(0.43 Myr)	(0.37 Myr)

Notes: with $H_0=69.6$, $\Omega_{\text{M}}=0.286$, $\Omega_{\text{vac}}=0.714$ using the cosmological calculator <http://www.astro.ucla.edu/wright/CosmoCalc.html> (Wright 2006, PASP, 118, 1711).

Acknowledgements

I would like to deeply thank all the people that I meet during my doctorate in München. I thank my supervisor Ortwin Gerhard for the great opportunity to work at the Max Planck Institute for extraterrestrial Physics, a challenging and amazing opportunity to be part of a community of people that are the world leaders in their fields. I thank my IMPRS committee and my thesis exam committee members Roberto Saglia, Peter Erwin, Jan Lipfert, Martin Kerscher, Gerhard Buchalla, and Klaus Dolag. I specially thank Christopher Wegg for scientifically mentoring and supporting me during these challenging years, from whom I learn so much (but I still cannot talk to machines like him). I also thank the Deutscher Akademischer Austauschdienst (DAAD) for their support to my doctoral project with its Research Grant for Doctoral Candidates and Young Academics and Scientists (57076385), particularly to the persons in charge of my scholarship Patricia Guzman and Elke Massa.

A collateral blessing from Astronomy is the opportunity I had to meet people from the five continents from whom I have learned so much, not only scientifically, but also spiritually. I would like to thank all my friends and colleagues that I meet during these years in Germany, particularly thank my most dear Waikiki buddies Laura Morselli (Loca), Florian Hoffmann, Karina Voggel, Julian Alvarado, and my Italian friends, who also teach me the cannons and commandments of pizza, pasta and coffee, Alessia Longobardi, Anna Brucalasi, Federica Peponi, Claudia Pulsoni, Alessandrito, and my philosophical *consigliere* Alessandro Ballone. I thank my most dear drei Tekkannische Muskeitiere Manuel Behrend (Manuloco), Fabrizio Finozzi (Gorlami, Granpa) and Michael Opitsch, and my roommate and eternal friend Jethro (the Dude, Chewbi, Jeti, Sasquash) Ridl. I thank my Chilean friends Daniel Rivas, Rodrigo Herrera Camus (de Acuario) and his family (Fa & Olivita), Salvador Salazar and his family, my South American friends Eliana Amazo, Ximena Mazzalay (good mate tea), Ariel Sanchez and Almita; and my German friends Michael Fellhauer, Annette Gerlach and Niko Beller. I also thank my dear friends from the Montania that visited me during these years: Michael Wendler, Victor Valenzuela, Ingo Stotz, Renato Valverde, Stephan Mier, Cristian Piel, Ulrich Gamm, Miguel Saez, Klaus Hohf. I also thank my officemates and friends Sotiris Chatzopolous and Maria de los Angeles Perez Villegas (Ankeles), and my group friends with whom I shared so many moments Isabella Söldner-Rembold, Matthieu Portail, Johanna Hartke, Shela Whyllie, Jonathan Clarke, the OPINAS friends Jiamin Hou, Martha Lippich, Matteo Fossati, the highly energetic friends Philip Wiseman, Fabian Knust, Karla Varela, Georgios Vasilopoulos and Mohit Tanga, and the astrochemical friends Vlas Sokolov, Ana Chacón, Domenico Prudenzano, Johanna Chantzios. I thank Christa Ingram for her support, always happy to help me, and particularly for helping me

finding an apartment in Munich when I arrived, a task that is extremely difficult in this city, and I thank Achim Bohnet for constantly helping me, saving my computers from me.

Finally, I thank my beloved family Claudio, Ana, Heidi, Claudio and his family for always by my side in difficult and happy times, I specially thank my beloved and beautiful Carolina, for being by my side supporting and tolerating my grumpiness all these years.

This is not the end, but the beginning of new adventures. It was a pleasure meeting all of you. I wish everyone best success in your present and future endeavours and a profound happiness.

The Last Toast

*Whether we like it or not,
We have only three choices:
Yesterday, today and tomorrow.*

*And not even three
Because as the philosopher says
Yesterday is yesterday
It belongs to us only in memory:
From the rose already plucked
No more petals can be drawn.*

*The cards to play
Are only two:
The present and the future.*

*And there aren't even two
Because it's a known fact
The present doesn't exist
Except as it edges past
And is consumed...,
like youth.*

*In the end
We are only left with tomorrow.
I raise my glass
To the day that never arrives.*

*But that is all
we have at our disposal.*